

Jiaqi Yan

Precision Therapeutics: Harnessing Receptor-targeted and Dynamic DNA Nanotechnology





Jiaqi Yan

Born 1994, Liaoning, China

Previous studies and degrees

Master of Pharmacy, Guangdong Pharmaceutical University, 2020

Bachelor of Science, Shenyang Pharmaceutical University, 2017



Precision Therapeutics: Harnessing Receptor-targeted and Dynamic DNA Nanotechnology

Jiaqi Yan

Pharmaceutical Sciences Laboratory
Faculty of Science and Engineering
Åbo Akademi University
Åbo, Finland, 2024

Main supervisor	Professor Hongbo Zhang Pharmaceutical Sciences Laboratory Åbo Akademi University Finland Turku Bioscience Centre University of Turku and Åbo Akademi University Finland
Co-supervisors	Adjunct Professor Outi M. H. Salo-Ahen Pharmaceutical Sciences Laboratory & Structural Bioinformatics Laboratory, Biochemistry Åbo Akademi University Finland Professor Wenguo Cui Ruijin Hospital, School of Medicine Shanghai Jiao Tong University China
Reviewers	Professor Mauri Kostinen Department of Bioproducts and Biosystems Aalto University Finland Professor Andreas Herrmann Institute for Technical and Macromolecular Chemistry RWTH Aachen University Germany
Opponent	Professor Mauri Kostinen Department of Bioproducts and Biosystems Aalto University Finland

ISBN 978-952-12-4361-5 (printed)
ISBN 978-952-12-4362-2 (digital)
Painosalama, Turku, Finland 2024

Wish for world peace

Abstract

In recent years, significant progress has been made in the development of nanomedicines. Nanosystems for targeted drug delivery are a class of nanomaterials capable of delivering drugs to specific cellular locations, achieving precise, efficient, and safe treatments. Currently, a common approach for cancer-targeted nanotechnology-based drug delivery is to modify the nanoparticle surface with cell-targeting ligands. However, ligand-adorned nanoparticles may also be uptaken by normal tissues. Furthermore, due to significant variation in receptor expression levels between cancers and individuals, there is a lack of suitable, precise ligands for each individual case. MicroRNAs (miRNAs) are intrinsic non-coding small RNA molecules. It has been observed that cancer-related miRNA is overexpressed at cancer sites. Hence, the combination of miRNA targeting strategies and the traditional receptor-mediated targeting should be a promising approach for more precise cancer therapy.

DNA materials possess extensive utility in construction of gene-responsive materials. Among them, dynamic DNA nanotechnology allows for the miRNA-responsive self-assembly of therapeutic oligonucleotides within cells, thereby unleashing sophisticated therapeutic and diagnostic functionalities. Hence, through construction of miRNA-responsive DNA materials, dynamic DNA nanotechnology could contribute to targeted therapies.

In this dissertation, we have studied precise cancer treatment by designing miRNA-targeted DNA nanomaterials and combining them with traditional receptor-mediated targeting techniques. First, nanomaterials were developed to validate their receptor-targeted therapeutic ability. Second, a miRNA-21-responsive DNA nanogel system was built to explore the feasibility of miRNA-21-responsive nanomaterials for targeted cancer therapy. Third, to achieve dual systems that are simultaneously receptor-targeting and miRNA-responsive, DNazymes (man-made DNA sequence that can cleave target RNA molecules at specific sites) were innovatively transformed into miRNA-responsive entities and encapsulated within arginylglycylaspartic acid (RGD)-targeted micelle systems. This achieved carrier-mediated receptor targeting as well as DNzyme-mediated miRNA-21-targeting capabilities. The results indicated the ability of this system to distinctly discriminate between cancerous tissues and adjacent healthy tissues, thereby potentially achieving precise targeted therapy. Finally, to reduce the cost and complexity of DNA nanomaterials, we developed DNA-metal self-assembly techniques. From a materials perspective, we simplified the construction of DNA materials, which is instrumental in advancing their clinical translation.

Sammanfattning

De senaste åren har betydande framsteg gjorts inom utvecklingen av nanomediciner. Nanosystem för riktad läkemedelsleverans är en typ av nanomaterial som kan leverera läkemedel till specifika cellplatser och uppnå exakta, effektiva och säkra behandlingar. För närvarande är en vanlig metod för cancerriktad nanoteknikbaserad läkemedelsleverans att modifiera nanopartikelns yta med cellriktande ligander. Dock kan liganddekorerade nanopartiklar även tas upp av normala vävnader. Dessutom, på grund av betydande variation i receptorexpressionsnivåer mellan cancerformer och individer, finns det brist på lämpliga, precisa ligander för varje individuellt fall. MikroRNA (miRNA) är intrinsiska icke-kodande små RNA-molekyler. Det har observerats att cancerrelaterat miRNA är överuttryckt vid cancerlokaler. Därför bör kombinationen av miRNA-riktade strategier och den traditionella receptor-medierade riktningen vara ett lovande tillvägagångssätt för mer precisa cancerterapi.

DNA-material har omfattande användning inom konstruktionen av genresponsiva material. Bland dem möjliggör dynamisk DNA-nanoteknik miRNA-responsiv självmontering av terapeutiska oligonukleotider inom celler och därigenom släpper loss sofistikerade terapeutiska och diagnostiska funktioner. Således kan dynamisk DNA-nanoteknik genom konstruktion av miRNA-responsiva DNA-material bidra till riktade terapier.

I denna avhandling har vi studerat exakt cancerbehandling genom att designa miRNA-riktade DNA-nanomaterial och kombinera dem med traditionella receptormedierade riktningstekniker. För det första utvecklades nanomaterial för att validera deras receptormålade terapeutiska förmåga. För det andra byggdes ett miRNA-21-responsivt DNA-nanogelsystem för att utforska möjligheten med miRNA-21-responsiva nanomaterial för riktad cancerterapi. För det tredje, för att uppnå dubbla system som samtidigt är receptormålade och miRNA-responsiva, omvandlades DNazymmer (konstgjord DNA-sekvens som kan klippa mål-RNA-molekyler på specifika platser) innovativt till miRNA-responsiva enheter och inkapslades inom arginylglycylaspartat (RGD)-målade micellsystem. Detta uppnådde bärar-medierad receptormålning samt DNazym-medierad miRNA-21-målning. Resultaten indikerade förmågan hos detta system att tydligt särskilja mellan cancer vävnader och intilliggande friska vävnader, därigenom potentiellt uppnå precision inriktad terapi. Slutligen, för att minska kostnaderna och komplexiteten hos DNA-nanomaterial utvecklade vi DNA-metallsjälvmonteringstekniker. Ur ett materialperspektiv förenklade vi konstruktionen av DNA-material, vilket är väsentligt för att främja deras kliniska översättning.

Table of Contents

Abstract.....	i
Sammanfattning	ii
List of original publications	vii
Contribution of the author	viii
Supplementary publications.....	ix
Abbreviations	xi
1 Introduction.....	1
2 Review of literature	3
2.1 Cancer characteristics-based targeting strategy	3
2.2 Introduction of Nanomedicine.....	3
2.2.1 Development of nanomedicine	3
2.2.2 Classification of nanomaterials	4
2.2.2.1 Inorganic nanomaterials	4
2.2.2.2 Organic nanomaterials	6
2.2.2.3 Hybrid nanomaterials	7
2.2.3 Challenges and directions for nanomedicine	8
2.3 Categorization of cancer targeted strategies.....	9
2.3.1 Receptor mediated nanoparticle-based targeting.....	9
2.3.1.1 Folate receptor	9
2.3.1.2 RGD peptide receptors (integrins)	10
2.3.1.3 HER-2 receptor	11
2.3.2 Receptor targeting through DNA strategies.....	12
2.3.3 Local delivery based targeting	14
2.3.4 MiRNA-responsive targeting.....	15
2.4 Introduction of DNA nanotechnology for targeted drug delivery	16
2.4.1 Structural DNA nanotechnology	17

2.4.2 Dynamic DNA nanotechnology	18
2.4.2.1 Toehold mediated strand displacement	18
2.4.2.2 Self-assembly.....	21
2.4.3 DNA oligonucleotides based therapy.....	23
2.4.3.1 DNAzymes	23
2.4.3.2. Antisense oligonucleotides	25
3 Hypothesis and objectives of the work	27
4 Materials and methods	28
4.1 Materials	28
4.2 Nanomaterials preparation approaches	28
4.2.1 Synthesis of folate receptor-targeted zeolitic imidazolate framework-8 (ZIF-8) (I)	28
4.2.2 Synthesis of mesoporous silica nanoparticles (MSNs) (II&III).....	29
4.2.3 Synthesis of a reservoir for bone hydroxyapatite targeted Au@MSN nanocomposite (II)	29
4.2.4 Synthesis of miRNA-21 targeted MSN@DNA nanocomposite (III)	30
4.2.5 Synthesis of RGD and miRNA-21 targeted micelles@calcium phosphate nanocomposite (M@CaP) (IV)	29
4.2.6 Synthesis of HER-2 targeted calcium/DNA framework (V)	30
4.3 Methods for nanosystem characterization.....	30
4.3.1 Structure analysis (I-V)	30
4.3.2 <i>In vitro</i> studies (I-V)	31
4.3.3 <i>In vivo</i> biodistribution study (I- V).....	33
4.3.4 <i>In vivo</i> anticancer efficacy (I- V)	33
4.3.5 <i>In vivo</i> safety evaluation from organ histology (I- V)	34
5 Results and discussion	35
5.1 Development of receptor-targeted nanomaterials (I&II)	35
5.1.1 Design and characterization of the receptor-mediated cancer-targeting nanoparticles.....	35

5.1.1.1 Folate-receptor-targeted nanoparticles (I)	35
5.1.1.2 Bone tissue-targeted nanosystem (II)	37
5.1.1.3 Microgel reservoir of targeted NPs for local drug delivery (II)	39
5.1.2 Cytotoxicity and cell uptake analysis (I&II)	41
5.1.3 <i>In vivo</i> biodistribution evaluation for NPs.....	44
5.1.3.1 Tumor targeting (I&II)	44
5.1.3.2 Therapeutic efficiency assay (II)	46
5.1.3.3 <i>In vivo</i> toxicity study (II)	47
5.2 Fabrication of miRNA and receptor-targeted materials using dynamic DNA nanotechnology (III&IV)	49
5.2.1 Design and characterization of the miRNA-mediated cancer-targeting NPs.....	49
5.2.1.1 MiRNA-targeted DNA hydrogel (III)	49
5.2.1.2 DNA hydrogel/MSN nanocomposite (III)	51
5.2.1.3 miRNA targeted MNAzyme (IV)	53
5.2.1.4 RGD- modified micelle coated by calcium phosphate NPs (IV)	54
5.2.2 <i>In vitro</i> cell targeting and investigation of therapeutic efficiency of NPs	56
5.2.2.1 Cancer cell targeting and (III&IV)	56
5.2.2.2 Gene/ion/photothermal therapy (IV)	58
5.2.3 <i>Evaluation of in vivo biodistribution and treatment outcomes of NPs</i>	59
5.2.3.1 Tumor targeting (IV)	60
5.2.3.2 Gene/chemo/photothermal synergistic therapy (IV)	60
5.3 Simplifying the preparation complexity of cancer-targeting DNA nanotechnology (V)	62
5.3.1 Design and characterization of the aptamer-intergrated DNA nanomaterials	62
5.3.1.1 Metal-nuclear acid framework (V)	62
5.3.1.2 Evaluation of the therapeutic mechanisms of NPs (V)	65
5.3.2 <i>In vivo</i> biodistribution and assessment of the therapeutic effect.....	68
5.3.2.1 tumor targeting (V)	68

5.3.2.2 Therapeutic efficiency assay (V).....	69
6 Concluding and future perspectives	71
6.1 Summary	71
6.2 Future perspectives.....	72
7 Acknowledgements.....	74
8 References	76

List of original publications

I. Mineralization of pH-Sensitive Doxorubicin Prodrug in ZIF-8 to Enable Targeted Delivery to Solid Tumors

Jiaqi Yan, Chang Liu, Qiwei Wu, Junnian Zhou, Xiaoyu Xu, Lirong Zhang, Dongqing Wang,* Fan Yang,* and Hongbo Zhang*. *Analytical Chemistry*. **2020**, 92, 11453–11461. (DOI: 10.1021/acs.analchem.0c02599)

II. Peritumoral Microgel Reservoir for Long-Term Light- Controlled Triple-Synergistic Treatment of Osteosarcoma with Single Ultra-Low Dose

Jiaqi Yan, Yichuan Wang, Meixin Ran, Rawand A. Mustafa, Huanhuan Luo, Jixiang Wang, Jan-Henrik Smått, Jessica M. Rosenholm, Wenguo Cui, Yong Lu,* Zhenpeng Guan,* and Hongbo Zhang*. *Small*. **2021**, 17, 2100479. (DOI: 10.1002/sml.202100479)

III. Self-assembly of DNA nanogels with endogenous microRNA toehold self-regulating switches for targeted gene regulation therapy

Jiaqi Yan, Haixia Zou, Wenhui Zhou, Xiaowan Yuan, Zhijun Li, Xiaodong Ma, Chang Liu, Yonghui Wang, Jessica M. Rosenholm, Wenguo Cui, Xiangmeng Qu* and Hongbo Zhang*. *Biomaterials Science*. **2022**, 10, 4119–4125. (DOI: 10.1039/d2bm00640e)

IV. An Autocatalytic Deoxyribozyme Based Nanomachine for Orthotopic Pancreatic Tumor Targeted and Multilevel Synergistic Photothermal Therapy

Jiaqi Yan, Xiaodong Ma, Danna Liang, Dongdong Zheng, Meixin Ran, Shichong Zhou, Weijian Sun*, Xian Shen*, Hongbo Zhang*. *Nature Communications*. **2023**, 14, 6905. (<https://doi.org/10.1038/s41467-023-42740-2>)

V. Streamlined Aptamer-Deoxyribozyme Based Metal-Nucleic Acid Framework for Reactive Oxygen Species Augmentation Triggered Gastric Cancer Therapy

Jiaqi Yan, Rajendra Bhadane, Meixin Ran, Xiaodong Ma, Outi M. H. Salo-Ahen, Hongbo Zhang*. *Nature Communications*. Revised Manuscript Submitted.

The research reported in this study took place from 2020 to 2023 and was conducted under the supervision of Professor Hongbo Zhang, with co-supervision by Outi M. H. Salo-Ahen at Åbo Akademi University's Pharmaceutical Sciences Laboratory. Part of the study were carried out in collaboration with researchers from Jiangsu University and Wenzhou Medical University in China.

Contribution of the author

1. In publication I, the author undertook experimental work, data analysis, and manuscript writing. Chang Liu conducted the project design. Qiwei Wu provided guidance for animal experiments. Junnian Zhou offered guidance for cell experiments. Xiaoyu Xu contributed to project conceptualization. Lirong Zhang, Dongqing Wang, and Fan Yang provided financial support. Hongbo Zhang conceived the idea, handled manuscript revisions and financial support.
2. In publication II, the author conceived the idea, conducted experiments, analyzed data, and wrote the manuscript. Yichuan Wang contributed to the animal experimental work. Meixin Ran assisted in processing infrared data. Rawand A. Mustafa was involved in the synthesis of gold nanorods. Huanhuan Luo and JiXiang Wang guided the synthesis of gold nanorods. Jan-Henrik Smått helped obtain the characterization parameters of MSN. Jessica M. Rosenholm assisted in refining the language of the manuscript. Wenguo Cui, Yong Lu, Zhenpeng Guan, and Hongbo Zhang contributed to conceiving the idea, manuscript revisions, and provided financial support.
3. In publication III, the author conceived the idea, conducted experiments, data analysis, and manuscript writing. Haixia Zhou provided guidance for the DNA hydrogel experiments. Wenhui Zhou guided the WB experiments. Xiaowan Yuan and Zhijun Li provided experimental equipment. Xiaodong Ma, Chang Liu, and Yonghui Wang assisted in TEM experiments. Jessica M. Rosenholm, Wenguo Cui, Xiangmeng Qu, and Hongbo Zhang assisted in idea conceiving, language editing and provided financial support.
4. In publication IV, the author was responsible for conceptualizing the article, conducting experiments, and manuscript writing. Xiaodong Ma provided experimental materials. Danna Liang was responsible for animal experiments. Dongdong Zheng assisted in obtaining patient tissues. Meixin Ran handled data processing. Shichong Zhou, Weijian Sun, Xian Shen, and Hongbo Zhang helped with designing the experiment, language editing and provided financial support.
5. In manuscript V, the author was responsible for experimental design, execution, and manuscript writing. Rajendra Bhadane assisted in obtaining computer simulation results. Meixin Ran and Xiaodong Ma helped acquire experimental materials. Outi M. H. Salo-Ahen provided guidance on computer simulation techniques. Hongbo Zhang revised the manuscript, conceived the idea, and provided funding support.

Supplementary publications

1. Therapeutic DNazymes: From Structure Design to Clinical Applications

Jiaqi Yan, Meixin Ran, Xian Shen*, Hongbo Zhang*, Advanced Materials. **2023**, 35, 2300374 (DOI: 10.1002/adma.202300374)

2. DNA Nanoflower Eye Drops with Antibiotics-resistant Gene Regulation Ability for MRSA Keratitis Target Treatment

Meixin Ran, Rong Sun, **Jiaqi Yan**, Arto T. Pulliainen, Yu Zhang*, Hongbo Zhang*. Small **2023**, 2304194 (DOI: 10.1002/smll.202304194) (Co-first author)

3. Fabrication of a pH/Redox-Triggered Mesoporous Silica-Based Nanoparticle with Microfluidics for Anticancer Drugs Doxorubicin and Paclitaxel Codelivery

Jiaqi Yan, Xiaoyu Xu, Junnian Zhou, Chang Liu, Lirong Zhang, Dongqing Wang, Fan Yang*, and Hongbo Zhang*, ACS Appl. Bio Mater. **2020**, 3, 2, 1216–1225, (DOI: 10.1021/acsabm.9b01111)

4. A scientific debate: The sword that cleaves chaos of DNzyme catalysis research

Jiaqi Yan, Meixin Ran, Hongbo Zhang*, Biomedical Technology. **2023**, 4, 21–23 (DOI: 10.1016/j.bmt.2023.01.004)

5. Neovascularization-directed bionic eye drops for noninvasive renovation of age-related macular degeneration

Meixin Ran, Yaxin Deng, **Jiaqi Yan**, Anan Zhang, Ying Wei, Xiaowen Li, Haibing He, Jingxin Gou, Tian Yin, Xing Tang, Jun Kong, Han Zhang, Hongbo Zhang*, Yu Zhang*, Chem. Eng. J. **2022**, 450, 138291 (DOI:10.1016/j.cej.2022.138291) (Co-first author)

6. Pharmaceutical electrospinning and 3D printing scaffold design for bone regeneration

Zhen Wang, Yichuan Wang, **Jiaqi Yan**, Keshi Zhang, Feng Lin, Lei Xiang, Lianfu Deng, Zhenpeng Guan, Wenguo Cui*, Hongbo Zhang*, Advanced drug delivery reviews. **2021**, 174, 504–534. (DOI: 10.1016/j.addr.2021.05.007) (Co-first author)

7. Ca²⁺ enhanced photosensitizer/DNase I nanocomposite mediated bacterial eradication through biofilm disruption and photothermal therapy

Meixin Ran, Zahra Gounani, **Jiaqi Yan**, Jessica M. Rosenholm*, Hongbo Zhang*,

Nano Select. **2022**, 3, 1201. (doi.org/10.1002/nano.202200026) (Co-first author)

8. Progress of delivery methods for CRISPR-Cas9

Wu Yang, **Jiaqi Yan**, Pengzhen Zhuang, Tao Ding, Yu Chen, Yu Zhang, Hongbo Zhang* and Wenguo Cui*, Expert Opinion on Drug Delivery. **2022**, 19, 913-926, (DOI: 10.1080/17425247.2022.2100342)

Abbreviations

ALN	Alendronate
ASOs	Antisense oligonucleotides
ATP	Adenosine triphosphate
AuNRs	Gold nanopaticles
CaP	Calcium phosphate, $\text{Ca}_9(\text{PO}_4)_6$
Ce6	2,6-dihydroxyanthraquinone
CTAB	Hexadecyl trimethyl ammonium bromide
CTAC	Cetyltrimethylammonium chloride
Cy5.5	Sulfo-Cyanine5.5 NHS ester
DDS	Drug delivery system
DOX	Doxorubicin
DCM	Dichloromethane
DSB	Double strand break
DAPI	4',6-diamidino-2-phenylindole
DMAP	4-dimethylaminopyridine
DMSO	Dimethyl sulfoxide
DNA	Deoxyribonucleic acid
DNAzyme	DNA enzyme (deoxyribozyme)
DCFH-DA	2',7'-Dichlorodihydrofluorescein diacetate
DLS	Dynamic light scattering
DTT	Dithiothreitol
ECM	Extracellular matrix
EPR	Enhanced permeation and retention
FA	Folic acid
FTIR	Fourier-transform infrared spectroscopy
FBS	Fetal bovine serum
FRET	Förster/Fluorescence resonance energy transfer
GSH	Glutathione
GeIMA	Gelatin Methacrylamid
HCR	Hybridization chain reaction
HER-2	Human epidermal growth factor receptor 2
IRF-1	IRF1 interferon regulatory factor 1
LNPs	Lipid nanoparticles

LPNPs	Lipid-polymer hybrid nanoparticles
MiRNA	MicroRNA
miR-21	microRNA-21
MSN	Mesoporous silica nanoparticle
MS	Mass spectrum
MFI	Mean fluorescent intensity
MA	Methacrylic anhydride
MOFs	Metal-Organic Frameworks
NMR	Nuclear magnetic resonance spectroscopy
NPs	Nanoparticles
NHS	N-Hydroxy succinimide
NNI	National Nanotechnology Initiative
NSTC	National Science and Technology Council
PBS	Phosphate-buffered saline
PDT	Photodynamic therapy
PEG	Polyethylene glycol
PMI	Precision Medicine Initiative
PNA	Peptide nucleic acid
PTT	Photothermal therapy
PTEN	Phosphatase and TENsin homolog deleted on chromosome 10
PDCD4	Programmed Cell Death 4
RES	Reticuloendothelial system
ROS	Reactive oxygen species
RNAi	RNA interference
RISC	RNA-induced silencing complex
RGD	Arg-Gly-Asp
TAT	Thrombin-antithrombin complex
TEM	Transmission electron microscopy
TEOS	Tetraethoxysilane
TMSPMA	3-(Trimethoxysilyl)propyl methacrylate
WST-1	water-soluble tetrazolium salt (cell proliferation assay Roche diagnostics reagent)
ZIF	Zeolitic imidazolate framework

1 Introduction

Cancer is a disease that poses a serious threat to public health and has a low cure rate, with a tendency for easy relapse and metastases. Thanks to continuous advancements in treatment methods, the cancer mortality rate has been steadily declining since 2019, with a decrease of 1.5% (Siegel et al., 2023). However, with changes in lifestyle, the morbidity for developing cancer has been increasing year by year.

To date, surgical intervention, chemotherapy, and emerging gene therapies are the primary means of treating cancer in clinical practice. Surgical treatment involves the physical removal of tumors, but it leads to significant trauma, and has limited effectiveness for metastatic tumors. Chemotherapy uses chemical drugs to inhibit tumor growth, and it can kill both local and metastatic tumor cells, but it also damages healthy cells. Oligonucleotide-mediated gene therapy can precisely target specific genes, enhancing treatment selectivity. However, off-target effects and susceptibility to degradation limit their applications (Kulkarni et al., 2021). Therefore, it is crucial to develop methods that can protect oligonucleotide-based drugs from degradation and enable targeted therapy of only cancer cells, to alleviate the serious side-effects.

In the past two decades, nanomedicine for cancer treatment has rapidly advanced. Nanocarriers possess unique characteristics such as small size, large surface area, and strong adsorption capabilities, enabling them to bind or carry drugs or genes. Moreover, nanomedicine delivery systems can reduce off-target effects of anticancer drugs, increase the stability of nucleic acids, and enable site-specific drug release. Among different targeting strategies, receptor-mediated targeting mechanisms are of utmost importance. However, although surface modification of nanocarriers using targeting ligands has been successfully employed for targeting cancer cells (Zhou et al., 2016), surface-modified ligands may interact with serum proteins during system administration, or react with enzymes at cancer sites, leading to covering or degradation of ligands (Wang et al., 2016). Furthermore, receptor-mediated targeting approaches face limitations due to the limited variety of suitable receptors. This is because receptor expression levels vary significantly both between cancers and individuals, making it challenging to identify receptors with 100% cancer specificity.

To solve these issues, it is of great significance to construct other cancer-targeting strategies, to synergize with receptor-mediated targeting. For example, miRNAs are a class of naturally occurring non-coding small RNA molecules that have been found to be associated with cancer occurrence, progression, diagnosis, and prognosis (Lu et al., 2005). For instance, microRNA-21 (miR-21) is highly expressed in pancreatic cancer tumors and has been shown to promote pancreatic cancer metastasis, recurrence, and even the growth of tumor stem cells (Sicard et al., 2013). Therefore, targeting miRNAs holds promise for achieving cancer-specific therapeutic outcomes.

Additionally, miRNA regulation can also confer therapeutic benefits, thus realizing a dual effect of targeted and gene therapies.

However, the miRNA targeting technology is still immature, and the research field is currently focused mostly on the detection and regulation of miRNA (Hou et al., 2022; Li et al., 2022) rather than the use of miRNA to achieve targeted therapies. Dynamic DNA nanotechnology can realize the construction of miRNA-responsive materials, including hydrogel materials (Guo et al., 2023), or realize the dynamic self-assembly of DNA sequences under miRNA stimuli (Sánchez-Visedo et al., 2023). Nevertheless, the complex design of DNA nanomaterials and their high cost make it difficult for pure DNA nanotechnology to achieve large-scale clinical translation. Therefore, reducing the number of fabrication procedures of DNA materials could solve the above problems and enhance the efficacy of DNA materials in the field of targeted cancer therapies.

In this thesis, miRNA targeting strategy was investigated through dynamic DNA nanotechnology, to synergize receptor-targeted strategy. Furthermore, the fabrication methods of DNA materials were simplified to improve the clinical translation potential of DNA nanotechnology.

2 Review of literature

2.1 Cancer characteristics-based targeting strategy

Traditional tumor-targeted drug delivery systems (DDS) encounter numerous challenges, including poor systemic circulation, low targeting efficiency, limited tumor penetration, and uncontrolled drug release (Li et al., 2019). In recent years, intelligent DDS design principles have been based on utilizing the physicochemical differences between cancer cells and normal cells, such as variations in pH, amount of ROS (reactive oxygen species) and GSH (glutathione), cellular hypoxia, and enzymatic activity within tumor cells compared to normal tissues and intracellular compartments (Sun and Jiang 2023). Additionally, receptors that are highly expressed on tumor cell surfaces can also be exploited as targets for drug delivery.

The cellular targeting characteristics mentioned above require drugs to accumulate at tumor sites in a stable form, or at least stable during the *in vivo* circulation. Therefore, achieving excellent drug solubility and stability, as well as great accumulation at tumor sites is of utmost importance. In recent years, nanomaterials have been widely employed to achieve these goals, primarily due to the enhanced permeability and retention (EPR) effect, which enables their targeting to tumor cell sites (Nakamura et al., 2016). Therefore, the physiological differences between cancer cells and normal cells and the overexpression of suitable receptors can be harnessed to create nanocarriers for controlled drug release and even multi-stage drug delivery.

2.2 Introduction of Nanomedicine

2.2.1 Development of nanomedicine

Early efforts in nanoparticle research focused on enhancing the solubility of encapsulated cargo and prolonging circulation time to improve safety and efficacy (Blanco et al., 2015). The National Science and Technology Council (NSTC) of the United States initiated the National Nanotechnology Initiative (NNI) in 2000 to advance nanotechnology development. NNI outlined research priorities, plans, and challenges, contributing to advancements in nanotechnology research (Mitchell et al., 2021). With promising outcomes in *in vitro* and small animal models, nanomaterials have displayed significant potential (Mitragotri et al., 2017).

However, despite NNI's impetus, the clinical application of nanomedicine remains below expectations, partly due to species differences between animals and humans (Wechsler et al., 2019). Physiological and pathological variations between species have not been thoroughly explored, particularly how these differences alter the behavior of nanomaterials *in vivo* (Hua et al., 2018). Moreover, species differences are not the sole limiting factors in clinical translation. Heterogeneity among patients also restricts the *in vivo* performance of nano-delivery systems. Specifically, the structural and

functional changes at cancer sites can affect the distribution and performance of nanoparticles.

Current nanoparticle design primarily focuses on integrating complex structures, bio-responsive components, and targeting modules to enhance delivery (Culver et al., 2017; Wagner et al., 2018). New endeavors to address patient subpopulation-specific biological environment through novel types of nanoparticles benefited from the Precision Medicine Initiative (PMI) established by the Obama administration in 2015 (Collins and Varmus 2015). The aim of precision medicine is to formulate personalized treatment plans, minimizing the impact of patient heterogeneity and achieving more accurate patient stratification. Based on the accurate stratification (for example, different gene expression for specific stratified patients), nanosystems can play a more accurate way for targeting drug delivery.

In summary, nanomedicine has evolved from its traditional focus on increasing drug solubility and improving drug safety to stratified drug delivery for different patient groups based on gene sequencing, as well as more personalized drug delivery methods. In order to enhance drug therapy while reducing drug dosage, many nanocarrier materials have been developed (**Figure 1**), providing a wealth of choices and design space for nanomedicine (Nasra et al., 2022). In the following paragraphs, different material classes used in nanomedicine are reviewed.

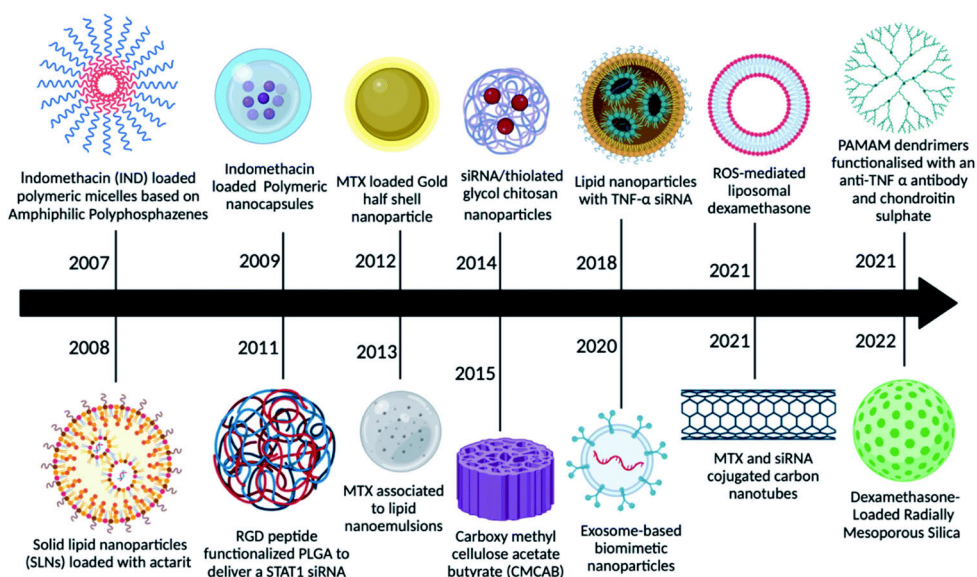


Figure 1. Nanoparticles used in the last decade for enhanced drug delivery. (Nasra et al., 2022) (Copyright © 2022, The Royal Society of Chemistry)

2.2.2 Classification of nanomaterials

2.2.2.1 Inorganic nanomaterials

Currently, the extensive development of inorganic materials has not only made significant contributions to the field of drug delivery but also provided substantial support for advancements in diagnostic techniques. Within this context, inorganic materials, notably mesoporous silica and gold, have emerged as pivotal nanostructured agents with versatile applications in drug delivery and imaging. These inorganic nanoparticles can be precisely engineered to exhibit various sizes, structures, and geometrical shapes.

One of the most extensively studied materials, mesoporous silica nanoparticles (MSNs), has gained widespread applications due to the particles' porous nature, large surface area, ease of modification, and low toxicity. When used as nanocarriers for drug delivery, MSNs not only reduce the toxicity of drugs but also prolong their circulation within the body. MSNs are often employed to load chemotherapeutic agents for tumor treatment. By delivering drugs to tumor sites, the drugs are protected from rapid clearance in the body. Furthermore, due to the characteristics of tumors' rich vasculature (wide gaps between blood vessel walls, poor structural integrity of vessels, and limited lymphatic drainage at tumor sites; EPR effect), MSNs can easily penetrate tumor blood vessels and accumulate at the tumor site, achieving controlled drug release to targetedly destroy tumor cells. Additionally, the pore size of MSNs can be adjusted to accommodate drugs of different sizes, and their surfaces can be modified with targeting ligands for achieving targeted drug delivery.

On the other hand, gold nanoparticles (AuNPs) have also found extensive use in drug delivery. They are suitable for carrying nucleic acid-based drugs and can facilitate photothermal therapy as well. Gold nanomaterials can take various forms, such as nanospheres and nanorods (Yang et al., 2019). The surface of gold nanoparticles contains free electrons that oscillate at specific frequencies, granting them photothermal properties (Wang et al., 2020). Additionally, AuNPs are easily functionalized, providing them with multi-functional features and drug delivery capacities (Yang et al., 2019).

Within the family of inorganic materials, compared to synthetic materials, biomimetic calcium phosphate (CaP) materials that naturally exist within the body have also been utilized for drug and DNA delivery (Liu et al., 2023). Among these, amorphous CaP is the most commonly used CaP nanoparticle for drug delivery, possessing good biocompatibility, gentle preparation conditions, and pH-responsive behavior (Li et al., 2021). Most drugs are adsorbed onto CaP nanoparticles through charge interactions and hydrogen bonding. Some drugs can form strong ionic bonds or complexes with calcium ions. CaP nanoparticles have demonstrated effective protection, sustained drug release, and facilitation of cellular uptake of e.g. antibiotics, bisphosphonates, growth factors, anti-inflammatory factors, and nucleic acid molecules (Qiu et al., 2022).

To conclude, inorganic nanoparticles offer distinctive attributes for various applications. However, inorganic nanoparticles sometimes suffer from poor biocompatibility, leading to challenges for clinical translations (Bobo et al., 2016; Manshian et al., 2017). Hence, organic nanomaterials, as reviewed in the next

paragraph, have also been extensively studied to combat the biocompatibility challenges.

2.2.2.2 Organic nanomaterials

Organic nanomaterials encompass lipid-based nanomaterials, polymer micelles, and emerging structural DNA nanomaterials. Among these, lipid-based nanomaterials are the most widely used in clinical applications, including the earliest marketed liposomal formulations such as amphotericin B liposomes (AmBisome®) and the more recent mRNA lipid nanoparticle vaccines.

Lipid nanoparticles (LNPs) are currently extensively employed for nucleic acid delivery. Their primary distinction from conventional liposomes lies in the formation of a micellar structure within the nanoparticle core (Leung et al., 2015). LNP materials consist of cationic polymers that interact with DNA, RNA, and other negative charged drugs, as well as pegylated lipids that enhance stability and circulation of the particles (Cheng and Lee 2016). The high efficacy and serum stability of LNPs in nucleic acid delivery have positioned them as prominent players in the field of gene therapy (Cheng et al., 2020; Patel et al., 2019). However, the notable uptake of LNP systems by the liver and spleen has restricted their broad applicability (Fenton et al., 2018).

Polymeric micellar nanoparticles can be formulated to precisely control various nanoparticle characteristics and are often excellent delivery carriers due to their biocompatibility and simple formulation parameters. Therapeutic agents can be encapsulated within the core of polymeric micellar nanoparticles, embedded within the polymer matrix, chemically conjugated to the polymer, or attached to the nanoparticle surface (Knight et al., 2019). Polymer micelles often consist of responsive block copolymers that self-assemble into nanospheres, aiding in protecting water-soluble drug cargoes and improving circulation time. Polymer micelles can load various types of therapeutic agents, and have been used to deliver cancer treatment drugs in clinical trials (Lee et al., 2018).

2.2.2.3 Hybrid nanomaterials

The combination of organic and inorganic materials to create novel hybrid nanomaterials offers a dual advantage by harnessing the strengths of both components. These materials exhibit stable physicochemical properties while also providing a flexible design space (Singh et al., 2020).

Firstly, Metal-Organic Frameworks (MOFs) are hybrid porous materials composed by metal ions and organic ligands. They possess high porosity, large surface area, and structural diversity, making them widely applicable in areas such as gas storage, substance separation, and catalysis (Baumann et al., 2019). Nanoscale MOFs retain the ordered structure of traditional MOFs while also exhibiting unique properties of nanoparticles, making them excellent drug carriers in the field of biomedical sciences (Chen et al., 2021). Compared to conventional nanocarriers, MOFs offer various modes of drug binding, showcasing multiple drug loading patterns to meet diverse preparation requirements and to optimize performance by incorporating different functional

molecules (Chen et al., 2021). Recently, many studies have reported multifunctional application of MOFs in drug delivery, achieving stimulus-responsive controlled release (Moharramnejad et al., 2023).

Furthermore, nanoscale MOFs have emerged as promising candidates for non-viral carriers in the realms of gene delivery and detection. MOFs present transformative possibilities in the realm of nucleic acid delivery, encompassing Small Interfering RNA (siRNA), miRNA, and mRNA delivery, DNA gene transfer, and transfection, as well as the deployment of probes for the purpose of gene expression assessment.

Another novel type of DNA hybrid material is metal-nuclear acid framework (MNF) nanomaterials. Due to multiple (negatively charged) phosphate moieties, DNA exhibits strong coordination ability with (positively charged) metal ions (Li et al., 2019). Discovered in 2019, this material has been gaining prominence in the field of cancer treatment. MNFs can be prepared by simply mixing metals with oligonucleotides and synthesizing them at high temperatures. Because of its straightforward synthesis method and the inherent advantages of a synergistic treatment platform, MNFs have been utilized for various oligonucleotide drugs, small molecule drugs, and metal delivery scenarios in research purpose (Li et al., 2019).

For example, Liu et al. (2021) mixing a solution of $\text{CuCl}_2 \cdot 2\text{H}_2\text{O}$ with a DNA enzyme (DNAzyme, Dzy) solution and vigorously rotating for 10 seconds, followed by incubation at 95°C for 3 hours, produced Cu-Dzy (Liu et al., 2021). Their results demonstrated that nanosynthesis without DNA did not yield spherical nanoparticles, confirming the crucial role of DNA in synthesizing such hybrid structures. Furthermore, when DNAzyme was replaced with random DNA, spherical nanoparticles still form, indicating the general applicability of this method. Thus, the ability to combine metals with unique properties into DNA nanostructures serves as a reference for designing multifunctional nanomaterials. Moreover, based on copper's redox properties, Liu et al. (2021) coated tannic acid (TA) on the surface of Cu-DNAzyme, forming the Cu-Dzy@TA structure (**Figure 2**). Its high co-loading capacity effectively delivered DNAzyme and Cu^{2+} for combined catalytic therapy to cancer cells. On one hand, Cu^{2+} is reduced to Cu^+ by glutathione, catalyzing the formation of hydroxyl radicals for chemical kinetic therapy using endogenous hydrogen peroxide. On the other hand, DNAzyme catalytically cleaves Vascular endothelial growth factor receptor 2 (VEGFR2) mRNA, achieving effective dual-catalytic tumor treatment. This innovative approach demonstrated the potential of DNA-metal hybrid nanomaterials in advancing cancer therapy.

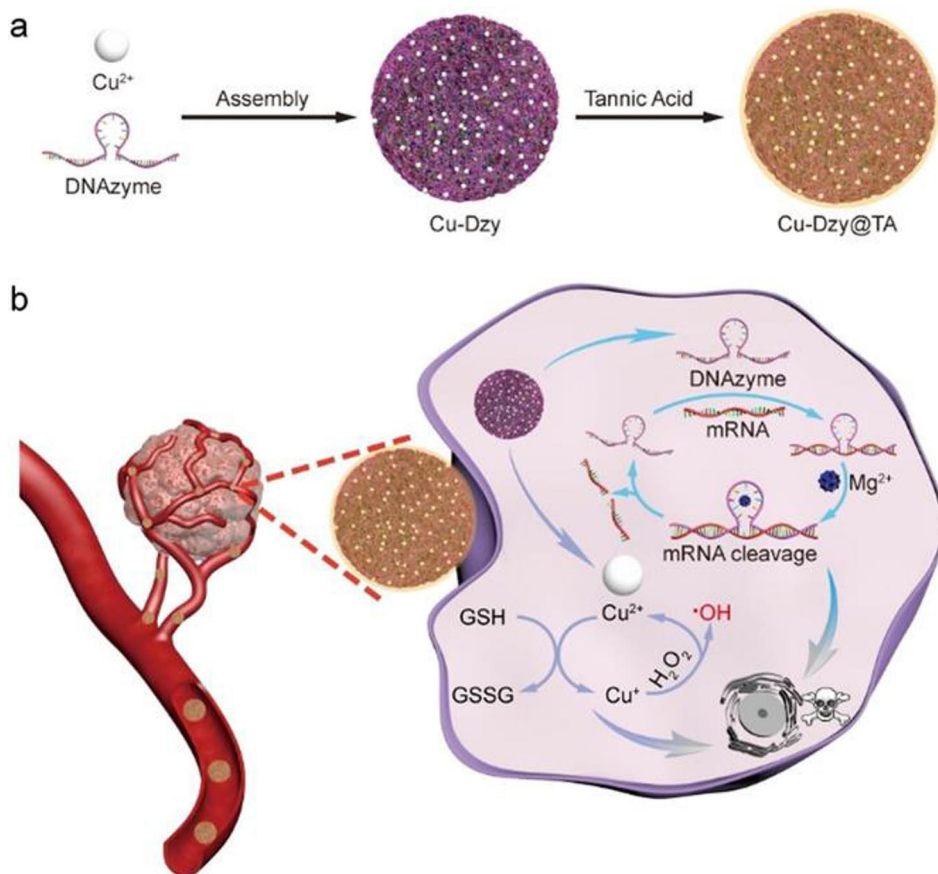


Figure 2. Synthesis of Cu-Dzy@TA and its application for dual-catalytic tumor therapy (Liu et al., 2021). Panel (a) The fabrication of Cu-Dzy with TA coating. Panel (b) The therapeutic mechanism for the DNAzyme and the copper ions within cancer cells. (Copyright © 2021 Wiley-VCH GmbH)

2.2.3 Challenges and directions for nanomedicine

From the outset, nanomedicine predominantly focused on targeted drug delivery for cancer treatment (Tran et al., 2017). Despite this, the outcomes have fallen short of expectations, with a limited number of approved anticancer nanomedicines such as Mylotarg® (approved by FDA in 2017), Doxil® (approved by FDA in 2015), and Abraxane® (a protein-bound paclitaxel complex, approved by FDA in 2012 for lung cancer therapy), standing as representatives. Nevertheless, the approval of Doxil® and Abraxane® primarily stemmed from their ability to mitigate side effects rather than significantly enhance the drug's therapeutic efficacy.

On the other hand, the delivery and distribution of nanoparticles are influenced by factors such as administration route, cancer type, and cancer progression. Local delivery methods may help nanoparticles overcome some of the obstacles associated with systemic delivery. However, these methods often

involve invasive procedures and complex technologies (Yan et al., 2021). Additionally, local administration is suitable for cancers localized to specific sites, such as certain solid tumors or trauma.

Hence, to address the aforementioned challenges, the development of targeted nanomaterials theoretically promises more effective products with reduced side effects. However, as mentioned earlier, the common strategy for targeted drug delivery is receptor-mediated cell targeting. Relying solely on surface-modified nanomaterials for targeted drug delivery has several drawbacks, such as surface ligand degradation and low targeting efficiency. Therefore, developing additional targeting strategies based on tumor heterogeneity, and combining them with different receptor-based approaches holds promise for precision therapy. In the following chapters, different receptors will be introduced first, and then, DNA-based nanosystems will be introduced subsequently.

2.3 Categorization of cancer targeted strategies

2.3.1 Receptor mediated nanoparticle-based targeting

Cells within various tissues of the human body possess distinct receptors on their cell membrane surfaces. Particularly, specific tissues or tumors tend to Overexpress particular receptors. For instance, interleukin and ganglioside receptors are significantly elevated in T lymphocytes and brain endothelial structures, respectively (Van Den Eeckhout et al., 2021) (Yu et al., 2011). Malignant tumor tissues such as breast cancer and glioblastoma demonstrate intensified presence of receptors such as biotin receptors and diphtheria toxin receptors (Saito et al., 2001). The utilization of receptor-mediated active targeting carriers facilitates the precise delivery of therapeutic agents to designated organs, tissues, or cells, thereby enhancing the therapeutic effects. In this chapter, several well studied receptors will be showcased.

2.3.1.1 Folate receptor

Folate receptors are overexpressed in tumor and arthritis cells, showing a specific affinity for folate and its analogs. By conjugating drugs with folate, an active targeting approach can be achieved, directing drugs towards tumor or arthritis cells using the folate receptor as the point of interaction. This enables precise targeted diagnosis and treatment. Presently, there are studies focusing on incorporating folate into liposomes or nanoparticles to serve as carriers for targeted therapy against tumors.

In a research by Liu et al. (2010), they employed docetaxel as a drug model and crafted lipid-polymer hybrid nanoparticles (LPNPs) with a lipid monolayer shell and a poly(lactic-co-glycolic acid) (PLGA) core. They compared the cellular uptake of LPNPs with folate-modified LPNPs in MCF7 breast cancer cells with overexpressed folate receptors. Their research findings demonstrated a notable increase in cellular uptake of folate-modified LPNPs through receptor-mediated endocytosis. Another investigation by Zheng et al. (2010) designed folate-

Poly(ethylene glycol) (PEG)-grafted- trimethylchitosan (TMC)/ Fluorescein isothiocyanate (FITC)-Bovine serum albumin (BSA) conjugates. The study showcased that SKOV3 cells with high folate receptor expression exhibited increased endocytosis of folate-PEG-grafted-TMC/FITC-BSA when the folate ratio in the complex was elevated, showing dose-dependent behavior within a certain range. Meanwhile, under the same conditions, complexes without Folate modification displayed no remarkable increase in cellular uptake. Upon introducing free folate, the cellular endocytosis of folate-NPs dropped by around 80%. No significant difference in cellular uptake of the two complexes was observed in folate receptor-deficient A549 cells, confirming that the cellular endocytosis of folate-NPs is mediated through the folate receptor.

Sodium alendronate (ALN) is a second-generation bisphosphonate drug, designated as a first-line treatment for osteoporosis. ALN has been extensively utilized as an effective bone-targeting moiety. It possesses amino active reaction sites that can be directly linked to drugs or nanocarriers through chemical bonds. Miller et al. (2009) presented one of the initial investigations in which the notions of targeting and combination therapy were combined within a unique conjugate. They achieved this by covalently linking paclitaxel (PTX) and ALN to an N-(2-hydroxypropyl) methacrylamide (HPMA) copolymer.

Another study employed a strategy of combining ALN with another, folate (FA), to achieve dual-targeting in bone metastases. Specifically, this approach aimed to significantly enhance the therapeutic efficacy against bone metastatic breast cancer through bone/tumor targeting drug delivery system. The nano-delivery system comprised a hydrophobic core coated with ALN-modified polymer and folate-conjugated polymer for delivering paclitaxel (PTX). The ALN/FA-modified nanoparticles demonstrated excellent ALN-mediated binding to hydroxyapatite-rich bone tissue and enhanced the therapeutic effect of PTX in cancer cells. Following treatment with PTX-loaded NPs modified with ALN/FA, bone destruction and loss were substantially delayed in tumor-bearing mice, with reduced adverse effects on normal tissues. These findings underscore the tremendous potential of the developed ALN/FA-modified drug delivery system (Chen et al., 2020).

2.3.1.2 RGD peptide receptors (integrins)

Arginylglycylaspartic acid (RGD) is a short peptide composed of the sequence of arginine-glycine-aspartic acid. It serves as a recognition motif for interactions between integrins and their ligand proteins. Since Pierschbacher and others first reported that the RGD sequence in fibrinogen is a cell recognition site (Ruoslahti and Pierschbacher 1987), RGD peptides and their derivatives have become a hot topic of research and attention among many scholars.

With the introduction of the theory "tumor growth relies on tumor vasculature" (Siemann 2011), targeted receptor drugs for tumor neovascularization have emerged as a new and promising approach to enhancing tumor treatment efficacy. Integrin $\alpha\beta 3$ is an ideal target for tumor-directed therapy, and the RGD peptide can specifically bind to it while carrying

effectors. This can effectively inhibit tumor growth and the formation of new blood vessels. Therefore, utilizing RGD peptides to target cytotoxic drugs to specific tumor sites holds significant potential as an advanced tumor-targeted therapy technique.

Traditional ligand-modified nanomaterials often encounter issues during transportation within the body, such as ligand degradation or coverage. However, a recent report discusses the development of an intelligent drug delivery system to address these challenges associated with traditional receptor-targeted nanomaterials during *in vivo* transportation (Deng et al., 2017). The researchers utilized a modified RGD peptide and employed a series of complex chemical reactions to attach it onto the surface of nanoparticles. Specifically, the researchers initially coated the surface of nanoparticles with a thermosensitive copolymer in a uniform manner. Subsequently, they used RGD ligands containing azobenzene groups and attached them to the nanoparticles via specific chemical bonds. Within this controllable targeting system, the RGD ligand molecules undergo conformational changes under specific light conditions, thereby regulating the interactions between the nanoparticles and cells and thus, protecting the RGD ligand on the way to the target cells. First, under 365-nm ultraviolet light exposure, the azobenzene groups within the RGD ligands undergo a conformational switch (to the *cis* conformer) that leads to shielding of the RGD ligands. Then, upon exposure to 808-nm near-infrared laser light, the thermosensitive copolymer contracts due to photothermal effects, causing the azobenzene groups to transition from one conformation to another (from *cis* to *trans*). These intricate changes lead to the exposure of the RGD ligands under specific conditions, thereby enhancing the targeting interactions between the nanoparticles and tumor cells.

2.3.1.3 HER-2 receptor

The human epidermal growth factor receptor-2 (HER-2) plays a significant role in the occurrence and development of tumors due to its tyrosine kinase activity (An et al., 2017). Under normal physiological conditions, HER-2 remains inactive, but it can be abnormally activated in response to certain adverse stimuli. It participates in regulating cell proliferation, apoptosis, the generation of tumor-promoting factors, angiogenesis, tumor infiltration, and metastasis through multiple signaling pathways.

Current research indicates that HER-2 is involved in various malignant tumors such as breast cancer, gastric cancer, bladder cancer, colorectal cancer, and lung cancer (Qiu et al., 2017). For instance, in invasive breast cancer, approximately 15%-36% of patients exhibit abnormally high HER-2 expression, which correlates with poorer prognosis (Shin et al., 2018). In gastric cancer, HER-2 expression is also considered an independent risk factor affecting patient outcomes. In gastric cancer, about 11%-28% of patients show HER-2 overexpression, although detection rates vary significantly among different regions and populations. Reports from Europe suggest that the positive detection rate of HER-2 in gastric cancer is mostly below 20%, with higher rates

observed in intestinal-type gastric cancer (Cho et al., 2017). In America, the incidence of HER-2 overexpression is around 12%, and the detection rate is similarly higher in intestinal-type gastric cancer (Cronin et al., 2010). In addition to variations in HER-2 expression among different ethnicities and regions, other factors include a notably higher HER-2 positivity in well to moderately differentiated adenocarcinomas, and a significantly higher detection rate of HER-2 in intestinal-type gastric cancer compared to other types. However, patient age, gender, Tumour, node and metastasis (TNM)staging, and tumor location appear to have no significant impact on the expression status of HER-2.

Therefore, this also underscores the crucial concept of precision medicine. Firstly, patients should be classified based on different receptor expressions, and then targeted modifications of nanomaterials should be chosen according to the specific receptors.

2.3.2 Receptor targeting through DNA strategies

The above four receptors are commonly targeted through ligand binding on the surface of nanomaterials. Currently, in addition to traditional ligands, a novel strategy for receptor targeting is the aptamer targeting method, which involves screening DNA sequences for achieving receptor specificity.

Antibodies have been widely employed to target the delivery of nanomaterials containing cancer diagnosis and treatment components to cancer sites. However, They have shown significant issues, such as poor stability, high cost, and challenges in chemical modification. Aptamers, known as "chemical antibodies," have emerged as a novel type of DNA molecular probe (Keefe et al., 2010). They possess several ideal characteristics for clinical application. They can be chemically synthesized and easily integrated into various applications. Due to their distinctive three-dimensional folding, aptamers can bind with many targets including metals, nucleotides, enzymes, proteins, entire cells, and even whole organisms, with high affinity and specificity (Walia et al., 2021). In addition to this versatility, their small size, ease of modification, structural and conformational flexibility, biocompatibility, make them suitable for applications in tumor diagnosis and targeted drug delivery. Among the various advantages of aptamers over antibodies, the most significant is their ability to tolerate extensive chemical modifications on their main chain or terminal ends without losing significant activity (Wang et al., 2007). For instance, functionalized aptamer conjugates have become significant tools for targeted imaging and cancer treatment. However, the instability of aptamer molecules within the body poses limitations on their broader applications. To address this issue, researchers need to covalently modify aptamers, a complex process that involves sequential sequence design and multi-step synthesis.

In light of this, a recent study introduces a non-covalent modification strategy to enhance the stability of aptamers during system administration (Xia et al., 2022). Specifically, this strategy involves the simple combining of aptamers with gold nanoclusters (GNCs) to form self-assembled GNCs@aptamer structures (**Figure 3**). Taking Sgc8 aptamer as an example, experimental results

demonstrate significantly enhanced cancer cell-specific internalization capabilities of GNCs@Sgc8 conjugates. Furthermore, the self-assembled GNCs@aptamer structures effectively resist degradation by nucleases, maintaining stability for up to 48 hours, compared to a mere 3 hours of degradation time for individual nucleic acid aptamers. The findings also indicate substantial enhancement in tumor-targeted recognition effects of GNCs@aptamer self-assembled structures, with a 9-fold augmentation in signal within tumors compared to individual aptamers.

As this strategy avoids the need for complex chemical modification steps, it is practically applicable to nearly all types of aptamers. To conclude, the findings of this study not only provide a comprehensive approach to enhancing the stability of aptamers but also open up new avenues for their utilization in both imaging and therapeutic applications. This strategy holds the potential to revolutionize the field by addressing one of the crucial challenges in aptamer-based technologies, ultimately paving the way for more effective and versatile advancements in biomedical research and clinical practice.

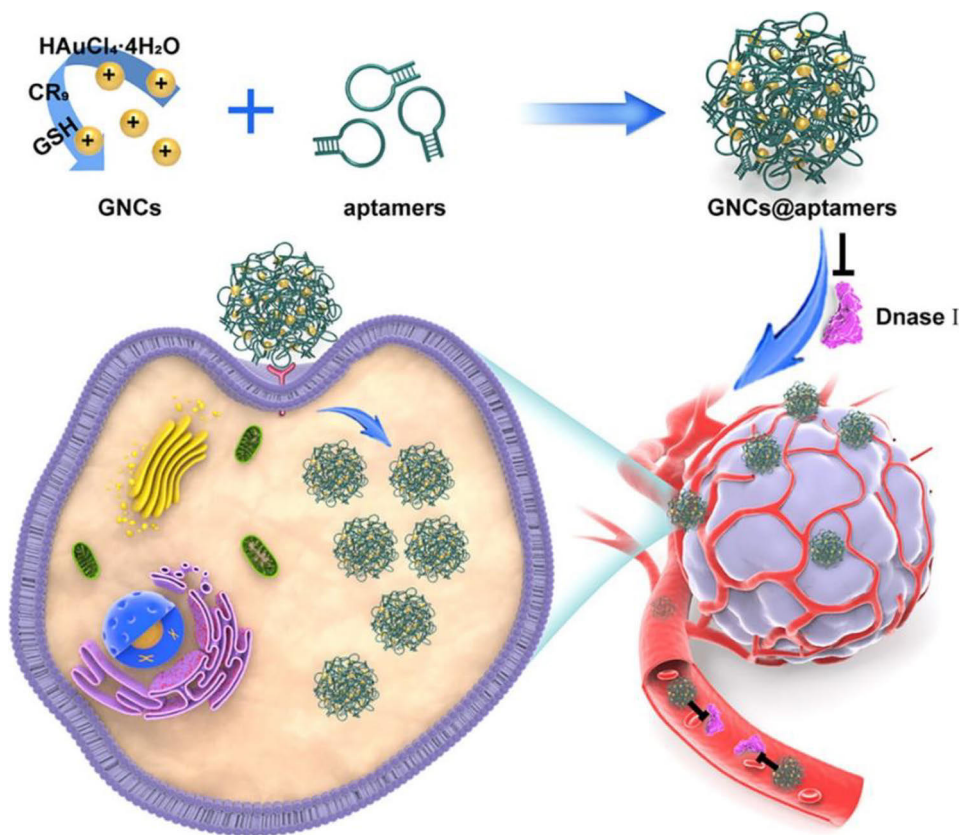


Figure 3. Depicts the process of creating GNCs@aptamer assemblies for effective targeted delivery to tumors. (Xia et al., 2022) (Copyright © 2022, American Chemical Society).

2.3.3 Local delivery based targeting

Local drug administration is a therapeutic approach that allows direct targeting of the affected area. This method primarily focuses on cancers with well-defined sites, including ocular drug delivery, transdermal drug administration, and even solid tumor drug delivery. Despite being invasive in certain cases, this approach still holds significant advantages in specific treatment domains.

Specifically, targeted local drug delivery to solid tumors is a crucial pathway for enhancing drug delivery efficiency and reducing chemotherapy toxicity. Researchers have developed various carriers for in-situ drug delivery, including colloids, tablets, particles, and films (Wolinsky et al., 2012). In-situ gel systems, due to their excellent biocompatibility, degradability, aqueous environment, and injectability, have been widely employed for local tumor drug delivery. In this approach, the drug is typically dispersed in a pre-gel solution, and after gel formation, the drug becomes loaded within the gel.

In-situ gels for local tumor drug delivery offer several advantages, including sustained and controlled drug release and distribution within the tumor, ensuring effective drug diffusion or penetration into cells. They utilize the interaction between polymers or solvents and hydrophobic drugs for loading and controlled release. Directly delivering drugs to the tumor site can reduce the required drug dosage, enhance drug bioavailability, minimize toxic side effects, and the injectable nature of these systems reduces harm to the organism (Wolinsky et al., 2012). However, due to significant variations in physiological conditions between normal microenvironments in the human body and different cancer sites, conventional hydrogels used as local drug release systems might not achieve the desired outcomes. Therefore, for drug delivery, there is a pressing need for polymer materials that possess environmental responsiveness to address these challenges.

Recently, a thermoresponsive MXene-DNA hydrogel platform has been developed (He et al., 2022). This innovative platform combines DNA hydrogel with MXene-based nanotherm-agents and loaded doxorubicin (DOX) chemotherapy agents, creating a promising synergistic photothermal-chemotherapy cancer treatment approach (**Figure 4**). Under near-infrared (NIR) irradiation, the temperature increase induced by the MXene nanotherm agent triggers a transition of the MXene-DNA hydrogel loaded with DOX, during which the double-stranded DNA's cross-linked structure unfolds, releasing the chemotherapy agent for effective localized cancer treatment. Upon cessation of NIR irradiation, the double-stranded DNA structure and hydrogel re-form, enabling the re-encapsulation of free DOX back into the hydrogel.

The synthesis of the DNA hydrogel involved the creation of a cross-linked structure using DNA and polyacrylamide (pAM) main chains. This was achieved through a process of radical polymerization, which entailed combining acrylate-modified DNA with acrylamide monomers. The double-stranded DNA's cross-linked structure in the hydrogel unfolds above the double-stranded DNA's melting temperature (T_m , 44.2 °C), indicating that the hydrogel can serve as a

thermoresponsive matrix under mild hyperthermia (at temperatures of 42–48°C). Notably, during the gel-to-solution transition triggered by the photothermal treatment, the double-stranded DNA structure within the hydrogel matrix can reversibly unfold and re-form, facilitating the reversible release and encapsulation of DOX. This implies that the reformed DNA hydrogel can capture free DOX, reducing adverse effects on healthy tissues during therapy. Additionally, the 1,2-dimethylhyrazine (DMH) hydrogel can adaptively deform according to the mold shape under NIR irradiation.

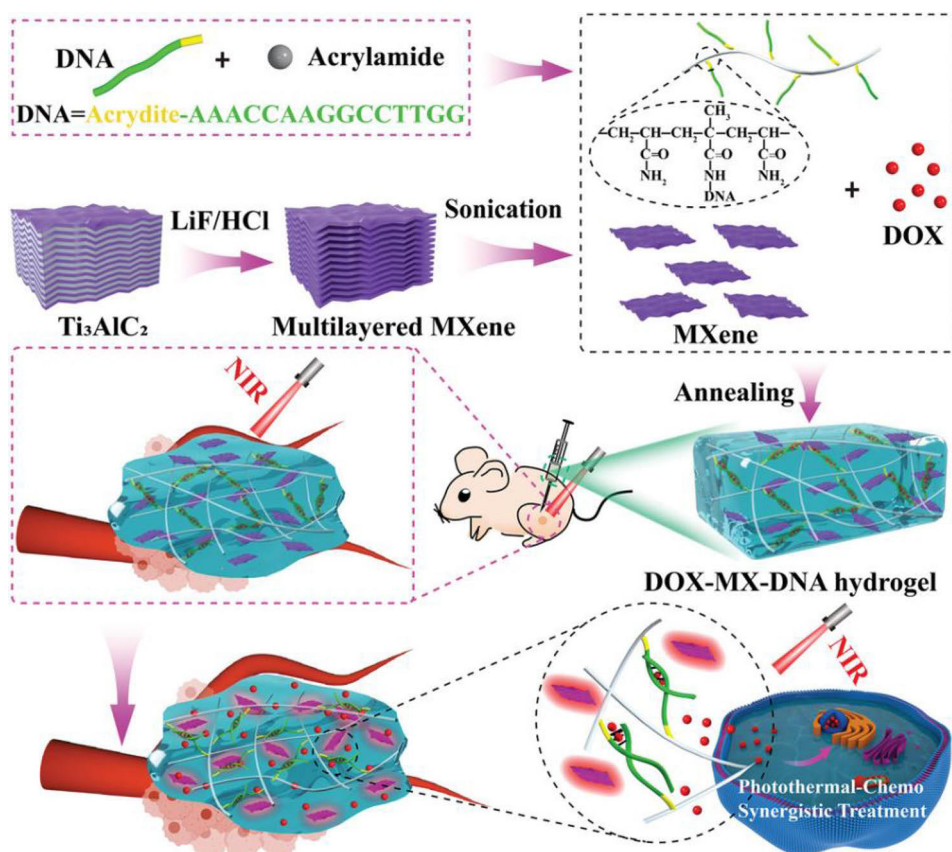


Figure 4. Diagram depicting the fabrication process of DOX-loaded MXene-DNA hydrogel and its utilization as a near-infrared (NIR)-responsive injectable platform for synergistic photothermal-chemotherapy in tumor treatment. First, the DNA is riveted to the hydrogel polymer monomer. Doxorubicin is loaded into the double-stranded DNA. After being heated by near-infrared light, the DNA double helix is unwound, allowing thermo-responsive drug release (He et al., 2022) (Copyright © 2022 Wiley-VCH GmbH).

2.3.4 MiRNA-responsive targeting

MicroRNAs (miRNAs) play a pivotal role in regulating fundamental cellular processes, encompassing cell differentiation, proliferation, and programmed cell death. Perturbations in miRNA expression levels have been implicated in a

spectrum of disorders, including cancer and diabetes. Many scientists have honed in on cancer-specific miRNAs, viewing them as potential indicators for diagnosing and prognosticating cancers. For instance, miRNA-21 functions as a pivotal regulator in carcinogenesis and is frequently overexpressed in numerous cancer cells. As a result, miRNA-21 emerges as a promising candidate for both diagnosing and treating cancer. Notably, recent research has leveraged endogenous miRNAs as triggers for drug release and activation within drug delivery systems. This offers a distinct cell-targeting strategy beyond receptor-mediated endocytosis, providing alternative approaches to address tumor heterogeneity.

Moreover, miRNA can act as a therapeutic indicator for cancer treatment. For example, Lee et al. (2016) have introduced a miRNA-responsive therapeutic and diagnostic platform comprising a nanocolloid consisting of a photosensitizer (PS), 2,6-dihydroxyanthraquinone (chlorin e6, Ce6), peptide nucleic acid (PNA), and dextran-coated reduced graphene oxide (Dex-RGON). In this approach, Dex-RGON serves as a drug delivery carrier and quencher, utilized for chemically tethering the fluorescence and photosensitive properties of Ce6 to PNA. On the other hand, PNA possesses a sequence complementary to the cancer-specific miRNA miR-21. Upon internalization of the nanomaterial complex into cancer cells, Ce6-PNA hybridizes with miR-21, leading to the release of Ce6-PNA from Dex-RGON. Subsequently, under exposure to NIR irradiation, laser-induced activation of Ce6 as a PS occurs and its fluorescence is restored. The miRNA-21 detection threshold is at picomolar concentrations, making it highly suitable for diagnostic sensing and image-guided photodynamic therapy (PDT). However, in the absence of miR-21, even under NIR, the nanocolloid platform does not exhibit measurable fluorescence or generate singlet oxygen atoms. The authors also validated this strategy using an *in vivo* xenograft mouse model, wherein the tumor significantly decreased following the miRNA-21 specific laser-induced PDT. This marks the first application of PS-conjugated PNA for dual purposes: facilitating PDT drug delivery and achieving fluorescence-based diagnostic imaging.

2.4 Introduction of DNA nanotechnology for targeted drug delivery

After decades of rapid DNA nanotechnology development, an increasing number of DNA nanostructures have been developed (Lacroix and Sleiman 2021). DNA nanotechnology achieves self-assembly through precise design of DNA sequences. The base pairing rules allow DNA segments with complementary base sequences to bind together, forming robust double helical structures (Zhan et al., 2019). Selective assembly enables the creation of highly precisely controlled complex nanoscale structures.

2.4.1 Structural DNA nanotechnology

Precision engineering of materials at the atomic scale to tailor their properties according to specific requirements stands as a pivotal objective within the realms of chemistry and materials science. However, this remains a significant challenge to this day. Over the past few decades, scientists have been searching for materials with controllable and modular properties in order to drive rapid advancements in the field of nanomaterials (Madsen and Gothelf 2019). Unlike traditional organic and inorganic materials, DNA possesses excellent programmability, controllability, and weak interactions between DNA strands, making it an ideal candidate for synthesizing nanomaterials.

In the past, DNA was mainly seen as a carrier of genetic information. However, this perspective underwent a complete transformation with the discovery by Professor N.C. Seeman from the New York University (Chen and Seeman 1991). N.C. Seeman accidentally found that DNA's sticky ends could be used to connect pre-designed branching structures, forming three-dimensional target structures. As early as 1991, he successfully synthesized a rigid DNA cube, opening up a new realm of research in the field of DNA nanotechnology. DNA nanotechnology leverages the specificity of Watson-Crick base pairing and DNA's inherent properties, employing a self-assembly strategy to construct novel molecular nanostructures with repeating arrays in two-dimensional and three-dimensional directions. To today, to achieve finer control and synthesize more intricate structures, scientists have proposed several different assembly methods, primarily including DNA tiles (also known as DNA tilings) method (Fu and Seeman 1993), DNA origami method (Rothemund 2006), and DNA bricks method (Ke et al., 2012).

Currently, targeted drug delivery using origami-based structural DNA nanotechnology is thriving. Research on promoting the release of cargo from DNA nanostructures through enzymatic cleavage has shown promising results. By strategically designing the higher-order structure of DNA origami and adjusting the loading concentration of the drug DOX, it has been found that DOX, a commonly used therapeutic drug, can be released from DNA origami nanostructures under the action of deoxyribonuclease I (DNase I) enzyme (Ijas et al., 2021). This nucleases break down the DNA origami nanostructures into short single strand DNA fragments, leading to the release of bound DOX as the double-stranded DNA structure disintegrates (**Figure 5**). Additionally, Sun et al. (2014) have developed a cocoon-like DDS, composed of DNase I, DNA nanochannel structures (NCl), and acid-responsive DNase I nano-capsules (NCa). The NCl is assembled from DNA chains and can carry DOX, while the negatively charged DNase I is encapsulated within positively charged acid-degradable nano-gels. Through electrostatic interactions, DNase I is incorporated into NCl. Under acidic conditions, the nano-gels degrade, activating DNase I activity, which leads to the degradation of nanochannel structures and facilitates the release of DOX.

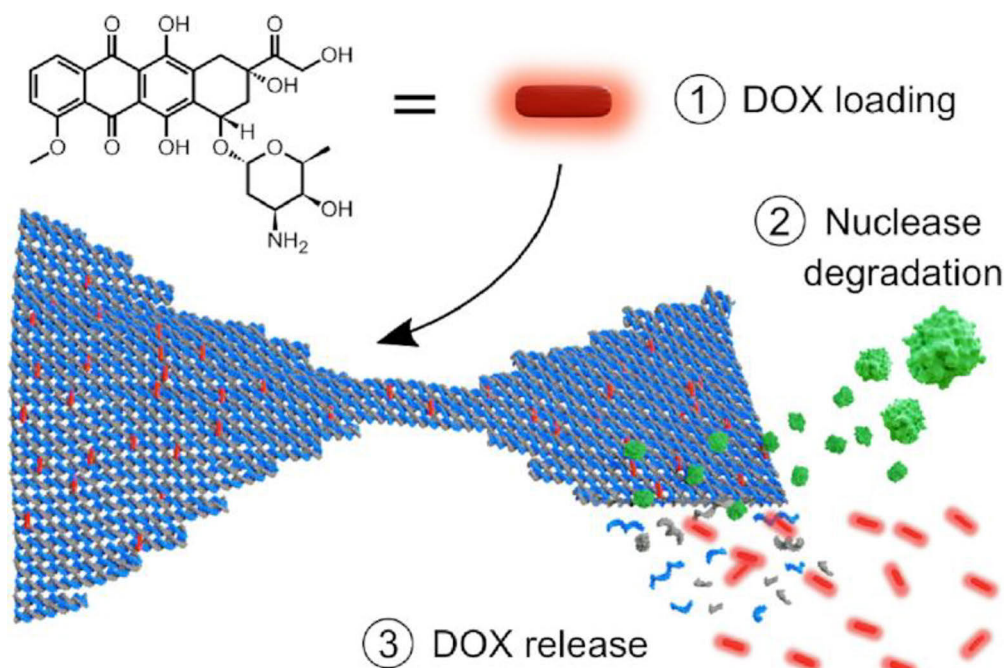


Figure 5. The schematic illustration of the loading of doxorubicin (DOX) into DNA origami nanostructures and the subsequent release upon enzymatic degradation. (Ijas et al., 2021) (Copyright © 2021, Oxford University Press)

2.4.2 Dynamic DNA nanotechnology

In contrast to the origami based structural DNA nanotechnology, dynamic DNA nanotechnology encompasses various DNA self-driven reactions. Through these dynamic responses, DNA nanomaterials can achieve spatiotemporal control, including logic bio-circuits responsive to miRNA and mRNA, self-assembling into biologically active DNA structures, and even forming nanomaterials.

2.4.2.1 Toehold mediated strand displacement

The DNA strand displacement reaction is the key mechanism for designing autonomous enzyme-free DNA circuits. The introduction of various methods for regulating DNA strand displacement reactions has enriched the design rules of complex DNA computing systems, providing additional flexibility and diversity in design, thus greatly promoting the development of DNA-based molecular computing and molecular robotics technology (Yurke et al., 2000).

The DNA strand displacement reaction involves the process of exchanging partially or fully complementary single DNA strands during hybridization, where a new chain replaces the previously bound one. This process starts from the complementary single-stranded structure domain, known as the toehold region, and is followed by branch migration, similar to a random walk, which releases the originally bound chain. As shown in the diagram (**Figure 6**), DNA molecules are represented as directional lines, with the 3' end indicated as a toehold. In the

processes of hybridization, branch migration, and dissociation, these structural domains act as reaction units, each represented by a number. Regions with asterisks denote complementary sequences, while regions without asterisks indicate non-complementary sequences. Generally, DNA molecular devices based on the strand displacement mechanism are theoretically applicable to a variety of sequence selection scenarios, hence the sequence is universal.

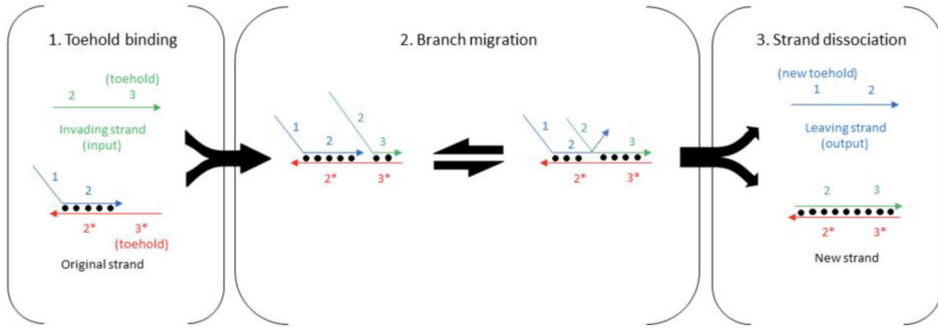


Figure 6. The mechanism for toehold-mediated strand displacement reaction (By Terdiv4 - Own work, CC BY-SA 4.0)

Researchers have also attempted to confer environment-responsive behavior to DNA strand displacement reactions, aiming to enhance their applications in areas such as biosensing. In 2011, a responsive "hidden toehold" was developed on a metastable DNA hairpin structure (Xing et al., 2011), where the reaction activity is restricted by the formation of a metastable double-stranded state and can be regulated by the concentration of ATP to control the kinetics of the strand displacement reaction. In 2013, a photo-controlled toehold formation method was reported (Huang et al., 2013) that involves linking two complementary DNA strands with a photocleavable nitrobenzyl linker (PC linker). Under ultraviolet light irradiation, the linker is cleaved and the DNA duplex with a toehold can be formed. By simply adjusting the dosage of UV irradiation, the formation of toeholds can be finely controlled, demonstrating the potential for constructing dynamic DNA nanodevices.

A pH-dependent strategy based on Hoogsteen base pairing was utilized to rationally design two triple-strand-based DNA strand displacement strategies (Amodio et al., 2014), which can trigger and finely modulate the kinetics of the strand displacement reaction under alkaline or acidic pH environments. This approach holds promise for achieving pH-responsive DNA nanomachines capable of generating specific pH-dependent output molecular signals (such as drug release). Additionally, researchers have employed inducible toehold strategies, such as protein binding and metal ion binding, to regulate DNA strand displacement reactions (Zhang and Seelig 2011).

Additionally, barrel-shaped DNA nanomachines can encapsulate "cargo" within their cavities. For example, weaving DNA molecules like threads, intertwining them in a grid-like pattern, and folding them as an envelope to

"mail" drugs to tumors is an intriguing concept (Li et al., 2018). This approach aims to ensure that the envelope unfolds only upon encountering the tumor, thereby minimizing the risk of inadvertently affecting areas beyond the tumor. For example, in this "envelope"-type DNA nanorobot design, researchers first utilized the M13 bacteriophage genome DNA to create a rectangular DNA origami sheet measuring 90 nm × 60 nm × 2 nm (Li et al., 2018) (**Figure 7**). Subsequently, they connected this sheet to thrombin, resulting in the formation of a tubular nanorobot. The researchers also devised a DNA fastener that, when bound to nucleolin (a specific protein found on the surface of tumor blood vessels), could unlock the tubular nanorobot. This allowed the exposure of the drug intended to kill the tumor. Thus, upon opening, the DNA tube revealed thrombin, which has the ability to coagulate the blood supplied to the tumor cells. This effectively cut off the nutrient supply to the tumor, ultimately leading to its demise. To validate the efficacy of this nanorobot system in living organisms, the researchers conducted tests on mouse models of breast cancer, melanoma, and human ovarian cancer. The results showed that, compared to the control group, the nanorobots caused significant blood clotting within tumor blood vessels. Importantly, they did not induce abnormalities in normal tissues. Given the potential for immune reactions and other side effects when introducing foreign entities like nanorobots into the body, it was crucial to assess their immunogenicity. However, the researchers discovered that the nanorobots did not trigger significant immune responses in the mouse models, and there were no instances of clotting observed in major organs in pigs. These findings strongly suggest a certain level of safety for this system.

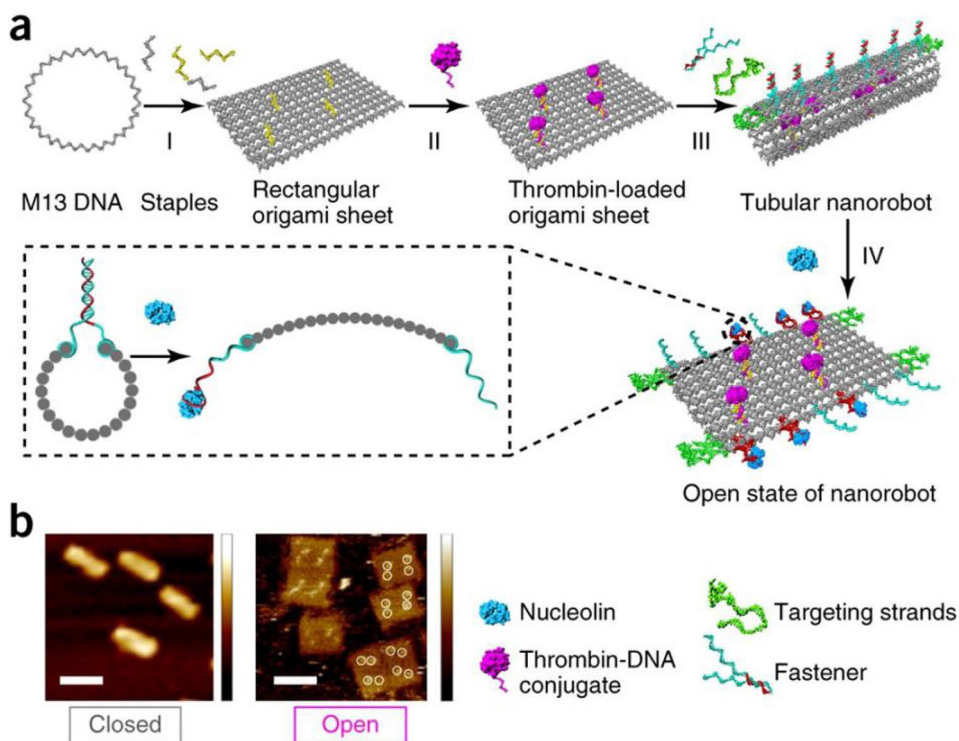


Figure 7. Schematic illustration of the envelope-like DNA nanorobot. Panel (a) The M13 template was used, and a staple chain was employed for constructing the origami structure. Subsequently, hemagglutinin was encapsulated onto the origami structure. Finally, targeting strands were affixed to cap the structure. Panel (b) The AFM picture showing the opening process of the nanorobot. In this constructed configuration, when a tumor was encountered, the targeting loop specifically bound to the targeting sequence through the principle of competitive complementarity. This action resulted in the unlocking of the lock structure. Consequently, hemagglutinin was released, facilitating blood coagulation at the tumor site and enabling starvation treatment. (Li et al., 2018) (Copyright © 2018, Springer Nature America, Inc.)

2.4.2.2 Self-assembly

The dynamic self-assembly of DNA involves various assembly pathways, including the aforementioned toehold-mediated dynamic self-assembly, as well as DNA sequences that undergo simple complementary pairing to achieve active structural self-assembly within cells. Toehold-mediated dynamic self-assembly includes hybridization chain reaction (HCR). This technique is a temperature-dependent enzyme-free amplification method that avoids the use of complex thermal cycling reactions and stringent enzyme activity requirements. Complementary pairing involves nanomaterials such as multi-component nucleotide acid enzymes (MNAzymes) that possess specific nucleic acid cleavage functions. Their precursors bind to specific gene sequences within cells and assemble into MNAzymes with cleavage activity.

First, HCR is a commonly used enzyme-free signal amplification method (Zhou et al., 2018). In the absence of the target, probes do not react with each other, maintaining their stable hairpin configurations within the individual molecules. When the target is introduced, it first hybridizes with the first probe, opening the probe's hairpin structure. Subsequently, the second probe can hybridize with the exposed single-stranded region of the first probe, opening the hairpin structure of the second probe and forming a more stable duplex. Simultaneously, the target is displaced from the duplex, continuing the next round of reactions to achieve the target recycling amplification. Through this method, the signal can be augmented times by times, even at a very low concentration of the target strand.

On the other hand, HCR has also been explored for miRNA-responsive self-assembly, enabling miRNA-mediated targeted cancer therapy (**Figure 8**) (Wei et al., 2020). Initially, a set of four hairpin structures were employed to achieve miR-21-mediated HCR self-assembly. During this process, the oncogenic miRNA-21 itself was consumed, thereby enabling a certain degree of gene therapy. Furthermore, miRNA-21 triggered the assembly of the four hairpin structures, leading to the assembly of active DNazymes. As a result, these DNazymes could accomplish the cleavage of the target gene. Therefore, the miR-21-mediated gene therapy function holds potential to serve as an effective solution for addressing tumor heterogeneity.

In conclusion, the current research focus aims to utilize DNA nanotechnology to achieve targeted activation of constructed systems at tumor sites. This involves responding to intracellular biomarkers such as highly expressed mRNA, miRNA, and other endogenous indicators within the tumor. Its major advantage lies in the ability to treat tumors without adversely affecting surrounding non-cancerous tissues.

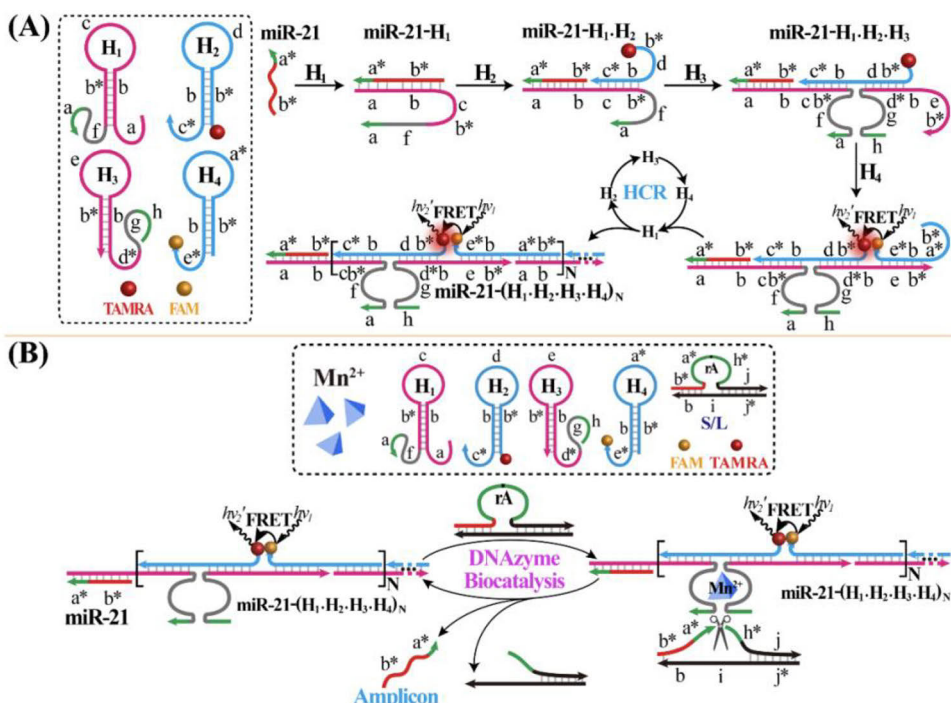


Figure 8. Schematic illustration of the HCR (Hybridization Chain Reaction) system, highlighting the HCR-assembled DNAzyme biocatalysis and the autocatalytic DNAzyme biocircuit. Panel (A) HCR-assembling strategy illustration. Panel (B) DNAzyme assembling mechanism and function introduce. (miR-21: microRNA-21; FRET: Fluorescence resonance energy transfer). (Copyright © 2020 Wiley-VCH Verlag GmbH & Co. KGaA, Weinheim)

2.4.3 DNA oligonucleotides based therapy

Within the realm of gene therapy, the restoration of normal gene expression for genes with diminished levels of expression often involves DNA transfection, while the curbing of overexpressed genes is accomplished through the delivery of molecules such as antisense RNAs, small interfering RNAs (siRNAs), or ribozymes into cells. Among the diverse array of cancer gene therapies, the role of short oligonucleotide drugs is paramount. This category encompasses antisense oligonucleotides, DNAzymes, and other entities. Distinct types of oligonucleotides can achieve precise gene expression modulation through a range of targeted mechanisms.

2.4.3.1 DNAzymes

DNAzymes represent a class of single-stranded DNA fragments engineered using computer-aided methods to possess catalytic capabilities. Given the prevalence of double-stranded DNA in nature, DNAzymes' active centers are single-stranded DNA segments, making them synthetically attainable only through *in vitro* synthesis, as naturally occurring DNAzymes have not yet been identified. Up to

now, numerous variations of DNazymes have been artificially created, with functions including RNA cleavage ability, DNA ligase functionality, porphyrin metalloenzyme and peroxidase attributes, DNA hydrolysis potential, DNA kinase behavior, N-glycosylase properties, and DNA-capping functionality(Ponce-Salvatierra et al., 2021).

A fundamental feature of DNazymes is their ability to cleave RNA molecules. In 1994, Gerald F. Joyce successfully synthesized DNzyme capable of RNA cleavage, which effectively cleaved target RNA molecules (Santoro and Joyce 1997). The therapeutic potential of these RNA-cleaving DNazymes has been extensively proven through both *in vivo* and *in vitro* experiments(Yan et al., 2023).

In 1997, Santoro S.W. reported two distinct classes of DNazymes capable of cleaving complete RNA sequences: the 10-23 DNzyme and the 8-17 DNzyme. The names "8-17" and "10-23" assigned to DNazymes do not correspond to the sizes of the DNazymes but rather signify the specific experimental protocols used for their selection. The DNzyme includes a catalytic center, flanked by two binding arms of seven nucleotides each, which interact with substrate RNAs. Substrate RNA cleavage yields a 5'-end product with a 2'-3' cyclic phosphate group and a 3'-end product containing a free 5'-OH group (Cairns et al., 2002). Enzyme kinetic studies suggest that the catalytic efficiency of the 10-23 DNzyme can exceed 10^9 mol/L·min⁻¹, surpassing that of RNAase, hammerhead ribozymes, and hairpin ribozymes. Its catalytic efficiency and specificity towards target molecules are correlated with the lengths and sequences of the binding arms. In earlier research, scientists utilized the 10-23 DNzyme AM9D to suppress matrix metalloproteinase-9 (MMP-9) expression, achieving breast cancer treatment (Hallett et al., 2013).

With the benefits from chemical modifications, and utilization of nanomaterial based approaches, DNazymes show great synergistic effects in different cancer therapies (**Figure 9**). Presently, DNazymes are often combined or shielded with different substances, encompassing both organic and inorganic components. These strategies for carrier integration are designed to enhance DNzyme stability, increase payload capacity, and facilitate the implementation of synergistic therapeutic methodologies.

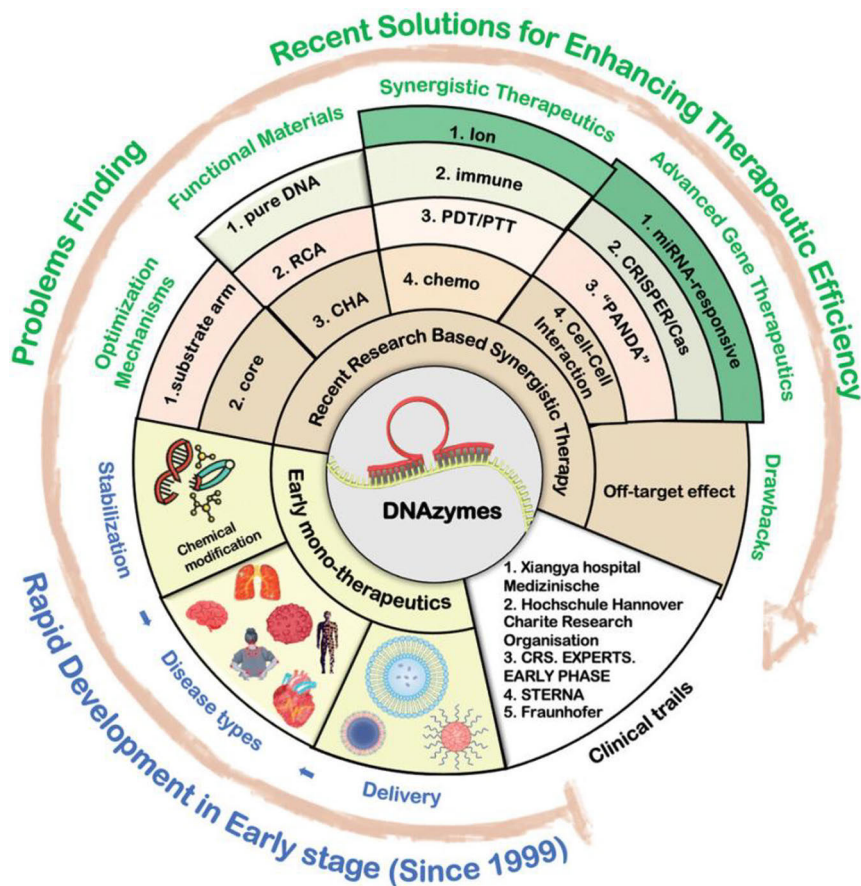


Figure 9. Illustration depicting the progression of therapeutic research utilizing DNAzymes, encompassing earlier investigations to the most recent studies. (Yan et al., 2023) (RCA rolling circle amplification, CHA catalytic hairpin assembly, PTT photothermal therapy, PDT photodynamic therapy) (Copyright © 2023 The Authors. Advanced Materials published by Wiley-VCH GmbH)

2.4.3.2. Antisense oligonucleotides

Antisense oligonucleotides (ASOs) encompass short DNA or RNA molecules that interact with target RNA through complementary base pairing, resulting in either inhibition of function or induction of degradation (Barranco 2023). DNA ASOs, typically ranging from 15-18 nucleotides, have gained prominence due to their stability, chemical modifiability, and cost-effectiveness (DeVos and Miller 2013). The pairing of short DNA ASO molecules with target RNA triggers the activation of intracellular ribonuclease H (RNase H), which specifically identifies and cleaves the RNA strand within the DNA-RNA hybrid helix, rendering the target RNA dysfunctional (Larrouy et al., 1992). Another category of ASOs influences RNA editing by binding to specific precursor mRNA sites, curbing detrimental spliceosome formation. The potent capabilities of ASOs were

recognized early; Zamecnik and Stephenson (1978) first verified ASOs' ability to restrain the replication and transformation of Rous sarcoma virus in cellular contexts. Subsequently, during the 1980s, ASOs witnessed a rapid growth in development. In 1998, the FDA greenlit the inaugural ASO drug, fomivirsen for treating cytomegalovirus retinitis in HIV-infected individuals. However, as this primary indication waned, the ASO drug ultimately departed from the market (He et al., 2023). Hindered by restrictions in modifying small nucleic acids and lacking adequate *in vivo* delivery systems, many related drug trials failed to yield anticipated results, leading to a lull in ASO research. Prominent pharmaceutical firms consequently abandoned ASO drug development.

Overcoming the hurdle of effectively delivering ASO drugs to target tissues and cells and facilitating their release to enact effects poses the greatest challenge. Recently, breakthroughs have emerged in strategies for delivering small nucleic acid drugs. In January 2013, the American companies ISIS Pharmaceuticals and Genzyme collaborated to produce the antisense oligonucleotide drug Mipomersen, which received certification from the US FDA (Hair et al., 2013). Mipomersen, a synthetic alkyl-modified antisense oligonucleotide, works by inhibiting the mRNA of apolipoprotein B-100, thereby reducing low-density lipoprotein cholesterol (LDL-C), apolipoprotein B (Apo B), total cholesterol (TC), and non-high-density lipoprotein cholesterol (non-HDL-C) in patients with familial hypercholesterolemia (HoFH).

Hepatocyte surface sialic acid glycoprotein receptors can discern N-acetylgalactosamine (GalNAc) with specificity. Khvorova et al. (2017) fused therapeutic small nucleic acid molecules with GalNAc, promoting their internalization into cells through the sialic acid glycoprotein receptor-GalNAc interaction. This actively targeted delivery mechanism, mediated by nucleic acid molecules and GalNAc, holds immense promise. Moreover, continuous advancements in nucleic acid modification techniques rekindle prospects for small nucleic acid drugs. Sulfur-modified phosphorothioate modification, the first-generation method, confers augmented degradation resistance to ASOs. However, excessive modification could induce non-specific cell toxicity and diminish target affinity. The second-generation approach generally entails mixed backbone modification, which heightens specificity but retains some cellular toxicity and lacks activation of RNase H-mediated degradation.

3 Hypothesis and objectives of the work

The overall objective of this thesis was to achieve precise cancer treatment through multi-targeted drug delivery strategies. More specifically, miRNA-responsive targeting methods were constructed through dynamic DNA nanotechnology, to synergize the receptor-based targeting process.

It was hypothesized that combining receptor-mediated targeted drug delivery strategies with miRNA targeting strategies can benefit distinguishing between tumor tissue and peri-cancerous tissue. Furthermore, this thesis also involves advancements in DNA nanotechnology from a material synthesis perspective. The complexity of metal-nuclear acid framework material synthesis is streamlined, enhancing yields and enabling the encapsulation of bioactive macromolecules, such as proteins, for therapeutic purposes.

In this context, the precise objectives of this dissertation were:

1. To establish receptor-targeted nanomedicine delivery systems (I&II).
2. To create miRNA-responsive drug delivery systems using dynamic DNA nanotechnology, to be able to develop a dual-targeted therapeutic system that combines miRNA and receptor targeting (III&IV).
3. Simplify the intricate preparation steps of DNA nanotechnology to enhance its translational potential (V).

4 Materials and methods

Within this segment, a comprehensive account of the materials and methodologies employed in the thesis is provided. The preparation approaches section expounds on the primary techniques employed for characterization of designed nanosystem. For a more intricate understanding, please refer to the attached Papers I-V, which furnish additional particulars on the subject matter.

4.1 Materials

All reagents utilized in this investigation were procured from reputable commercial sources including Sigma-Aldrich, Abcam, Novex, and VWR. The synthesis and HPLC purification of all oligonucleotides were carried out by Sangon Biotechnology Co., Ltd. (Shanghai, China). No supplementary purification procedures were conducted prior to their application in the experiments.

4.2 Nanomaterials preparation approaches

4.2.1 Synthesis of folate receptor-targeted zeolitic imidazolate framework-8 (ZIF-8) (I)

The synthesis of the pH-sensitive prodrug of cis-aconitic anhydride-doxorubicin (CAD) involves dissolving hydrochloric acid (HCl)-dissolved DOX in distilled water and cooling on ice. Simultaneously, cis-aconitic anhydride is dissolved in 1 mL of 1,4-dioxane and slowly added to the DOX solution under stirring. The pH is adjusted to 9.0 using NaOH, and the mixture is maintained in an ice bath for 20 minutes. Subsequently, the pH is adjusted to 7.0 using cold HCl. The product is extracted with ethyl acetate, evaporated, and CAD is obtained. For the synthesis of folic acid-conjugated ethylenediamine (FA-NH₂), folate (220 mg) was reacted with ethylenediamine (3.2 mL) using carbodiimide 1-ethyl-3-(3-dimethylaminopropyl) carbodiimide (EDC)/N-hydroxysuccinimide (NHS) as a catalyst. The reaction mixture was stirred overnight and then extracted with ether to yield FA-NH₂.

Synthesis of cis-aconitic anhydride-doxorubicin loaded zeolitic imidazolate framework (CAD@ZIF-8) and folatemoified CAD@ZIF-8 (CAD@ZIF-8-FA) involved these steps: The pH-sensitive prodrugs of doxorubicin were first mixed in 2 mL of water. Dimethylimidazole was then added dropwise to the above solution. After stirring for 5 minutes, centrifuging and washing with Milli-Q water 3 times, CAD@ZIF-8 was obtained. Different ratios of CAD@ZIF-8 were dispersed in 10 mL of water, and EDC (1.5 mg) and NHS (1.3 mg) were added. Then, 5 mg of the modified product FA-NH₂ was added.

4.2.2 Synthesis of mesoporous silica nanoparticles (MSNs) (II&III)

The synthesis of MSNs involved a two-phase method. An aqueous solution of cetyltrimethylammonium chloride (CTAC) and triethylamine (TEA) was initially

prepared and stirred for 1 hour. Then, 20 mL of tetraethyl orthosilicate (TEOS) was gradually added to the solution and stirred at 60°C for 24 hours. Afterward, the supernatant was discarded, and the resulting product was obtained through centrifugation. The product exhibited saturation with surfactant and demonstrated a positive charge. Conversely, the mesoporous material was dripped into an ethanol solution containing ammonium nitrate (NH_4NO_3) and thoroughly cleaned until the nanomaterial acquired a negative charge. Subsequently, 6 mL of 3-(trimethoxysilyl)propyl methacrylate (TMSPMA) was stirred with 0.2 g of MSN in 50 mL of methanol for 5 hours, resulting in the formation of MSN-TMSPMA.

4.2.3 Synthesis of a reservoir for bone hydroxyapatite targeted Au@MSN nanocomposite (II)

The seed-mediated synthesis of gold nanorods capped with CTAB (Au seed@CTAB) started with a water bath procedure, involving the addition of 30 μL of 50 mM HAuCl_4 solution to 5 mL of 0.1 M cetyltrimethylammonium bromide solution. This was followed by the introduction of 300 μL of 10 mM NaBH_4 . Simultaneously, a growth solution was prepared for the subsequent growth of seed@CTAB nanoparticles. The composition of the growth solution included 190 μL of 1 M HCl solution and 100 μL of 50 mM HAuCl_4 solution, combined with 10 mL of 0.1 M CTAB solution. It also incorporated 120 μL of a solution containing 10 mM AgNO_3 and 100 μL of a 100 mM ascorbic acid solution. The prepared gold nanorods (AuNRs) were subjected to centrifugation for 25 minutes, and the resulting solution was diluted with water to reach a final volume of 20 mL. Concurrently, in the stirred mixture, 200 μL of 0.1 M NaOH solution was added. Following this, every 30 minutes, 60 μL of a 20% TEOS methanol solution was sequentially introduced into the solution. Subsequent to this stage, modifications were carried out, including $-\text{NH}_2$ modification, resulting in the formation of AuNR@ $\text{SiO}_2\text{-NH}_2$, and $-\text{COOH}$ modification, resulting in AuNR@ $\text{SiO}_2\text{-COOH}$.

4.2.4 Synthesis of miRNA-21 targeted MSN@DNA nanocomposite (III)

DNA nano-hydrogels were fabricated through the initial step of modifying the termini of DNA sequence components using polyacrylamide monomers. This modification enabled the integration of a DNA segment into the newly developed linear polymer structure. Simultaneously, the antisense sequence of the miRNA acted as a cross-linking agent. Upon addition to the linear polymer monomers, the hydrogel's formation was promoted, facilitating the creation of bulk DNA hydrogels. In the case of nano-DNA hydrogels, the DNA was initially anchored onto MSN, followed by the synthesis of DNA polymers. By adjusting the preparation duration, hydrogel layers of varying thicknesses were achieved.

4.2.5 Synthesis of RGD and miRNA-21 targeted micelles@calcium phosphate nanocomposite (M@CaP) (IV)

The synthesis of calcium phosphate nanoparticles (CaP NPs) was achieved using a simple one-step method at room temperature. This process involved the combination of two distinct solutions for a duration of 5 minutes. Solution A was prepared by mixing CaCl_2 and Tris buffer in a total volume of 2 mL of Milli-Q H_2O . On the other hand, solution B comprised 0.43 mL of HEPES buffer (containing 280 mM NaCl, 15 mM Na_2HPO_4 , and 50 mM HEPES) along with 0.3 mL of Milli-Q H_2O .

For co-loading both drugs, 50 mg of Distearyl acylphosphatidyl ethanolamine (DSPE) polyethylene glycol (PEG) (DSPE-PEG-RGD) polymers were dissolved in 5 ml of an organic solvent composed of 70% ethanol and 30% chloroform. Different drug concentrations with various photothermal therapy (PTT) dye IR780/Curcumin were dissolved. The solution was evaporated using a rotary evaporator to form a film. Afterward, 10 ml of water was added for hydration over 24 hours, followed by centrifugation at 3000 rpm for 5 minutes to eliminate any unencapsulated drugs due to their low water solubility. Subsequently, 10 mL of $\text{RM}_{(\text{I}+\text{C})}$ micelles were prepared.

For $\text{RM}_{(\text{I}+\text{C})}@\text{CaP}_{(\text{p})}$ NPs, micelle solution was used instead of the 2 mL Milli-Q H_2O in solution A during CaP NP preparation. Prior to CaP mineralization, different concentrations of partial DNAzymes (Partzyme) (1 μM , 10 μM , 50 μM , 100 μM , 200 μM) were pre-cultured with solution A. Partzymes were modified with Sulfo-Cyanine3 (Cy3) for quantification using UV spectrophotometry to measure non-encapsulated DNAzymes.

The drug loading for each components were determined using UV-Visible spectroscopy. For NPs containing CaP, centrifugation was employed to isolate NPs from the reaction mixture, and subsequent washing with an appropriate solvent was done multiple times to remove impurities.

4.2.6 Synthesis of HER-2 targeted calcium/DNA framework (V)

For the synthesis of metal-nucleic acid framework (MNF) nanocomposites, DNA fragments (2 μL , 1 mM) were incubated with 1M CaCl_2 in a reaction volume of 200 μL at room temperature. The total weight of the resulting MNF material was determined through freeze-drying. The presence of calcium (Ca) within the MNF material was assessed using a Ca detection assay kit. The quantification of DNA content was achieved by subtracting the DNA content present in the supernatant from the initial amount of DNA prior to the reaction, as quantified using a nanodrop spectrophotometer.

4.3 Methods for nanosystem characterization

4.3.1 Structure analysis (I-V)

Transmission electron microscopy (I-V)

In order to observe the morphology of nanoparticles, determine their size, and confirm the success of synthesis, Transmission electron microscopy (TEM) images were acquired using a JEM-1400 Plus TEM microscope provided by

JEOL Ltd., Japan. The procedure involved immersing a copper grid in the solution containing the nanomaterials.

Dynamic light scattering and zeta-potential (I-V)

In order to observe the hydrated particle size of nanomaterials and ensure their circulation *in vivo*, Dynamic light scattering (DLS), and zeta-potential analyses were performed using a Zetasizer Nano ZS instrument manufactured by Malvern Instruments Ltd., UK. This equipment enabled the measurement of particle size and zeta potential characteristics.

Fourier-transform infrared spectroscopy (II, III, VI)

To confirm the successful synthesis, Fourier-transform infrared spectroscopy (FTIR) spectra were acquired using a Thermo Nicolet IS10 spectrometer at room temperature. The range of 4000-1000 cm^{-1} was scanned with a resolution of 4 cm^{-1} .

Molecular dynamics simulations (V)

To explore the MNF formation at the molecular level, molecular dynamics (MD) simulations of DNA oligonucleotide constructs with calcium (Ca^{2+}) ions were carried out using the Desmond software (2006) as implemented in Maestro Molecular Modeling Suite (Schrödinger Release 2023-1: Maestro, Schrödinger, LLC, New York, NY, 2023) with the OPLS4 force field (Lu et al., 2021). The DNA constructs were modelled using the 3D Builder panel of Maestro and the amorphous simulation systems were built using the Disordered System Builder panel of the Maestro Material Science Suite (Schrödinger Release 2023-1, New York, USA). In addition to the calcium salt, neutralizing chloride atoms were added into the orthorhombic simulation box. Prior to the production simulation, the simulation system was equilibrated using Desmond's relaxation protocol that included short (12-24 ps) simulations first at 10 K in the NVT ensemble and then at 300 K and 1 atm (1.01325 bar) pressure in the NPT ensemble, with and without restraints on the DNA heavy atoms. The production simulation ran for 100 ns at 300 K and 1 atm, utilizing the Nose-Hoover chain thermostat (Nosé 1984) and the Martyna-Tobias-Klein barostat (Martyna et al., 1994) with isotropic coupling. Long-range Coulombic interactions were managed using the U-series method (Predescu et al., 2020), and a 9.0-Å cut-off radius was set for short-range interactions. The radial distribution function (RDF) between Ca^{2+} ions and the negatively charged phosphate oxygen atoms (O^-) was calculated and plotted from the MD simulation trajectory. In addition, persistence length of the DNA constructs was calculated from their respective MD trajectories.

4.3.2 *In vitro* studies (I-V)

Assessment of cytotoxicity through cell proliferation assay (I-V)

The safety and effectiveness of nanomaterials are fundamental aspects of studying nanosystems. The samples were tested for *in vitro* cytotoxicity using

the WST-1 assay. Various cell lines were obtained from ATCC®, including breast cancer cell line (MDA-MB-231), non-tumorigenic epithelial cell line (MCF-10A), pancreatic cancer cell line (PANC-1), gastric cancer cell line (N87), and normal human skin fibroblasts (NHDF). These were used to assess sample toxicity. Cells (5×10^3 cells/well) were seeded in a plate and treated with the samples for 24 or 48 hours. Afterwards, the WST-1 testing kit was utilized, followed by the measurement of absorbance using an enzyme-labeled instrument.

Cellular uptake analysis (I-V)

Whether nanomaterials can be internalized by cells is a crucial factor in their cellular functioning. Cells were cultured in 6-well plates (1×10^5 cells per well) and allowed to attach. Once adhered, the culture media was replaced with solutions containing either free drug or nanoparticles. After 1-hour and 8-hour incubation periods, cells were observed using Confocal Laser Scanning Microscopy (CLSM). The red fluorescence represents the fluorescence of drugs CAD and DOX, while the blue fluorescence is DAPI, representing the cell nucleus. Green fluorescence is indicative of live cells. (I,II) The FITC fluorescence is represented by a green signal, indicating Curcumin, while the IR780 drug is represented by a red signal. (III, IV) In manuscript V, the DNzyme is represented by a red signal, and the GLUT-1 protein is indicated by yellow fluorescence. Additionally, cells were harvested using trypsin, washed with phosphate-buffered saline (PBS), and analyzed using a BD LSRFortessa flow cytometer (BD Biosciences). Flowjo_V10 software was employed for data analysis, focusing on live cells and recording 10,000 cells per sample.

Fluorescence *in situ* hybridization (VI, V)

To determine whether the genes were silenced inside the cells, we employed the Fluorescence In Situ Hybridization (FISH) method. The FISH was bought as kit. The hybridization buffer-diluted probe underwent denaturation at 85°C for 2 minutes. This denatured probe then engaged in a 72-hour hybridization with cells fixed in 4% paraformaldehyde. DAPI (4',6-diamidino-2-phenylindole, a nuclear staining dye) staining ($A_{max} = 358$, $E_{max} = 461$) was employed for cell labeling, while the probe's fluorescence was represented by sulfo-cyanine5.5 NHS ester (Cy5.5) ($A_{max} = 683$, $E_{max} = 703$). Utilizing ImageJ software, the relative intensity of each experimental group was quantified.

Lysosome escape assessment (III, VI, V)

The ability of nanomaterials to be released from cells after internalization is also crucial. LysoTracker Green was utilized as the lysosome probe. Cells were cultured on the confocal dishes and allowed to adhere overnight. Subsequently, the lysosomal escape behavior of the nanoparticle groups was evaluated at 2h and 24h intervals. For each group, after co-culturing NPs with cells for 2h and 24h, the cell media were replaced. Following laser irradiation, cells were subjected to a 2-hour incubation with LysoTracker Green, succeeded by a 5-

minute incubation with 4% paraformaldehyde. Subsequent observation of the cells was carried out using fluorescence confocal microscopy. The co-location scatterplots for each group were quantified using ImageJ software.

Western blot assay (III, VI, V)

The internal gene expression of cells in response to the material can be detected through Western blot analysis. To investigate cellular responses, the cells were exposed to various nanomaterial groups for 48 hours. Subsequently, cell lysis was performed using radioimmunoprecipitation assay buffer (RIPA) and Tris-HCl lysis buffers. For comprehensive cell lysis, RIPA was applied, with 20 μ l of 1% protease inhibitor and 20 μ l of 1% 0.5M EDTA added to every 2 mL of RIPA. Simultaneously, Tris-HCl lysis was employed for cytoplasmic cleavage. SDS-PAGE gradient gel was employed to separate cell proteins, followed by their transfer to a polyvinylidene fluoride (PVDF) membrane. Samples were mixed with protein loading buffer, denatured at 98°C for 10 minutes, and subsequently incubated with primary antibodies targeting Phosphatase and tensin homolog (PTEN), HSP70, Cyto-C, β -Actin, Pro-Caspase 3, cleaved-caspase 3, and Glyceraldehyde 3-phosphate dehydrogenase (GAPDH) (Abcam, Cambridge, UK) (1:1000). After primary antibody incubation, the membranes were exposed to secondary antibodies at 37°C for 1 hour. The Bio-RAD ChemiDoc MP Imaging System facilitated the assessment of protein bands, with subsequent fluorescence quantitative analysis conducted using ImageJ software.

Measurement of Mitochondrial membrane potential ($\Delta\Psi_m$) using 5,5',6,6'-Tetrachloro-1,1',3,3'-tetraethylbenzimidazolylcarbocyanine, iodide (JC-1) monomer and aggregates (VI, V)

The mitochondrial membrane potential of cells is a crucial indicator reflecting the health status of mitochondria. Cells were plated in 6 wells plate with 2.0 mL of Dulbecco's Modified Eagle Medium (DMEM) and incubated for 24 h. The culture medium was then substituted with 1.0 mL of various treatment solutions. Following two washes with PBS, cells were stained with JC-1 and examined using CLSM. For this assessment, 1.0 mL of JC-1 working solution was combined with cells in 1.0 mL of DMEM.

4.3.3 *In vivo* biodistribution study (I- V)

Understanding the distribution of nanomaterials in the body is crucial for assessing their therapeutic effectiveness. Various groups of mice were established to assess the biodistribution of nanodevices following intravenous administration, with equal concentrations of each therapeutic. *In vivo* imaging was conducted at timepoints of 1h, 8h, 24h, and 48h.

4.3.4 *In vivo* anticancer efficacy (I- V)

Investigating the therapeutic effects of nanomaterials *in vivo* is the most direct way to characterize the efficacy of the system. Tumor models were established

by injecting luciferase-containing cells into the organs of mice to create orthotopic tumor models. Additionally, subcutaneous injections were used to develop subcutaneous tumor models. The mice were stratified into different groups, with equivalent concentrations of each therapeutic. In the laser treatment groups, real-time monitoring of tumor site temperature was conducted using *In Vivo* Imaging Systems. Tumor volumes were calculated through the software of the *In Vivo* Imaging Systems. The terminal deoxynucleotidyl transferase dUTP nick end labeling (TUNEL) assay were determined for evaluate the therapeutc efficiency of each nanosystem.

4.3.5 *In vivo* safety evaluation from organ histology (I- V)

In vivo safety testing is crucial for the clinical translation of nanomaterials. The major organs were fixed and 3 μm thick slices were prepared for sectioning. Hematoxylin and eosin (H&E) staining was performed on the sections to facilitate the observation of potential damage related to the cancer.

5 Results and discussion

5.1 Development of receptor-targeted nanomaterials (I&II)

In this chapter, I discuss the multifunctional nanostructures that were constructed for targeting receptors using folic acid receptor ligands and bone targeting ligands. Specifically, in the folate receptor-targeted nanoparticle system, we conjugated doxorubicin with a carboxyl-containing pH-sensitive linker to synthesize a carboxyl-containing pH-sensitive prodrug. This prodrug was then encapsulated within ZIF-8 nanostructures. This step enhanced the carboxyl content on the surface of ZIF-8, facilitating further surface modification. Additionally, we transformed the carboxyl groups in folate to amino groups for covalent binding to the carboxyl groups on the ZIF-8 surface, thereby enabling folate receptor-targeting ability in the ZIF-8 system.

On the other hand, for bone tissue-targeted systems, we introduced alendronate (ALN) modification onto the surface of gold nanorods loaded with doxorubicin, conferring bone-targeting capabilities to this nanostructure. Furthermore, to enhance the drug targeting efficiency for specific tumor sites, we encapsulated the above ALN-modified nanostructures within hydrogel microspheres using microfluidic technology. This resulted in the development of an injectable hydrogel reservoir material for *in situ* use, facilitating localized and sustained targeted therapy.

In each project, comprehensive material characterization was conducted, and the therapeutic efficacy of the nanomedicines was evaluated through *in vitro* and *in vivo* experiments.

5.1.1 Design and characterization of the receptor-mediated cancer-targeting nanoparticles

5.1.1.1 Folate-receptor-targeted nanoparticles (I)

The conversion of DOX into the prodrug CAD was achieved as shown in **Figure 10A**. The carboxyl group served a dual purpose—enhancing carrier affinity and enabling subsequent carboxylized ZIF-8 for further folate (FA) conjugation. The synthetic procedure is illustrated in **Figure 10A**. The ^1H NMR spectra revealed distinct peaks at 6.1 and 6.8 ppm after DOX was modified with cis-aconitic anhydride (CAA). These observed peaks were assigned to the resonances of protons ($\text{CH}-\text{COO}-$) inherent in the CAA component within the CAD structure. (**Figure 10B**). Moreover, the mass spectra of CAD (depicted in **Figure 10C**) showcased a notable peak at 698 mass units, aligning closely with the theoretically calculated mass. This congruence between the observed and calculated masses provided strong confirmation of the accurate molecular composition of the synthesized CAD compound.

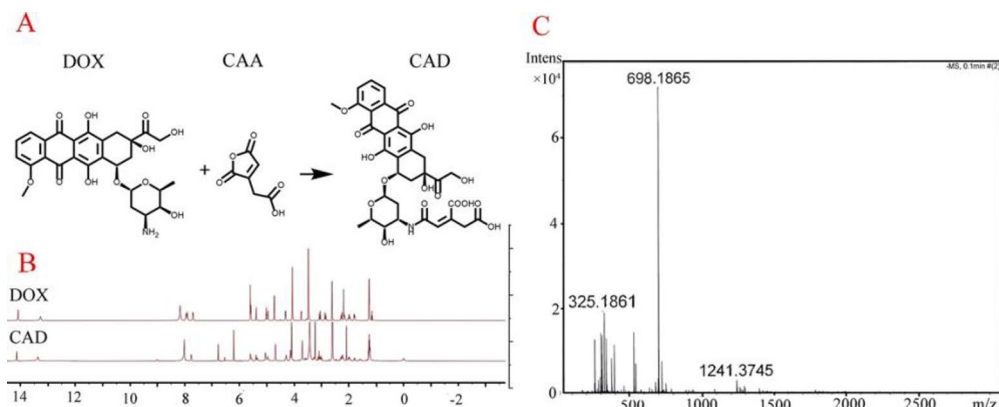


Figure 10. NMR and mass spectrometry analysis for the CAD. Panel (A) synthetic pathway for CAD. Panel (B) ¹H NMR spectra of CAD and DOX in DMSO-d₆, allowing for a comparison of their chemical signatures. Panel (C) the mass spectrometry (MS) spectra of CAD, providing insight into its molecular composition and structure. (Copyright © 2020 American Chemical Society)

CAD@ZIF-8 nanoparticles were constructed at room temperature for 5 minutes. TEM images (**Figure 11A**) showed that as the drug loading degree increased, the nanoparticle size grew. Concurrently, the hydrodynamic sizes tested by DLS (**Figure 11B**) ranged 159 - 590 nm, closely aligning with the TEM images. As shown in **Figure 11C**, we observed that the zeta potential decreased slightly when the loading increased from 0% to 34.75%, but reduced by 23.9 mV as the loading increased from 34.75% to 43.97%. These findings suggested the mineralization of CAD within ZIF-8 and significant impact on zeta potential at higher CAD loadings.

Based on the characterization of CAD@ZIF-8, we selected a CAD loading of 34.75% for subsequent FA conjugation. To facilitate the conjugation, FA was modified with ethylenediamine for subsequent amidation reaction. Even after extensive washing and ultrasonication, a substantial FA layer was observed within CAD@ZIF-8-FA NPs (**Figure 11A**). Meanwhile, as depicted in **Figure 11D**, the FA binding efficiency of blank ZIF-8 was as low as 25%. However, with the increase in CAD loading from 12.1% to 43.97%, the FA loading efficiency rose from 44% to 67.4%. Higher CAD loading promoted FA conjugation and thus facilitated the FA binding efficiency (binding of FA to the CAD moiety in the NPs). Additionally, FTIR results (**Figure 11E**) displayed two new peaks, indicating the formation of new amide bonds. These outcomes confirmed that FA was covalently bound to CAD@ZIF-8, rather than physically adsorbed.

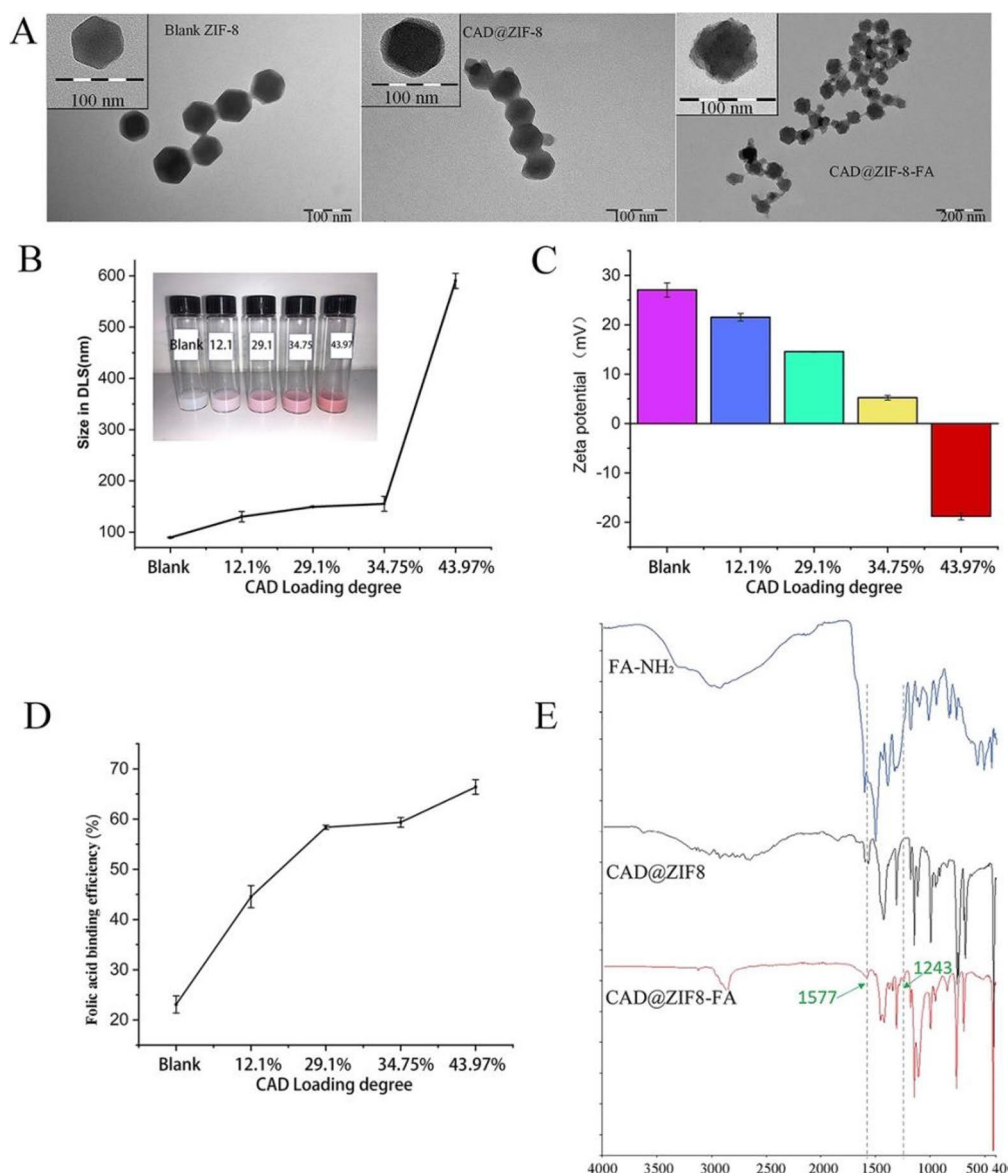


Figure 11. Characterization of ZIF-8-based nanoparticles. Panel (A) TEM images. Panel (B) Size data acquired from DLS measurements. Panel (C) Zeta potential variations at different CAD concentrations. Panel (D) Binding degree of FA to the CAD moiety in the NPs. Panel (E) FTIR spectra ($n = 3$). Copyright © 2020 American Chemical Society

5.1.1.2 Bone tissue-targeted nanosystem (II)

In the initial step, gold nanorods (AuNRs) were synthesized using a well-established method. Afterward, a uniformly thick layer of SiO₂ was coated onto their surface to facilitate both the loading of DOX and the subsequent surface modification with ALN. This was verified through TEM imaging, where the presence of the SiO₂ layer and the modifications were clearly observed. The longitudinal surface plasmon resonance (SPR) peak of the AuNRs at 849 nm

experienced a red-shift to 889 nm after the SiO₂ coating, as evident from the UV-vis absorption spectra. TEM images and elemental mapping highlighted the development of a mesoporous layer on the surface of the AuNRs subsequent to the SiO₂ coating (**Figure 12a–f**). Following the drug loading and ALN surface modification, the distinctiveness of the surface pores diminished (**Figure 12c**).

To delve into the photothermal effect of the nanoparticles, distinct concentrations of NPs/DOX (NPs containing DOX) were subjected to continuous irradiation by a 980 nm laser for durations ranging 0 - 300 s (**Figure 12 g,h**). Specifically, upon irradiation for 300 s with a laser intensity of 1 W cm⁻², the temperature surged by 60 °C for a solution containing 1 mg mL⁻¹ of NPs/DOX (**Figure 12g,h**). In contrast, pure water exhibited minimal temperature fluctuation under the identical laser intensity. Moreover, the photostability and photothermal conversion efficiency (η) of the NPs/DOX were thoroughly evaluated across three consecutive heating-cooling cycles. (**Figure 12i**), culminating in a calculated photothermal conversion efficiency of 27%.

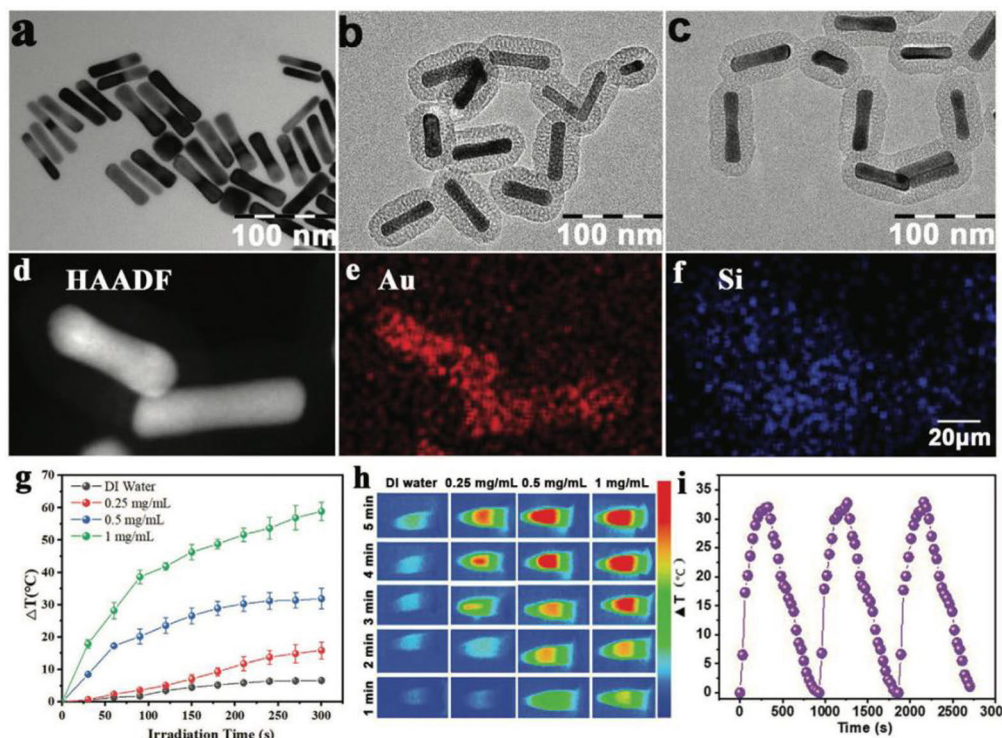


Figure 12. Characterization of nanoparticle morphology and photothermal effect. Panels (a-c): TEM images of Au nanorod, MSN coated Au nanorod (AuNRs@MSN), and alendronate modified AuNRs@MSN. Panels (d-f): The elemental distribution within NPs. HAADF means annular dark-field imaging. Panel (g): The photothermal heating curves associated with different nanoparticle concentrations. Panel (h): Infrared thermal images corresponding to distinct concentrations of NPs. Panel (i): The temperature elevation of AuNR@SiO₂ NPs across three successive cycles of NIR-induced irradiation switching. © 2021 The Authors. Small published by Wiley-VCH GmbH

5.1.1.3 Microgel reservoir of targeted NPs for local drug delivery (II)

Employing the versatility of gelatin methacrylate (GelMA), a photocrosslinkable hydrogel renowned for its biocompatibility, we embarked on a quest to redefine its application in cell scaffolds and wearable devices. The challenge of tailoring in situ degradability and adaptability for minimally invasive uses within bulk GelMA hydrogels led us to explore innovative approaches. Microfluidic technology emerged as our solution, enabling the creation of injectable GelMA microgels with varying dimensions. These microgels not only offered a spectrum of degradability profiles but also preserved the core properties characteristic of bulk gels.

By precisely orchestrating the internal phase flow rates (comprising GelMA and photo-initiator) and the external phase (comprising mineral oil and Span 80) within the microfluidic system (internal flow speed: external flow speed = 1:1, 1:2, 1:3), we successfully synthesized uniform microspheres (**Figure 13a**). Subsequently, these nanohybrid microspheres underwent UV crosslinking under conditions of 20 mW cm⁻² illumination at 480 nm for a duration of 20 seconds.

Throughout our investigation, the flexibility of preparing distinct concentrations of NPs/DOX and 5,6-dimethylxanthene-4-acetic acid (DMXAA) loaded GelMA hydrogels was evident (**Figure 13b**). These nanoparticles encompassed 30% DOX content, and to enhance the synergistic effect, we maintained a constant DOX to DMXAA ratio of 1:3 based on previous research. Importantly, it should be emphasized that the GelMA hydrogel showcases notable compressive elasticity. However, it is observed that an excessive loading of drugs leads to a complete compromise of the hydrogel's capacity to endure pressure. This phenomenon stemmed from the disruptive effects of the substantial NPs/DOX and DMXAA concentrations on the GelMA hydrogel's structural integrity, rendering it incapable of forming a resilient network (**Figure 13b**).

Drawing upon these insights, we proceeded to select the optimal loading conditions, precisely 10 mg mL⁻¹ NPs/DOX (containing 3 mg mL⁻¹ DOX) and 9 mg mL⁻¹ DMXAA. Capitalizing on microfluidic technology, we then fabricated microgels of NPs/DOX@GelMA/DMXAA with diverse dimensions (**Figure 13c**).

Subsequently, we harnessed confocal microscopy to evaluate the distribution of NPs within the microgel. Initially, Cy5.5-NHS was chemically conjugated to the surface of AuNR@MSN-NH₂ NPs to prevent dye release. A small quantity of FITC was then introduced for the microfluidic process. To prevent droplet fusion during microgel sphere preparation via microfluidic technology, we introduced Span 80 as a surfactant. Merging the fluorescence from both FITC and Cy5.5-NHS allowed us to visually assess the distribution of NPs within the microgel. FITC generated a green halo, delineating the microgel, while NPs exhibited an even distribution within the microgel (**Figure 13d**).

The degradation profiles of NPs/DOX@GelMA/DMXAA microgels of varying sizes, were subsequently monitored (**Figure 13e**). During the initial 6-day incubation period without laser irradiation, the 1:1 group exhibited a

degradation of $7 \pm 2.4\%$. In contrast, the 1:2 and 1:3 groups experienced mass losses of $13 \pm 1.8\%$ and $37 \pm 3\%$, respectively, within the same timeframe. These results indicated that as the microgel size increased and the surface area decreased, the degradation rate gradually extended. Notably, the 1:1 group displayed a longer degradation time, lasting up to 24 days, making it suitable for sustained treatment purposes. Hence, we selected the 1:1 flow rate as optimal for preparing microgels with approximately 265 μm diameters.

The microgel exhibited uniform sizing, accompanied by abundant surface pores that facilitate exchange between the microgel and the tumor microenvironment *in vivo* (**Figure 13f,g**). Additionally, the release profiles of DOX and DMXAA were determined through UV absorbance (**Figure 13h**). Upon irradiation with a 980 nm laser for 10 minutes on the 6th and 12th day, accelerated release of both DOX and DMXAA was observed. These findings underscored the remarkable light-controlled drug release capacity and long-term degradability of the microgel system. Moreover, fluorescence microscopy captured the microgel's morphological changes, as illustrated in **Figure 13i-l**, the red microgel's shape remained largely unchanged. However, upon laser irradiation on the 6th day, significant alterations were observed, highlighting the system's dynamic response to external stimuli.

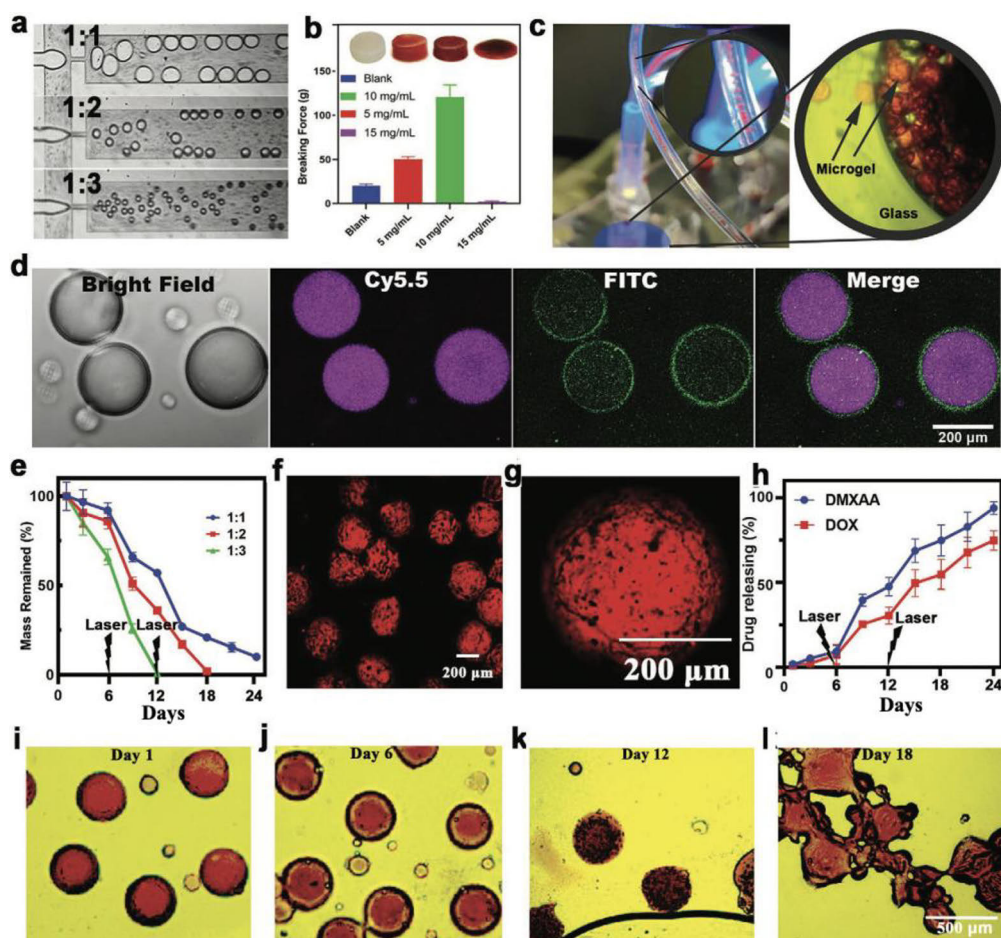


Figure 13. Morphological Characterization of Microgels. Panel (a) Microscopic image of microgels within a microfluidic chip, (internal flow speed: external flow speed = 1:1, 1:2, 1:3). Panel (b) Assessment of fracture force for hydrogels with varying concentrations of NPs and drugs. Panel (c) Micrograph showcasing the concentration of microgel material within the microfluidic outlet tube. Panel (d) Analysis of colocalization. Panel (e) Degradation curve. Panel (f, g) Fluorescence microscopy images displaying freeze-dried microgels and the dispersion of individual microgels. Panel (h) Cumulative drug release profiles of DMXAA and DOX within microgels. Panel (i–l) Time-lapse fluorescence images capturing the degradation dynamics of same microgels for three weeks. ©2021 The Authors. Small published by Wiley-VCH GmbH

5.1.2 Cytotoxicity and cell uptake analysis (I&II)

To comprehensively assess the cytotoxicity of NPs, WST-1 assays were conducted. The results depicted in **Figure 14A** demonstrated the potent tumor-killing efficacy of CAD@ZIF-8-FA NPs against MDA-MB-231 cells. Notably, when DOX concentration was below 1 $\mu\text{g/mL}$, pure DOX displayed heightened toxicity compared to CAD@ZIF-8-FA NPs. However, at higher concentrations (≥ 2.5 $\mu\text{g/mL}$), CAD@ZIF-8-FA NPs exhibited increased toxicity. This phenomenon could be attributed to the prodrug exhibiting reduced toxicity compared to the

parent drug under similar incubation times. At higher concentrations, the presence of ZIF-8 carriers intensified the toxicity of DOX.

Conversely, assessments conducted on healthy MCF-10A cells revealed negligible toxicity by both CAD experimental group and CAD@ZIF-8-FA experimental group (**Figure 14B**). At 10 $\mu\text{g/mL}$ DOX concentration, cell variability was significantly higher for both the pure ZIF-8 group and the CAD@ZIF-8 group compared to lower concentrations. The presence of the FA layer in the CAD@ZIF-8 group appeared to mitigate the extent of cell variability, suggesting a potential role in reducing toxicity in healthy cells while targeting tumor cells.

Subsequent to this, to visualize the cellular internalization of the drug, we conducted confocal experiments. **Figure 14C** illustrates the CAD groups, with a noticeable but moderate red signal detected within cells over a 2-hour period. Interestingly, the CLSM images demonstrated a considerably higher uptake of CAD@ZIF-8-FA NPs compared to CAD@ZIF-8 NPs in cancer cells. This enhanced uptake was attributed to the role of FA receptor-mediated endocytosis. Notably, both particles were initially confined to the cytoplasm, gradually accumulating around the cell nuclei after a 2-hour period (**Figure 14C**). These observations underscore the controlled DOX release achieved through the NPs in the initial stages.

For the bone tissue-targeting project, the evaluation of targeting and cytotoxicity on osteosarcoma cells involved fluorescence microscopy imaging and cholecystokinin octapeptide (CCK-8) experiments with DOX@AuNR@SiO₂-ALN NPs and microgel. Initially, CLSM images depicted a substantial increase in uptake efficiency for the DOX@AuNR@SiO₂-ALN NPs, following ALN modification, compared to the unmodified DOX@AuNR@SiO₂ NPs. (**Figure 14D**). Furthermore, upon laser stimulation, an increased amount of drug could penetrate the nuclear space. Conversely, within the absence of laser irradiation, NPs/DOX merely accumulated around the nucleus, indicative of a lower degree of drug release, given that DOX primarily exerts its effects upon entering the nucleus (**Figure 14D**). These observations demonstrated that DOX@AuNR@SiO₂-ALN NPs not only exhibited excellent uptake capacity but also showcased remarkable NIR sensitivity.

Subsequently, CCK-8 based cytotoxicity assays were performed. The results illustrated that the group exposed to laser induction exhibited heightened tumor-killing potential, particularly when DOX concentrations exceeded 1 $\mu\text{g/mL}$ (**Figure 14E**). Remarkably, the DOX@AuNR@SiO₂-ALN +Laser group containing 10 $\mu\text{g/mL}$ DOX showcased inhibition of over 85% of cells, surpassing the effectiveness of other groups. These outcomes suggested that the ALN-modified system presented superior tumor-inhibiting capabilities, attributed to the synergistic effect of laser-triggered photothermal therapy (PTT) and enhanced uptake facilitated by ALN-mediated bone-tissue targeting.

Subsequent live/dead cell staining experiments were conducted to further explore the cytotoxicity of each system. As depicted in **Figure 14F**, control and NPs/DOX@GelMA/DMXAA -Laser groups displayed minimal presence of dead

cells (depicted in red) after 24 hours of incubation, indicating lower toxicity compared to the pure DOX group. However, upon laser irradiation (+Laser), a substantial portion of MNNG/HOS osteosarcoma cells exhibited cell death within 24 hours.

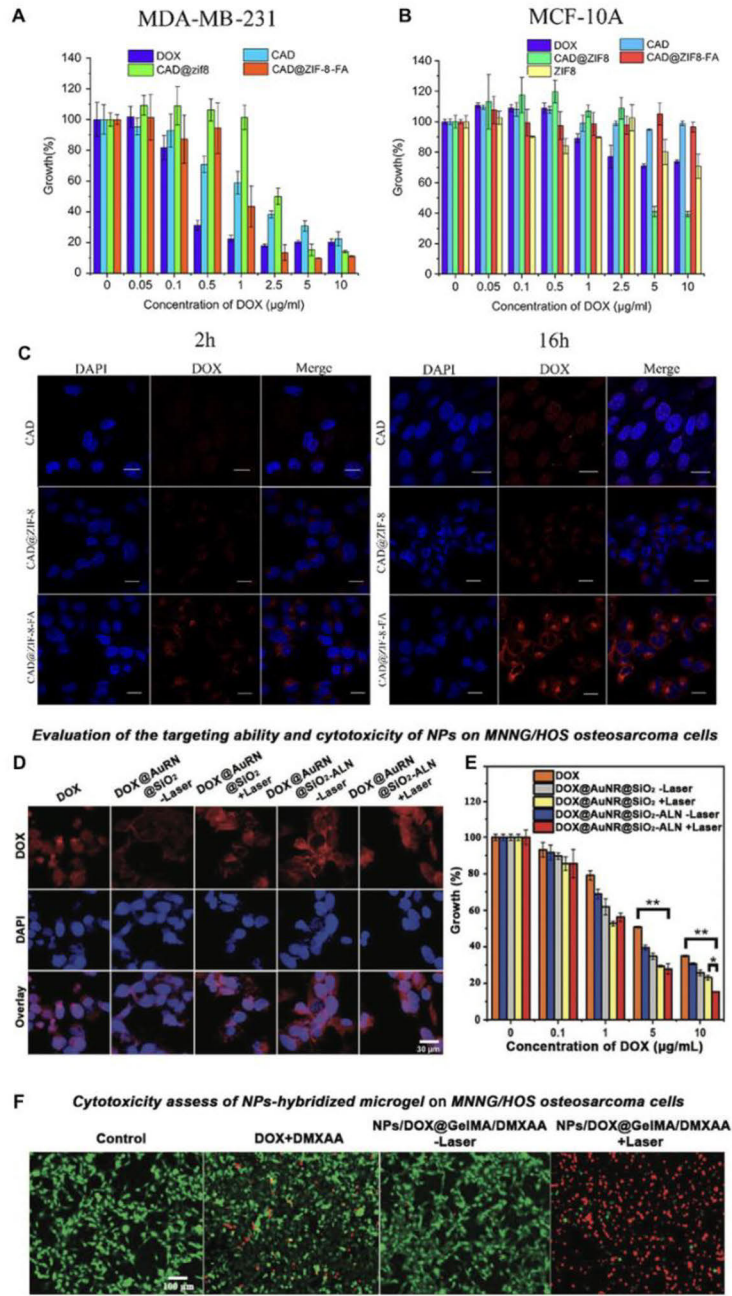


Figure 14. Cellular Uptake and Cytotoxicity Assays of nano-formulations. Paper I: Panel (A) Cytotoxicity evaluation of MDA-MB-231 cells upon treatment with various pure drugs and NP formulations. Panel (B) Assessment of cytotoxicity in MCF-10A cells subjected to differently dosed formulation groups. Panel (C) Confocal laser scanning microscopy

(CLSM) image illustrating the endocytosis of nanomaterials by MDA-MB-231 cancer cells. Scale bar: 20 μ m. (Copyright © 2020 American Chemical Society). Paper II: Panel (D, E) Evaluation of cytotoxicity. F) Fluorescence microscopy images from the live/dead cell staining assay conducted on the microgel set (red depicts the dead cells). (©2021 The Authors. Small published by Wiley-VCH GmbH)

5.1.3 *In vivo* biodistribution evaluation for NPs

5.1.3.1 Tumor targeting (I&II)

For the visualization of NPs distribution within mice, fluorescence imaging was conducted. The observations demonstrated evident NPs accumulation at tumor sites, whereas DOX exhibited dispersion throughout the mice's entire body (**Figure 15A**). Moreover, the NIR fluorescence imaging data obtained from various organs in treatment groups (**Figure 15B**) unmistakably exhibited a substantial elevation in red fluorescence specifically within the tumor tissues of the NP-treated group. This remarkable observation provides compelling evidence of the CAD@ZIF-8-FA NPs' exceptional capability to significantly augment drug accumulation within tumor sites, thereby substantially enhancing the overall efficiency of drug delivery.

In contrast, in the context of the bone tissue-targeting project, DOX exhibited a tendency to disperse into the surrounding tissues rather than penetrating the solid tumor core (**Figure 15C**). Additionally, both the NPs/DOX (IV: Intravenous) and DOX (PT: Peritumoral) groups showed limited retention within the body, with metabolism leading to their elimination within three days. Consequently, whether through direct intratumoral drug injection or administering 20% dosage of NPs/DOX through vein administration, the drugs struggled to effectively reach the tumor site.

On the other hand, for the NPs/DOX@GelMA/DMXAA formulation, the hydrogel remained at the tumor site and maintained its integrity for up to two weeks without laser irradiation (**Figure 15D**). However, following 10 minutes of laser irradiation, the distribution of DOX within the tumor became apparent. Of significant note, the fluorescence intensity emanating from the tumor tissue in the NPs/DOX@GelMA/DMXAA (PT) treatment group was remarkably amplified, exhibiting a staggering 5.8-fold increase compared to both the DOX (PT) group and the DOX/NPs group. (**Figure 15D,E**). These compelling findings affirm the nanoparticle-loaded microgel's exceptional drug delivery efficacy, NIR-responsive drug release capability, and its capacity to enhance tumor phagocytosis.

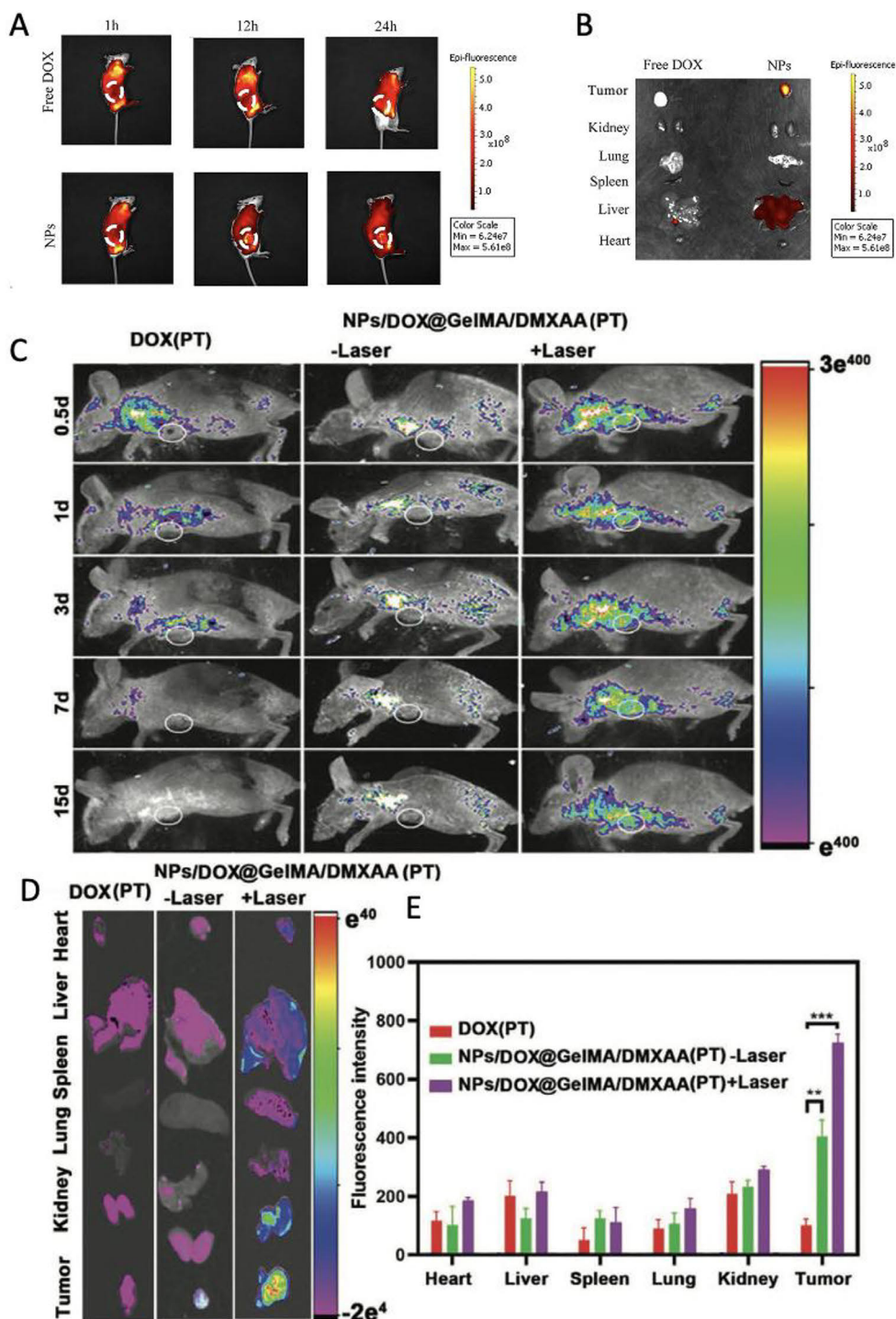


Figure 15. Panel (A): In vivo fluorescence imaging of tumor-bearing mice following the administration of free DOX and NPs. Panel (B): Ex vivo bioluminescent imaging illustrating drug distributions in different organs. (Copyright © 2020 American Chemical Society) Panel (C,D): In vivo and in vitro imaging, showcasing the distribution of DOX fluorescence.

Panel (E): Quantification of DOX fluorescence intensity quantified using ImageJ ($n = 3$, $*p < 0.05$ and $***p < 0.001$). (©2021 The Authors. Small published by Wiley-VCH GmbH)

5.1.3.2 Therapeutic efficiency assay (II)

Motivated by the promising tumor-targeting capability of the nanocomposite microgel *in vivo*, we proceeded to validate its tumor inhibition potential across various formulations using a mouse model of MNNG/HOS osteosarcoma xenograft tumors. In the +Laser groups, we employed 980 nm laser (1 W/cm^2) irradiation for 10 minutes, repeated every three days. Results revealed that the NPs/DOX@GelMA/DMXAA +Laser (PT) group exhibited the most favorable therapeutic outcome, leading to a gradual reduction and eventual disappearance of tumor volume (**Figure 16a, b**). Concurrently, the corresponding tumor weight data indicated that the microgel +Laser group displayed the lowest tumor mass (**Figure 16c**).

Notably, the NPs/DOX@GelMA/DMXAA +Laser (PT) group exhibited an impressive tumor suppression rate of $94.5 \pm 5.5\%$ (**Figure 16d**). These collective findings underscored the microgel system's robust capability for inhibiting tumor growth, which stemmed from the enhanced uptake of ALN-modified NPs/DOX by osteosarcoma cells.

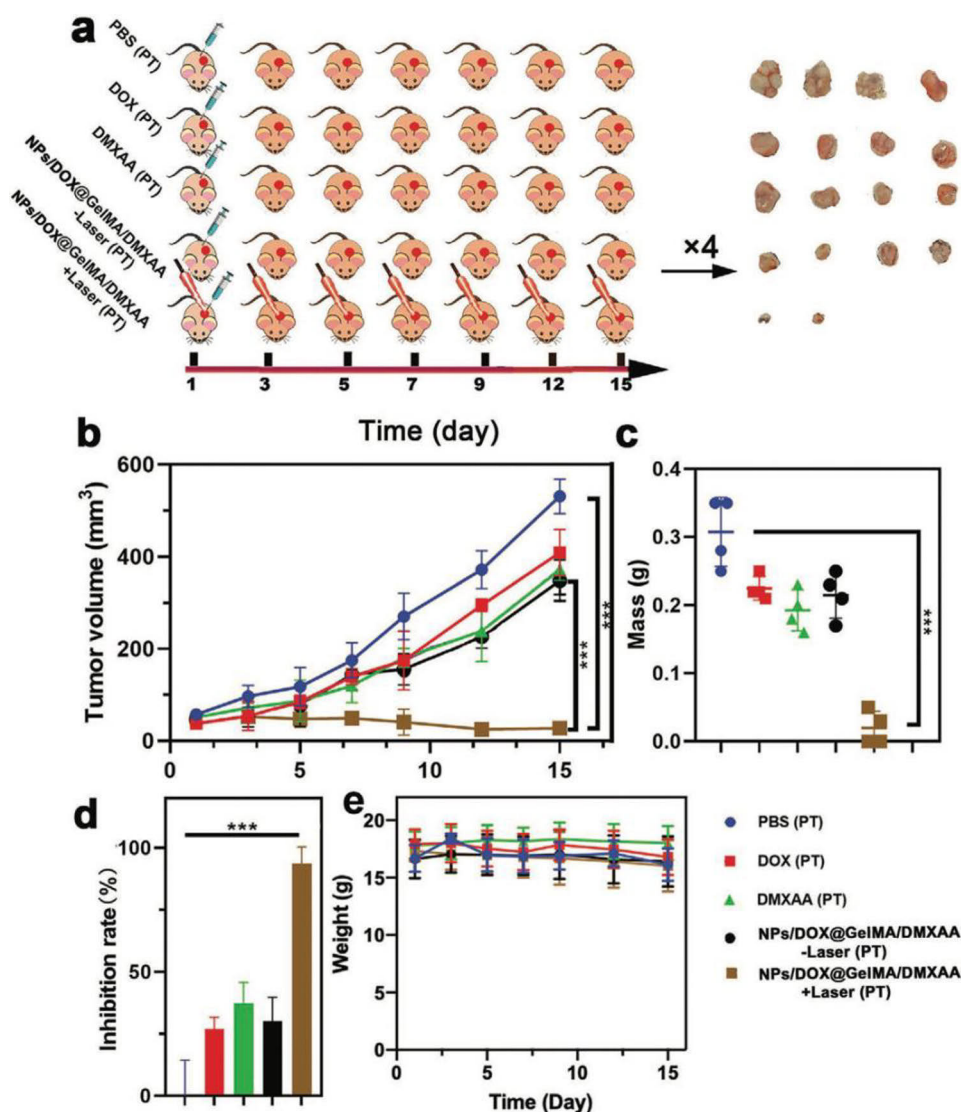


Figure 16. Characterization of Tumor Treatment after Peritumoral (PT) Administration. Panel a) Experimental design and photographs of extracted tumors after treatment. Panel b) Changes in tumor volume during the treatment period. Panel c) Tumor masses from different groups. Panel d) Tumor inhibition rates on the 15th day for various groups. e) Changes in body weight during the treatment process. ($n = 4$, ** $p < 0.01$ and *** $p < 0.001$). (©2021 The Authors. Small published by Wiley-VCH GmbH)

5.1.3.3 *In vivo* toxicity study (II)

Additionally, a systemic safety evaluation was conducted by monitoring changes in body weight and conducting hematoxylin and eosin (H&E) staining on different organs. The results revealed no significant differences across the various groups (**Figure 16e**). Similarly, the H&E imaging of the organs revealed

no discernible toxicity, confirming the minimized toxic effects of high concentrations (**Figure 17**).

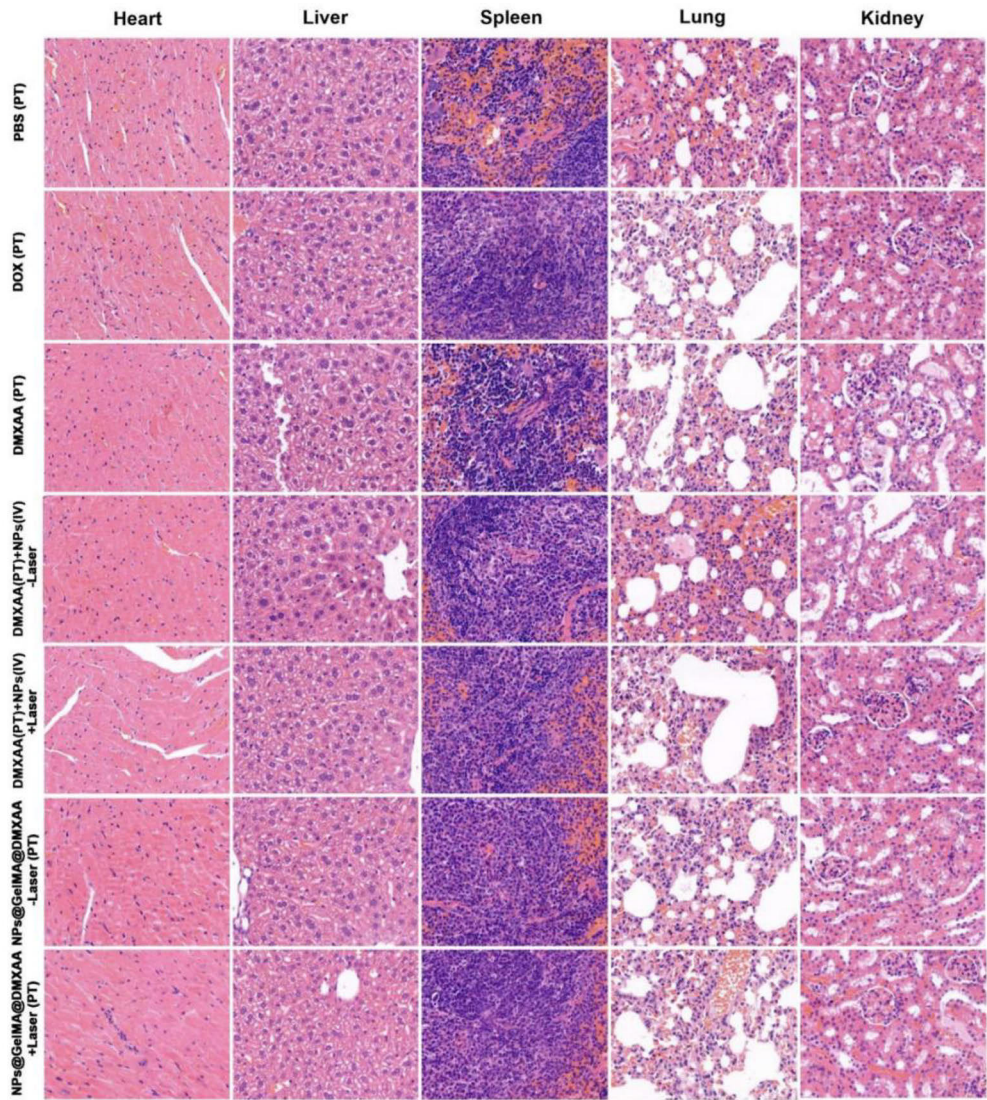


Figure 17. Hematoxylin and eosin stain (H&E) staining of different main organs. (©2021 The Authors. Small published by Wiley-VCH GmbH)

5.2 Fabrication of miRNA and receptor-targeted materials using dynamic DNA nanotechnology (III&IV)

This chapter focuses on the exploration of miRNA-mediated targeted cancer therapy, which offers a distinct approach due to the overexpression of miRNA in cancer cells. This alternative targeting mechanism diverges from receptor-mediated methods. The primary focus of this thesis involves the development of miRNA-responsive materials in two key directions.

Firstly, the study delves into the creation of miRNA-21-responsive DNA hydrogels. These hydrogels are encapsulated onto mesoporous silica surfaces, enabling the controlled release of drugs in response to miRNA-21. Concurrently, the DNA hydrogel can silence miRNA-21, thereby facilitating gene therapy.

Additionally, this thesis explores the design of miRNA-responsive DNazymes. These DNazymes are engineered by dividing the catalytic ring into two segments and attaching the complementary miRNA-21 sequence to the cleavage site. Consequently, the target gene can be selectively cleaved by DNazymes only in the presence of miRNA-21. This strategy permits the assembly of active DNazymes within cancer cells, leading to a heightened selective therapeutic effect.

Finally, the research investigates the integration of miRNA-21-targeting DNazymes and receptor-targeted approaches for a dual-targeted therapy to combat pancreatic cancer in its local environment.

5.2.1 Design and characterization of the miRNA-mediated cancer-targeting NPs

5.2.1.1 MiRNA-targeted DNA hydrogel (III)

In the process of designing the DNA hydrogel layer, the loading content of the miRNA-21 antisense strand plays a crucial role in ensuring effective cancer treatment. In the context of pancreatic cancer cell lines, 100 nM of miRNA-21 antisense oligonucleotides has exhibited substantial gene silencing effects in cytotoxicity studies conducted in vitro (Li et al., 2017).

We prepared 6 experimental groups (**Figure 18A1**), each containing 200 μ g of MSN, and numbered them from 1 to 6. Subsequently, we added the same concentration of Cy3-labeled adhesive chains into the system, as shown in **Figure 18A2**. After a period of incubation, we centrifuged (**Figure 18A3**) and collected the supernatant (**Figure 18A4**) for UV-vis absorption analysis (**Figure 18B**). The experimental results confirmed the efficient assembly of Cy3-labeled binding sequences within DNA nanohydrogels. Finally, the centrifuged NPs were washed and diluted to 1 mL, at which point the final concentration of miRNA-21 antisense strand was 10 μ M.

The adhesive chain facilitates the cross-linking of two DNA strand named strand A and strand B, and this outcome was verified through the polyacrylamide gel experiment (**Figure 18C**). Upon the interaction of the A chain or the B chain

with the adhesive chain, a distinct cross-linking pattern emerges at approximately 20 base pair intervals, as evidenced by the GelRed labeling. This coincided with the disappearance of the A/B strand band, signifying the successful combination of each strand. To clarify overlapping results due to the double-strand band and the prior adhesive strand, DAPI, which selectively binds to A-T base-pair regions, was used as a labeling dye. Consequently, only one new band emerged when the three single strands were combined (**Figure 18C**).

Given the intricacy of the newly formed bands following the three-chain reactions, interpreting the results becomes challenging. Therefore, we employed the NUPACK web application to conduct a detailed analysis of potential reactions, as illustrated in **Figure 18D** (Wolfe et al., 2017). When each strand was added at 1 mM, alongside the 0.94 mM product, 0.017 mM of strand A remained, accounting for the band at approximately 14 bp (**Figure 18C**). Additionally, strand A–adhesive strand and strand B–adhesive strand were produced (**Figure 18D**), coinciding with the location of the final product band (**Figure 18C**).

To validate the "unlocking" mechanism of the hydrogel, we created bulk hydrogel samples for better visualization of macroscopic changes in the DNA hydrogel structure (**Figure 18E and 18F**). Notably, the DNA hydrogel exhibited a noticeable transition (**Figure 18E**) from its initial state to a transparent milky liquid form (**Figure 18F**). These observations provide strong evidence that miRNA-21 is capable of competitively binding to the adhesive strands within the hydrogel, consequently leading to its degradation.

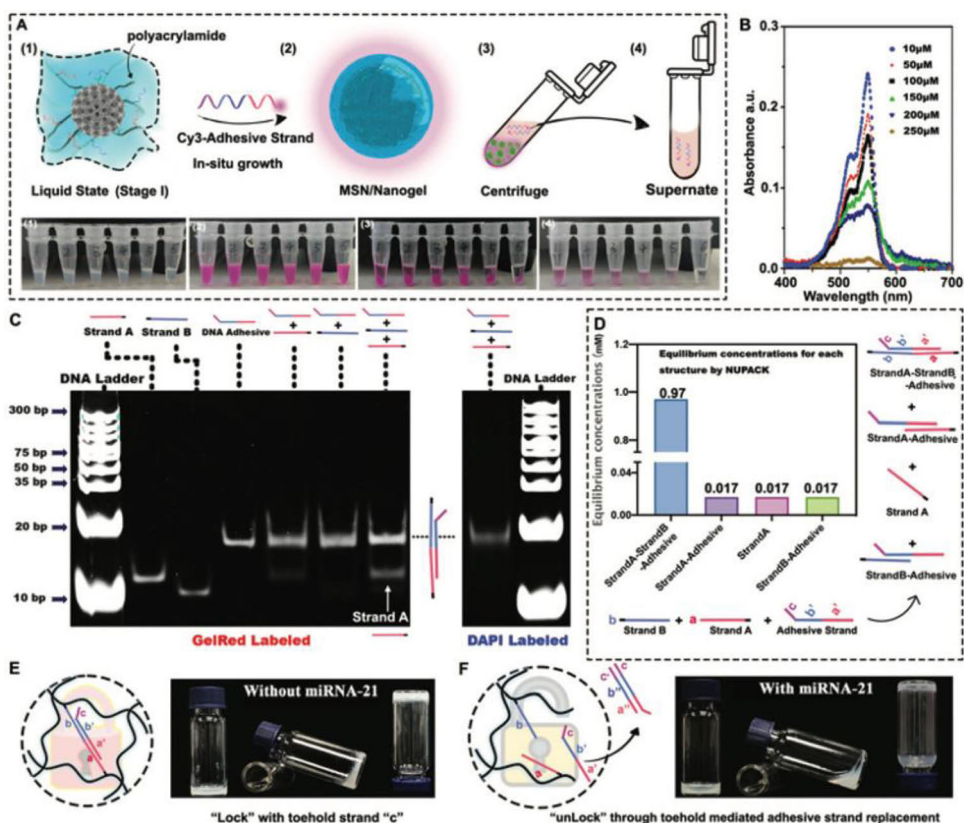


Figure 18. Characterization of DNA hydrogel. Panel (A) Assessment of adherent strand content. Panel (B) UV absorbance of adherent strands in the post-centrifugation supernatant. Panel (C) Polyacrylamide gel experiment to confirm cross-linking. Panel (D) Simulated prediction of response results using the NUPACK Web application. Panel (E) Macroscopic image of DNA hydrogel exposed to various miRNAs. Panel (F) Macroscopic image of DNA hydrogel treated with miRNA-21 strands. (© The Authors. The Royal Society of Chemistry 2022)

5.2.1.2 DNA hydrogel/MSN nanocomposite (III)

To verify the successful integration of DNA hydrogels with pure MSN NPs, we analyzed the nanomaterials using Dynamic Light Scattering (DLS) and Transmission Electron Microscopy (TEM) techniques. Concurrently, by incubating the mesoporous silica and DNA hydrogel materials, we observed an augmentation in particle size, from an initial 120 nm to around 150 nm. (**Figure 19A**). However, after incubating with miRNA-21 (miR-21), the particle size reverted to 120 nm, suggesting the excellent miRNA-21 responsive degradation capability of the nanogel shell. Correspondingly, zeta potential data revealed that TMSPMA-modified MSN exhibited a negative charge of around -33 mV. Once enveloped by the DNA hydrogel, the final NPs acquired a neutral zeta potential (**Figure 19B**), enhancing their phagocytosis by cancer cells due to the negative-

to-neutral transition. The confirmation of a DNA hydrogel layer was further evident through TEM (**Figure 19C**). Notably, the DNA hydrogel layer on the surface of MSNs disappeared after incubation with miR-21, indicating the successful construction of miRNA-responsive DNA hydrogels (**Figure 19D**).

The "gate material," represented by the DNA nanogel, safeguarded gemcitabine (Gem)-loaded MSN NPs, ensuring drug release occurs post accumulation within the tumor tissue (**Figure 19D**). Furthermore, utilizing the NUPACK software, the calculated free energy of secondary structure formation for strands A and B, along with the adhesive strand, was determined to exceed the energy associated with the binding of miRNA-21 and the adhesive strand (**Figure 19E**). Hence, these simulations substantiated the NPs' potential for responsive miRNA-21-driven disintegration. Moreover, as NPs degrade, miRNA-21 will be silenced and suppressed by the antisense strands.

Consequently, a miRNA-21 releasing profile was determined, selecting different concentrations based on previous investigations. Gem within the NPs showed an increased release profile. Within 40 hours, a 5 nM miRNA-21 concentration in the release medium resulted in over 80% release of Gem. In contrast, when exposed to lower concentrations of miRNA-21, the nanomaterials exhibited a release of only 30% of Gem within the same time frame. Moreover, in the absence of miRNA-21 in the release medium, minimal drug release occurred, confirming the proficient miRNA-21-responsive recognition capability of the nanoparticles (**Figure 19F**). It is worth mentioning that the release of Cy3-labeled adhesive strands also exhibited responsiveness to miRNA-21 (**Figure 19G**). However, the Cy3-labeled strands exhibited faster and higher-rate release, with over 95% of Cy3-anti-miRNA-21 released within 4 hours at 5 nM miRNA-21, attributed to the facile degradation of the outermost nanogel shell upon encountering miRNA-21.

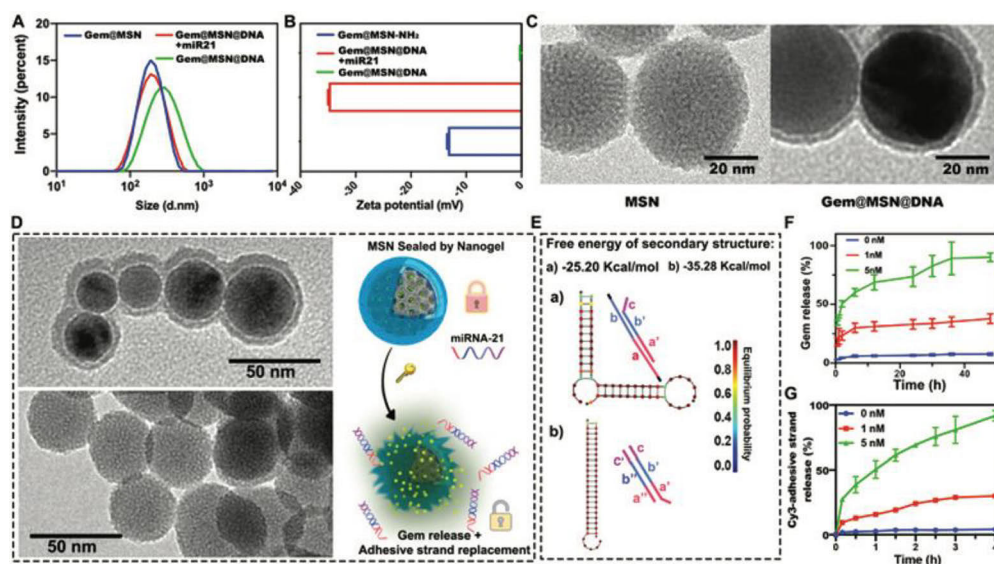


Figure 19. Characterization of miRNA-21-targeted nanoformulations and their intracellular assessment. Panel (A) Changes in nanoparticle size determined by DLS. Panel (B) Variation in nanoparticle zeta potential. Panel (C) TEM images illustrating different nanoparticles pre- and post-DNA hydrogel coating. Panel (D) Mechanisms depicting DNA hydrogel degradation and release of therapeutic agents. Panel (E) Free energy alteration of secondary structure post-DNA binding. Panel (F) Profile of miRNA-21-responsive drug release. (G) Profile of Cy3-labeled anti-miRNA-21 strand release. (© The Authors. The Royal Society of Chemistry 2022)

5.2.1.3 miRNA targeted MNzyme (IV)

To develop a miRNA-21 responsive DNzyme system for controlling HSP70 mRNA levels, two commonly used DNzyme models, 17E and 10-23, can be chosen (Peracchi 2000; Zhou et al., 2016). These models are versatile, allowing customization through the design of subdomain sequences to target specific mRNAs (**Figure 20A, B**). Alterations in different sequence segments within the catalytic ring impact its activity and response to various metal ions. Notably, substituting three base pairs at stem positions (N3-N5, N9-N11) and switching thymine (T) at position N12 with adenine (A) significantly enhances the Ca^{2+} affinity of the 17E DNzyme (**Figure 20C**). Thus, this study employed the 17E DNzyme to design a highly effective Ca^{2+} responsive MNzyme system for dual-gene (In this study were miRNA-21 and heat shock protein 70 (HSP70) mRNA) regulation.

The initial design involved creating a Ca^{2+} -specific MNzyme system by incorporating a target sequence complementary to miRNA-21 (T) and a substrate arm complementary to HSP70 mRNA (S). The MNzyme undergoes cleavage into right Partzyme (R) and left Partzyme (L) upon catalytic core splitting (**Figure 20D**). Using the NUPACK Web application, potential reaction scenarios were explored (**Figure 20E**). Analysis of the equilibrium state of the T+R+L system suggested a strong affinity between T (miRNA-21) and R (right Partzyme), resulting in a tight complex formation. However, T and L (left Partzyme) exhibited a lower, 3-nM affinity for complex formation. Surprisingly, T, R, and L together form a 47-nM affinity complex, the MNzyme system (T-R-L). Hence, the results showed the assembling process of MNzyme following two steps: 1) T and R initially assemble, 2) L binding to the T-R complex, thus completing the MNzyme construction.

Practical assessment of the MNzyme-based dual-gene regulation is performed using 20% polyacrylamide gel electrophoresis (PAGE) experiments (**Figure 20F**). Distinct bands for each L, R, S, and T chain are evident in lanes 1, 2, 3, and 4. After 30 minutes of incubation at 37°C, new bands appear for L, R, and T (lane 5). These results proofed the binding between Partzymes and miRNA-21, facilitating the MNzyme assembly. Deeper insight into the MNzyme system's catalytic cleavage of HSP70 substrate chain (S) is gained by co-incubating an excess of S chain (4 μM) with the system (lane 6). Importantly, metal ion catalysis is absent in lane 6, resulting in intact S chains. Upon adding 10 mM Ca^{2+} to the system in lane 7, substrate chain S is cleaved and disappears,

resulting in a new band formation as shown in PAGE results (lane 7). These findings highlight the designed Partzymes' ability to mediate miRNA-21-triggered, Ca^{2+} -mediated cleavage of 4 μM HSP70, achieving dual-gene regulation.

Metal-ion dependency of the Partzyme system is further confirmed by substrate catalytic hydrolysis tests at varying Ca^{2+} concentrations over 4 hours (**Figure 19G**). Using L (1 μM), R (1 μM), and 0.2 μM T chains, substrate S (4 μM) content gradually decreases while the product yield increases with the increasing Ca^{2+} concentration up to 50 mM. Moreover, the hydrolysis rate of HSP70 mRNA substrate chain reaches saturation at around 20 mM Ca^{2+} . These findings demonstrate that sufficient Ca^{2+} levels in the mRNA regulatory system ensure high catalytic efficiency of the MNzyme system.

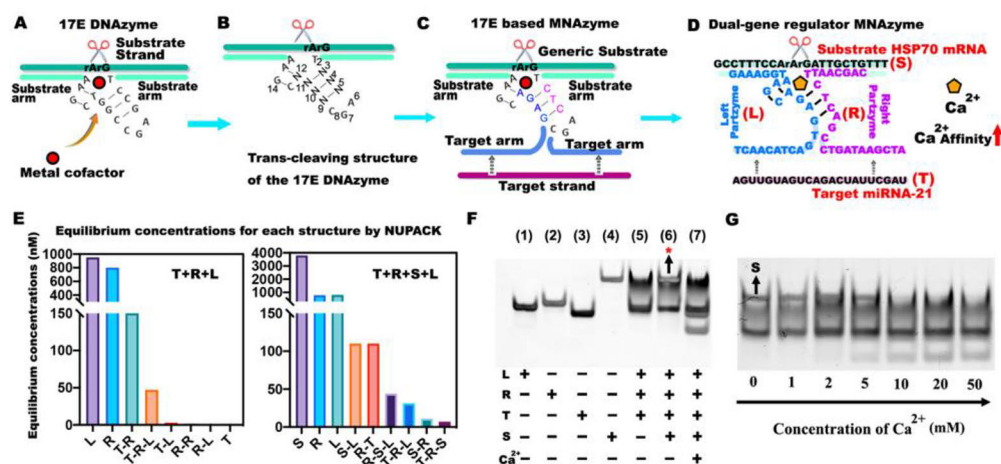


Figure 20. Schematic Representation of the Ca^{2+} Responsive MNzyme System. (A) 17E DNAzyme illustration. "r" in rArG means ribonucleic acid. (B) Various structural variants of the 17E DNAzyme. N' show the site can be any from A, T, G, or C deoxynucleotide. (C) Ca^{2+} responsive 17E-based MNzyme system. (D) The ultimate configuration of the MNzyme system demonstrates enhanced Ca^{2+} affinity for miRNA-21-triggered HSP70 mRNA cleavage. (E) A simulation using the NUPACK web application illustrates the equilibrium concentrations for each binding event. (F) Electrophoresis experiment on a 20% polyacrylamide gel demonstrating different formulations. (G) Validation of the MNzyme system's Ca^{2+} concentration-dependent behavior. (© 2023, The Author(s). Springer Nature)

5.2.1.4 RGD- modified micelle coated by calcium phosphate NPs (IV)

Despite verifying the miRNA-21 dependent MNzyme self-assembly and specific gene cleavage function triggered by Ca^{2+} , challenges remain in intracellular activation due to poor cellular internalization and low cytoplasmic Ca^{2+} levels ($\sim 0.1 \mu\text{M}$). To address this, a smart and robust Partzyme delivery strategy utilizing Ca^{2+} as a multi-cargo carrier for target site Ca^{2+} enhancement has been explored. Nanostructured amorphous calcium phosphate (CaP) is considered an

exceptional delivery system for nucleic acids due to its strong affinity for gene phosphate backbones (**Figure 21A**). Nonetheless, amorphous calcium phosphate (ACP) serves as an unstable precursor, easily converting into hydroxyapatite (HA) within minutes in aqueous solutions, thereby impeding efficient cargo delivery (Lai et al., 2014; Roohani et al., 2021). To confirm this, transmission electron microscopy results revealed ACP's transition from a complete, smooth sphere with irregular surface channels within 10 minutes to dissolved ACP, nucleation, and HA crystallization after 48 hours (**Figure 21B**). Notably, this transformation was observed when NPs cocultured with cells in cell culture medium after 24 hours, hindering nucleotide drug and calcium ion delivery (**Figure 21C**).

Zinc was found to stabilize the ACP phase for over 20 days at a Zn/Ca ratio of 10%. This stabilization approach yielded highly stable ACP NPs (**Figure 21D**). This phenomenon is attributed to smaller zinc ions replacing Ca^{2+} , inhibiting crystallization by distorting atomic order, and reducing the solubility of amorphous calcium phosphate (ACP). However, without surface ligand modification, stabilized APC NPs still lacked enhanced endocytosis by cancer cells. Moreover, as the tight zinc-phosphate ion cooperation reduced surface pores, impeding the loading of multiple therapeutic molecules. To address these issues, RGD-modified DSPE-PEG amphiphilic micelles ($^{\text{RM}}$) were used as the template for Zn^{2+} -doped CaP synthesis. The oxygen atom in the $\text{CH}_2\text{-O-CH}_2$ group of PEG, possessing a partial charge, forms electrostatic interactions with Ca^{2+} or Zn^{2+} . (**Figure 21E**) (Chen et al., 2011). Additionally, the micelles allowed the loading of multiple hydrophobic drug molecules, while the RGD-label facilitated cancer cell targeting (Wang et al., 2018).

Mineralization of Partzyme (P) using PO_4^{2-} , Zn^{2+} , and Ca^{2+} yielded $^{\text{RM}}_{(\text{I+C})}@\text{CaP}_{(\text{P})}$ (I: IR780, C: Curcumin, P:Partzyme) (**Figure 21F**). Particle size, zeta potential, and chemical bonding of the nanocarrier were characterized using DLS and Fourier-transform infrared spectroscopy (FTIR). $^{\text{RM}}_{(\text{I+C})}@\text{CaP}_{(\text{P})}$ remained highly stable in aqueous solution for over two weeks (**Figure 21G**), attributed to a combination of the zinc additive and steric repulsion forces between the PEG chains. In a pH=7.4 PBS buffer (**Figure 21G**), $^{\text{RM}}_{(\text{I+C})}$ displayed a zeta potential of -10.21 mV due to the carboxyl groups present on RGD. The ultimate formulation, $^{\text{RM}}_{(\text{I+C})}@\text{CaP}_{(\text{P})}$, exhibited a zeta potential of -2.53 mV, likely due to the exposed RGD, making the formulation slightly negative.

FTIR analysis of DSPE-PEG-COOH revealed a -COOH absorption band at 1738 cm^{-1} (Kebebe et al., 2019). Following the RGD modification, a novel band emerged at 1657 cm^{-1} , signifying the presence of the O=C-N-H group between PEG and RGD within the micelles. Subsequent CaP coating of the micelles led to the emergence of the 1657 cm^{-1} band in the $^{\text{RM}}_{(\text{I+C})}@\text{CaP}$ group, affirming the successful integration of CaP nanoparticles into the DSPE-PEG-RGD micelles (**Figure 21H**).

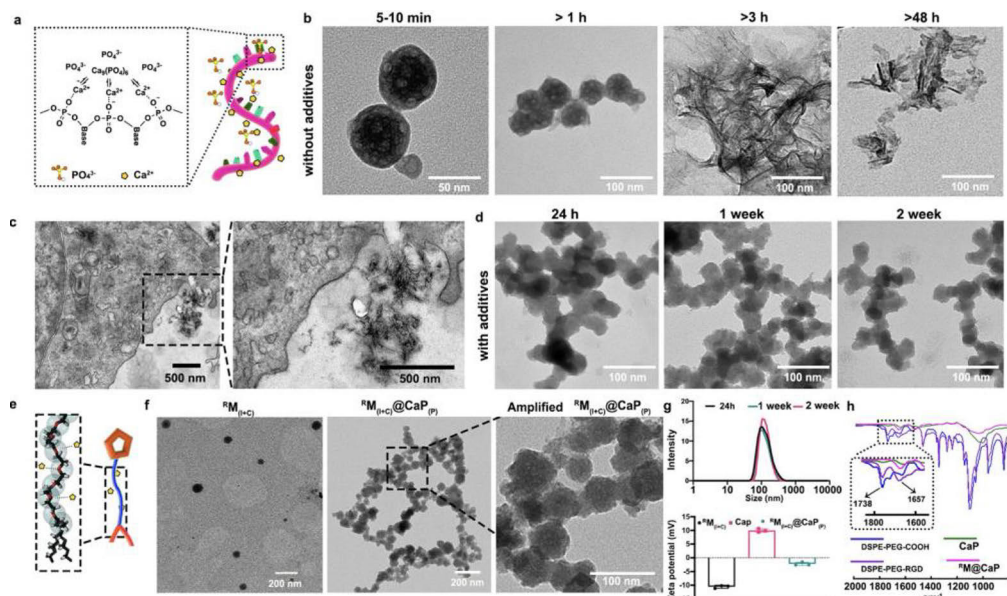


Figure 21. Design, Loading, and Photothermal Characteristics of Engineered Nano-System. (A) Illustration outlining the biomineralization process of DNA and calcium phosphate (CaP). (B) Visualizing the degradation of CaP in Milli-Q aqueous solution. (C) PANC-1 cells exposed to APC nanoparticles for 24 hours. (D) Persistence of Zn-substituted CaP in Milli-Q aqueous solution. (E) Depiction of the interaction between PEG and Ca^{2+} and Zn^{2+} . Carbon, oxygen, and hydrogen atoms represented in black, red, and white, respectively. (F) Transmission Electron Microscopy (TEM) images displaying $\text{RM}_{(l+c)}$ and $\text{RM}_{(l+c)}@CaP_{(p)}$. (G) Size distribution of $\text{RM}_{(l+c)}@CaP_{(p)}$ nanoparticles over two weeks and corresponding zeta potential readings for $\text{RM}_{(l+c)}$, Zn-doped CaP, and $\text{RM}_{(l+c)}@CaP_{(p)}$. (H) Fourier-Transform Infrared (FTIR) findings for Zn-substituted CaP and $\text{RM}@CaP$. (© 2023, The Author(s). Springer Nature)

5.2.2 In vitro cell targeting and investigation of therapeutic efficiency of NPs

5.2.2.1 Cancer cell targeting and (III&IV)

For miRNA-21 responsive DNA hydrogel coated MSN (MSN@DNA) nanosystem project (III), we initiated our study by incorporating the FITC fluorescent dye (green) within the nanoparticles (FITC/MSN@DNA) to enable the tracking of NP endocytosis by various cell types, utilizing both confocal microscopy and flow cytometry experiments (**Figure 22A and B**) (Paper III). Results for the PANC-1 cell line unveiled that the NP uptake by cells progressively increased with extended incubation time. Notably, within a span of 10 hours, the NPs were internalized by all of the cells, highlighting the NPs' efficient cellular endocytosis capability. Simultaneously, mouse insulinoma 6 (Min6) as healthy normal cells also demonstrated proficient NP endocytosis, with 100% of cells internalizing

the NPs within 10 hours. Comparable endocytosis efficiency across different cell types could be due to the absence of any cell-targeting ligands on the NP surface.

However, from the results at 10 hours, for PANC-1 cell with high concentration of endogenous miR-21, the FITC signal within the FITC/MSN@DNA NPs distribute to all place inside cell. While, for Min-6 group with lower miRNA-21 content, the FITC signal within the FITC/MSN@DNA NPs did not appear to diffuse extensively. Instead, it accumulated at specific locations within the cytosol. This result indicated that, with lower intracellular miRNA-21 content, the diffusion of FITC was hindered by the miRNA-21 responsive DNA hydrogel layer.

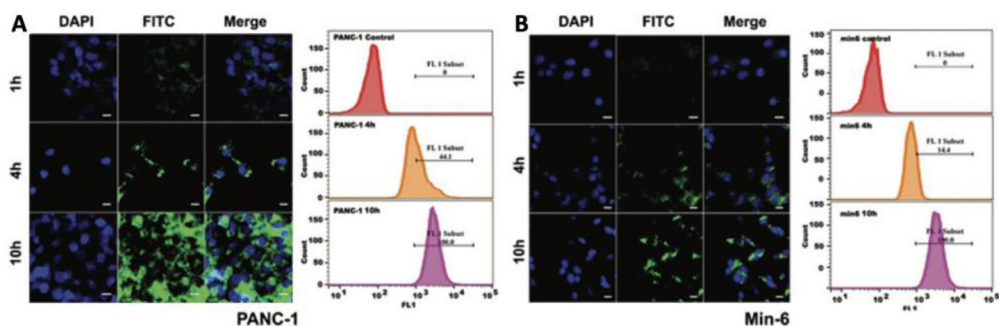


Figure 22. (A) Confocal micrographs and flow cytometry results depicting the presence of FITC loaded MSN@DNA (FITC/MSN@DNA) NPs in cancer cells. (B) Confocal micrographs and flow cytometry outcomes showing the distribution of nanoparticles in healthy cells. Scale bar: 20 μm. (© The Authors. The Royal Society of Chemistry 2022)

For the paper IV with miRNA-21-responsive DNAzyme system, the uptake of therapeutic agents from pure drug (IR780 and Curcumin) experimental group, $M_{(I+C)}@CaP_{(p)}$ experimental group, and $RM_{(I+C)}@CaP_{(p)}$ experimental group was assessed in PANC-1 cells. This was accomplished by monitoring the fluorescence of IR780 (red), Cy3-modified Partzyme (green), and curcumin (light blue) using confocal laser scanning microscopy (CLSM) and flow cytometry (**Figure 23A**). In PANC-1 cells, the uptake of each therapeutic agent progressively increased with extended incubation (**Figure 23A**). After 8 hours, the pure drug demonstrated the diffusion of IR780 and curcumin into PANC-1 cells, while Cy3-labeled Partzyme did not internalize. However, for RGD modified group $RM_{(I+C)}@CaP_{(p)}$, the results showed better uptake comparing with the $M_{(I+C)}@CaP_{(p)}$ group

After confirming the efficient delivery of multiple cargoes into PANC-1 cells by $RM_{(I+C)}@CaP_{(p)}$, the study investigated intracellular escape of NPs from endosomes (**Figure 23B**). After culturing NPs with cells for 2 and 24 hours, the medium was replaced, and a 1-W laser was applied for 5 minutes. Pearson Correlation Coefficients (PCC) determined colocalization of NPs with endosomes (PCC > 0.5 indicating moderate correlation; PCC < 0.5 indicating low correlation). Without laser irradiation, $RM_{(I+C)}@CaP_{(p)}$ NPs showed substantial overlap of red (IR780) and green (lysosomes) fluorescence after 2 hours, with a PCC of 0.673 (PCC > 0.5), denoting colocalization. After 24 hours, $RM_{(I+C)}@CaP_{(p)}$ NPs showed

less IR780-lysosome overlap (PCC = 0.454). Importantly, after laser irradiation, there was minimal red-green overlap (PCC = 0.413), confirming effective escape of the therapeutic agent from lysosomes.

5.2.2.2 Gene/ion/photothermal therapy (IV)

To validate Partzyme's binding to intracellular miRNA-21 (**Figure 23C**), Fluorescence in Situ Hybridization (FISH) was utilized to visualize miRNA-21 (**Figure 23D**). Groups were compared: PBS, IR780+Cur, ${}^{\text{RM}}_{(\text{I+C})}\text{@CaP}$ (without Partzyme), and ${}^{\text{RM}}_{(\text{I+C})}\text{@CaP}_{(\text{p})}$ (with Partzyme). Endogenous miRNA-21 was marked in red fluorescence. Results showed the PBS group exhibited substantial Cy5.5 fluorescence (miRNA). Introduction of IR780 and curcumin led to a nearly 32% decrease in miRNA fluorescence intensity. Curcumin has been reported to regulate various miRNAs, including miRNA-21, in other cancer cell lines, suggesting its capacity to inhibit endogenous miRNA-21 in PANC-1 cells. Importantly, the experiment's timepoint replacements of therapeutic-containing cell culture medium at 6 hours led to shorter intracellular retention for pure drug, while the nano-system extended Cur's retention time and therapeutic efficiency. Consequently, red fluorescence intensity in the ${}^{\text{RM}}_{(\text{I+C})}\text{@CaP}$ group decreased by about 76%. Most intriguingly, in the ${}^{\text{RM}}_{(\text{I+C})}\text{@CaP}_{(\text{p})}$ group, red fluorescence intensity almost vanished, indicating the efficient utilization of miRNA-21 by the Partzyme system, ensuring MNzyme formation.

The subsequent step was to investigate whether MNzyme could effectively down-regulate HSP70 protein expression and upregulate PTEN protein expression (**Figure 23E**). Regarding HSP70 protein, the pure drug with laser treatment group showed significantly increased HSP70 expression compared to the PBS group (1 and 2). This suggests that photothermal therapy (PTT) could activate HSP70 as a defense mechanism against thermal stress. Significantly, in the groups labeled 7 and 8, the HSP70 gene was entirely suppressed in both \pm Laser groups, demonstrating the effective HSP70 mRNA cleavage function of the MNzyme system.

The upregulation of PTEN protein expression due to miRNA-21 silencing was explored next. Compared to the PBS groups (1 and 2), the pure drug groups (3 and 4) showed modest PTEN upregulation, attributed to curcumin's inhibitory effect on miRNAs. Furthermore, in the ${}^{\text{RM}}_{(\text{I+C})}\text{@CaP}_{(\text{p})}$ groups (7 and 8), a substantial increase in PTEN/GAPDH relative ratio (3 times higher than PBS groups) was observed, confirming the miRNA-21 silencing effect of the MNzyme system.

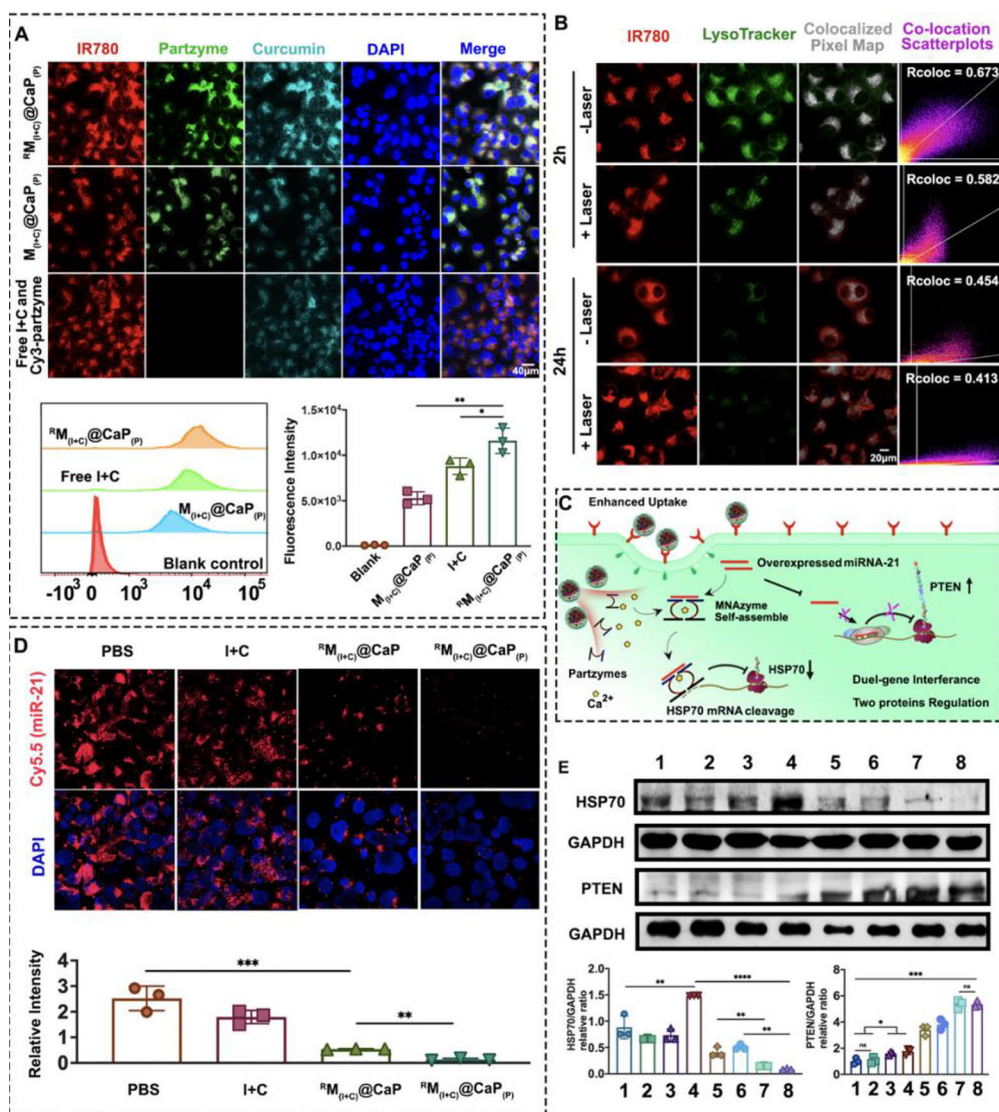


Figure 23. Therapeutics Function of MNazyme System. (A) Uptake of NPs and pure drug by PANC-1 cells. (B) Lysosomal escape of $^{RM}_{(I+C)}@CaP_{(p)}$ (\pm Laser) in PANC-1 cells at 2h and 24h. (C) Schematic depicting of the intracellular self-assembly of the MNazyme system for PTEN and HSP70 protein expression regulation. (D) Intracellular miRNA-21 content assessment using Fluorescence in Situ Hybridization (FISH) method. (E) HSP70 and PTEN protein expression analyzed by Western blot experiment. ($n = 3$, $*p < 0.05$, $**p < 0.01$, $***p < 0.001$, and $****p < 0.0001$). Group 1-8: 1: PBS; 2: PBS +Laser; 3: I+C; 4: I+C +Laser; 5: $^{RM}_{(I+C)}@CaP$; 6: $^{RM}_{(I+C)}@CaP$ +Laser; 7: $^{RM}_{(I+C)}@CaP_{(p)}$; 8: $^{RM}_{(I+C)}@CaP_{(p)}$ +Laser. (© 2023, The Author(s). Springer Nature)

5.2.3 Evaluation of in vivo biodistribution and treatment outcomes of NPs

5.2.3.1 Tumor targeting (IV)

The biodistribution of NPs following intravenous administration was examined using live animal imaging (**Figure 24A**). Three groups were tracked at 1, 8, 24, and 48 hours after administration: IR780+Cur+P, $M_{(I+C)}@CaP_{(p)}$, and ${}^RM_{(I+C)}@CaP_{(p)}$ groups. The pure drug I+C+P group displayed a significant signal throughout the mice's body at 1-hour timepoint, which diminished after 8 hours due to the rapid metabolism of IR780. In contrast, the ${}^RM_{(I+C)}@CaP_{(p)}$ group, benefiting from the RGD modification, exhibited an excellent tumor-specific accumulation, resulting in the highest fluorescence signal. Subsequent imaging of the harvested main organs confirmed a pronounced fluorescence in the tumor tissue of the ${}^RM_{(I+C)}@CaP_{(p)}$ NPs group, indicating the enhanced tumor-targeting effect facilitated by RGD.

5.2.3.2 Gene/chemo/photothermal synergistic therapy (IV)

To evaluate the mild photothermal therapy (PTT) efficiency of the photothermal dye IR780-loaded nanosystems, a tumor temperature elevation experiment was conducted. After the administration of the drug (IR780: 1 mg/kg), the four groups were subjected to a 1 W cm⁻² 808 nm laser 24 hours later, as illustrated in **Figure 24B**. The PBS group showed minimal temperature variation even after 4 minutes of irradiation. Conversely, the pure drug (I+C+P) group demonstrated inadequate treatment temperatures (below 43°C) after 4 minutes, attributed to the poor solubility and instability of IR780. The $M_{(I+C)}@CaP_{(p)}$ NPs group exhibited an improved photothermal conversion effect, increasing the tumor temperature to 42°C in just 20 seconds of irradiation. Remarkably, the ${}^RM_{(I+C)}@CaP_{(p)}$ group, with the advantage of RGD-mediated enhanced tumor cell uptake, experienced a significant temperature elevation to 44.4 °C, suggesting its potential as an effective mild photothermal agent.

Subsequently, the therapeutic efficacy of pure drug, $M_{(I+C)}@CaP_{(p)}$ and ${}^RM_{(I+C)}@CaP_{(p)}$ nanosystems was evaluated *in vivo* (**Figure 24C**). **Figure 24D** displays the quantitative analysis of luciferase intensity. The findings suggest that the combination of the pure drug and laser treatment (I+C+P +Laser) failed to effectively impede tumor growth, possibly due to the susceptibility of the pure drug to degradation *in vivo*. Conversely, encapsulation of Partzyme into the nanosystems significantly enhanced the therapeutic efficacy of the ${}^RM_{(I+C)}@CaP_{(p)}$ +Laser group, which continued to be effective until day 40, with a total bioluminescence flux of 5.04×10⁸ photons/s. Furthermore, from the in-situ tumor photos (**Figure 24E**) and tumor weight analysis (**Figure 24F**), it was evident that the ${}^RM_{(I+C)}@CaP_{(p)}$ +Laser group exhibited the best therapeutic effect, reducing the tumor weight to 0.049g, approximately 50% of the PBS group's weight. The terminal deoxynucleotidyl transferase dUTP nick end labeling (TUNEL) assay also supported the therapeutic efficiency of Partzyme (**Figure 24G**), with the ${}^RM_{(I+C)}@CaP_{(p)}$ +Laser group showing increase in TUNEL signal compared to the ${}^RM_{(I+C)}@CaP$ +Laser group (**Figure 24H**).

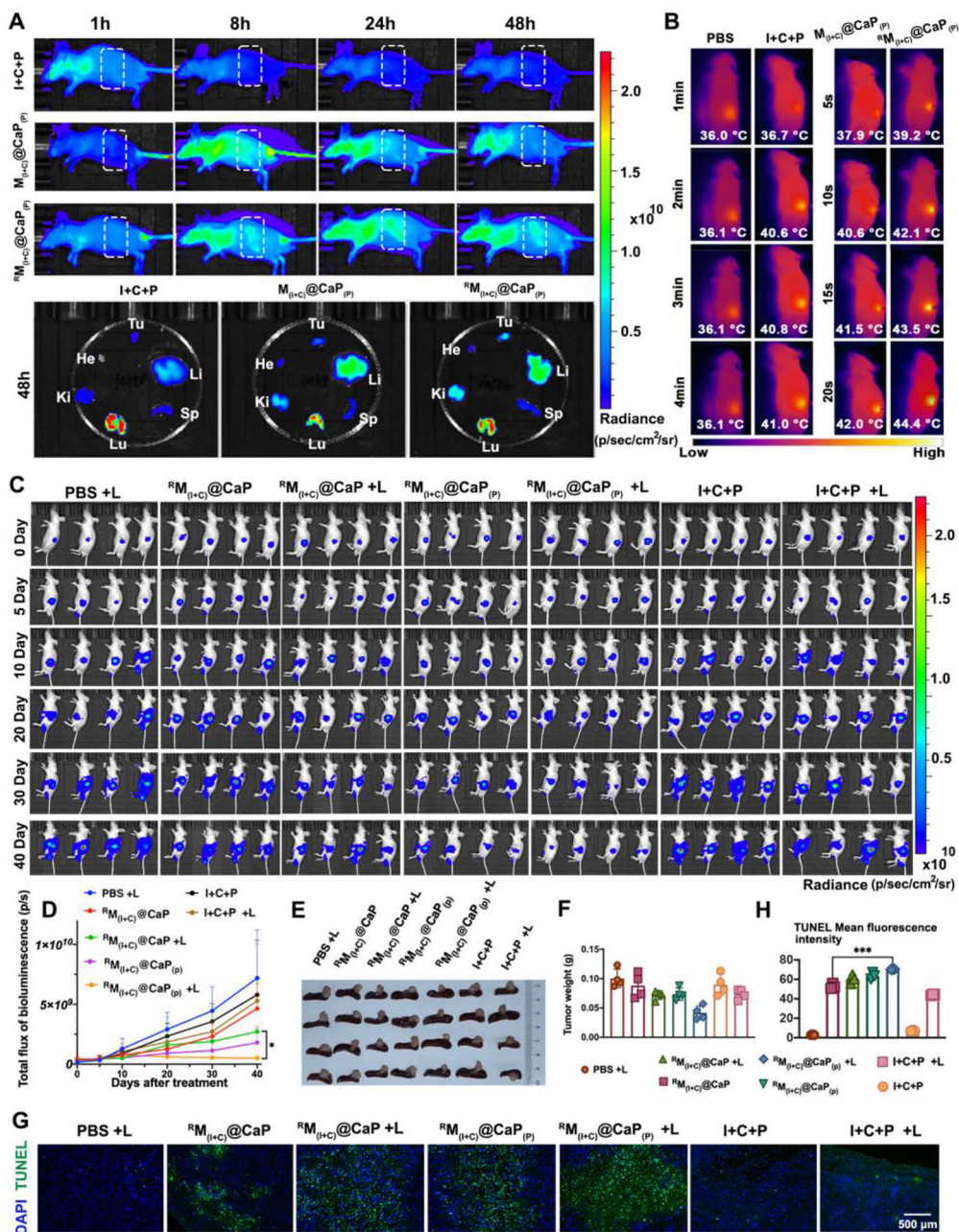


Figure 24. In vivo distribution and therapeutic efficacy of Various Nanoparticle Formulations. (A) Biodistribution of nanomaterials in live animals. (B) Images depicting tumor temperature elevation. (C) Bioluminescence measurements at different time points. (D) Quantitative analysis of total bioluminescence flux signal intensity (photons/sec) over time. (E) Images of isolated tumors. (F) Tumor weights. ($n=4$, $*P<0.05$). (G) TUNEL labeling of tumor slices. (H) Quantitative analysis of TUNEL fluorescence using ImageJ. ($n=3$, $***P<0.001$). (© 2023, The Author(s). Springer Nature)

5.3 Simplifying the preparation complexity of cancer-targeting DNA nanotechnology (V)

In this chapter, the primary focus is on streamlining the design and fabrication methods in DNA nanotechnology, and extending the application of this technology to the treatment of various cancers. Initially, we addressed the limitations of the previous DNA hydrogel systems, which were relatively expensive to produce. This was attributed to the need for modifying DNA sequences with linkers capable of attaching to mesoporous silica and acrylamide gel, posing significant obstacles to the clinical translation of DNA hydrogels. On the other hand, even though the cost of DNA is relatively low when DNAszymes are modified into MNAszymes, the fabrication of nanomaterials for loading both DNA and drugs remains complex. The development of a rapid one-pot method for producing DNA-metal nanomaterials would hold significant implications.

In recent years, MNFs have gradually gained momentum in the field of cancer treatment by combining the catalytic functions of metal ions with the therapeutic functions of nucleic acid drugs (Liu et al., 2021; Wang et al., 2022; Yang et al., 2022; Zhang et al., 2021). It has been reported that nanomaterials formed by the binding of metal ions such as Hf^{4+} , Zn^{2+} , Ca^{2+} with DNA do possess a lattice structure by using selected area electron diffraction (SAED) methods. However, despite their advantageous characteristics combining those of both metal-organic-frameworks (MOFs) and DNA nanotechnology, MNFs have not been fully developed to unleash their tremendous potential. One of the major drawbacks is the stringent synthesis conditions required for MNF materials, while there is also the need for surface modifications to enhance stability or achieve further cellular targeting (Liu et al., 2021; Wang et al., 2022). For example, the most extensively studied Fe^{2+} /nucleic acid MNF was prepared at 95°C for 3 h, but it degraded completely within 2 hours in PBS and required further MOF layering to protect it (Li et al., 2019; Liu et al., 2019). Furthermore, for metals such as calcium, which do not easily form MNF structures with nucleic acids, the synthesis process required 120°C for 3 days (Yang et al., 2022), which makes it difficult to load macromolecular active drugs. Hence, it's of great significance to design and develop universal methods for fabrication stable MNF materials under mild conditions.

5.3.1 Design and characterization of the aptamer-integrated DNA nanomaterials

5.3.1.1 Metal-nuclear acid framework (V)

To assess the enhanced metal-nuclear acid framework (MNF) synthesis potential of longer DNA segments, we designed three distinct functional DNA fragments at equimolar concentrations (83 mM nucleotides), each with different lengths (20 nucleotides, 41 nucleotides, and 83 nucleotides). Among them, the 41-nucleotide sequence represented the glucose transporter 1 (GLUT-1) DNAszymes with a

built-in fluorescence lock, labeled as GDz (**Figure 25Aa**). The 83-nucleotide sequence extended GDz with a HER-2 aptamer, forming H-GDz (**Figure 25Aa**). Lastly, the 20-nucleotide sequence served as the GLUT-1 substrate strand. Surprisingly, H-GDz exhibited superior calcium ion binding capability, yielding nanoparticles with a remarkable 20% higher efficiency compared to the 41-nucleotide GDz (**Figure 25Ab**). In contrast, the 20-nucleotide sequence failed to bind calcium ions and form nanoparticles (**Figure 25Ab**).

Continuing our investigation into MNF structural composition, we analyzed DNA and calcium content in the resulting nanomaterials. H-GDz showed a DNA utilization efficiency of 95.6%, with around 50.08 μg DNA synthesized out of approximately 52.39 μg input of nucleotides. Similarly, GDz exhibited 94.0% DNA utilization, with approximately 48.4 μg DNA formed out of 51.5 μg input. However, a key difference emerged in calcium utilization. H-GDz contained 10.3 μg of calcium (16.7% calcium mass ratio), whereas GDz contained 6.0 μg of calcium (11.7% calcium mass ratio). These observations underscore that longer DNA sequences possess a heightened affinity for calcium ions, leading to increased binding capacity during MNF synthesis.

Calcium binding phenomenon can be attributed to the intrinsic characteristics of oligonucleotides, characterized by flexible spatial conformations and weaker base stacking forces (Maassen et al., 2018). Lengthening oligonucleotide sequences, rather than simply increasing nucleotide concentration, enhances their folding and entanglement probability during reactions (Chi et al., 2013; Roth et al., 2018). Hence, we hypothesize the entanglement of longer oligonucleotide chains endowing the intertwined DNA clusters with a higher potential, which in turn enhances the affinity of DNA for calcium ions, thus, obtaining higher MNF production.

To gain mechanistic insights into the molecular level interactions during the MNF synthesis, molecular dynamics (MD) simulations were conducted. Two simulation systems containing 0.15 M calcium chloride (CaCl_2) and roughly an equivalent count of nucleotides in water were constructed (**Figure 25B and C**). The first system contained ten GDz sequences ($10 \times 41 \text{ nt} = 410 \text{ nt}$; chain length 273 \AA), while the second contained five H-GDz sequences ($5 \times 83 \text{ nt} = 415 \text{ nt}$; chain length 645 \AA). The 100-ns simulations revealed that the shorter GDz sequences remained dispersed, exhibiting minimal entanglement with each other during the entire simulation. In contrast, the longer H-GDz sequences exhibited pronounced intertwining, forming dense aggregates by 100 ns (**Figure 25D**). The calculated persistence lengths for the Gz and H-Gz sequences were 9.5 \AA and 5.5 \AA , respectively, which is consistent with the longer sequence's higher flexibility.

In both systems, calcium ions displayed strong affinity towards the DNA sequences, forming prominent binding interactions, whereas the negative chloride counterions did not exhibit discernible tendency to bind with the DNA (**Figure 25B and C**). Visual analysis of the MD trajectories indicated that the positively charged calcium ions formed direct (Long et al., 2020) electrostatic

interactions (coordination bonds) with the negatively charged phosphate backbone oxygen atoms of DNA (**Figure 25E and F**).

To explore if there was any difference in the calcium ion interaction pattern with the shorter or the longer DNA sequences, we calculated the radial distribution function (RDF) between calcium atoms and the oxygen atoms (O^-) in the DNA phosphate backbone (**Figure 25G**). RDF offers insights into the probability distribution of atom-to-atom distances within the system. As shown in **Figure 25G**, H-GDz sequences exhibited higher density of calcium ions compared to the GDz sequence (Higher RDF $g(r)$ value) at around 2.3\AA . This disparity suggests the increased capacity of the entangled H-GDz structure to attract a greater number of calcium ions at this distance range. These findings provide valuable insights into the calcium binding behavior of longer DNA sequences, hinting at their potential in crafting calcium-based MNFs.

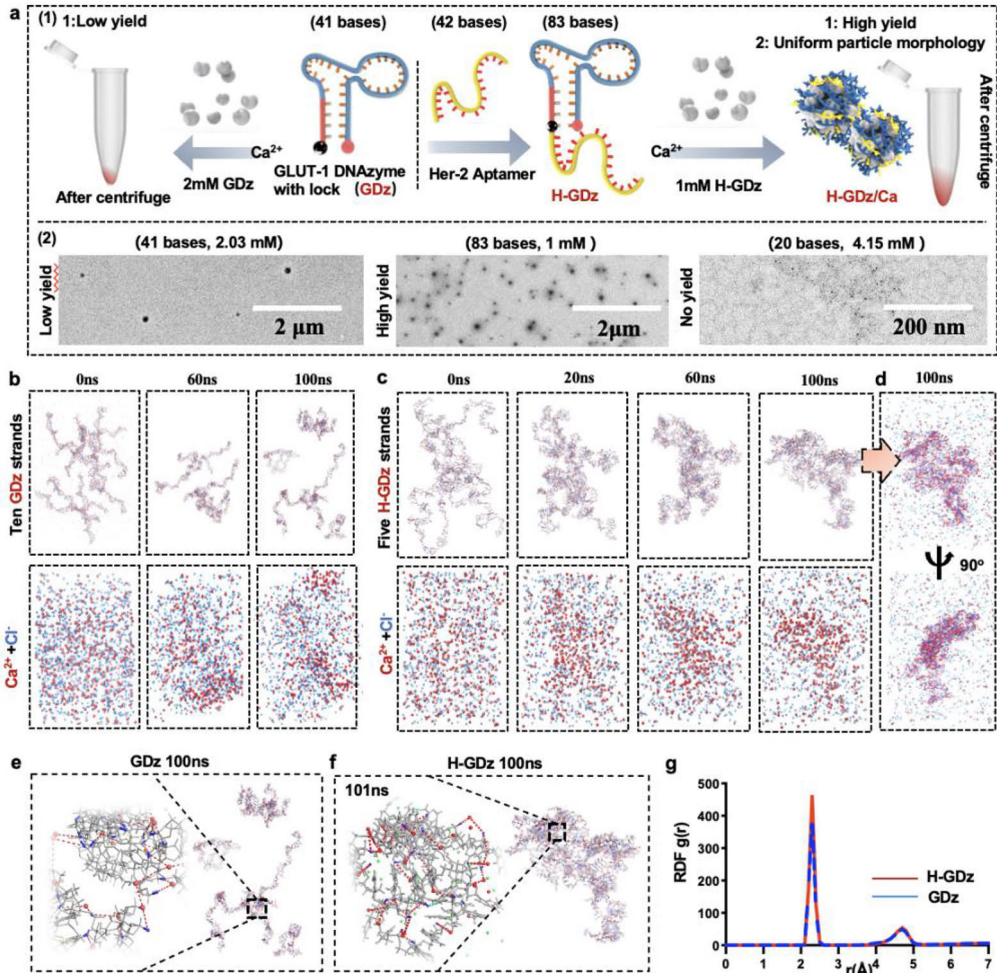


Figure 25: Mechanism of MNF Synthesis. Fig. 1. Mechanism of MNF synthesis based on long-chain DNA binding with calcium ions and regulation of MNF properties. (a) MNF

synthesis process of GDz and H-GDz, and the MNF TEM results for GDz (41 bases), H-GDz (83 bases) and the substrate strand (20 bases). (b, c, d) Molecular dynamics (MD) simulation results of 10 GDz and 5 H-GDz with the nearly same nucleotide content and the same concentration of calcium ions. Calcium ions are depicted as red spheres, while chloride ions are represented by blue spheres. (e, f) Electrostatic binding interactions between calcium ions and the oxygen atoms of the phosphate backbone in the DNA sequences. Atom color code: gray – DNA bases; blue – oxygen atom in phosphate backbone; . Red color spheres depict Ca^{2+} ; green color spheres depict Cl^- ; red dashed lines denote electrostatic interactions. (g) The radial distribution function (RDF) analysis of GDz and H-GDz sequences. The horizontal axis represents the distance between calcium ions and the negatively charged oxygen atoms in the DNA phosphate backbone, while the vertical axis represents the probability (density) of finding a calcium ion at a certain distance from a negatively charged phosphate oxygen atom.

5.3.1.2 Evaluation of the therapeutic mechanisms of NPs (V)

After successfully synthesizing stable calcium-based MNF NPs at room temperature, we conducted a thorough investigation into their functionalities in regulating the GLUT-1 gene, imaging performance, and cell-targeting potential on HER-2 positive gastric cancer (NIC-N87 cell line). The MNF material in this work contained a GLUT-1 mRNA cleaving DNAzyme for GLUT-1 silencing, a HER-2 targeting aptamer for N87 cell targeting, and a molecular beacon for GLUT-1 imaging.

Initially, we assessed the cleavage capability of H-GDz on GLUT-1 mRNA at varying calcium ion concentrations (ranging 0 – 4 mM) using PAGE analysis (**Figure 25A**). Results indicated that in a Ca^{2+} -free environment, when H-GDz was incubated with GLUT-1 mRNA, a delayed shifted band emerged, implying successful sequence binding (**Figure 26A**). Yet, mRNA cleavage did not occur due to the absence of calcium ions. As calcium ion concentration increased, the GLUT-1 mRNA band intensity decreased notably at 0.5 mM. At 2 mM Ca^{2+} , a cleaved GLUT-1 mRNA band appeared, confirming gene cleavage. At 4 mM Ca^{2+} , the target GLUT-1 gene was entirely silenced (**Figure 26A**). These findings highlighted that H-GDz's depleting action on GLUT-1 mRNA was influenced by calcium ion concentration, with higher levels yielding more potent gene regulation effects.

Subsequently, we validated the H-GDz-based molecular beacon's ability to detect GLUT-1 mRNA (**Figure 26B**). This molecular beacon contained a dual-labeled fluorescent probe (Fluorescein amidite/Black Hole Quencher 1, FAM/BHQ-1), where FAM fluorescence was quenched by BHQ-1 in the absence of GLUT-1 mRNA via the fluorescence resonance energy transfer (FRET) effect. Interaction with the target gene induced a conformational change, releasing FAM fluorescence and rendering the target gene visible as red color. This fluorescent probe enabled GLUT-1 detection and confirmed the binding process between GLUT-1 mRNA and H-GDz.

The fluorescence intensity increased with rising concentrations of GLUT-1 mRNA substrate, indicating the H-GDz molecular beacon's specific recognition

and binding to GLUT-1 mRNA (**Figure 26B**). This led to an intensified fluorescence signal in the presence of the GLUT-1 mRNA.

We further examined H-GDz's targeting capability towards HER-2 positive NIC-N87 gastric cancer cells. For a comparative evaluation of HER-2 aptamer functionality, we designed H-GDz sequences with the HER-2 aptamer, MH-GDz sequences with a Mutated-HER-2 aptamer (same base count as H-GDz), and GDz sequences lacking the HER-2 aptamer for MNF material preparation (**Figure 26C**). Results showed comparable production yields for H-GDz/Ca and MH-GDz/Ca nanomaterials, while the HER-2-lacking GDz group exhibited significantly lower yields. Consequently, for nanosystem design, H-GDz/Ca and MH-GDz/Ca groups were chosen for further analysis.

H-GDz's targeting effect on NIC-N87 cells manifested in material and DNA sequence aspects (**Figure 26D**). Each material group's endocytic ability was reflected by detected GLUT-1 mRNA (FAM's red signal), with higher endocytic intensity indicating stronger GLUT-1 detection.

Later, we test the cell uptake efficiency for the free DNA (H-GDz + Ca^{2+} and MH-GDz + Ca^{2+}), and the MNF NPs (MH-GDz/Ca, H-GDz/Ca). **Figure 26E** results demonstrated that compared to the MH-GDz/Ca NPs group, the H-GDz/Ca NPs group exhibited 2.95 times more efficient GLUT-1 detection, indicating robust cell internalization of H-GDz/Ca NPs. Due to their high negative charge, free DNA sequences exhibited reduced cellular uptake and GLUT-1 signal. Importantly, even with this charge, the H-GDz + Ca^{2+} group showed better imaging for GLUT-1 compared to the MH-GDz + Ca^{2+} group, emphasizing the pivotal targeting role of the HER-2 aptamer. Moreover, as gene detection signal increased, GLUT-1 mRNA depletion occurred, leading to reduced GLUT-1 protein expression.

Flow cytometry analysis further substantiated the cell-targeting proficiency of the HER-2 integrated materials, for the free DNA (H-GDz + Ca^{2+} and MH-GDz + Ca^{2+}), and the MNF NPs (MH-GDz/Ca, H-GDz/Ca). (**Figure 26F**). When compared to the blank cell control group, there was an approximate 37.5% reduction in GLUT-1 expression in the H-GDz + Ca^{2+} group, while a significantly more substantial decrease of up to 70% was observed in the H-GDz/Ca NPs group. Notably, there was a noticeable migration of cells from the Q3 region (71.0%), characterized by elevated GLUT-1 expression and low GLUT-1 detection, to the Q1 region (41.3%). Q3 region means low GDz signal and high GLUT-1 signal, while Q1 region means high GDz signal with low GLUT-1 signal. These observations provided compelling support for the assertion that the conversion of H-GDz into nanostructured MNF materials through self-mineralization techniques markedly heightened its intracellular gene monitoring and regulatory capacities.

Furthermore, Western blotting was employed to further corroborate the expression of GLUT-1 within the cells (**Figure 26G**). The outcomes indicated that the HER-2 modified H-GDz + Ca^{2+} group exhibited a slight reduction in GLUT-1 protein expression, surpassing the effect observed in the HER-2 mutated MH-GDz + Ca^{2+} group. Remarkably, the H-GDz/Ca nanomaterial group demonstrated the most potent inhibitory effect on GLUT-1, underscoring once again that the

nanomaterials possessed superior capabilities in regulating GLUT-1 expression compared to free DNA strands.

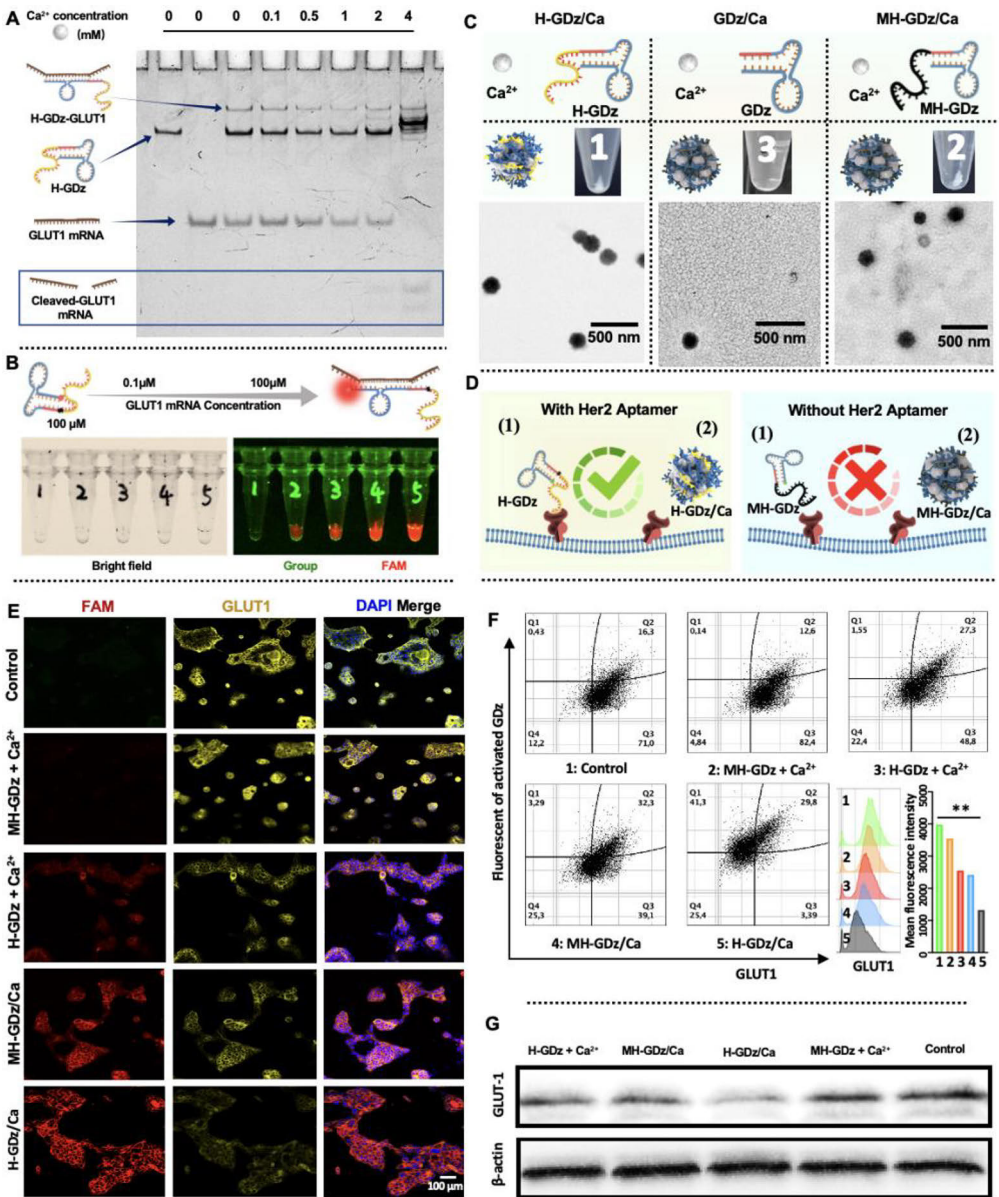


Figure 26. Verification of Targeting Efficiency and Assessment of Detection and Regulation Capabilities Towards GLUT-1 Using Different Materials. (A) Electrophoresis analysis (PAGE) confirming GLUT-1 recognition and cleavage capacities of H-GDz sequences. (B) Responsiveness of H-GDz towards GLUT-1. The system included 100 μM of H-GDz and GLUT-1 mRNA substrates at concentrations ranging 0.1 μM – 100 μM . (C) Design and synthesis of targeted materials. (D) Schematic depiction of the targeting mechanism of HER-2 modified material. (E) Fluorescence confocal microscopy evaluating

detection and regulation capabilities of diverse materials on the GLUT-1 gene in a cellular context. Intracellular GLUT-1 protein was labeled with antibodies, represented as yellow fluorescence, while cell nuclei were stained with DAPI, appearing blue. (F) Flow cytometry analysis images assessing the silencing efficiency of various groups on GLUT-1 expression. The x-axis represents fluorescence detection intensity of GLUT-1, while the y-axis represents fluorescence of activated GDz following GDz and GLUT-1 hybridization. (G) Western blot analysis illustrating the silencing efficacy of different groups on GLUT-1 expression.

5.3.2 *In vivo* biodistribution and assessment of the therapeutic effect

5.3.2.1 tumor targeting (V)

Gastric cancer cells exhibit elevated expression of RAD51 (Anand et al., 2022; Tan et al., 2020; Taylor et al., 2015), a protein involved in homologous recombination DNA repair, for rapid DNA repair and provides protection to cancer cells. To overcome this challenge, we employed a mild condition MNF preparation system to load interferon regulatory factor-1 (IRF) (Rosain et al., 2023; Schmalzl et al., 2022; Tanaka et al., 1996) to suppress RAD51 expression (Tan et al., 2020).

The IRF loaded MNF NPs (IRF/H-GDz/Ca and IRF/MH-GDz/Ca MNF), as the final formulations were selected to evaluate their tumor-targeting specificity and anti-tumor efficacy in an *in vivo* setting. “M” in the MH-GDz means the mutated HER-2 sequence. The first step, as depicted in **Figure 27A**, involved an *in vivo* distribution study of MNF materials in mice. Cy5.5/BHQ-3 probes were employed for labeling the MNF, with their primary function being the validation of GDz and GLUT-1 binding rather than tumor-specific imaging.

Results indicated that MNF NPs constructed using the mutated HER-2 sequence (IRF/MH-GDz/Ca) exhibited substantial accumulation in the kidneys, as evidenced by lateral and prone positions. This selective accumulation could be attributed to the innate renal sequestration of negatively charged nanomaterials (Choi et al., 2010; Du et al., 2018). Conversely, IRF/H-GDz/Ca demonstrated significant tumor region accumulation within the stomach, with noticeable fluorescence signals even at the 48-hour mark. This emphasized the significant contribution of the HER-2 aptamer within the MNF material, facilitating precise delivery of MNFs to the tumor site.

At the designated 48-hour time point, the mice were euthanized for *ex vivo* analysis of nanodevice fluorescence distribution across various organs (**Figure 27B**). Consistent with *in vivo* imaging, MNFs accumulated prominently in the kidneys and liver, particularly in the IRF/MH-GDz/Ca group, where the kidneys showed the highest accumulation. Remarkably, IRF/H-GDz/Ca NP kidney accumulation was reduced by roughly 50% compared to IRF/MH-GDz/Ca. Moreover, fluorescence intensity in the tumor region of IRF/H-GDz/Ca was 2.15 times higher than in IRF/MH-GDz/Ca. These *ex vivo* findings further underscored the enhanced tumor-targeting prowess achieved through HER-2 sequence incorporation.

Furthermore, tumor sections were prepared to assess Cy5.5 fluorescence intensity (in cyan) of nanomaterials within the tumor tissue (**Figure 27C**). Outcomes suggested that the IRF/H-GDz/Ca NPs group displayed substantial fluorescence signal from nanomaterials within the tumor tissue, signifying successful GDz binding to GLUT-1 mRNA for gene regulation. In contrast, minimal Cy5.5 fluorescence was observed in the IRF/MH-GDz/Ca NPs group, further highlighting the HER-2 segment's role in augmenting nanosystem targeting capability.

5.3.2.2 Therapeutic efficiency assay (V)

Subsequently, to comprehensively validate the therapeutic effectiveness of our tailored MNF materials, we conducted *in vivo* antitumor experiments employing luciferin fluorescence intensity to monitor orthotopic tumor growth progression (**Figure 27D**). Through average radiance calculation, we observed gradual tumor size increase over time in the control and MH-GDz/Ca groups (**Figure 27E**). By day 21, luciferin fluorescence intensity was approximately 2.5 times higher compared to day one (**Figure 27F**). Conversely, the H-GDz/Ca and IRF/MH-GDz/Ca groups exhibited notable tumor reduction, with approximately 60% and 75% size reduction, respectively (**Figure 27E**). Notably, the IRF/H-GDz/Ca group achieved nearly complete tumor eradication by day 21, showcasing an impressive tumor shrinkage of over 90% (**Figure 27F**).

Further, green fluorescent protein (GFP) was employed for *ex vivo* visualization of the gastric tumor (**Figure 27G**). *Ex vivo* GFP fluorescence imaging findings for the gastric tumor were consistent with *in vivo* fluorescence results, with the IRF/H-GDz/Ca group showing the most potent therapeutic effect. Notably, this study marked the first successful integration of diverse functional sequences in constructing MNF nanomaterials through a one-step process at room temperature, with each function successfully verified. These outcomes underscored the flexibility and efficacy of DNA sequence design in MNF fabrication, forming a robust basis for subsequent MNF material advancements.

Subsequent to this, the safety profiles of each group were meticulously evaluated. Initially, the mice's body weight changes during the treatment period were closely monitored. No significant differences were observed between the treatment and control groups, affirming the absence of adverse effects on the overall health of the animals (**Figure 27H**).

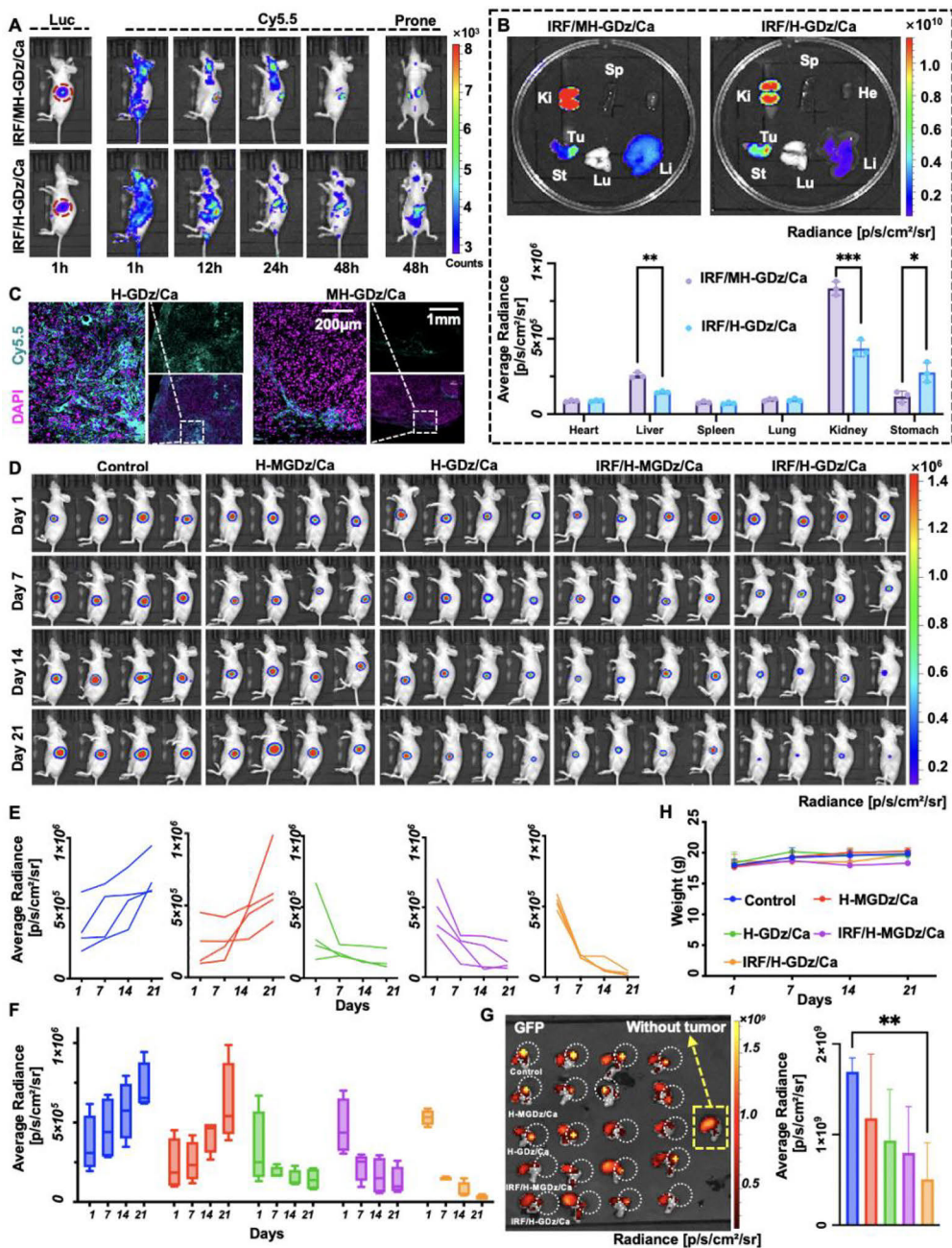


Figure 27. Nanomaterial Distribution and Therapeutic Effectiveness in Mice. (A) The intravenous administration of MNF materials and their subsequent distribution in mice. (B) Imaging of the materials in ex vivo organs, including the heart, liver, spleen, lungs, kidneys, and stomach. (C) Imaging of the materials in the tumor site of mice, utilizing DAPI staining for cell nuclei labeling. (D) An in vivo antitumor experiment conducted in mice. (E) The time-dependent changes in average radiance at the tumor site for individual mice. (F) Box plots illustrating the average changes in average radiance at the tumor site for each group

of mice. (G) GFP fluorescence imaging and quantification of gastric tumors in mice. (H) Monitoring of body weight changes during the treatment period.

6 Concluding and future perspectives

6.1 Summary

In the studies of this research, various drug delivery strategies were explored and evaluated for their efficacy in cancer treatment. Receptor-based drug delivery demonstrated promising efficacy, leveraging specific interactions with cancer cells. However, the non-uniform receptor expression underscore the importance of addressing variability for optimal outcomes. The integration of a local injection strategy alongside receptor targeting exhibited notable improvements in efficiency and dosage reduction. Despite these advantages, inherent shortcomings like low tolerability and only for solid tumors persist, prompting ongoing efforts for refinement. The miRNA-responsive nanoparticle strategy showcased effectiveness, but the high associated costs pose challenges to its broader application. Integrating miRNA-responsive nanoparticles with RGD receptor targeting emerged as a strategy to enhance precision with low cost, however it introduced complexities in the system's design and implementation. Lastly, the exploration of a one-way step approach to nanoparticle fabrication represents a novel and potential solution to existing challenges. As this study advances, the delicate balance between efficacy and practical applicability becomes evident, guiding the way for further refinement and optimization in the field of cancer drug delivery.

The overall objective of this thesis was to achieve precise cancer treatment through multi-targeted drug delivery strategies. From the results, a combination of pH-sensitive technologies and localized injection treatment strategies was designed. More importantly, exploiting the differential miRNA-21 expression in cancer tissue and the surrounding healthy tissue, along with dynamic DNA nanotechnology, this thesis improved the development of a series of miRNA-21-responsive DNA nanomaterials. These materials exhibited either miRNA-21-mediated degradation capabilities or miRNA-21-activated self-assembly capabilities. This innovative approach fully leveraged the unique potential of dynamic DNA nanotechnology in the domain of cancer-targeted therapy. Simultaneously, by combining miRNA-21-responsive therapeutic materials with conventional receptor-targeted therapeutic strategies, the accuracy of cancer-targeted treatment was significantly augmented.

Parallely, by fully tapping into the capabilities of dynamic DNA nanotechnology, the complexity of DNA material preparation was simplified. For traditional dynamic DNA nanomaterials, if we want to integrate multiple therapeutic strategies, we need multiple response modules, and the design sequence will be very cumbersome and complicated. On the other hand, modified DNA is expensive, leading to prohibitive drug costs. Consequently, this thesis unveiled a simplified approach for the rapid synthesis of DNA

nanomaterials at room temperature. This technique considerably mitigated the challenges associated with synthesizing DNA nanomaterials, while concurrently conferring multifunctionality upon DNA materials, thus facilitating their transition into clinical applications. Moreover, as a proof of concept, this methodology was employed to engineer a nanomaterial capable of targeting HER-2 overexpressing gastric cancer cells, resulting in successful elimination of tumor cells.

In summary, through the utilization of dynamic DNA nanotechnology, this thesis successfully generated an array of innovative miRNA-targeted nanomaterials. This was further coupled with conventional receptor-targeted nanotechnology, ultimately leading to the realization of highly precise targeted therapies. Additionally, from a materials perspective, the preparation methodologies were optimized, thereby advancing the clinical application potential of these materials.

6.2 Future perspectives

Building upon the insights gained in this thesis, future endeavors in constructing targeted drug delivery systems should prioritize several key aspects.

First and foremost, future exploration of DNA nanosystems should place a heightened emphasis on fundamental research. While our investigation in paper V revealed the significant impact of DNA length on the synthesis of metal-DNA complexes, there are several aspects that merit further exploration. These include the types of metal ions employed, the ratios of metal ions, and the spatial conformations of DNA sequences. The intricate interplay of these factors in the synthesis of metal-DNA complexes remains an area ripe for continued investigation. As we delve deeper into the complexities of metal-DNA interactions, a more comprehensive understanding of these fundamental elements will undoubtedly contribute to the advancement and refinement of DNA nanosystems for various applications.

On another front, our progression from receptor targeting to the gradual integration of intracellular miRNA-targeting strategies has significantly enhanced the targeting capability of the system. However, there exists untapped potential for further elevating the targeting prowess of the materials. Specifically, we can design DNA materials to respond to mutations base variants at disease sites, achieving single-base mutation targeting technology. Additionally, leveraging Crispr-Cas technology or peptide nucleic acid (PNA) technology, we can extend our targeting strategies beyond single-stranded RNA or single-stranded DNA to target double-stranded DNA. This is made possible as Crispr-Cas and PNA have the capability to unwind double-stranded DNA, allowing the targeted DNA to be liberated. This opens up new avenues for advancing the precision and adaptability of our targeting strategies, offering promising directions for future research in this domain.

Crucially, as we advance the development of these technologies, it is imperative not only to obtain experimental results but also to delve deeply into the mechanisms underpinning these techniques. For instance, understanding

how PNA invades double-stranded DNA and ensuring that PNA itself does not compromise the subsequent therapeutic efficacy of the targeted DNA is pivotal. Additionally, unraveling the mechanisms behind how DNA materials can identify single-base mutations and the recognition process poses intriguing questions. Molecular simulation techniques emerge as a valuable avenue for exploration, offering the potential to simulate and understand the intricate molecular interactions and dynamics involved in these targeting strategies. By employing molecular simulation technologies, we can gain insights into the detailed mechanisms, optimize design strategies, and further enhance the precision and effectiveness of these groundbreaking technologies.

Therefore, in the exploration of future targeted nanotechnology, the emphasis goes beyond utilizing and integrating existing targeting techniques. More importantly, it entails the development of novel targeting technologies and a profound exploration of their underlying mechanisms. This approach paves the way for the development and exploration of a series of innovative targeting strategies. By continuously innovating and delving into the intricate mechanisms, we can not only enhance the precision and adaptability of existing targeting approaches but also uncover entirely new avenues for targeted nanotechnology, contributing to the advancement of therapeutic strategies in biomedical research.

7 Acknowledgements

I want to express my deep gratitude to all the professors who have guided me with their insightful advice during my doctoral journey. I am immensely thankful for the unwavering support of my family, the constant encouragement from my beloved wife, who stood by my side, and the uplifting words from my senior colleagues. I also extend my appreciation to my junior colleagues, whose assistance has been invaluable. Your support, encouragement, and help have been the driving forces behind my progress and have contributed significantly to my achievements today.

I would like to extend my heartfelt gratitude to my supervisor, Hongbo Zhang. In 2018, he showed me tremendous respect, helping me realize my individual worth. He not only assisted me in addressing urgent research challenges but also taught me how to write articles, conduct experiments, create presentations, and craft project proposals. This series of guidance has laid down essential steps for me in my journey through scientific research. I am deeply honored to have gone through this process under the guidance of Hongbo Zhang. Furthermore, I want to sincerely thank Hongbo Zhang's wife, Li Chen. During times of financial hardship, she not only provided me with meals but also shared homemade mooncakes and even took me on trips. Five years have passed, and those memories are vivid in my mind. The support from both my mentor's family has been akin to the awe-inspiring purity of the snow-covered forests we encountered on our way to Northern Rovaniemi.

I extend my heartfelt gratitude to my wife, Meixin Ran. She has walked beside me through my university years, graduate studies, and doctoral journey. I am thankful for her presence in Finland, where she took care of my daily life, eased my anxieties, and became both my mentor and dear friend. Through life's challenges and moments of solitude, she has been my unwavering support, even shouldering burdens on my behalf. Thanks to her, I have had the opportunity to focus on my career and detach from the distractions of the outside world.

I wish to express my gratitude to the Department Head, Jessica M. Rosenholm. In 2018, she extended an invitation to me, providing me with the opportunity to set foot on the soil of Finland and experience the beauty and warmth of the country. Her personal charisma and leadership have left a deep impression on me. What's more, during moments of my mistakes, she offered me a second chance, allowing me to complete my coursework and gain insights into the meticulousness of research and the dignity of academia.

I am grateful to my co-supervisor, Outi Salo-Ahen, who provided me with foundational education about computational modeling during the "Methods in pharmaceutical analysis" course. She also provided me with the opportunity to learn about the possibilities of Molecular Dynamics (MD) simulations. Her gentle voice, graceful demeanor, and approachable nature bolstered my confidence along the research path. I would also like to express my appreciation to Rajendra Bhadane for his substantial assistance in my project involving MD simulations.

Despite my numerous questions, he patiently guided me without any sign of impatience.

I would also like to thank professors Wenguo Cui, who have introduce me to the great experiment enviroment. Also for Junnian Zhou, Yong Guo, Yuezhou Zhang, Yonghai Feng, Minjia Meng, and Yue Ma for their guidance in the experiment. I also want to extend my gratitude to my senior colleague, Chang Liu and Xiaoyu Xu. Their support and companionship provided me with much-needed solace and lifted me out of the shadows of failure.

I'm grateful to my lab mate, Xiaodong Ma. Countless days spent discussing research topics have allowed us to share the joy of our achievements. Our four years as classmates have taught me how to foster companionship and collaboration with peers. I appreciate Senior Wenhui for teaching me various experimental techniques, enabling me to fully explore a wide range of project topics. I am grateful to Senior Yunru Yu for her extensive knowledge, which has been immensely helpful in revising my articles and projects. She has provided a wealth of information regarding work and has also been a great support in my personal life. At the same time, I am also very grateful to Feika and Yu Wang for their care and support towards me.

I would like to express gratitude to Dhayakumar Rajan Prakash for providing me with diverse life insights and introducing me to different perspectives. Thanks to Wali for guiding me through scholarship applications and sharing survival skills. Special thanks to Oliver for assisting me in cell experiments and reagent ordering; his warm, kind-hearted, and humorous nature has been a great support. To Wu Yang, Yu Chen, Chengcheng, Pengzhen, Shengyi, Xiaochao, Yuanqiang, thank you for your assistance in experiments and the respect you show in our work interactions. And to Li Wang, Lu Fan, and Kexin Yi in Wenzhou, thank you for your support. I am thankful to Rawand A. Mustafa for our passionate communication and also the help for experiments. I also appreciate Fanny Frejborg for inviting us to her home, enjoying hotpot together, and celebrating birthdays as a group. To Ezgi, thank you for greeting me every day and sharing intresting stories to me. I am grateful to Jessica Salo, for always smiling at me and saying hello. Likewise, I am also grateful to my colleagues from PSL, for the greetings and smiles every time we meet.

I would like to express my gratitude to the teachers and classmates who have supported me throughout my journey. Your guidance and care have played a significant role in helping me successfully complete my graduation. While there's not enough space to thank everyone individually, please know that your contributions have been deeply appreciated.

Turku, 2023

Jiaqi Yan

8 References

- Amodio, A., Zhao B., Porchetta A., Idili A., Castronovo M., Fan C. H., Ricci F., 2014. Rational Design of pH-Controlled DNA Strand Displacement. *J Am Chem Soc.* 136, 16469-16472. <https://doi.org/10.1021/ja508213d>
- An, E., Ock C. Y., Kim T. Y., Lee K. H., Han S. W., Im S. A., Kim T. Y., Liao W. L., Cecchi F., Blackler A., Thyparambil S., Kim W. H., Burrows J., Hembrough T., Catenacci D. V. T., Oh D. Y., Bang Y. J., 2017. Quantitative proteomic analysis of HER2 expression in the selection of gastric cancer patients for trastuzumab treatment. *Ann Oncol.* 28, 110-115. <https://doi.org/10.1093/annonc/mdw442>
- Anand, R., Buechelmaier E., Belan O., Newton M., Vancevska A., Kaczmarczyk A., Takaki T., Rueda D. S., Powell S. N., Boulton S. J., 2022. HELQ is a dual-function DSB repair enzyme modulated by RPA and RAD51. *Nature.* 601, 268-273. <https://doi.org/10.1038/s41586-021-04261-0>
- Barranco, C., 2023. Antisense oligonucleotide slows glioma growth. *Nat Rev Drug Discov.* 22, 445-445. <https://doi.org/10.1038/d41573-023-00077-x>
- Baumann, A. E., Burns D. A., Liu B., Thoi V. S., 2019. Metal-organic framework functionalization and design strategies for advanced electrochemical energy storage devices. *Communications Chemistry.* 2, 86. <https://doi.org/10.1038/s42004-019-0184-6>
- Blanco, E., Shen H., Ferrari M., 2015. Principles of nanoparticle design for overcoming biological barriers to drug delivery. *Nat Biotechnol.* 33, 941-951. <https://doi.org/10.1038/nbt.3330>
- Bobo, D., Robinson K. J., Islam J., Thurecht K. J., Corrie S. R., 2016. Nanoparticle-Based Medicines: A Review of FDA-Approved Materials and Clinical Trials to Date. *Pharm Res-Dordr.* 33, 2373-2387. <https://doi.org/10.1007/s11095-016-1958-5>
- Cairns, M. J., Saravolac E. G., Sun L. Q., 2002. Catalytic DNA: A novel tool for gene suppression. *Curr Drug Targets.* 3, 269-279. <https://doi.org/10.2174/1389450023347722>
- Chen, F., Zhu Y.-J., Zhang K.-H., Wu J., Wang K.-W., Tang Q.-L., Mo X.-M., 2011. Europium-doped amorphous calcium phosphate porous nanospheres: preparation and application as luminescent drug carriers. *Nanoscale Research Letters.*

- 6, 67.
<https://doi.org/10.1186/1556-276X-6-67>
- Chen, J. H., Seeman N. C., 1991. Synthesis from DNA of a Molecule with the Connectivity of a Cube. *Nature*. 350, 631-633.
<https://doi.org/DOI10.1038/350631a0>
- Chen, S. H., Liu T. I., Chuang C. L., Chen H. H., Chiang W. H., Chiu H. C., 2020. Alendronate/folic acid-decorated polymeric nanoparticles for hierarchically targetable chemotherapy against bone metastatic breast cancer. *J Mater Chem B*. 8, 3789-3800.
<https://doi.org/10.1039/d0tb00046a>
- Chen, X., Zhuang Y., Rampal N., Hewitt R., Divitini G., O'Keefe C. A., Liu X., Whitaker D. J., Wills J. W., Jugdaohsingh R., Powell J. J., Yu H., Grey C. P., Scherman O. A., Fairen-Jimenez D., 2021. Formulation of Metal–Organic Framework-Based Drug Carriers by Controlled Coordination of Methoxy PEG Phosphate: Boosting Colloidal Stability and Redispersibility. *J Am Chem Soc*. 143, 13557-13572.
<https://doi.org/10.1021/jacs.1c03943>
- Cheng, Q., Wei T., Farbiak L., Johnson L. T., Dilliard S. A., Siegwart D. J., 2020. Selective organ targeting (SORT) nanoparticles for tissue-specific mRNA delivery and CRISPR-Cas gene editing. *Nat Nanotechnol*. 15, 313-+.
<https://doi.org/10.1038/s41565-020-0669-6>
- Cheng, X. W., Lee R. J., 2016. The role of helper lipids in lipid nanoparticles (LNPs) designed for oligonucleotide delivery. *Adv Drug Deliver Rev*. 99, 129-137.
<https://doi.org/10.1016/j.addr.2016.01.022>
- Chi, Q., Wang G., Jiang J., 2013. The persistence length and length per base of single-stranded DNA obtained from fluorescence correlation spectroscopy measurements using mean field theory. *Physica A: Statistical Mechanics and its Applications*. 392, 1072-1079.
<https://doi.org/https://doi.org/10.1016/j.physa.2012.09.022>
- Cho, J. H., Lim J. Y., Cho J. Y., 2017. Survival analysis based on human epidermal growth factor 2 status in stage II-III gastric cancer. *World J Gastroentero*. 23, 7407-7414.
<https://doi.org/10.3748/wjg.v23.i41.7407>
- Choi, H. S., Liu W., Liu F., Nasr K., Misra P., Bawendi M. G., Frangioni J. V., 2010. Design considerations for tumour-targeted nanoparticles. *Nature Nanotechnology*. 5, 42-47.
<https://doi.org/10.1038/nnano.2009.314>

- Collins, F. S., Varmus H., 2015. A New Initiative on Precision Medicine. *New Engl J Med.* 372, 793-795.
<https://doi.org/10.1056/NEJMp1500523>
- Cronin, K. A., Harlan L. C., Dodd K. W., Abrams J. S., Ballard-Barbash R., 2010. Population-based Estimate of the Prevalence of HER-2 Positive Breast Cancer Tumors for Early Stage Patients in the US. *Cancer Investigation.* 28, 963-968.
<https://doi.org/10.3109/07357907.2010.496759>
- Culver, H. R., Clegg J. R., Peppas N. A., 2017. Analyte-Responsive Hydrogels: Intelligent Materials for Biosensing and Drug Delivery. *Accounts Chem Res.* 50, 170-178.
<https://doi.org/10.1021/acs.accounts.6b00533>
- Deng, X. R., Li K., Cai X. C., Liu B., Wei Y., Deng K. R., Xie Z. X., Wu Z. J., Ma P. A., Hou Z. Y., Cheng Z. Y., Lin J., 2017. A Hollow-Structured CuS@Cu₂S@Au Nanohybrid: Synergistically Enhanced Photothermal Efficiency and Photoswitchable Targeting Effect for Cancer Theranostics. *Advanced Materials.* 29, 1701266.
<https://doi.org/10.1002/adma.201701266>
- DeVos, S. L., Miller T. M., 2013. Antisense Oligonucleotides: Treating Neurodegeneration at the Level of RNA. *Neurotherapeutics.* 10, 486-497.
<https://doi.org/10.1007/s13311-013-0194-5>
- Du, B., Yu M., Zheng J., 2018. Transport and interactions of nanoparticles in the kidneys. *Nature Reviews Materials.* 3, 358-374.
<https://doi.org/10.1038/s41578-018-0038-3>
- Fenton, O. S., Olafson K. N., Pillai P. S., Mitchell M. J., Langer R., 2018. Advances in Biomaterials for Drug Delivery. *Advanced Materials.* 30, 1705328.
<https://doi.org/10.1002/adma.201705328>
- Fu, T. J., Seeman N. C., 1993. DNA Double-Crossover Molecules. *Biochemistry-Us.* 32, 3211-3220.
<https://doi.org/DOI10.1021/bi00064a003>
- Guo, Z. Y., Zhou J. R., Yu Y. Y., Krishnan N., Noh I., Zhu A. T., Borum R. M., Gao W. W., Fang R. H., Zhang L. F., 2023. Immunostimulatory DNA Hydrogel Enhances Protective Efficacy of Nanotoxoids against Bacterial Infection. *Adv Mater.* 35,
<https://doi.org/10.1002/adma.202211717>
- Hair, P., Cameron F., McKeage K., 2013. Mipomersen sodium: first global approval. *Drugs.* 73, 487-493.
<https://doi.org/10.1007/s40265-013-0042-2>
- Hallett, M. A., Teng B., Hasegawa H., Schwab L. P., Seagroves T. N., Pourmotabbed T., 2013. Anti-matrix metalloproteinase-9

- DNAzyme decreases tumor growth in the MMTV-PyMT mouse model of breast cancer. *Breast Cancer Res.* 15, R12
<https://doi.org/10.1186/bcr3385>
- He, K. W., Barsoumian H. B., Puebla-Osorio N., Hu Y., Sezen D., Wasley M. D., Bertolet G., Zhang J., Leuschner C., Yang L. P., Leyton C. S. K., Fowlkes N. W., Green M. M., Hettrick L., Chen D. W., Masrourpour F., Gu M. D., Maazi H., Revenko A. S., Cortez M. A., Welsh J. W., 2023. Inhibition of STAT6 with Antisense Oligonucleotides Enhances the Systemic Antitumor Effects of Radiotherapy and Anti-PD-1 in Metastatic Non-Small Cell Lung Cancer. *Cancer Immunol Res.* 11, 486-500.
<https://doi.org/10.1158/2326-6066.Cir-22-0547>
- He, P. P., Du X. X., Cheng Y., Gao Q., Liu C., Wang X. W., Wei Y. H., Yu Q. L., Guo W. W., 2022. Thermal-Responsive MXene-DNA Hydrogel for Near-Infrared Light Triggered Localized Photothermal-Chemo Synergistic Cancer Therapy. *Small.* 18, 2200263.
<https://doi.org/10.1002/smll.202200263>
- Hou, T. L., Zhu L., Zhang X. L., Chai Y. Q., Yuan R., 2022. Multiregion Linear DNA Walker-Mediated Ultrasensitive Electrochemical Biosensor for miRNA Detection. *Anal Chem.* 94, 10524-10530.
<https://doi.org/10.1021/acs.analchem.2c02004>
- Hua, S., de Matos M. B. C., Metselaar J. M., Storm G., 2018. Current Trends and Challenges in the Clinical Translation of Nanoparticulate Nanomedicines: Pathways for Translational Development and Commercialization. *Front Pharmacol.* 9, 790
<https://doi.org/10.3389/fphar.2018.00790>
- Huang, F. J., You M. X., Han D., Xiong X. L., Liang H. J., Tan W. H., 2013. DNA Branch Migration Reactions Through Photocontrollable Toehold Formation. *J Am Chem Soc.* 135, 7967-7973.
<https://doi.org/10.1021/ja4018495>
- Ijas, H., Shen B. X., Heuer-Jungemann A., Keller A., Kostianinen M. A., Liedl T., Ihalainen J. A., Linko V., 2021. Unraveling the interaction between doxorubicin and DNA origami nanostructures for customizable chemotherapeutic drug release. *Nucleic Acids Res.* 49, 3048-3062.
<https://doi.org/10.1093/nar/gkab097>
- Ke, Y. G., Ong L. L., Shih W. M., Yin P., 2012. Three-Dimensional Structures Self-Assembled from DNA Bricks. *Science.* 338, 1177-1183.
<https://doi.org/10.1126/science.1227268>

- Kebebe, D., Wu Y., Zhang B., Yang J., Liu Y., Li X., Ma Z., Lu P., Liu Z., Li J., 2019. Dimeric c(RGD) peptide conjugated nanostructured lipid carriers for efficient delivery of Gambogic acid to breast cancer. *Int J Nanomedicine*. 14, 6179-6195.
<https://doi.org/10.2147/IJN.S202424>
- Keefe, A. D., Pai S., Ellington A., 2010. Aptamers as therapeutics. *Nature Reviews Drug Discovery*. 9, 537-550.
<https://doi.org/10.1038/nrd3141>
- Khvorova, A., 2017. Oligonucleotide Therapeutics - A New Class of Cholesterol-Lowering Drugs. *New Engl J Med*. 376, 4-7.
<https://doi.org/10.1056/NEJMp1614154>
- Knight, F. C., Gilchuk P., Kumar A., Becker K. W., Sevimli S., Jacobson M. E., Suryadevara N., Wang-Bishop L., Boyd K. L., Crowe J. E., Joyce S., Wilson J. T., 2019. Mucosal Immunization with a pH-Responsive Nanoparticle Vaccine Induces Protective CD8(+) Lung-Resident Memory T Cells. *Acs Nano*. 13, 10939-10960.
<https://doi.org/10.1021/acsnano.9b00326>
- Kulkarni, J. A., Witzigmann D., Thomson S. B., Chen S., Leavitt B. R., Cullis P. R., van der Meel R., 2021. The current landscape of nucleic acid therapeutics. *Nat Nanotechnol*. 16, 630-643.
<https://doi.org/10.1038/s41565-021-00898-0>
- Lacroix, A., Sleiman H. F., 2021. DNA Nanostructures: Current Challenges and Opportunities for Cellular Delivery. *ACS Nano*. 15, 3631-3645.
<https://doi.org/10.1021/acsnano.0c06136>
- Lai, R.-H., Dong P.-J., Wang Y.-L., Luo J.-B., 2014. Redispersible and stable amorphous calcium phosphate nanoparticles functionalized by an organic bisphosphate. *Chinese Chemical Letters*. 25, 295-298.
<https://doi.org/10.1016/j.ccl.2013.11.012>
- Larrouy, B., Blonski C., Boiziau C., Stuer M., Moreau S., Shire D., Toulme J. J., 1992. Rnase H-Mediated Inhibition of Translation by Antisense Oligodeoxyribo-Nucleotides - Use of Backbone Modification to Improve Specificity. *Gene*. 121, 189-194. [https://doi.org/10.1016/0378-1119\(92\)90121-5](https://doi.org/10.1016/0378-1119(92)90121-5)
- Lee, J. S., Kim S., Na H. K., Min D. H., 2016. MicroRNA-Responsive Drug Release System for Selective Fluorescence Imaging and Photodynamic Therapy In Vivo. *Adv Healthc Mater*. 5, 2386-2395.
<https://doi.org/10.1002/adhm.201600328>
- Lee, S. W., Kim Y. M., Cho C. H., Kim Y. T., Kim S. M., Hur S. Y., Kim J. H., Kim B. G., Kim S. C., Ryu H. S., Kang S. B., 2018. An

- Open-Label, Randomized, Parallel, Phase II Trial to Evaluate the Efficacy and Safety of a Cremophor-Free Polymeric Micelle Formulation of Paclitaxel as First-Line Treatment for Ovarian Cancer: A Korean Gynecologic Oncology Group Study (KGOG-3021). *Cancer Res Treat.* 50, 195-203. <https://doi.org/10.4143/crt.2016.376>
- Leung, A. K. K., Tam Y. Y. C., Chen S., Hafez I. M., Cullis P. R., 2015. Microfluidic Mixing: A General Method for Encapsulating Macromolecules in Lipid Nanoparticle Systems. *J Phys Chem B.* 119, 8698-8706. <https://doi.org/10.1021/acs.jpcb.5b02891>
- Li, C., Wang J., Wang Y., Gao H., Wei G., Huang Y., Yu H., Gan Y., Wang Y., Mei L., Chen H., Hu H., Zhang Z., Jin Y., 2019. Recent progress in drug delivery. *Acta Pharm Sin B.* 9, 1145-1162. <https://doi.org/https://doi.org/10.1016/j.apsb.2019.08.003>
- Li, J. X., Cai R., Tan W. H., 2022. A Novel ECL Sensing System for Ultrahigh Sensitivity miRNA-21 Detection Based on Catalytic Hairpin Assembly Cascade Nonmetallic SPR Effect. *Anal Chem.* 94, 12280-12285. <https://doi.org/10.1021/acs.analchem.2c03238>
- Li, M., Wang C., Di Z., Li H., Zhang J., Xue W., Zhao M., Zhang K., Zhao Y., Li L., 2019. Engineering Multifunctional DNA Hybrid Nanospheres through Coordination-Driven Self-Assembly. *Angew Chem Int Ed Engl.* 58, 1350-1354. <https://doi.org/10.1002/anie.201810735>
- Li, M. Y., Wang C. L., Di Z. H., Li H., Zhang J. F., Xue W. T., Zhao M. P., Zhang K., Zhao Y. L., Li L. L., 2019. Engineering Multifunctional DNA Hybrid Nanospheres through Coordination-Driven Self-Assembly. *Angew Chem Int Edit.* 58, 1350-1354. <https://doi.org/10.1002/anie.201810735>
- Li, N., Cui W., Cong P. F., Tang J., Guan Y., Huang C. H., Liu Y. N., Yu C. Z., Yang R., Zhang X., 2021. Biomimetic inorganic-organic hybrid nanoparticles from magnesium-substituted amorphous calcium phosphate clusters and polyacrylic acid molecules. *Bioact Mater.* 6, 2303-2314. <https://doi.org/10.1016/j.bioactmat.2021.01.005>
- Li, S., Jiang Q., Liu S., Zhang Y., Tian Y., Song C., Wang J., Zou Y., Anderson G. J., Han J.-Y., Chang Y., Liu Y., Zhang C., Chen L., Zhou G., Nie G., Yan H., Ding B., Zhao Y., 2018. A DNA nanorobot functions as a cancer therapeutic in response to a molecular trigger in vivo. *Nat Biotechnol.* 36, 258-264.

- <https://doi.org/10.1038/nbt.4071>
- Li, Y., Chen Y., Li J., Zhang Z., Huang C., Lian G., Yang K., Chen S., Lin Y., Wang L., Huang K., Zeng L., 2017. Co-delivery of microRNA-21 antisense oligonucleotides and gemcitabine using nanomedicine for pancreatic cancer therapy. *Cancer Science*. 108, 1493-1503. <https://doi.org/https://doi.org/10.1111/cas.13267>
- Liu, B., Hu F., Zhang J., Wang C., Li L., 2019. A Biomimetic Coordination Nanoplatforrm for Controlled Encapsulation and Delivery of Drug-Gene Combinations. *Angew Chem Int Ed Engl*. 58, 8804-8808. <https://doi.org/10.1002/anie.201903417>
- Liu, B., Yang Q., Cheng Y., Liu M., Ji Q. F., Zhang B. L., Yang Z. F., Zhou S. Y., Liu D. Z., 2023. Calcium phosphate hybrid micelles inhibit orthotopic bone metastasis from triple negative breast cancer by simultaneously killing cancer cells and reprogramming the microenvironment of bone resorption and immunosuppression. *Acta Biomater*. 166, 640-654. <https://doi.org/10.1016/j.actbio.2023.05.038>
- Liu, C., Chen Y., Zhao J., Wang Y., Shao Y., Gu Z., Li L., Zhao Y., 2021. Self-Assembly of Copper–DNAzyme Nanohybrids for Dual-Catalytic Tumor Therapy. *Angewandte Chemie International Edition*. 60, 14324-14328. <https://doi.org/https://doi.org/10.1002/anie.202101744>
- Liu, C. Z., Chen Y. X., Zhao J., Wang Y., Shao Y. L., Gu Z. N., Li L. L., Zhao Y. L., 2021. Self-Assembly of Copper–DNAzyme Nanohybrids for Dual-Catalytic Tumor Therapy. *Angew Chem Int Edit*. 60, 14324-14328. <https://doi.org/10.1002/anie.202101744>
- Liu, Y. T., Li K., Pan J., Liu B., Feng S. S., 2010. Folic acid conjugated nanoparticles of mixed lipid monolayer shell and biodegradable polymer core for targeted delivery of Docetaxel. *Biomaterials*. 31, 330-338. <https://doi.org/10.1016/j.biomaterials.2009.09.036>
- Long, M. P., Alland S., Martin M. E., Isborn C. M., 2020. Molecular dynamics simulations of alkaline earth metal ions binding to DNA reveal ion size and hydration effects. *Physical Chemistry Chemical Physics*. 22, 5584-5596. <https://doi.org/10.1039/C9CP06844A>
- Lu, C., Wu C., Ghoreishi D., Chen W., Wang L., Damm W., Ross G. A., Dahlgren M. K., Russell E., Von Bargen C. D., Abel R., Friesner R. A., Harder E. D., 2021. OPLS4: Improving Force Field Accuracy on Challenging Regimes of Chemical Space. *Journal of*

- Chemical Theory and Computation. 17, 4291-4300.
<https://doi.org/10.1021/acs.jctc.1c00302>
- Lu, J., Getz G., Miska E. A., Alvarez-Saavedra E., Lamb J., Peck D., Sweet-Cordero A., Ebet B. L., Mak R. H., Ferrando A. A., Downing J. R., Jacks T., Horvitz H. R., Golub T. R., 2005. MicroRNA expression profiles classify human cancers. *Nature*. 435, 834-838.
<https://doi.org/10.1038/nature03702>
- Maassen, S. J., de Ruiter M. V., Lindhoud S., Cornelissen J., 2018. Oligonucleotide Length-Dependent Formation of Virus-Like Particles. *Chemistry*. 24, 7456-7463.
<https://doi.org/10.1002/chem.201800285>
- Madsen, M., Gothelf K. V., 2019. Chemistries for DNA Nanotechnology. *Chemical Reviews*. 119, 6384-6458.
<https://doi.org/10.1021/acs.chemrev.8b00570>
- Manshian, B. B., Jimenez J., Himmelreich U., Soenen S. J., 2017. Personalized medicine and follow-up of therapeutic delivery through exploitation of quantum dot toxicity. *Biomaterials*. 127, 1-12.
<https://doi.org/10.1016/j.biomaterials.2017.02.039>
- Martyna, G. J., Tobias D. J., Klein M. L., 1994. Constant pressure molecular dynamics algorithms. *The Journal of Chemical Physics*. 101, 4177-4189.
<https://doi.org/10.1063/1.467468>
- Miller, K., Erez R., Segal E., Shabat D., Satchi-Fainaro R., 2009. Targeting Bone Metastases with a Bispecific Anticancer and Antiangiogenic Polymer-Alendronate-Taxane Conjugate. *Angew Chem Int Edit*. 48, 2949-2954.
<https://doi.org/10.1002/anie.200805133>
- Mitchell, M. J., Billingsley M. M., Haley R. M., Wechsler M. E., Peppas N. A., Langer R., 2021. Engineering precision nanoparticles for drug delivery. *Nat Rev Drug Discov*. 20, 101-124.
<https://doi.org/10.1038/s41573-020-0090-8>
- Mitragotri, S., Lammers T., Bae Y. H., Schwendeman S., De Smedt S., Leroux J. C., Peer D., Kwon I. C., Harashima H., Kikuchi A., Oh Y. K., Torchilin V., Hennink W., Hanes J., Park K., 2017. Drug Delivery Research for the Future: Expanding the Nano Horizons and Beyond. *J Control Release*. 246, 183-184.
<https://doi.org/10.1016/j.jconrel.2017.01.011>
- Moharramnejad, M., Ehsani A., Shahi M., Gharanli S., Saremi H., Malekshah R. E., Basmenj Z. S., Salmani S., Mohammadi M., 2023. MOF as nanoscale drug delivery devices: Synthesis and recent progress in biomedical applications. *Journal of Drug*

- Delivery Science and Technology. 81, 104285.
<https://doi.org/https://doi.org/10.1016/j.jddst.2023.104285>
- Nakamura, Y., Mochida A., Choyke P. L., Kobayashi H., 2016. Nanodrug Delivery: Is the Enhanced Permeability and Retention Effect Sufficient for Curing Cancer? *Bioconjugate Chemistry*. 27, 2225-2238.
<https://doi.org/10.1021/acs.bioconjchem.6b00437>
- Nasra, S., Bhatia D., Kumar A., 2022. Recent advances in nanoparticle-based drug delivery systems for rheumatoid arthritis treatment. *Nanoscale Advances*. 4, 3479-3494.
<https://doi.org/10.1039/D2N A00229A>
- Nosé, S., 1984. A unified formulation of the constant temperature molecular dynamics methods. *The Journal of Chemical Physics*. 81, 511-519.
<https://doi.org/10.1063/1.447334>
- Patel, S., Ryals R. C., Weller K. K., Pennesi M. E., Sahay G., 2019. Lipid nanoparticles for delivery of messenger RNA to the back of the eye. *J Control Release*. 303, 91-100.
<https://doi.org/10.1016/j.jconrel.2019.04.015>
- Peracchi, A., 2000. Preferential Activation of the 8–17 Deoxyribozyme by Ca²⁺ Ions: EVIDENCE FOR THE IDENTITY OF 8–17 WITH THE CATALYTIC DOMAIN OF THE MG5 DEOXYRIBOZYME*. *Journal of Biological Chemistry*. 275, 11693-11697.
<https://doi.org/https://doi.org/10.1074/jbc.275.16.11693>
- Ponce-Salvatierra, A., Boccaletto P., Bujnicki J. M., 2021. DNAMoreDB, a database of DNAzymes. *Nucleic Acids Res*. 49, D76-d81.
<https://doi.org/10.1093/nar/gkaa867>
- Predescu, C., Lerer A. K., Lippert R. A., Towles B., Grossman J. P., Dirks R. M., Shaw D. E., 2020. The u-series: A separable decomposition for electrostatics computation with improved accuracy. *The Journal of Chemical Physics*. 152, 084113
<https://doi.org/10.1063/1.5129393>
- Qiu, C., Wu Y., Guo Q., Shi Q., Zhang J., Meng Y., Xia F., Wang J., 2022. Preparation and application of calcium phosphate nanocarriers in drug delivery. *Materials Today Bio*. 17, 100501.
<https://doi.org/https://doi.org/10.1016/j.mtbio.2022.100501>
- Qiu, M. Z., Shi S. M., Chen M., Wang J., Wu Q. N., Sheng H., Zhang H. Z., Yun J. P., Zhou Z. W., Wang F. H., Yang D. J., Xu R. H., 2017. Comparison of HER2 and Lauren Classification between Biopsy and Surgical Resection Samples, Primary and

- Metastatic Samples of Gastric Cancer. *J Cancer*. 8, 3531-3537.
<https://doi.org/10.7150/jca.19984>
- Roohani, I., Cheong S., Wang A., 2021. How to build a bone? - Hydroxyapatite or Posner's clusters as bone minerals. *Open Ceramics*. 6, 100092
<https://doi.org/10.1016/j.openram.2021.100092>
- Rosain, J., Neehus A.-L., Manry J., Yang R., Le Pen J., Daher W., Liu Z., Chan Y.-H., Tahuil N., Türel Ö., Bourgey M., Ogishi M., Doisne J.-M., Izquierdo H. M., Shirasaki T., Le Voyer T., Guérin A., Bastard P., Moncada-Vélez M., Han J. E., Khan T., Rapaport F., Hong S.-H., Cheung A., Haake K., Mindt B. C., Pérez L., Philippot Q., Lee D., Zhang P., Rinchai D., Al Ali F., Ahmad Ata M. M., Rahman M., Peel J. N., Heissel S., Molina H., Kendir-Demirkol Y., Bailey R., Zhao S., Bohlen J., Mancini M., Seeleuthner Y., Roelens M., Lorenzo L., Soudée C., Paz M. E. J., González M. L., Jeljeli M., Soulier J., Romana S., L'Honneur A.-S., Materna M., Martínez-Barricarte R., Pochon M., Oleaga-Quintas C., Michev A., Migaud M., Lévy R., Alyanakian M.-A., Rozenberg F., Croft C. A., Vogt G., Emile J.-F., Kremer L., Ma C. S., Fritz J. H., Lemon S. M., Spaan A. N., Manel N., Abel L., Macdonald M. R., Boisson-Dupuis S., Marr N., Tangye S. G., Di Santo J. P., Zhang Q., Zhang S.-Y., Rice C. M., Béziat V., Lachmann N., Langlais D., Casanova J.-L., Gros P., Bustamante J., 2023. Human IRF1 governs macrophagic IFN- γ immunity to mycobacteria. *Cell*. 186, 621-645.e633.
<https://doi.org/10.1016/j.cell.2022.12.038>
- Roth, E., Glick Azaria A., Girshevitz O., Bitler A., Garini Y., 2018. Measuring the Conformation and Persistence Length of Single-Stranded DNA Using a DNA Origami Structure. *Nano Letters*. 18, 6703-6709.
<https://doi.org/10.1021/acs.nanolett.8b02093>
- Rothemund, P. W. K., 2006. Folding DNA to create nanoscale shapes and patterns. *Nature*. 440, 297-302.
<https://doi.org/10.1038/nature04586>
- Ruoslahti, E., Pierschbacher M. D., 1987. New Perspectives in Cell-Adhesion - Rgd and Integrins. *Science*. 238, 491-497. <https://doi.org/DOI10.1126/science.2821619>
- Saito, M., Iwawaki T., Taya C., Yonekawa H., Noda M., Inui Y., Mekada E., Kimata Y., Tsuru A., Kohno K., 2001. Diphtheria toxin receptor-mediated conditional and targeted cell ablation in transgenic mice. *Nat Biotechnol*. 19, 746-750.
<https://doi.org/10.1038/90795>

- Sánchez-Visedo, A., Gallego-Martínez B., Royo L. J., Soldado A., Valledor M., Campo J. C., Ferrero F. J., Costa-Fernández J. M., Fernández-Argüelles M. T., 2023. MNAzymes and gold nanoparticles as isothermal signal amplification strategy for visual detection of miRNA. *Microchim Acta*. 190, 292.
<https://doi.org/10.1007/s00604-023-05868-y>
- Santoro, S. W., Joyce G. F., 1997. A general purpose RNA-cleaving DNA enzyme. *P Natl Acad Sci USA*. 94, 4262-4266.
<https://doi.org/DOI10.1073/pnas.94.9.4262>
- Schmalzl, A., Leupold T., Kreiss L., Waldner M., Schürmann S., Neurath M. F., Becker C., Wirtz S., 2022. Interferon regulatory factor 1 (IRF-1) promotes intestinal group 3 innate lymphoid responses during *Citrobacter rodentium* infection. *Nature Communications*. 13, 5730.
<https://doi.org/10.1038/s41467-022-33326-5>
- Shin, S. H., Park S. S., Ju E. J., Park J., Ko E. J., Hwang J. J., Suh Y. A., Jang S. J., Lee J. S., Ko B. K., Kim K. T., Lee J. S., Song S. Y., Jeong S. Y., Choi E. K., 2018. Establishment of a Patient-derived Xenograft for Development of Personalized HER2-targeting Therapy in Gastric Cancer. *Anticancer Res*. 38, 287-293.
<https://doi.org/10.21873/anticancerres.12220>
- Sicard, F., Gayral M., Lulka H., Buscail L., Cordelier P., 2013. Targeting miR-21 for the Therapy of Pancreatic Cancer. *Mol Ther*. 21, 986-994.
<https://doi.org/10.1038/mt.2013.35>
- Siegel, R. L., Miller K. D., Wagle N. S., Jemal A., 2023. Cancer statistics, 2023. *Ca-Cancer J Clin*. 73, 17-48.
<https://doi.org/10.3322/caac.21763>
- Siemann, D. W., 2011. The unique characteristics of tumor vasculature and preclinical evidence for its selective disruption by Tumor-Vascular Disrupting Agents. *Cancer Treatment Reviews*. 37, 63-74.
<https://doi.org/https://doi.org/10.1016/j.ctrv.2010.05.001>
- Singh, S., Chen H., Shahrokhi S., Wang L. P., Lin C.-H., Hu L., Guan X., Tricoli A., Xu Z. J., Wu T., 2020. Hybrid Organic-Inorganic Materials and Composites for Photoelectrochemical Water Splitting. *ACS Energy Letters*. 5, 1487-1497.
<https://doi.org/10.1021/acsenergylett.0c00327>
- Sun, T., Jiang C., 2023. Stimuli-responsive drug delivery systems triggered by intracellular or subcellular microenvironments. *Adv Drug Deliver Rev*. 196, 114773.
<https://doi.org/https://doi.org/10.1016/j.addr.2023.114773>

- g/10.1016/j.addr.2023.114773
- Sun, W. J., Jiang T. Y., Lu Y., Reiff M., Mo R., Gu Z., 2014. Cocoon-Like Self-Degradable DNA Nanoclew for Anticancer Drug Delivery. *J Am Chem Soc.* 136, 14722-14725. <https://doi.org/10.1021/ja5088024>
- Tan, L., Yuan J., Zhu W., Tao K., Wang G., Gao J., 2020. Interferon regulatory factor-1 suppresses DNA damage response and reverses chemotherapy resistance by downregulating the expression of RAD51 in gastric cancer. *Am J Cancer Res.* 10, 1255-1270. <https://doi.org/http://dx.doi.org/10.2139/ssrn.3496917>
- Tanaka, N., Ishihara M., Lamphier M. S., Nozawa H., Matsuyama T., Mak T. W., Aizawa S., Tokino T., Oren M., Taniguchi T., 1996. Cooperation of the tumour suppressors IRF-1 and p53 in response to DNA damage. *Nature.* 382, 816-818. <https://doi.org/DOI10.1038/382816a0>
- Taylor, M. R. G., Špírek M., Chaurasiya K. R., Ward J. D., Carzaniga R., Yu X., Egelman E. H., Collinson L. M., Rueda D., Krejci L., Boulton S. J., 2015. Rad51 Paralogs Remodel Pre-synaptic Rad51 Filaments to Stimulate Homologous Recombination. *Cell.* 162, 271-286. <https://doi.org/10.1016/j.cell.2015.06.015>
- Tran, S., DeGiovanni P.-J., Piel B., Rai P., 2017. Cancer nanomedicine: a review of recent success in drug delivery. *Clinical and Translational Medicine.* 6, e44. <https://doi.org/https://doi.org/10.1186/s40169-017-0175-0>
- Van Den Eeckhout, B., Tavernier J., Gerlo S., 2021. Interleukin-1 as Innate Mediator of T Cell Immunity. *Frontiers in Immunology.* 11, 621931. <https://doi.org/10.3389/fimmu.2020.621931>
- Wagner, A. M., Gran M. P., Peppas N. A., 2018. Designing the new generation of intelligent biocompatible carriers for protein and peptide delivery. *Acta Pharm Sin B.* 8, 147-164. <https://doi.org/10.1016/j.apsb.2018.01.013>
- Walia, S., Chandrasekaran A. R., Chakraborty B., Bhatia D., 2021. Aptamer-Programmed DNA Nanodevices for Advanced, Targeted Cancer Theranostics. *Acs Appl Bio Mater.* 4, 5392-5404. <https://doi.org/10.1021/acsbm.1c00413>
- Wang, J. X., Potocny A. M., Rosenthal J., Day E. S., 2020. Gold Nanoshell-Linear Tetrapyrrole Conjugates for Near Infrared-Activated Dual Photodynamic and Photothermal Therapies. *Acs Omega.* 5, 926-940. <https://doi.org/10.1021/acso mega.9b04150>

- Wang, Q., Zhang X., Liao H., Sun Y., Ding L., Teng Y., Zhu W.-H., Zhang Z., Duan Y., 2018. Multifunctional Shell-Core Nanoparticles for Treatment of Multidrug Resistance Hepatocellular Carcinoma. *Advanced Functional Materials*. 28, 1706124. <https://doi.org/10.1002/adfm.201706124>
- Wang, S., Huang P., Chen X., 2016. Stimuli-Responsive Programmed Specific Targeting in Nanomedicine. *ACS Nano*. 10, 2991-2994. <https://doi.org/10.1021/acsnano.6b00870>
- Wang, W., Singh S., Zeng D. L., King K., Nema S., 2007. Antibody structure, instability, and formulation. *J Pharm Sci-US*. 96, 1-26. <https://doi.org/10.1002/jps.20727>
- Wang, Y., Chen J., Lu J., Xi J., Xu Z., Fan L., Dai H., Gao L., 2022. Metal ions/nucleotide coordinated nanoparticles comprehensively suppress tumor by synergizing ferroptosis with energy metabolism interference. *Journal of Nanobiotechnology*. 20, 199. <https://doi.org/10.1186/s12951-022-01405-w>
- Wechsler, M. E., Ramirez J. E. V., Peppas N. A., 2019. 110th Anniversary: Nanoparticle Mediated Drug Delivery for the Treatment of Alzheimer's Disease: Crossing the Blood-Brain Barrier. *Ind Eng Chem Res*. 58, 15079-15087. <https://doi.org/10.1021/acs.iecr.9b02196>
- Wei, J., Wang H. M., Wu Q., Gong X., Ma K., Liu X. Q., Wang F., 2020. A Smart, Autocatalytic, DNAzyme Biocircuit for in Vivo, Amplified, MicroRNA Imaging. *Angew Chem Int Edit*. 59, 5965-5971. <https://doi.org/10.1002/anie.201911712>
- Wolfe, B. R., Porubsky N. J., Zadeh J. N., Dirks R. M., Pierce N. A., 2017. Constrained Multistate Sequence Design for Nucleic Acid Reaction Pathway Engineering. *J Am Chem Soc*. 139, 3134-3144. <https://doi.org/10.1021/jacs.6b12693>
- Wolinsky, J. B., Colson Y. L., Grinstaff M. W., 2012. Local drug delivery strategies for cancer treatment: Gels, nanoparticles, polymeric films, rods, and wafers. *J Control Release*. 159, 14-26. <https://doi.org/10.1016/j.jconrel.2011.11.031>
- Xia, F. F., He A. X., Zhao H. T., Sun Y., Duan Q., Abbas S. J., Liu J. J., Xiao Z. Y., Tan W. H., 2022. Molecular Engineering of Aptamer Self-Assemblies Increases in Vivo Stability and Targeted Recognition. *Acs Nano*. 16, 169-179. <https://doi.org/10.1021/acsnano.1c05265>
- Xing, Y. Z., Yang Z. Q., Liu D. S., 2011. A Responsive Hidden Toehold To Enable Controllable DNA Strand Displacement

- Reactions. *Angew Chem Int Edit.* 50, 11934-11936.
<https://doi.org/10.1002/anie.201105923>
- Yan, J., Wang Y., Ran M., Mustafa R. A., Luo H., Wang J., Smått J.-H., Rosenholm J. M., Cui W., Lu Y., Guan Z., Zhang H., 2021. Peritumoral Microgel Reservoir for Long-Term Light-Controlled Triple-Synergistic Treatment of Osteosarcoma with Single Ultra-Low Dose. *Small.* 17, 2100479.
<https://doi.org/https://doi.org/10.1002/smll.202100479>
- Yan, J. Q., Ran M. X., Shen X., Zhang H. B., 2023. Therapeutic DNAzymes: From Structure Design to Clinical Applications. *Adv Mater.* 35, e2300374.
<https://doi.org/10.1002/adma.202300374>
- Yang, W. J., Liang H. Z., Ma S. H., Wang D., Huang J., 2019. Gold nanoparticle based photothermal therapy: Development and application for effective cancer treatment. *Sustain Mater Techno.* 22, e00109
<https://doi.org/10.1016/j.susmat.2019.e00109>
- Yang, Y., Liu B., Liu Y., Chen J., Sun Y., Pan X., Xu J., Xu S., Liu Z., Tan W., 2022. DNA-Based MXFs to Enhance Radiotherapy and Stimulate Robust Antitumor Immune Responses. *Nano Lett.* 22, 2826-2834.
<https://doi.org/10.1021/acs.nanolett.1c04888>
- Yu, R. K., Tsai Y.-T., Ariga T., Yanagisawa M., 2011. Structures, Biosynthesis, and Functions of Gangliosides-an Overview. *Journal of Oleo Science.* 60, 537-544.
<https://doi.org/10.5650/jos.60.537>
- Yurke, B., Turberfield A. J., Mills A. P., Simmel F. C., Neumann J. L., 2000. A DNA-fuelled molecular machine made of DNA. *Nature.* 406, 605-608.
<https://doi.org/10.1038/35020524>
- Zamecnik, P. C., Stephenson M. L., 1978. Inhibition of Rous-Sarcoma Virus-Replication and Cell Transformation by a Specific Oligodeoxynucleotide. *P Natl Acad Sci USA.* 75, 280-284.
<https://doi.org/10.1073/pnas.75.1.280>
- Zhan, Q., Shi X., Zhou J., Zhou L., Wei S., 2019. Drug-Controlled Release Based on Complementary Base Pairing Rules for Photodynamic-Photothermal Synergistic Tumor Treatment. *Small.* 15, 1803926.
<https://doi.org/https://doi.org/10.1002/smll.201803926>
- Zhang, D. Y., Seelig G., 2011. Dynamic DNA nanotechnology using strand-displacement reactions. *Nat Chem.* 3, 103-113.
<https://doi.org/10.1038/Nchem.957>
- Zhang, J., Di Z., Yan H., Zhao Y., Li L., 2021. One-Step Synthesis of Single-Stranded DNA-Bridged

Iron Oxide Supraparticles as MRI Contrast Agents. *Nano Lett.* 21, 2793-2799. <https://doi.org/10.1021/acs.nanolett.0c04825>

Zheng, Y., Song X. R., Darby M., Liang Y. F., He L., Cai Z., Chen Q. H., Bi Y. Q., Yang X. J., Xu J. P., Li Y. B., Sun Y. Y., Lee R. J., Hou S. X., 2010. Preparation and characterization of folate-poly(ethylene glycol)-grafted-trimethylchitosan for intracellular transport of protein through folate receptor-mediated endocytosis. *J Biotechnol.* 145, 47-53. <https://doi.org/10.1016/j.jbiotec.2009.09.007>

Zhou, F., Feng B., Yu H., Wang D., Wang T., Liu J., Meng Q., Wang S., Zhang P., Zhang Z., Li Y., 2016. Cisplatin Prodrug-Conjugated Gold Nanocluster for Fluorescence Imaging and Targeted Therapy of the Breast Cancer. *Theranostics.* 6, 679-687. <https://doi.org/10.7150/thno.14556>

Zhou, H., Liu J., Xu J. J., Zhang S. S., Chen H. Y., 2018. Optical nano-biosensing interface via nucleic acid amplification strategy: construction and application. *Chem Soc Rev.* 47, 1996-2019. <https://doi.org/10.1039/c7cs00573c>

Zhou, W., Zhang Y., Ding J., Liu J., 2016. In Vitro Selection in Serum: RNA-Cleaving DNazymes for Measuring

Ca²⁺ and Mg²⁺. *ACS Sensors.* 1, 600-606. <https://doi.org/10.1021/acssensors.5b00306>

Original publications

Mineralization of pH-Sensitive Doxorubicin Prodrug in ZIF-8 to Enable Targeted Delivery to Solid Tumors

Jiaqi Yan, Chang Liu, Qiwei Wu, Junnian Zhou, Xiaoyu Xu, Lirong Zhang, Dongqing Wang,* Fan Yang,* and Hongbo Zhang*. *Analytical Chemistry*. **2020**, 92, 11453–11461. (DOI: 10.1021/acs.analchem.0c02599)

Mineralization of pH-Sensitive Doxorubicin Prodrug in ZIF-8 to Enable Targeted Delivery to Solid Tumors

Jiaqi Yan,[¶] Chang Liu,[¶] Qiwei Wu,[¶] Junnian Zhou, Xiaoyu Xu, Lirong Zhang, Dongqing Wang,*
Fan Yang,* and Hongbo Zhang*



Cite This: *Anal. Chem.* 2020, 92, 11453–11461



Read Online

ACCESS |



Metrics & More

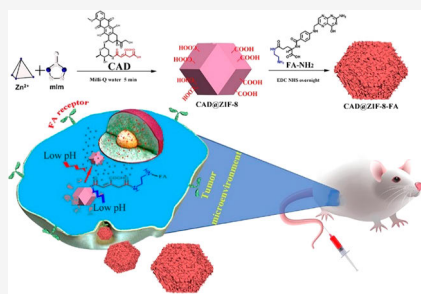


Article Recommendations



Supporting Information

ABSTRACT: The zeolitic imidazolate framework (ZIF-8), composed of zinc ion and dimethylimidazole, is widely used in drug delivery because of the easy fabrication process and the good biosafety. However, ZIF-8 suffers from low affinity to nonelectric-rich drugs and does not have surface functional groups. Here, to deliver doxorubicin (DOX) with ZIF-8 to specific target sites, DOX was first modified with a pH-sensitive linker containing two carboxyl groups to form the inactive prodrug CAD and subsequently seeded inside ZIF-8 by a 5 min mineralization process. CAD has high affinity to ZIF-8 because of the carboxyl groups and can anchor to the ZIF-8 surface to enable the surface modification with folic acid for tumor targeting. Moreover, the DOX release is precisely controlled by three steps of acidic pH response, with the dissociation of the FA layer, the breakdown of the ZIF-8 structure, and the cleavage of the pH-sensitive linker in prodrug. This novel “prodrug-ZIF-8” strategy has opened a new horizon in drug delivery.



Nanomedicine enables specific drug delivery at the target sites with controlled release, which shows great potential in cancer diagnosis and treatment.^{1–3} Metal–organic frameworks (MOFs) composed of metal clusters and organic ligands, which have various advantages compared with many other available drug-delivery systems (DDSs) because of the defined crystal structure and the flexibility in the ascendant combination of both organic and inorganic.^{4–7} Among different types of MOFs, the ZIF-8 system which is composed of Zn and dimethylimidazole is widely studied in the drug-delivery field because of the following: (1) The ZIF-8 system shows excellent biocompatibility at low concentration, since Zn is an essential element for the development of the human immune system and nervous system,⁸ and imidazolyl is part of the amino acid histidine;⁹ (2) ZIF-8 can be easily synthesized at room temperature in 5 min with tunable size, which can also be easily scaled up for future applications in the clinic;^{10–13} (3) The ZIF-8 system has acidic-responsive degradation, which benefits its drug delivery to a tumor microenvironment and an intracellular environment.¹⁴ Nevertheless, despite the many advantages of the ZIF-8 system, there are still some crucial issues that make it unable to fully meet the clinical needs for targeted drug delivery. For instance, (1) ZIF-8 NPs shows lower affinity with drugs that lack electric-rich groups like carboxyl groups, carbonyl, and so on. This character limits their loading capacity and causes undesired premature release of certain drugs;^{15–17} (2) Since no active chemical groups exist on the ZIF-8 structure, the system bears poor surface functionalization ability for

further active targeting design;^{18,19} (3) It has been found that at high concentration, ZIF-8 NPs also show a toxic effect. Therefore, the doses must be limited.^{14,20,21} Moreover, many other MOF candidates have suffered from similar drawbacks in biomedical applications.

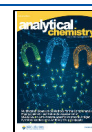
To overcome these problems, different strategies have been investigated to improve the ZIF-8 system, such as surface coating by ZrO_2 or polydopamine to decrease the ZIF-8 toxicity²⁰ and carbonating ZIF-8 at 800 °C and then reacting it with $(\text{NH}_4)_2\text{S}_2\text{O}_8$ and concentrated H_2SO_4 to achieve surface carboxylation for postmodification.²² However, these methods are complicated and need harsh reaction conditions; hence, they are difficult to scale up. Furthermore, the drug loading capacity cannot be improved with those methods.

Doxorubicin (DOX), a first-line anticancer drug, can inhibit cell proliferation by disturbing the synthesis of RNA and DNA. However, DOX lacks targeting ability and has strong cardiotoxicity; thus, more effective DOX delivery is still highly demanded. Prodrug strategies have been investigated in the design of DDSs. Modifying drugs into inactive prodrugs and releasing the parent drug after being triggered by specific

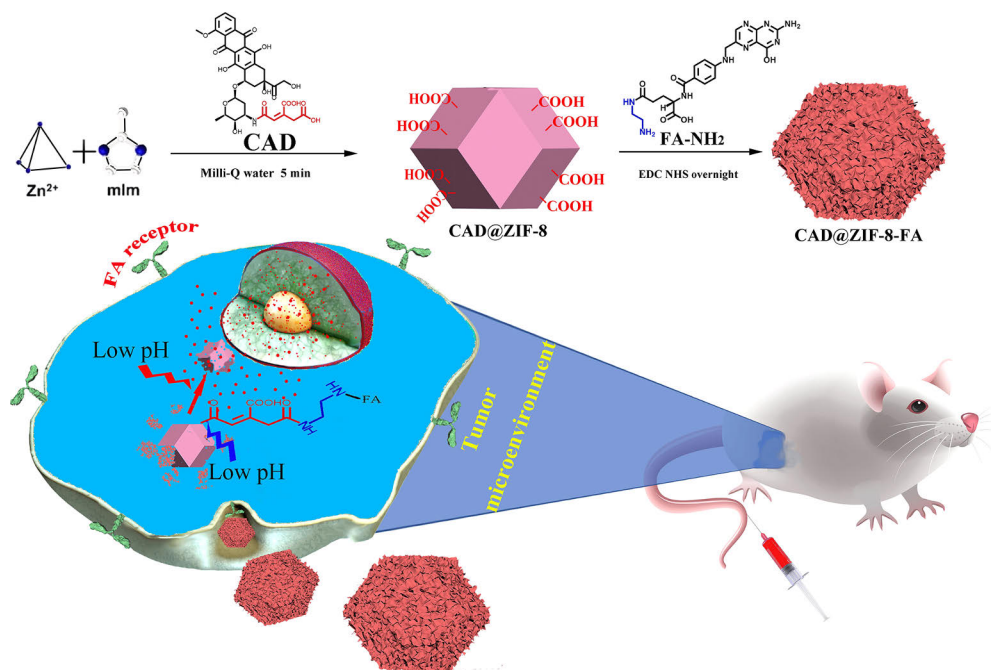
Received: June 17, 2020

Accepted: July 15, 2020

Published: July 15, 2020



Scheme 1. Fabrication of CAD@ZIF-8-FA NPs as a Versatile Nanovehicle for i.v. Injection Cancer Treatment



environments has been applied to reduce the drug toxicity and improve the target drug delivery.^{23,24} It has been reported that after modifying paclitaxel (PTX) with 3,3'-dithiodipropionic acid, the toxicity of PTX apparently decreased and redox-mediated releasing ability was achieved.²⁵ Moreover, the modification can also introduce active reaction groups for further functionalization.

Herein, we have developed a proof of concept methodology for target-specific and pH-responsive delivery of DOX by ZIF-8 (Scheme 1). DOX was first modified by a pH-sensitive linker *cis*-aconitic anhydride (CAA), which contains two carboxyl groups and forms the prodrug CAD, and then the CAD was loaded into ZIF-8 NPs through a 5 min mineralization process. Since CAD has two carboxyl groups, the affinity to ZIF-8 can be significantly improved, thus achieve high loading degree and negligible burst release. Moreover, the carboxyl groups anchored to the ZIF-8 surface can be further conjugated with a tumor-targeting ligand to achieve targeted drug delivery. The pH-responsive nature of ZIF-8 and the CAD can further improve the tumor selectivity. Therefore, this simple and effective CAD@ZIF-8 platform has opened up a new horizon in drug delivery, which extends the MOF-based DDSs and the targeted delivery of DOX.

■ EXPERIMENTAL SECTION

Materials. Doxorubicin (DOX·HCl) and folic acid (FA) were purchased from Arisun ChemPharm Co., Ltd. (China). *cis*-Aconitic anhydride (CAA), ethylenediamine, 4-dimethylaminopyridine (DMAP), *N*-hydroxy succinimide (NHS), and *N*-(3-(dimethylamino)propyl)-*N*-ethylcarbodiimide hydrochloride (EDC·HCl) were purchased from Alfa Aesar

(Finland). 2-Methylimidazole (MIM), Zn(NO₃)₂·6H₂O, *N,N*-dimethylformamide (DMF), triethylamine (TEA), dichloromethane (DCM), and menthol (MeOH) were purchased from Sigma-Aldrich (Finland).

Synthesis of CAD and FA-NH₂. Doxorubicin hydrochloride (200 mg) was dissolved in distilled water (20 mL) and cooled on ice. *cis*-Aconitic anhydride (300 mg) was dissolved in 1,4-dioxane (1 mL) and slowly added to the doxorubicin solution with continuous stirring. The pH of the reaction mixture was immediately adjusted to 9.0 and controlled in the range of 8.5–9.0 by carefully adding NaOH (0.5 M). The reaction mixture was placed in an ice bath for 20 min. Then the pH was adjusted to 7.0 with cold HCl (1 M), and the mixture was stirred for another 20 min. HCl (1 M) was added slowly to the mixture until a heavy precipitate (*cis*-aconitic anhydride-doxorubicin, CAD) was formed. Then the product was extracted with ethyl acetate (25 mL × 4) and evaporated. Folic acid was activated with ethylene diamine through the formation of an amide bridge. For the conjugation, folic acid (220 mg) has to be treated with ethylenediamine (3.2 mL), stirred overnight using EDC/NHS as catalyst, and then extracted in ether.

Synthesis of CAD@ZIF-8 and CAD@ZIF-8-FA. The prescription for different CAD loading ratios of CAD@ZIF-8 was tried and tested. Briefly, 135 mg of zinc nitrate and different amounts of CAD (0, 4, 8, 16, 32 mg) were dissolved in 2 mL of water, respectively, and sonicated for use. Next, 3.7 g of dimethylimidazole was dissolved in 8 mL of water, sonicated at 40 °C, and then poured into a 20 mL beaker with a 1 cm stir bar at 100 rpm. After that, the zinc nitrate and the CAD mixture were poured into the beaker instantly, stirred

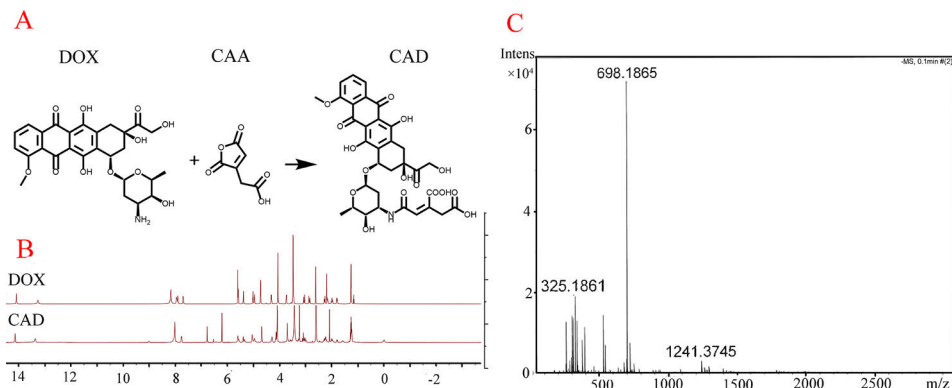


Figure 1. Nuclear magnetic spectrum and mass spectrometry results of prodrug CAD. (A) Synthesis route of CAD. (B) ¹H NMR spectra of CAD and DOX in DMSO-*d*₆. (C) MS spectra of CAD.

for 5 min, centrifuged at 16 000 rpm, and washed 3 times using milli-Q water; as a result, CAD@ZIF-8 was obtained. Subsequently, 20 mg of the different loading ratios of CAD @ ZIF-8 NPs were redispersed in 10 mL of water, separately, and 1.5 mg of EDC and 1.3 mg of NHS were added in each group. After activating the carboxyl groups of CAD which are on the surface of the nanoparticles for 1 h, 5 mg of FA-NH₂ was added for each loading ratio group. After being stirred overnight, centrifuged at 16 000 rpm, and washed 3 times, different loading ratios of CAD@ZIF-8-FA can be achieved.

Characterization of the CAD, FA-NH₂, and Nanoparticles. The ¹H NMR spectra of CAD, FA-NH₂ were recorded on Bruker 500 NMR spectrometers (Bruker, Billerica, MA, U.S.A.). Mass spectra were recorded for CAD on a Bruker Daltonics microTOF-Q mass spectrometer (Bruker, Billerica, MA, U.S.A.). In addition, the FTIR spectra of CAD, CAD@ZIF-8, and CAD@ZIF-8-FA were recorded on a Thermo Scientific Nicolet iSSO Fourier transform infrared spectrometer in the wavenumber of 400–4000 cm⁻¹. Particle sizing was performed using dynamic light scattering with Zetasizer Nano ZS (Malvern Instruments Ltd., U.K.). For each measurement, the sample (1.0 mL) was put in a disposable polystyrene cuvette (SARSTEDT AG & Co., Germany). The nanocarrier surface ζ-potential was measured with Zetasizer Nano ZS by using disposable folded capillary cells (DTS1070, Malvern, U.K.). Both the size and ζ-potential were recorded as the average of three measurements. The structure of the blank ZIF-8, CAD@ZIF-8, and CAD@ZIF-8-FA were evaluated by transmission electron microscope (TEM; JEOL 1400 Plus, JEOL, U.S.A.) at an acceleration voltage of 80 kV. The TEM samples were prepared by using a tweezer to hold the carbon-coated copper grids (200 mesh; Ted Pella, Inc., U.S.A.) and soaking them within the particle solution; they were then removed and dried in the air prior to imaging.

Characterization of Drug Loading Degree and Efficiency. The CAD loading degree (LC) and FA loading efficiency (LE) were calculated according to the following formulas (1) and (2):

$$LC (\%) = \frac{\text{entrapped drug}}{\text{weight of nanoparticles}} \times 100\% \quad (1)$$

LE (%)

$$= \frac{\text{total input of drug} - \text{amount of drug in the supernatant}}{\text{total input of drug}} \times 100\% \quad (2)$$

The DOX loading contents were quantified by gradient analytical HPLC assay. An HPLC assay was performed on an Agilent 1100 instrument, and 20 μL of solution was loaded onto a Waters reverse phase column (250 × 4.6 mm). Acetonitrile (TFA 0.1%):water (TFA 0.1%) (Acetonitrile increase from 5 to 95% with 20 min) was eluted at a flow rate of 1 mL/min at 490 nm by a UV detector (UV-975, Jasco). FA was detected by UV-vis absorption at 282 nm.

In Vitro Release of DOX. CAD@ZIF-8-FA was dispersed in 1.0 mL of PBS buffer solution (pH = 6; pH = 7.4) and then gently shaken at 37 °C in the darkroom. At selected time intervals, the solution was centrifuged at 16 000 rpm, and then 0.9 mL of supernatant was withdrawn and analyzed by HPLC. Subsequently, 0.9 mL of fresh medium was returned to the original solution and sonicated until the nanoparticles were dispersed well; the medium was then put back into the shaker. The standard curve detected by HPLC for DOX is $Y = 4.6348X - 0.0283$ ($R = 0.9998$). Here Y is UV absorption integral of DOX at 490 nm wavelengths; X is the concentration of DOX (μg).

In Vitro Assays. The drug efficacy in cancerous and healthy cells was determined by a WST-1 cell viability assay. MDA-MB-231 cancer cells and MCF-10A cells were incubated overnight in a 96-well-plate (3000 cells per well) in cell growth media at 37 °C with 5% CO₂. The following day, the cell growth media were replaced with fresh media containing a different concentration of CAD, DOX, CAD@ZIF-8, and CAD@ZIF-8-FA and incubated for 24 h. Free drug stock solutions (DOX, CAD) were prepared in DMSO, and nanoparticles were suspended in water. All the dilutions for the cell viability assay were prepared in cell growth media. After being incubated with free drug or nanoparticles, 10 μL of WST-1 reagent was added to each well, and the cells were incubated for 2 h at 37 °C with 5% CO₂. After incubation, the absorbance was measured by a Varioskan Flash Multimode Reader (Thermo Scientific Inc., Waltham, MA, U.S.A.) at 440 nm. The blank ZIF-8 concentration corresponds to the

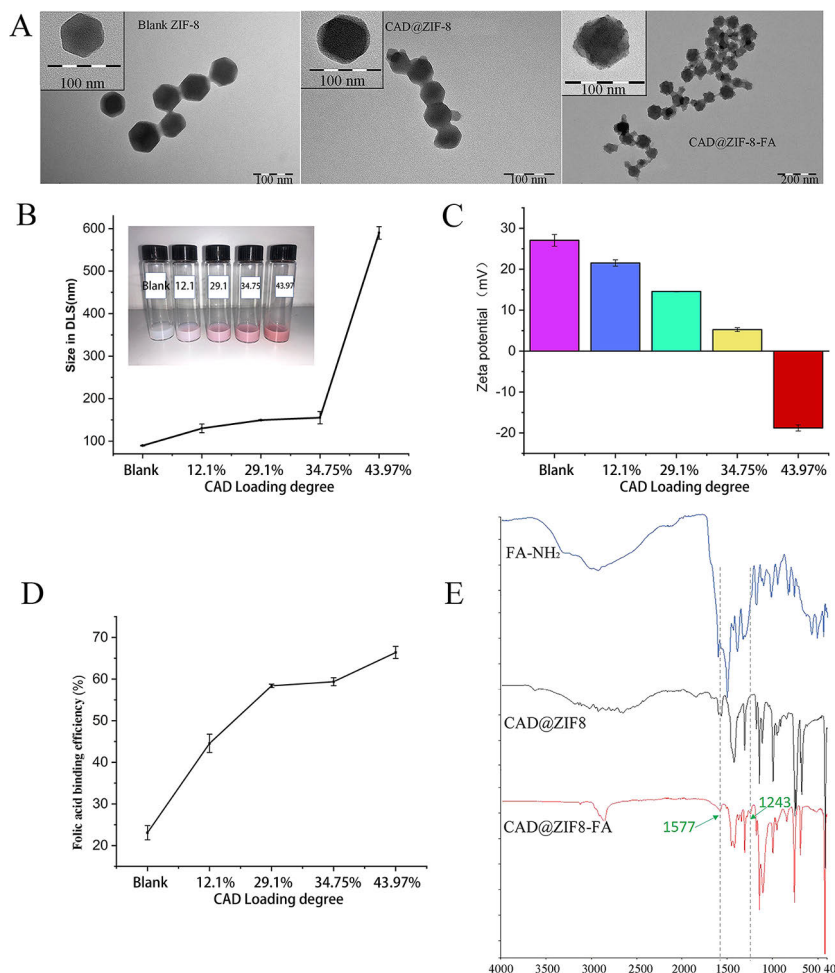


Figure 2. Characterization of blank ZIF-8, CAD@ZIF-8, and CAD@ZIF-8-FA NPs. (A) TEM images. (B) Size results from DLS. (C) Zeta potential of CAD@ZIF-8 with different concentrations of CAD. (D) Folic acid binding efficiency and (E) FTIR spectra ($n = 3$).

content of the ZIF-8 in each NPs at different loading ratio. For cell culture and maintenance, CLSM imaging, and flow cytometry assay, all the details are provided in the Supporting Information.

In Vivo Assays. All animal studies were performed in accordance with the Ethics Committee of Affiliated Hospital of Jiangsu University. huPBMC-NCG mice were established by implanting human peripheral blood mononuclear cells (PBMCs) into NCG mice. Human peripheral blood mononuclear cells (hPBMCs) were injected the caudal vein (1×10^7 cells) of NCG mice for huPBMC reconstitution. Subcutaneous inoculation of MDA-MB-231 cancer cells into the male NCG mice which were purchased from GemPharmatech. When the average body weight reached 19 g, the mice were randomly divided into four groups (six mice per group): the group treated with saline (200 μ L) served as the control, while the other three groups were, respectively, injected with

DOX, blank ZIF-8, and CAD@ZIF-8-FA (equal to 3 mg of DOX per gram mice, 200 μ L), respectively, every 3 days for 19 days. Meanwhile, the mice were weighed, and the tumor volumes were measured every 3 days. The tumor volumes were calculated using the following equations: $V = (\text{length} \times \text{width}^2)/2$. The mice were euthanized at the end of the treatments for histological analysis. The tumors and major organs (including heart, liver, spleen, kidney, and lung) were harvested for routine staining with hematoxylin–eosin (H&E). The final images were obtained and analyzed under a microscope (IVIS Lumina XRMS Series III, Perkin Elmer).

RESULTS AND DISCUSSION

Synthesis and Characterization of CAD. DOX were fabricated into a prodrug CAD through a one-step ring-opening reaction.²⁶ The active carboxyl group within CAD not only can achieve high carrier affinity but also can realize

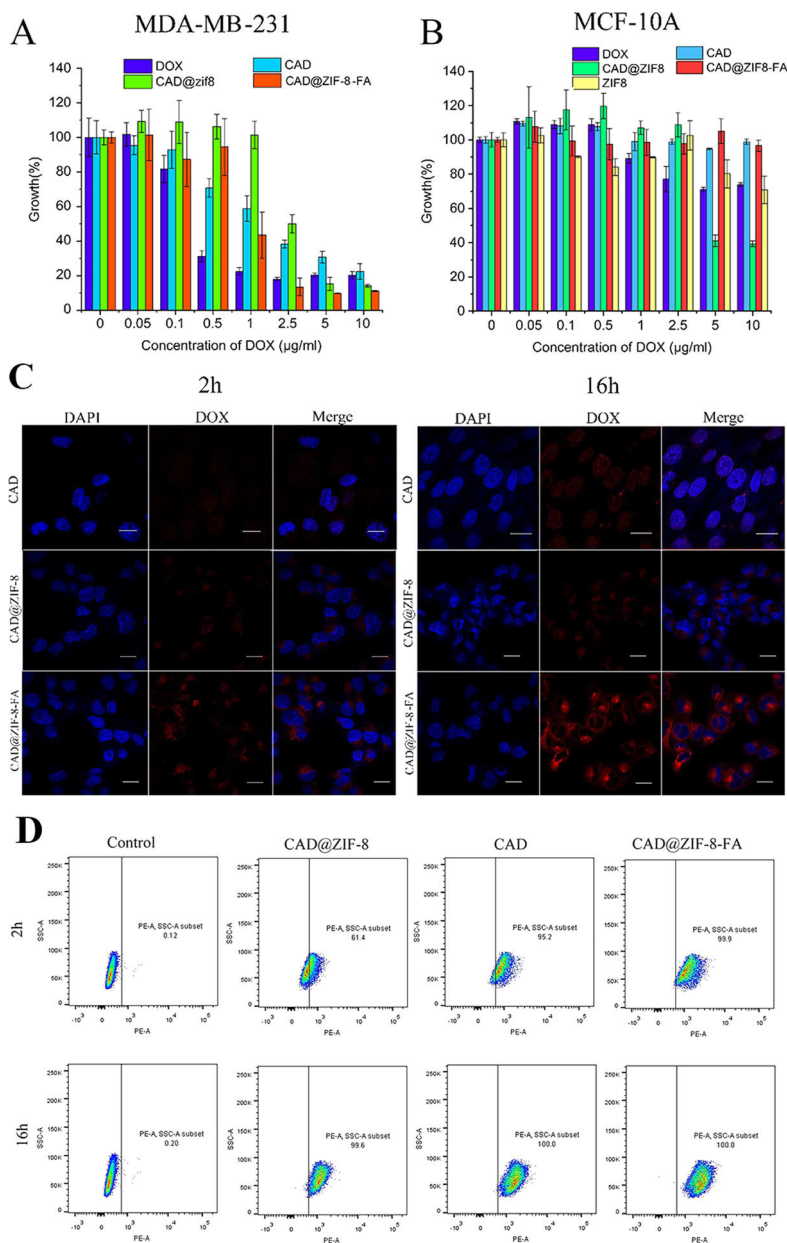


Figure 3. Cytotoxicity and cell uptake. (A) Cytotoxicity of DOX, CAD, CAD@ZIF-8, and CAD@ZIF-8-FA NPs for MDA-MB-231. (B) DOX, CAD, CAD@ZIF-8, CAD@ZIF-8-FA NPs, and blank ZIF-8 for MCF-10A. (C) Confocal microscopy images of CAD, CAD@ZIF-8, and CAD@ZIF-8-FA NPs uptake in cancer cells MDA-MB-231 at 2 and 16 h. The scale bars denote 20 μm . (D) Flow cytometry of cellular uptake of the control group, CAD, CAD@ZIF-8, and CAD@ZIF-8-FA at 2 and 16 h, respectively, for MDA-MB-231.

carboxylation of ZIF-8 for further folate conjugation. The synthetic scheme was shown in Figure 1A. The ^1H NMR spectra shows that after modifying DOX by *cis*-aconitic anhydride (CAA), new peaks at 6.1 and 6.8 ppm were found,

which were attributed to the protons ($\text{CH}-\text{COO}-$) of the CAA within the structure of CAD (Figure 1B). Moreover, the MS spectra of CAD (Figure 1C) gave a peak at a mass of 698.1865, corresponding to the calculated mass of 698.1727.

Furthermore, the successful preparation of CAD prodrug was also confirmed by HPLC. We can see that the DOX and CAD had different peaks with retention times of 4.957 and 12.428 min, respectively (Figure S1). Therefore, MS, NMR, and HPLC results together confirmed that the CAD was successfully synthesized.

Synthesis and Characterization of CAD@ZIF-8 and CAD@ZIF-8-FA NPs. CAD@ZIF-8 particles were synthesized in pure aqueous solutions for 5 min at room temperature.²⁷ The transmission electron microscopy (TEM) images (Figure 2A and Figure S2) revealed that when increasing the loading degree from 12.1% to 43.97%, the size of NPs changed from 80 to 450 nm. Meanwhile, the hydrodynamic size measured by dynamic light scattering (DLS) (Figure 2B) were 159 to 590 nm, which consisted well with the TEM image. More importantly, the CAD attached layer and ZIF-8 corners were found and marked with arrows at 43.97% CAD loading degree (Figure S2), indicating that with the increased CAD loading degree, CAD formed an attachment layer on the ZIF-8 surface.

As shown in Figure 2C, we found that when loading degree was enhanced from 0 to 34.75%, the zeta potential only decreased 16.3 mV, whereas when the loading degree was increased from 34.75% to 43.97%, a 23.9 mV decrease was found. These results suggested that CAD was mineralized by ZIF-8 and the zeta potential was significantly affected at higher CAD loading degree.

On the basis of the characterization results of CAD@ZIF-8, we chose CAD@ZIF-8 NPs with 34.75% of CAD loading for later FA conjugating. To enable the conjugation, we modified the FA with ethylenediamine for a later amidation reaction. The NMR results of FA-NH₂ are shown in Figure S3. After incubation, a significant FA layer was observed in the CAD@ZIF-8-FA NPs (Figure 2A) even after extensive washing and sonication, and the zeta potential decreased to -10 ± 1.03 mV (Figure S4). Meantime, Figure 2D indicated that the blank ZIF-8 had low FA binding efficiency of 25%. However, when CAD loading degree was increased from 12.1% to 43.97%, the FA loading efficiency increased from 44% to 67.4%. As mentioned above, when CAD loading degree increases, more CAD will be coordinated on the ZIF-8 surface and facilitate the FA conjugation, therefore enhancing the FA binding efficiency. Moreover, the FTIR results (Figure 2E) showed two new peaks at 1577 and 1243, which were attributed to the newly formed amide bond.²⁸ Those results proved that the FA is covalently binding instead of physical absorbing to the CAD@ZIF-8.

In Vitro Release of DOX. Taking advantage of the FA surface modification, pH-sensitivity of ZIF-8, and prodrug, the release of DOX within an acid tumor environment requires three steps, which greatly enhances the releasing selectivity (Figure S5). The first step is the cleavage of the pH-sensitive linker between "CAD-FA" on the surface of ZIF-8, which in turn exposes the ZIF-8 NPs. The second step is the pH-sensitive degradation of ZIF-8 NPs and then release of the prodrug CAD. The third step is the pH-sensitive breakage of the linker in the prodrug and then release of the parent drug DOX.

Cytotoxicity Assays. To further evaluate the cytotoxicity of CAD@ZIF-8-FA NPs, a standard in vitro WST-1 assay was performed. From the results of Figure 3A, CAD@ZIF-8-FA NPs exhibited a strong tumor-killing ability for MDA-MB-231 cells. Meanwhile, we also found that pure DOX exhibits more

toxicity when DOX concentration was lower than $1 \mu\text{g mL}^{-1}$, while CAD@ZIF-8-FA NPs showed more toxicity at high concentration ($\geq 2.5 \mu\text{g mL}^{-1}$). This may have occurred because the prodrug had less toxicity than parent drug under the same cultivated time, while at high concentration, the ZIF-8 carriers have enhanced the toxicity of DOX.

Meanwhile, the results of the healthy cell MCF-10A showed that the CAD and CAD@ZIF-8-FA groups had no toxicity for healthy cells even at a high concentration of $10 \mu\text{g mL}^{-1}$ (Figure 3B). However, at a DOX concentration of $10 \mu\text{g mL}^{-1}$, the cell variability was approximately 70%, and similar results were found with the pure ZIF-8. In the CAD@ZIF-8 group, the cell variability was around 40%. These results indicated that at high concentration, ZIF-8 and CAD@ZIF-8 NPs can induce cell toxicity for both healthy cells and tumor cells, while the FA layer can protect against toxicity in healthy cells and induce tumor-selective killing.

To investigate whether zinc will enhanced the toxicity of DOX, we performed the WST-1 assay with Zn^{2+} ion, ZIF-8, DOX, $\text{DOX} + \text{Zn}^{2+}$, and $\text{DOX} + \text{ZIF-8}$ groups (Figure S6). The results showed that zinc ions (corresponding with the DOX concentration in NPs) did not increase the toxicity of DOX, but a positive charge of CAD@ZIF-8 NPs may cause the enhanced cell uptake and then enhance the toxicity.

CLSM Imaging and Flow Cytometry Assay. Subsequently, to more intuitively observe the drug phagocytosis inside the cell, we conducted confocal experiments. The fluorescence excitative wavelength of CAD is similar to DOX as reported previously.²⁹ However, its fluorescent behavior in the presence of cells is unknown. Hence, as shown in Figure S7, we detected and found that the PE channel for DOX detection is also good for detecting CAD.

From CAD groups in Figure 3C, a small amount of red signal was found in cells within 2 h. This may occurred because the prodrug CAD was converted into the parent drug DOX in the acidic tumor microenvironment, then enter the nuclei to achieve the therapeutic effect (Figure S7). For the NPs groups, the CLSM and flow cytometry indicated that the CAD@ZIF-8-FA NPs showed significantly higher uptake than CAD@ZIF-8 (Figure 3C,D) in the MDA-MB-231 cancer cells, which was induced by folic-mediated endocytosis. Whereas, CAD@ZIF-8 and CAD@ZIF-8-FA particles were presented only in the cytoplasm after 2 h and accumulated around the cell nuclei (Figure 3C). These phenomenon illustrated that NPs had controlled the DOX release in the beginning.

Then we also investigated the localization of the drug in MCF-10A healthy cells using CLSM. As shown in Figure S8, for the CAD group of MCF-10A cells, since there is a lack of acidic environment, negatively charged CAD cannot break to form DOX, and only weak red fluorescence was found inside the nuclei within 16 h. Meanwhile, the CAD@ZIF-8-FA NPs showed almost no red signal in MCF-10A, whereas CAD@ZIF-8 NPs showed clear red signal in the cells (Figure S8). This was in good agreement with the WST-1 results in Figure 3B; these results indicate that FA modification has converted the positively charged particles to negatively charged particles, thus preventing the unspecific uptake to healthy cells and reducing the toxicity of the ZIF-8 carrier at high concentration.

In Vivo Assays. We next investigated the tumor suppression of the NPs by intravenous tail injection of PBS, blank ZIF-8, pure DOX, and CAD@ZIF-8-FA NPs into

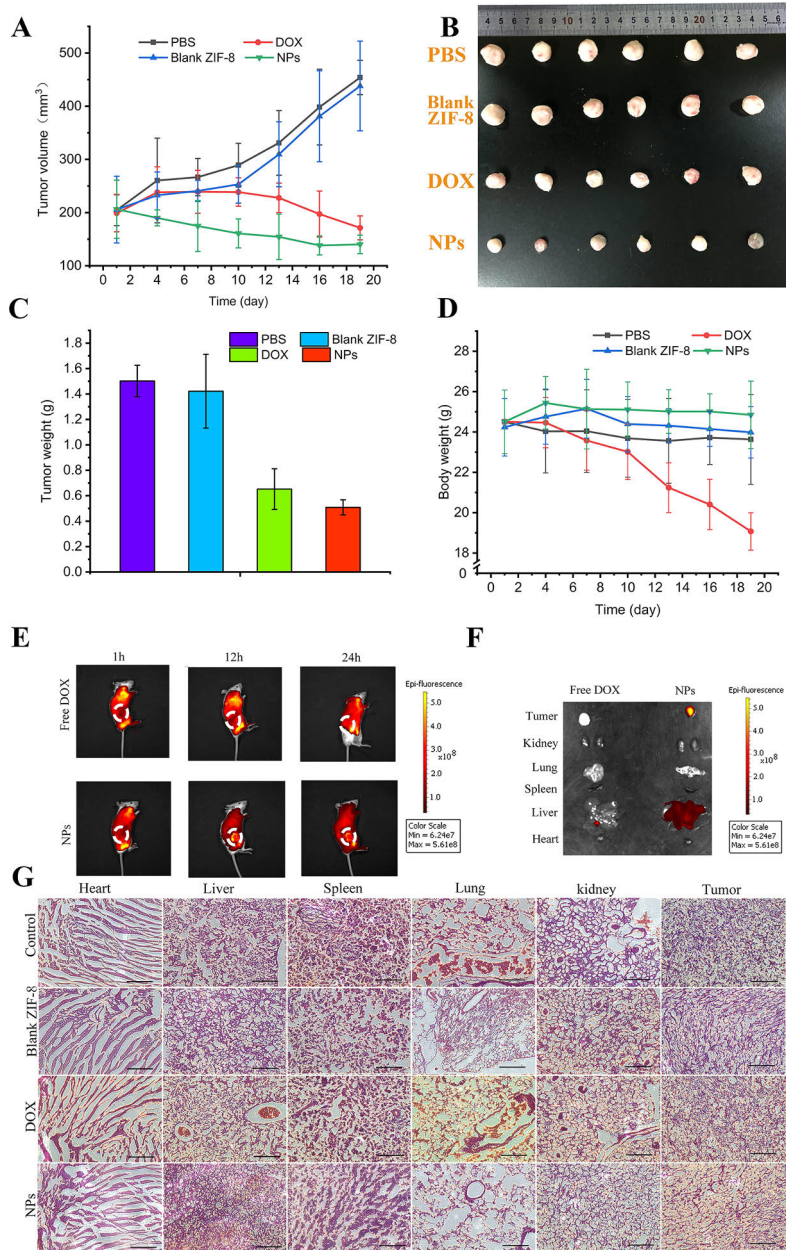


Figure 4. In vivo antitumor therapy. (A) Change of tumor volume during treatment. (B) Photo of tumors from different groups. (C) Tumor weight change during therapy. (D) Bodyweight changes during the treatment. (E) In vivo fluorescence imaging of MDA-MB-231 bearing mice at 1, 12, 24, 48, and 72 h after the injection of free DOX and CAD@ZIF-8-FA NPs. (F) Ex vivo bioluminescence imaging of different organs. (G) H&E staining of different organs.

different groups of tumor-bearing mice. The tumor growth curves in Figure 4A showed that the tumor volume was significantly reduced in the CAD@ZIF-8-FA NPs-treated

mice, and the therapeutic effect was stronger than pure DOX. After the mice were sacrificed, from the photos of excised organs (Figure 4B) and the tumor weight (Figure 4C) of each

group, we can visually observe that the CAD@ZIF-8-FA NPs group had the best treatment effect. Also, we observed that the weight of the mice was markedly reduced in the DOX-treated group but slightly increased in the CAD@ZIF-8-FA NPs-treated group, indicating that NPs can effectively reduce the side effects of DOX (Figure 4D).

To observe the distribution of CAD@ZIF-8-FA NPs in mice, we performed *in vivo* fluorescence imaging at 1, 12, and 24 h. We found that the NPs obviously accumulated at the tumor sites at 12 and 24 h, while DOX spread to the whole body of the mice (Figure 4E). The near infrared fluorescence imaging results of each organ in the DOX group and NPs group (Figure 4F) showed that the NPs group had the strongest red fluorescence in tumors. These results indicated that CAD@ZIF-8-FA NPs can promote the accumulation of drugs in tumors and increase the drug-delivery efficiency.

Afterward, we also performed a histological evaluation for saline, free DOX, blank ZIF-8, and CAD@ZIF-8-FA NPs groups. Because of the cytotoxic effect of CAD@ZIF-8-FA NPs on tumor cells, less nuclear staining was found in tumors because the cell nucleus will shrink and even lysis (Figure 4G and Figure S9). Furthermore, for the DOX-treated mice, the heart cells exhibit abnormal morphology because of the strong cardiotoxicity of DOX (Figure 4G and Figure S9), while no cardiotoxicity was found in the NPs group. Thus, these results indicated that the CAD@ZIF-8-FA nanopatform was a promising DDS for targeted cancer therapy with low system toxicity.

CONCLUSIONS

In conclusion, we combined the merits of the ZIF-8 system and the prodrug strategy, and we fabricated a novel “prodrug-ZIF-8” nanopatform for targeted DOX delivery. With this design, we solved several drawbacks of both prodrug and ZIF-8 systems. ZIF-8 carried the prodrug CAD to accumulate at the tumor site with an EPR effect. The prodrug introduced new carboxyl groups, which greatly improved the drug loading efficiency and prevented the premature release. In addition, the surface-anchored CAD also enabled the FA conjugation to form a FA layer to reduce the healthy cell uptake and enable the folic acid receptor mediated uptake in tumor cells. Moreover, the system has three steps of pH responsiveness, and the DOX release was precisely controlled. The *in vitro* and *in vivo* results showed that the FA-modified NPs could achieve tumor-selective therapeutics, accumulate at tumor site, and significantly inhibited the tumor growth and greatly reduced the cardiotoxicity of DOX. Overall, this *i.v.* injectable folate-surface-functionalized ZIF-8-based nanopatform is a promising delivery system for cancer therapy. More importantly, this prodrug strategy method opens a new horizon for the surface modification of other MOFs systems.

ASSOCIATED CONTENT

Supporting Information

The Supporting Information is available free of charge at <https://pubs.acs.org/doi/10.1021/acs.analchem.0c02599>.

Cell culture and maintenance; CLSM imaging; flow cytometry assay; Figure S1–S9 (PDF)

AUTHOR INFORMATION

Corresponding Authors

Dongqing Wang – Department of Radiology, Affiliated Hospital of Jiangsu University, Jiangsu University, 212001 Zhenjiang, P.R. China; Email: wangdongqing71@163.com

Fan Yang – The Center for Drug Research and Development, Guangdong Pharmaceutical University, Guangzhou, Guangdong 510006, China; Email: gzyangfan@hotmail.com

Hongbo Zhang – Pharmaceutical Sciences Laboratory and Turku Bioscience Center, Åbo Akademi University, FI-20520 Turku, Finland; orcid.org/0000-0002-1071-4416; Email: hongbo.zhang@abo.fi

Authors

Jiaqi Yan – The Center for Drug Research and Development, Guangdong Pharmaceutical University, Guangzhou, Guangdong 510006, China; Pharmaceutical Sciences Laboratory and Turku Bioscience Center, Åbo Akademi University, FI-20520 Turku, Finland

Chang Liu – Pharmaceutical Sciences Laboratory and Turku Bioscience Center, Åbo Akademi University, FI-20520 Turku, Finland

Qiwei Wu – Department of Radiology, Affiliated Hospital of Jiangsu University, Jiangsu University, 212001 Zhenjiang, P.R. China

Junnian Zhou – Experimental Hematology and Biochemistry Lab, Beijing Institute of Radiation Medicine, Beijing 100850, China

Xiaoyu Xu – Pharmaceutical Sciences Laboratory and Turku Bioscience Center, Åbo Akademi University, FI-20520 Turku, Finland

Lirong Zhang – Department of Radiology, Affiliated Hospital of Jiangsu University, Jiangsu University, 212001 Zhenjiang, P.R. China

Complete contact information is available at: <https://pubs.acs.org/10.1021/acs.analchem.0c02599>

Author Contributions

[†]J.Y., C.L., and Q.W. contributed equally to this work.

Notes

The authors declare no competing financial interest.

ACKNOWLEDGMENTS

This work was supported by Distinguished Clinical Investigator Grant of Jiangsu Province, China (Grant No. JSTP201701), Jiangsu Provincial Key Research and Development Programme (Grant No. BE2018690), Academy of Finland (Grant No. 328933), and Sigrid Jusélius Foundation (decision no. 28002247K1). F.Y. acknowledges grants from the Technological Project of Guangzhou Technology Bureau (Grant No. 20170402199).

REFERENCES

- (1) White, M. C.; Holman, D. M.; Goodman, R. A.; Richardson, L. C. *Gerontologist* **2019**, 59 (Supplement 1), S1–S6.
- (2) Miller, K. D.; Nogueira, L.; Mariotto, A. B.; Rowland, J. H.; Yabroff, K. R.; Alfano, C. M.; Jemal, A.; Kramer, J. L.; Siegel, R. L. *Ca-Cancer J. Clin.* **2019**, 69 (5), 363–385.
- (3) Bray, F.; Ferlay, J.; Soerjomataram, I.; Siegel, R. L.; Torre, L. A.; Jemal, A. *Ca-Cancer J. Clin.* **2018**, 68 (6), 394–424.
- (4) Abanades Lazaro, I.; Abanades Lazaro, S.; Forgan, R. S. *Chem. Commun. (Cambridge, U. K.)* **2018**, 54 (22), 2792–2795.

- (5) Wuttke, S.; Dietl, C.; Hinterholzinger, F. M.; Hintz, H.; Langhals, H.; Bein, T. *Chem. Commun. (Cambridge, U. K.)* **2014**, 50 (27), 3599–601.
- (6) Qin, J.; Cho, M.; Lee, Y. *ACS Appl. Mater. Interfaces* **2019**, 11 (12), 11743–11748.
- (7) Dodson, R. A.; Wong-Foy, A. G.; Matzger, A. J. *Chem. Mater.* **2018**, 30 (18), 6559–6565.
- (8) Jia, B.; Yang, H.; Han, Y.; Zhang, Z.; Qu, X.; Zhuang, Y.; Wu, Q.; Zheng, Y.; Dai, K. *Acta Biomater.* **2020**, 108, 358–372.
- (9) Griffiths-Jones, S.; Grocock, R. J.; van Dongen, S.; Bateman, A.; Enright, A. J. *Nucleic Acids Res.* **2006**, 34, D140.
- (10) Sun, C. Y.; Qin, C.; Wang, X. L.; Yang, G. S.; Shao, K. Z.; Lan, Y. Q.; Su, Z. M.; Huang, P.; Wang, C. G.; Wang, E. B. *Dalton Trans* **2012**, 41 (23), 6906–6909.
- (11) Shi, J.; Wang, X.; Zhang, S.; Tang, L.; Jiang, Z. *J. Mater. Chem. B* **2016**, 4 (15), 2654–2661.
- (12) Pan, Y.; Liu, Y.; Zeng, G.; Zhao, L.; Lai, Z. *Chem. Commun. (Cambridge, U. K.)* **2011**, 47 (7), 2071–2073.
- (13) Lan, X.; Huang, N.; Wang, J.; Wang, T. *Chem. Commun. (Cambridge, U. K.)* **2018**, 54 (6), 584–587.
- (14) Zheng, H.; Zhang, Y.; Liu, L.; Wan, W.; Guo, P.; Nystrom, A. M.; Zou, X. *J. Am. Chem. Soc.* **2016**, 138 (3), 962–968.
- (15) Zhang, F. M.; Dong, H.; Zhang, X.; Sun, X. J.; Liu, M.; Yang, D. D.; Liu, X.; Wei, J. *Z. ACS Appl. Mater. Interfaces* **2017**, 9 (32), 27332–27337.
- (16) Zheng, C. C.; Wang, Y.; Phua, S. Z. F.; Lim, W. Q.; Zhao, Y. L. *ACS Biomater. Sci. Eng.* **2017**, 3 (10), 2223–2229.
- (17) Tiwari, A.; Singh, A.; Garg, N.; Randhawa, J. K. *Sci. Rep.* **2017**, 7, 12598.
- (18) Zhang, H.; Jiang, W.; Liu, R.; Zhang, J.; Zhang, D.; Li, Z.; Luan, Y. *ACS Appl. Mater. Interfaces* **2017**, 9 (23), 19687–19697.
- (19) Roder, R.; Preiss, T.; Hirschle, P.; Steinborn, B.; Zimpel, A.; Hohn, M.; Radler, J. O.; Bein, T.; Wagner, E.; Wuttke, S.; Lachelt, U. *J. Am. Chem. Soc.* **2017**, 139 (6), 2359–2368.
- (20) Su, L.; Wu, Q.; Tan, L.; Huang, Z.; Fu, C.; Ren, X.; Xia, N.; Chen, Z.; Ma, X.; Lan, X.; Zhang, Q.; Meng, X. *ACS Appl. Mater. Interfaces* **2019**, 11 (11), 10520–10531.
- (21) Wu, Q.; Niu, M.; Chen, X.; Tan, L.; Fu, C.; Ren, X.; Ren, J.; Li, L.; Xu, K.; Zhong, H.; Meng, X. *Biomaterials* **2018**, 162, 132–143.
- (22) Cao, X.; Xia, J.; Meng, X.; Xu, J.; Liu, Q.; Wang, Z. *Adv. Funct. Mater.* **2019**, 29 (34), 1902237.
- (23) Walther, R.; Rautio, J.; Zelikin, A. N. *Adv. Drug Delivery Rev.* **2017**, 118, 65–77.
- (24) Bildstein, L.; Dubernet, C.; Couvreur, P. *Adv. Drug Delivery Rev.* **2011**, 63 (1–2), 3–23.
- (25) Yan, J.; Xu, X.; Zhou, J.; Liu, C.; Zhang, L.; Wang, D.; Yang, F.; Zhang, H. *ACS Applied Bio Materials* **2020**, 3, 1216–1225.
- (26) Du, C.; Deng, D.; Shan, L.; Wan, S.; Cao, J.; Tian, J.; Achilefu, S.; Gu, Y. *Biomaterials* **2013**, 34 (12), 3087–3097.
- (27) Benzaqui, M.; Semino, R.; Menguy, N.; Carn, F.; Kundu, T.; Guigner, J. M.; McKeown, N. B.; Msayib, K. J.; Carta, M.; Malpass-Evans, R.; Le Guillouzer, C.; Clet, G.; Ramsahye, N. A.; Serre, C.; Maurin, G.; Steunou, N. *ACS Appl. Mater. Interfaces* **2016**, 8 (40), 27311–27321.
- (28) Mallamace, F.; Corsaro, C.; Mallamace, D.; Vasi, S.; Vasi, C.; Dugo, G. *Comput. Struct. Biotechnol. J.* **2015**, 13, 33–7.
- (29) Hu, G.; Zhang, H.; Zhang, L.; Ruan, S.; He, Q.; Gao, H. *Int. J. Pharm.* **2015**, 496 (2), 1057–68.

Peritumoral Microgel Reservoir for Long-Term Light- Controlled Triple-Synergistic Treatment of Osteosarcoma with Single Ultra-Low Dose

Jiaqi Yan, Yichuan Wang, Meixin Ran, Rawand A. Mustafa, Huanhuan Luo, Jixiang Wang, Jan-Henrik Smått, Jessica M. Rosenholm, Wenguo Cui, Yong Lu,* Zhenpeng Guan,* and Hongbo Zhang*. *Small*. **2021**, 17, 2100479. (DOI: 10.1002 /sml.202100479)

Peritumoral Microgel Reservoir for Long-Term Light-Controlled Triple-Synergistic Treatment of Osteosarcoma with Single Ultra-Low Dose

Jiaqi Yan, Yichuan Wang, Meixin Ran, Rawand A. Mustafa, Huanhuan Luo, Jixiang Wang, Jan-Henrik Smått, Jessica M. Rosenholm, Wenguo Cui, Yong Lu,* Zhenpeng Guan,* and Hongbo Zhang*

Local minimally invasive injection of anticancer therapies is a compelling approach to maximize the utilization of drugs and reduce the systemic adverse drug effects. However, the clinical translation is still hampered by many challenges such as short residence time of therapeutic agents and the difficulty in achieving multi-modulation combination therapy. Herein, mesoporous silica-coated gold nanorods (AuNR@SiO₂) core-shell nanoparticles are fabricated to facilitate drug loading while rendering them photothermally responsive. Subsequently, AuNR@SiO₂ is anchored into a monodisperse photocrosslinkable gelatin (GelMA) microgel through one-step microfluidic technology. Chemotherapeutic drug doxorubicin (DOX) is loaded into AuNR@SiO₂ and 5,6-dimethylxanthenone-4-acetic acid (DMXAA) is loaded in the microgel layer. The osteosarcoma targeting ligand alendronate is conjugated to AuNR@SiO₂ to improve the tumor targeting. The microgel greatly improves the injectability since they can be dispersed in buffer and the injectability and degradability are adjustable by microfluidics during the fabrication. The drug release can, in turn, be modulated by multi-round light-trigger. Importantly, a single super low drug dose (1 mg kg⁻¹ DOX with 5 mg kg⁻¹ DMXAA) with peritumoral injection generates long-term therapeutic effect and significantly inhibited tumor growth in osteosarcoma bearing mice. Therefore, this nanocomposite@microgel system can act as a peritumoral reservoir for long-term effective osteosarcoma treatment.

1. Introduction

Chemotherapy is widely used in cancer treatment and the conventional anticancer drug administration is mostly achieved by oral administration and intravenous injection, which will cause the drug to be undistinctly distributed throughout the body, resulting in ineffective treatment and systemic toxicity.^[1] To achieve enhanced specific drug uptake in the tumor lesions, nanocarriers have been widely studied to achieve various sophisticated effects, including photothermal therapy,^[2] receptor-mediated targeting,^[3] multi-drug chemotherapy,^[4–6] and so forth. Dependent on the enhanced permeation and retention (EPR) effect, the tumor enrichment of anticancer therapies is indeed improved by nanocarriers after intravenous (IV) administration;^[7,8] however, the improvement is not significant, since the majority of the nanoparticles are still taken up by the liver and kidney.^[9–11] Hence, large doses and repeated administrations are still necessary to achieve long-term therapeutic effects.

J. Yan, M. Ran, Prof. W. Cui, Prof. Y. Lu, Prof. H. Zhang
Department of Radiology
Shanghai Institute of Traumatology and Orthopaedics
Ruijin Hospital LuWan Branch
Shanghai Jiao Tong University School of Medicine
149 ChongqingNan Road, Shanghai 200020, P. R. China
E-mail: 18917762053@163.com; hongbo.zhang@abo.fi

J. Yan, M. Ran, R. A. Mustafa, Dr. J. Wang, Prof. J. M. Rosenholm, Prof. H. Zhang
Pharmaceutical Sciences Laboratory
Faculty of Science and Engineering
Åbo Akademi University
Turku 20520, Finland

The ORCID identification number(s) for the author(s) of this article can be found under <https://doi.org/10.1002/smll.202100479>.

© 2021 The Authors. Small published by Wiley-VCH GmbH. This is an open access article under the terms of the Creative Commons Attribution License, which permits use, distribution and reproduction in any medium, provided the original work is properly cited.

DOI: 10.1002/smll.202100479

J. Yan, M. Ran, Dr. J. Wang, Prof. H. Zhang
Turku Bioscience Centre
University of Turku and Åbo Akademi University
Turku 20520, Finland

Y. Wang, Prof. Z. Guan
Department of Orthopaedics
Peking University Shougang Hospital
No.9 Jinyuanzhuang Rd, Shijingshan District, Beijing 100144, P. R. China
E-mail: guanzhenpeng@qq.com

H. Luo
Jiaxing Key Laboratory of Basic Research and Clinical Translation on Orthopedic Biomaterials
Department of Orthopaedics
The Second Affiliated Hospital of Jiaxing University
Jiaxing 314000, P. R. China

Dr. J. H. Smått
Laboratory of Molecular Science and Engineering
Faculty of Science and Engineering
Åbo Akademi University
Turku 20520, Finland

In recent years, in order to maximize the efficiency of drug delivery, local therapy has received widespread attention.^[12–14] Compared with oral administration and intravenous injection, local minimally invasive administration can directly deliver agents into the tumor site through a controlled manner, which can greatly reduce the drug dose, thus sparing the off-target toxicity.^[14] However, the clinical translation of local therapy is still impeded by many well-known challenges: i) short retention time of therapeutic agents,^[7] ii) poor uptake of anticancer therapies by drug-resistant tumor cells, and iii) difficulty in realizing responsive multi-modal therapy. Therefore, to prepare a tumor receptor targetable formulation with adjustable *in situ* biodegradability and multi-modal combination treatment capabilities, through minimally invasive injection, is of great significance.

Gold nanorods (AuNRs) with tunable localized surface plasmon resonance (SPR) is widely used in the development of near infrared (NIR) responsive cell imaging and theranostic platforms.^[15,16] The locally generated heat by NIR laser irradiation can not only achieve hyperthermia treatment, but also promote drug release and chemotherapy sensitization.^[17] Moreover, AuNRs can also achieve anti-tumor angiogenesis effect by targeting endothelial cell division process and disrupt cytokinesis through disturbing actin monomers assembly.^[18,19] However, bare AuNRs have several limitations in drug delivery, including 1) low drug loading capacity due to low surface area; 2) ease of aggregation and loss of deep-tissue response, since the NIR response window is very sensitive on the AuNRs size, and the growth in size will shift the NIR response window to the visible spectral region; 3) poor targeting and permeability due to limited possibilities to introduce targeting ligands on the surface. In order to overcome these defects, mesoporous silica with large surface area and flexibility in surface modification, is introduced to coat the AuNRs, to guarantee high drug loading capacity, protection of the AuNRs from aggregation, and enabling of ample surface functionalization possibilities with tumor targeting ligands.^[20,21] In this study, alendronate (ALN) is chosen for osteosarcoma targeting, introduced to the surface of AuNR@SiO₂ through EDC/sulfo-NHS coupling reaction (Scheme 1A). Therefore, the AuNR@SiO₂ core-shell nanosystem can realize effective anti-cancer drug loading, stable photothermal response, as well as enable the receptor-mediated endocytosis of cancer cells. Nevertheless, due to the small size, the AuNR@SiO₂ nanosystem does not have long-term retaining capability in tumor after local injection.

Hydrogels, on the other hand, with great *in situ* retention ability have been extensively studied as a non-toxic, non-immunogenic platform for tissue engineering and had been widely used for local therapy.^[22–24] GelMA hydrogel scaffold, fabricated by UV irradiating photo-initiator contained methacrylic anhydride (MA) conjugated gelatin, shows excellent biomechanical properties for extracellular matrix mimicking and high payload of hydrophilic therapeutic agents.

However, since GelMA based scaffolds are often used for cell-laden tissue engineering in bulk conditions,^[25,26] their injectability and degradation capabilities for local injection need to be further optimized.^[27,28] For example, to tightly host the drugs, the GelMA hydrogel must be dense, but if it is too dense, it is very difficult to inject. Furthermore, through traditional shearing, the injectability of GelMA can be improved,

but the therapeutic agents loaded inside will also suffer huge leaking. In light of this, AuNR@SiO₂-ALN NPs are sealed into monodisperse photocrosslinkable GelMA microgel by using a high-resolution controllable microfluidics technology. Through microfluidic technology, monodisperse microgels (abbreviated as NPs@GelMA) with different volumes and different degradation rates can be fabricated. The injectability can be greatly improved since the dense microgels can be dispersed in injection buffer for peritumoral injection (peritumoral injection). Moreover, coupled with the photothermal response and receptor-mediated targeting ability of the nanoparticles, the drug release and enhanced tumor cell uptake can be precisely controlled by the NPs@GelMA system.

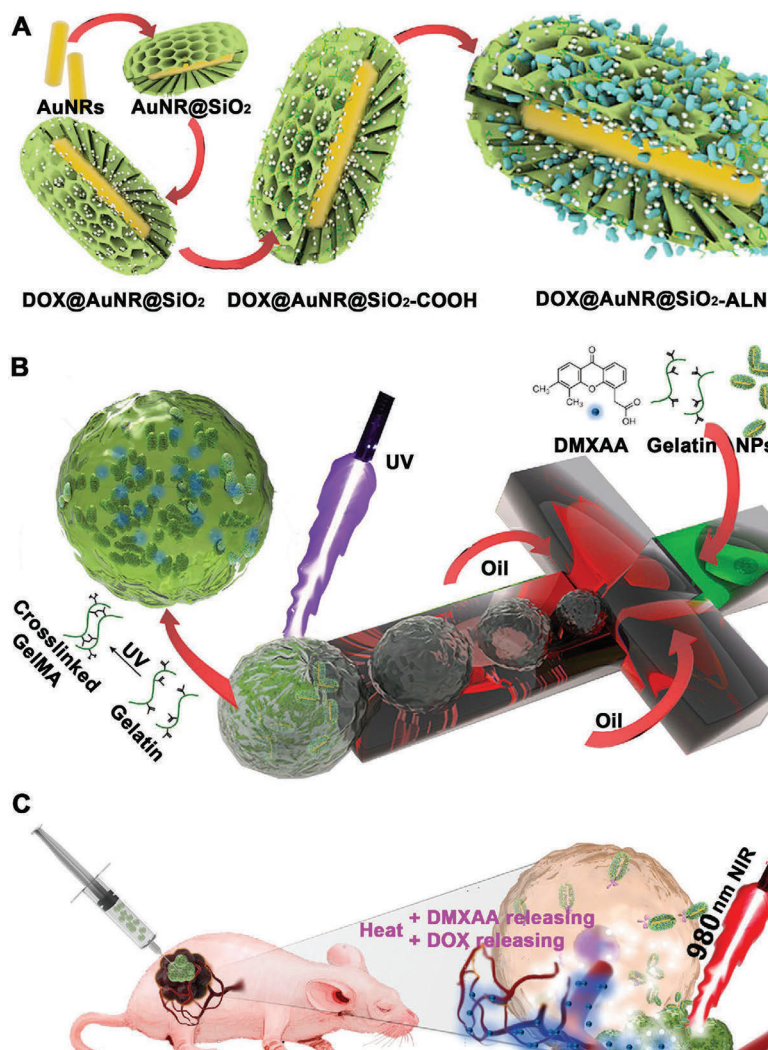
In this work, doxorubicin (DOX) and 5,6-dimethylxanthenone-4-acetic acid (DMXAA) were selected as model drugs to be loaded into AuNR@SiO₂-ALN NPs (NPs/DOX) and GelMA (GelMA/DMXAA) microgels, respectively. As an anthracycline anticancer drug, DOX is widely used because of its autofluorescence, which facilitates the detection of its *in vitro* and *in vivo* distribution.^[9] DMXAA, as a new type of small molecule vascular inhibitor in current clinical trials, can destroy the tumor vascular endothelial cells, cut off the tumor's oxygen and nutrient supply and prevent tumor metastasis.^[29] Combining these two different mechanisms, and the photothermal responsiveness of AuNRs, we anticipated to achieve chemo-antiangiogenesis-photothermal synergistic therapy for osteosarcoma treatment (Scheme 1B,C).

Consequently, the morphology, thermal conversion ability, and cell targeting ability of the nanoparticles were thoroughly studied in detail. The degradability of NPs/DOX@GelMA/DMXAA hydrogel with different volumes under 980 nm NIR laser irradiation was also investigated. The chemo-antiangiogenesis-photothermal combination therapeutic effect of this nanocomposite microgel, as well as biosafety of the NPs/DOX@GelMA/DMXAA system, are explored with osteosarcoma cells *in vitro* and osteosarcoma bearing mice *in vivo* through IV or peritumoral (PT) administration.

2. Results and Discussion

2.1. Synthesis and Characterization of Nanoparticles DOX@AuNR@SiO₂-ALN

Au nanorods with aspect ratio of ≈ 5 and average dimensions around 61 nm \times 12 nm were first synthesized according to a published procedure^[30] and then SiO₂ with a homogenous thickness of ≈ 11 nm was wrapped around the surface for DOX loading and ALN surface modification, as determined by transmission electron microscopy (TEM) (Scheme 1A; Figure S1, Supporting Information). The UV-vis absorption spectra showed that AuNRs had a longitudinal SPR peak at 849 nm and exhibited a red-shift to 889 after SiO₂ coating. A further red-shift to 917 was observed when DOX was loaded into the pores of SiO₂. (Figure S2A, Supporting Information) The TEM imaging and elemental mapping together showed that after SiO₂ coating, a mesoporous layer was formed on the surface of the AuNRs (Figure 1a–f). Subsequently, after drug loading and ALN surface decoration, the surface pores turned blurry (Figure 1c). In



Scheme 1. A) Fabrication of DOX@AuNR@SiO₂-ALN NPs. B) Fabrication of NPs /DOX/GelMA/DMXAA microgel. C) Nano-composite micro-gel with long-term therapeutic property controlled by repeatedly near-infrared-triggered release and combined with chemo-photothermal synergistic therapy.

addition, Fourier transform IR was implemented to verify the binding ability between ALN and NPs. After surface modification, we found that there is a new peak formed at 1633 cm⁻¹, which attribute to the C=O stretching of the new amide bond (Figure S3, Supporting Information). This result proved the effective combination of ALN with AuNR@SiO₂.

To investigate the photothermal effect of the NPs/DOX, different concentrations of NPs/DOX (0.25, 0.5, and 1 mg mL⁻¹) were irradiated with constant 980 nm laser (1 W cm⁻²) for 0–300 s (Figure 1g,h) and 0.5 mg mL⁻¹ NPs/DOX were irradiated under different laser powers (0.5, 1, and 1.5 W cm⁻²) for

0–300 s (Figure S4, Supporting Information). The photothermal response of the NPs/DOX exhibited positive correlation to concentration and laser intensity (Figure 1g,h; Figure S4, Supporting Information). With increased concentration of NPs/DOX and laser power intensity, the solution temperature rose rapidly. The temperature increased by 60 °C when 1 mg mL⁻¹ of NPs/DOX was irradiated for 300 s with 1 W cm⁻² laser intensity (Figure 1g,h), while pure water exhibited almost no temperature change under laser irradiation with the same intensity.

Moreover, the photostability and photothermal conversion efficiency (η) of NPs/DOX was also studied by conducting three

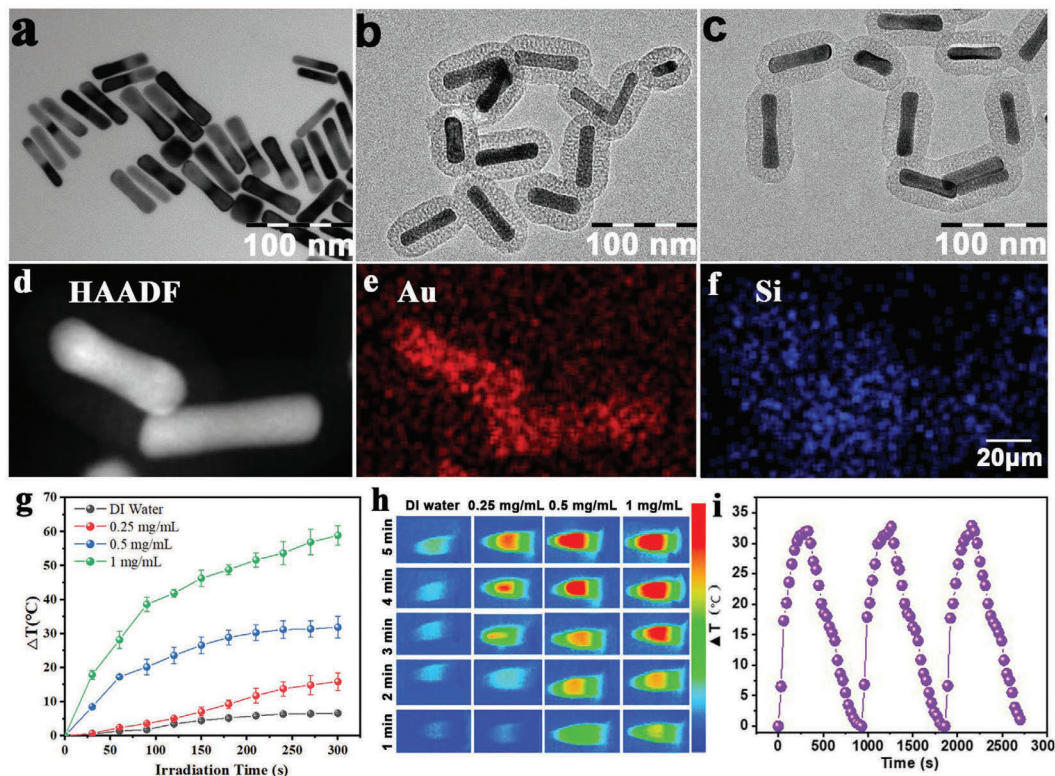


Figure 1. Characterization of nanoparticle morphology and photothermal effect. a–c) TEM of AuNRs, AuNR@SiO₂ NPs, and DOX@AuNR@SiO₂-ALN NPs. d–f) The high-angle annular dark-field imaging and elemental mapping of AuNR@SiO₂ NPs. g) Photothermal heating curves of DI water and AuNR@SiO₂ NPs with different nanoparticle concentrations (0.25, 0.5, and 1 mg mL^{−1}) under 1.0 W cm^{−2}, 980 nm laser irradiation. h) The infrared thermal images of DI water and AuNR@SiO₂ NPs (0.5 mg mL^{−1}) over three times of NIR on–off irradiated cycles (1.0 W cm^{−2}, 980 nm).

heating–cooling cycles (Figure 1i) whereby the photothermal conversion efficiency of NPs/DOX was calculated as 27% from the heating–cooling curves. (Figure 1i; Figure S5, Supporting Information) The (η) was calculated based on Equations (1) and (2):^[31]

$$\eta = \frac{hs\Delta T_{\max} - Q}{I(1 - 10^{-A_{980}})} \quad (1)$$

Here, ΔT_{\max} is the maximum value of temperature change, Q is the heat increase of the solvent, and I is the power of the laser. A_{980} is the absorbance of the NPs/DOX at the wavelength of 980 nm, while hs can be calculated by another formula:

$$hs = \frac{mc}{\tau} \quad (2)$$

Here, c and m are the specific heat capacity and mass of the solution, respectively. τ is the slope of the fitted line of t to $-\ln \frac{\Delta T}{\Delta T_{\max}}$.

Subsequently, Brunauer–Emmett–Teller analysis gave the nitrogen adsorption–desorption isotherms and pore size distribution curves of AuNRs@SiO₂. The pore size was mainly distributed in 2.3 nm, and the specific surface area was as high as 308 m² g^{−1} (Figure S6, Supporting Information). These results indicated that the nanoparticles possessed sufficient size and space for drug loading. The loading content (LC) of DOX in AuNRs@SiO₂ was 30.0 ± 6.7%, as quantified by UV–vis absorption at 490 nm (Table S1, Figure S2B, Supporting Information). For studying the drug release, the light-controlled drug release effect of NPs/DOX was confirmed by three times of NIR on–off irradiated cycles (Figure S7, Supporting Information), since the generated heat by PTT will weaken the interaction between DOX and silica. The releasing profiles showed that when laser was applied, a burst release (29.8%) at first 5 min irradiation was observed, then 20.8% and 21.1% DOX releasing was founded at second and third round of irradiation. While, without laser irradiation, only 10% of DOX released from the AuNRs@SiO₂ after 6 h. These results proved that DOX@AuNR@SiO₂-ALN NPs possessed great PTT effect and had NIR triggered drug releasing ability.

Finally, we investigated the size distribution of AuNR@SiO₂, DOX@AuNR@SiO₂, and DOX@AuNR@SiO₂-ALN NPs, as well as the dispersibility and stability of AuNR@SiO₂ NPs in the PBS buffer and Milli-Q water. The results shown that the NPs exhibited very good dispersibility in Milli-Q water, with size of 120.2 ± 17.5, 122.3 ± 10.9, and 130.7 ± 18.5 nm for AuNR@SiO₂, DOX@AuNR@SiO₂, and DOX@AuNR@SiO₂-ALN, respectively; however, the size increased to 354.5 ± 76.5, 357.5 ± 68.5, and 374.3 ± 52.4 nm in PBS, as shown in Figure S8, Supporting Information. In addition, long-term stability studies have shown that Au@MSN nanoparticles gradually aggregated in PBS buffer. After 7 days of incubation, the TEM results proved the degradability of the NPs under PBS buffer, while the NPs removed unchanged in Milli-Q water (Figure S9A,B, Supporting Information). In our designed microgel reservoir system, the NPs were loaded into the microgel in Milli-Q water, therefore this can protect the NPs from aggregation and significantly improve the NPs' bioavailability.

2.2. Synthesis and Characterization of NPs/DOX@GelMA/DMXAA Microgel

Gelatin methacrylate, as a photocrosslinkable hydrogel has been widely studied as cell scaffolds and wearable devices due to its excellent biocompatibility.^[32,33] Cells and drugs can be loaded into the GelMA solution before UV curing, or absorbed by the surface (microscale) and internal (nanoscale) pores of crosslinked GelMA hydrogel. However, for bulk GelMA hydrogel it has been challenging to achieve adjustable in situ degradability and shown to be difficult to be applied in minimally invasive applications. Therefore, herein we utilized microfluidic technology to prepare different sizes of injectable GelMA microgels that can not only achieve different degradability profiles, but also retain bulk gel properties. First, by controlling the flow rate of the internal phase (GelMA, photo-initiator) and external phase (mineral oil, Span 80) in microfluidics, we can easily fabricate monodisperse microspheres with particle size of 265 ± 20, 160 ± 24, and 50 ± 15 µm (aqueous:oil = 1:1, 1:2, and 1:3, respectively) (Figure 2a). Then, the nanohybrid microspheres were collected and crosslinked by UV (20 mW cm⁻² d⁻¹, 480 nm) for 20 s.

Subsequently, the degradation rate of nano-hybrid microgels was investigated from three aspects, including the size of the microgel, the LC of NPs/DOX and DMXAA, as well as the laser induced light-triggered degradation. It has been reported that the mechanical strength of GelMA hydrogel increases with mesoporous silica or gold nanorod incorporation since the internal porosity will decrease, thereby prolonging its degradation and drug release time.^[34] Moreover, since the microgels still retained bulk gel properties and the crosslinking ability of GelMA solution will not change due to the different crosslinking shape and size, the bulk hydrogel was used to simulate the microgel and investigate the best LC of NPs/DOX and DMXAA.

In this work, we can easily prepare GelMA hydrogels with different concentrations of NPs/DOX and DMXAA (Figure 2b). The NPs contained 30% of DOX, and we fixed DOX to DMXAA ratio to 1:3 to maximize the synergistic effect, according to the

previous article.^[9,29] We found that the GelMA hydrogel could resist increased crushing force by loading 5 mg mL⁻¹ NPs/DOX and 4.5 mg mL⁻¹ DMXAA, and the resistance further increased to 125 ± 11 g crushing force by loading 10 mg mL⁻¹ of NPs/DOX and 9 mg mL⁻¹ DMXAA. However, the GelMA hydrogel completely lost the resistance of crushing force when 15 mg mL⁻¹ of NPs/DOX and 13.5 mg mL⁻¹ DMXAA were loaded, since large amount of NPs/DOX and DMXAA destroyed the basic skeleton of GelMA hydrogel and the GelMA could not crosslink to a stable structure (Figure 2b). Based on these results, 10 mg mL⁻¹ NPs/DOX (3 mg mL⁻¹ DOX) together with 9 mg mL⁻¹ DMXAA were chosen and loaded into GelMA to fabricate the NPs/DOX@GelMA/DMXAA microgel with different sizes through microfluidics (Figure 2c).

We then used confocal to evaluate the NPs' distribution in the microgel. First we chemically conjugated Cy5.5-NHS to the surface of the AuNR@MSN-NH₂ NPs to prevent the dye releasing. By ultrasonic cleaning, we cleaned the free dye which adsorbed inside the nanoparticle pores. Then we added small amount of FITC inside the gel-NPs solution as the internal phase for the microfluidics. When preparing microgel spheres by microfluidic technology, in order to prevent the fusion of droplets, span 80 was added as a surfactant, which extracted FITC to the outer layer of the microgel. By merging the two types of fluorescence together, we could visually see the distribution of fluorescent nanoparticles inside the microgel. The FITC formed a green halo to exhibit the microgel. The Cy5.5 conjugated NPs distributed evenly inside the microgel (Figure 2d).

Subsequently, the degradation curves of different sizes of NPs/DOX@GelMA/DMXAA microgels prepared under different aqueous:oil flow rates (1:1, 1:2, and 1:3) were monitored (Figure 2e). We found that during the initial 6 days of laser-free incubation, the hydrogel showed 7 ± 2.4% degradation for the 1:1 group. However, for 1:2 and 1:3 groups, there were 13 ± 1.8% and 37 ± 3% of the mass lost within 6 days, respectively, which suggested that the degradation rate of the microgel will gradually extend as the microgel size increased and the surface area decreased. Moreover, after irradiated by 980 nm laser (1 W cm⁻²) for 10 min on the 6th and 12th day, the results showed that the three groups all exhibited multiple rounds of light-induced accelerated degradation, while the degradation time of the 1:1 group was longer than the other groups and up to 24 days, which may satisfy the long-term treatment purpose. Therefore, we chose 1:1 as the optimal flow rate to prepare a microgel with a particle size of around 265 µm.

Later, the NPs/DOX@GelMA/DMXAA microgel was freeze dried and observed under a fluorescent confocal microscope. The results showed that the microgel exhibited a uniform size, and there were abundant pores on the surface, which facilitated the media exchange between microgels and tumor microenvironment in vivo (Figure 2f,g). Furthermore, DOX and DMXAA release profiles were also calculated by UV absorbance at 490 and 350 nm (Figure 2h; Figure S2B, Supporting Information). After irradiation by 980 nm laser (1 W cm⁻²) for 10 min on the 6th and 12th day, accelerated release of DOX and DMXAA was found. Meanwhile, 90 ± 4% of DMXAA and 74 ± 5% of DOX were released during 24 days. These results proved that the NPs/DOX@GelMA/DMXAA microgel system possessed great

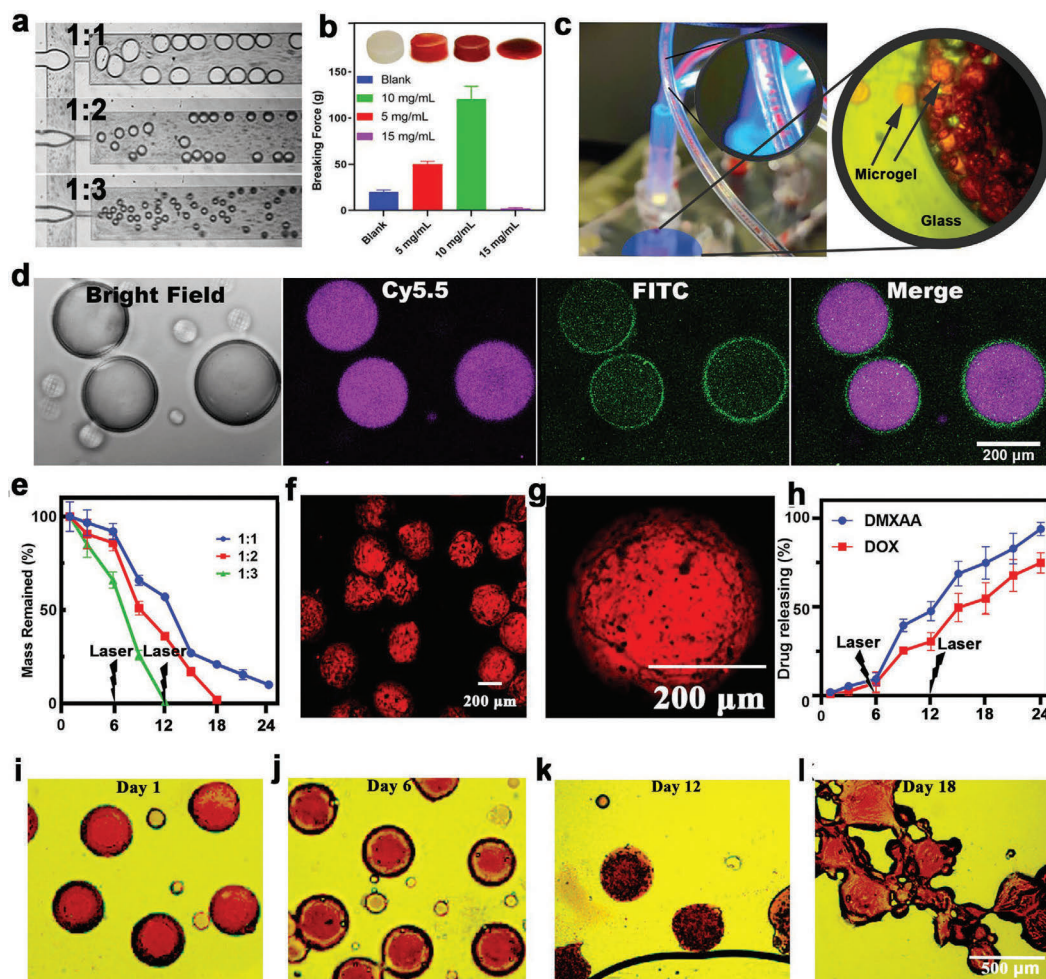


Figure 2. Characterization of microgel morphology. a) The microscope images of microgels within microfluidic chips under different aqueous:oil flow rates (1:1, 1:2, and 1:3). b) Photos and breaking forces of GelMA hydrogel which bearing different concentrations of NPs/DOX and DMXAA loaded microgels within microfluidic outlet tube and enriched in the reservoir. c) Co-localization test of nanoparticles and hydrogel. d) Bright field and fluorescence images of microgels. e) The degradation curve of NPs/DOX@GelMA/DMXAA microgel under different aqueous:oil flow rates (1:1, 1:2, and 1:3). f, g) Fluorescence microscope image of dispersed freeze-dried NPs/DOX and DMXAA loaded microgels and the mono-microgel. h) The accumulated drug releasing of DMXAA and DOX of microgel which fabricated under 1:1 aqueous:oil flow ratio. i–l) Fluorescence images of the NPs/DOX@GelMA/DMXAA over three weeks under different time-point NIR irradiation.

light-controlled drug release ability and long-term degradability. In addition, fluorescence microscopy was also used to observe the morphology of microgel on the 1st, 6th, 9th, and 18th day. As shown in Figure 2i–l, the shape of the red microgel hardly changed in the first 6 days, but after the laser irradiation on the 6th day, we observed significantly different phenomena on the 12th day. First, the drug was released in a burst fashion between the 6th and the 12th day (Figure S10A, Supporting Information). Second, the flattened surface of the microgel (Figure 2i;

Figure S10B, Supporting Information) became uneven on the 12th day, showing dense pores on the surface (Figure 2k; Figure S10C, Supporting Information). These pores may be induced by the heat-triggered GelMA degradation that was produced by nanoparticles inside the microgel. Therefore, these results once again confirmed this nano-hybrid microgel system possessed long-term controllability of precision photothermal therapy and accurate NIR-triggered drug release capability from the macroscopic morphology aspect.

2.3. Targeting and Cytotoxicity Evaluation of NPs/DOX and NPs/DOX@GelMA/DMXAA Microgel on Osteosarcoma Cells

In order to evaluate the therapeutic ability of the nanocomposite microgel in vitro, the targeting ability and tumor cell toxicity of the NPs/DOX, as well as the tumor cell suppression capacity of NPs/DOX@GelMA/DMXAA microgel were carried out through fluorescence microscopy imaging and CCK-8 experiments. First, the confocal laser scanning microscopy (CLSM) images showed that after the ALN modification, DOX@AuRN@SiO₂-ALN group exhibited much higher uptake efficiency compared with the undecorated DOX@AuRN@SiO₂ group, as shown in **Figure 3a**. Moreover, after laser irradiation, we found more drugs can penetrate into the nuclear space, while within the laser-absent group, the NPs/DOX can only accumulate surrounding the nucleus, which means a lesser degree of drug released, since the DOX will enter the nucleus to exert its effects (**Figure 3a**). These phenomena proved that the DOX@AuRN@SiO₂-ALN NPs not only had great uptake ability, but also held excellent NIR sensitivity.

Later, CCK-8 based cytotoxicity was conducted. From the results we can see that the laser induction group demonstrated stronger tumor killing ability when the DOX concentration exceeded 1 $\mu\text{g mL}^{-1}$ (**Figure 3b**). Then, with the DOX concentration of 10 $\mu\text{g mL}^{-1}$, more than 85% of the cells was inhibited in the DOX@AuRN@SiO₂-ALN +Laser group, which was more effective than the pure DOX and DOX@AuRN@SiO₂ +Laser groups. The results suggested that the ALN modified NPs/DOX system possessed the greatest tumor inhibiting ability, which was contributed to by the laser-triggered PTT effect and the ALN receptor mediated enhanced uptake.

Subsequently, through a live/dead cell staining experiment, we studied the cytotoxicity of NPs/DOX and DMXAA dual loaded microgel systems. From **Figure 3c** we can see that for control and NPs/DOX@GelMA/DMXAA -Laser group, there were negligible dead (red) cells exist after 24 h incubation, which showed less toxicity than pure DOX group. However, after these microgels were laser irradiated, almost all MNNG/HOS osteosarcoma cells died within 24 h. Also, from the local irradiation results, we can clearly see that cells can only be killed where the laser hit (**Figure S11**, Supporting Information). These results confirmed that this microgel system possessed great safety unless it had been triggered by NIR laser. Finally, flow cytometry was also used for the detection of the cell apoptosis of each group. The results showed that NPs/DOX@GelMA/DMXAA +Laser group exhibited the highest number of apoptotic cells (21.5% dead and 15.7% late-apoptotic cells) (**Figure 3d**), and showed the best therapeutic effect that corresponded with the dead/live experiment.

2.4. Tumor Vascular Disruption

Tumor angiogenesis is a hallmark feature of solid tumors. During tumor growth, a large number of new blood vessels can not only provide nutrients and remove waste from the tumor, but also provide a transport pathway for the distant metastasis of the tumor. Therefore, to complement the current chemotherapy, it is important to develop new methods to effectively

inhibit tumor angiogenesis. DMXAA, as one of the typical small molecule vascular disrupting agents can selectively target tumor vascular endothelium and destroy tumor blood vessels, and has been widely applied for clinic research.^[29] Moreover, nonlethal heat treatment of vascular endothelial cells can also inhibit the expression of adhesion molecules and may inhibit tumor growth by interfering with vascular supply.^[18] Consequently, in this experiment, while using the AuNRs to achieve PTT, DMXAA was also added to the microgel to achieve a dual effect of inhibiting blood vessels.

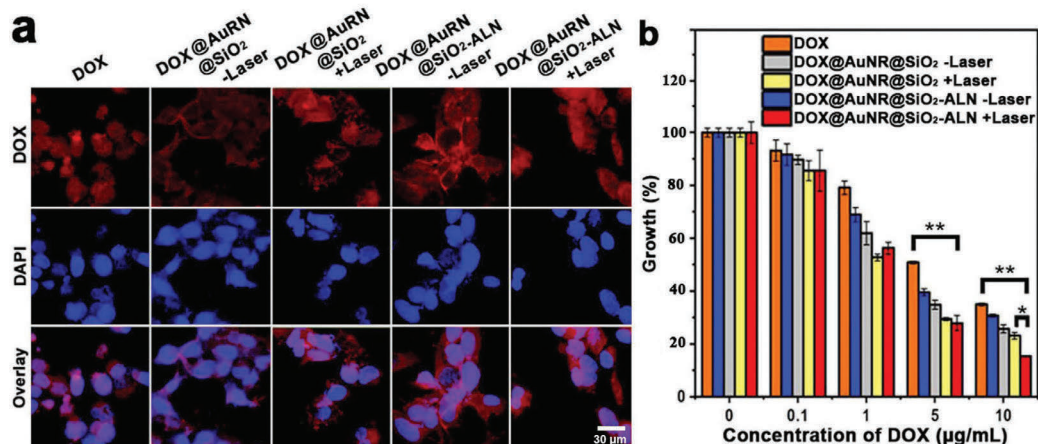
In the first step of studying the laser-induced inhibition of capillary formation, we used MNNG/HOS cell conditioned medium to stimulate the human umbilical vein endothelial cells (HUVEC), since the inflammatory factors in the tumor microenvironment can promote angiogenesis effect and affect the results of subsequent inhibition experiments.^[18] Then, different groups including: Control; NPs/DOX -Laser; NPs/DOX +Laser; NPs/DOX@GelMA/DMXAA -Laser; and NPs/DOX@GelMA/DMXAA +Laser group were tested for their antiangiogenic ability. The results showed that for each drug delivery system, the anti-capillary effect can be achieved only after laser was used (**Figure 4a**). Moreover, the NPs/DOX@GelMA/DMXAA +Laser group showed more inhibitability than pure NPs/DOX group which due to the synergistic therapy of both PTT and DMXAA vascular disturbing effect (**Figure 4a**). Furthermore, we also analyzed three major parameters through NIH ImageJ analysis:^[35] number of junctions (red spot), number of meshes (blue circle) and total length (yellow lines) of in vitro angiogenesis, as shown in **Figure 4b–d**. These three indicators can reflect the vigorous degree of angiogenesis. The more junctions and meshes and the longer the total length, the more vigorous blood vessels grow. Hence, from these results, we can see that for NPs/DOX@GelMA/DMXAA groups, the number of junctions decreased ten times after laser was used (**Figure 4b**), which confirmed near-infrared responsive vascular inhibition. Moreover, the number of meshes and total length results showed that NPs/DOX@GelMA/DMXAA +Laser group had less meshes (zero mesh) (**Figure 4c**) and 10% shorter length than NPs/DOX +Laser group (**Figure 4d**), which again proved the synergistic therapy of both PTT and DMXAA vascular disturbing effect.

2.5. Biodistribution of NPs/DOX and DOX Retention Ability In Vivo

Tumor-bearing mice were constructed by subcutaneous injection of MNNG/HOS cells for investigating the PTT effects of the formulation and drug distribution. It was found that after PT, the PTT effect of NPs/DOX@GelMA/DMXAA (PT) group was much higher than the PBS (PT) group and NPs/DOX (IV) group (**Figure 5a,b**; **Figure S12a,b**, Supporting Information). After 10 min irradiation of 980 nm laser (1 W cm⁻²), both of the NPs/DOX (IV) and NPs/DOX@GelMA/DMXAA (PT) group can be heated above 42 °C, where the cancer cells can be effectively killed.

Afterward, the fate of each formulation was examined through in vivo and in vitro fluorescence imaging experiments. Normally, the targeting efficiency of targeted formulations

Evaluation of the targeting ability and cytotoxicity of NPs on MNNG/HOS osteosarcoma cells



Cytotoxicity assess of NPs-hybridized microgel on MNNG/HOS osteosarcoma cells

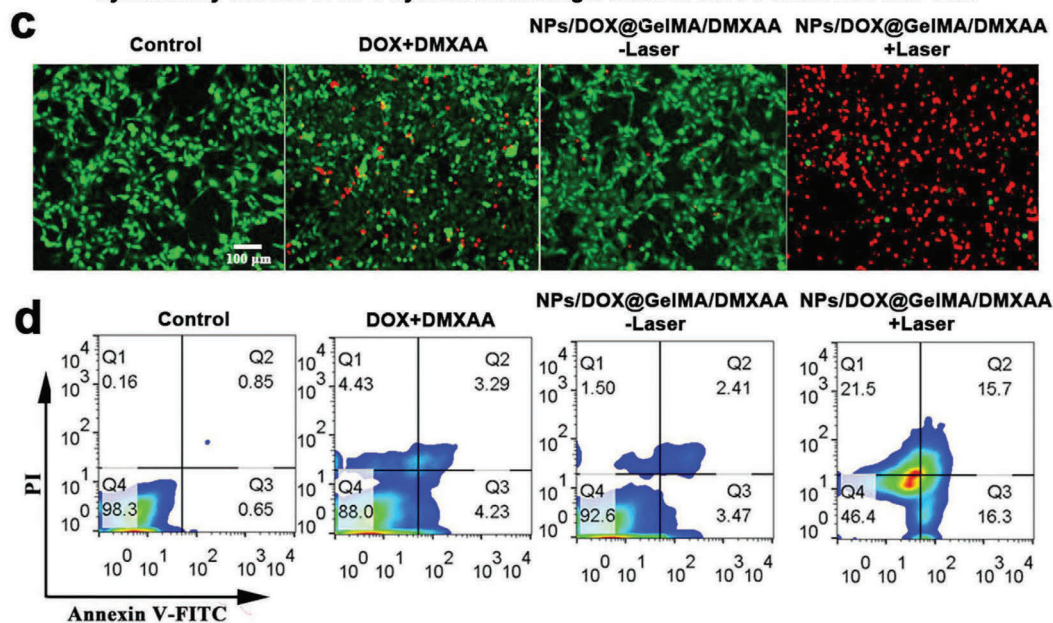


Figure 3. In vitro cell viability of osteosarcoma Silicatecells MNNG/HOS. a,b) The cell uptake experiments and CCK-8 cell toxicity assessment. c) Fluorescence microscope images of the live/dead cell staining assay of control, DOX+DMXAA, and NPs/DOX@GelMA/DMXAA (with or without laser) microgel groups. d) Flow cytometric apoptosis analysis of tumor cells under Annexin V-FITC/PI stained ($n = 3$, $^*p < 0.05$ and $^{**}p < 0.01$).

designed through the EPR effect will not exceed 5%.^[36] Thus, in order to prove that the delivery efficiency of PT injection is much higher than that of IV administration, 1 mg kg⁻¹ DOX and 3 mg kg⁻¹ DMXAA were delivered, which only 20% of

the doses relative to IV administration.^[9,29] Obviously, after reducing the dosage, the NPs/DOX (IV) group showed only little fluorescences gathered around the tumor (Figure S12c, Supporting Information). Then for pure DOX (PT) group, DOX

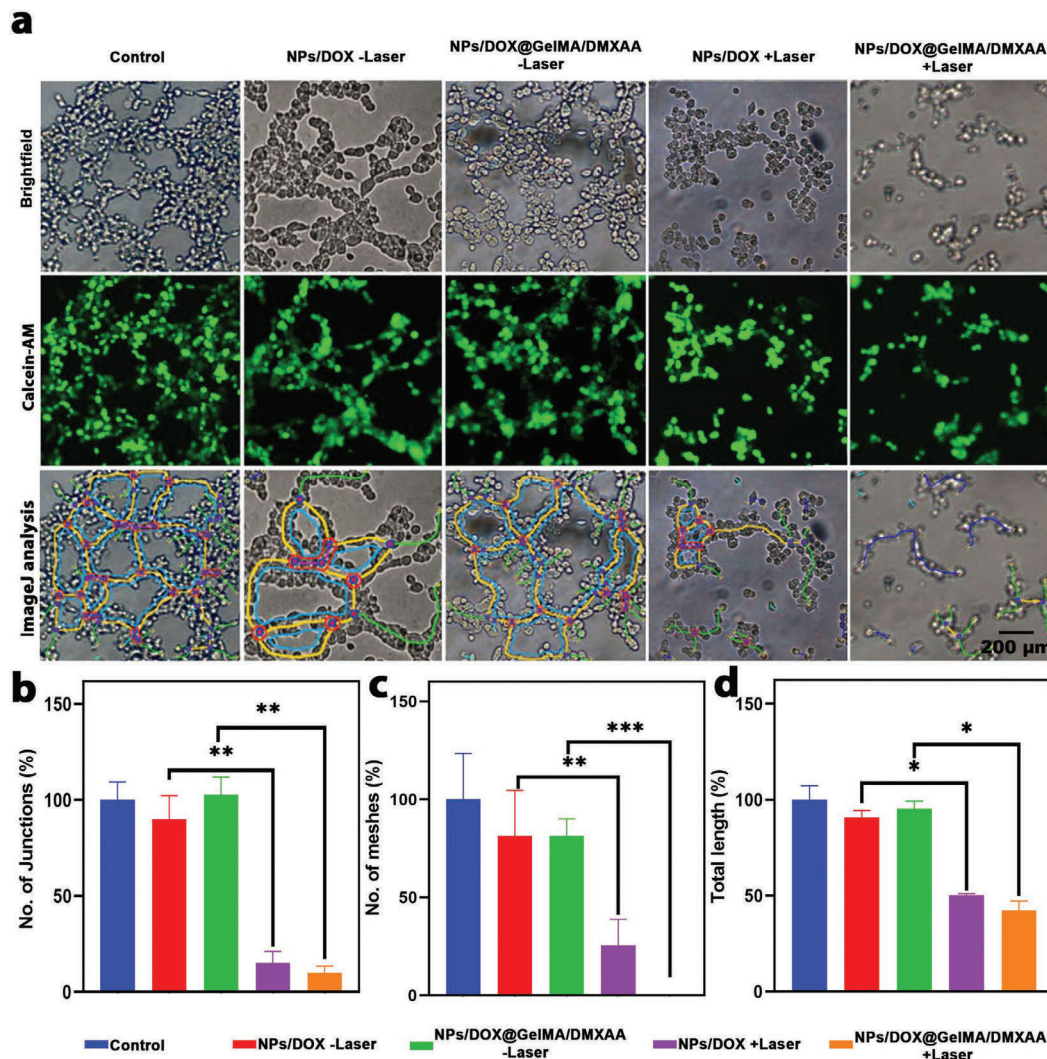


Figure 4. The inhibition experiments of angiogenesis. a) Tube formation effect of HUVEC and angiogenesis analyze results from ImageJ software for Control, NPs/DOX, NPs/DOX@GelMA/DMXAA, NPs/DOX +Laser, and NPs/DOX@GelMA/DMXAA +Laser groups, respectively (all scale bar equal to 200 μ m). b–d) Comparison of number of junction, meshes, and total length between different groups by using ImageJ plugins Angiogenesis Analyze ($n = 3$, * $p < 0.05$, ** $p < 0.01$, and *** $p < 0.001$).

was more likely to spread to the surrounding tissues rather than inside the solid tumor (Figure 5c). Furthermore, the DOX within both NPs/DOX (IV) and DOX (PT) groups only stayed in the body for a short time and were basically eliminated by metabolism in 3 days. Therefore, in the cases of simple intratumoral injection of drugs or 1/5 dose of NPs/DOX tail vein injection, the drugs cannot effectively enter the tumor site.

By contrast, for NPs/DOX@GelMA/DMXAA group, we can see that without laser irradiation, the hydrogel was kept

at the tumor site and remained unchanged for half a month (Figure 5c). However, after 10 min of laser irradiation every three days, we found DOX had spread into the tumor. The fluorescence intensity of tumor in NPs/DOX@GelMA/DMXAA (PT) group was 5.8-folds higher than DOX (PT) group and DOX/NPs group (Figure 5d,e; Figure S12d,e, Supporting Information). These results proved the excellent drug delivery efficiency, sensitive near-infrared responsive drug release ability, and the tumor-enhancing phagocytosis of the nanoparticle-loaded microgels.

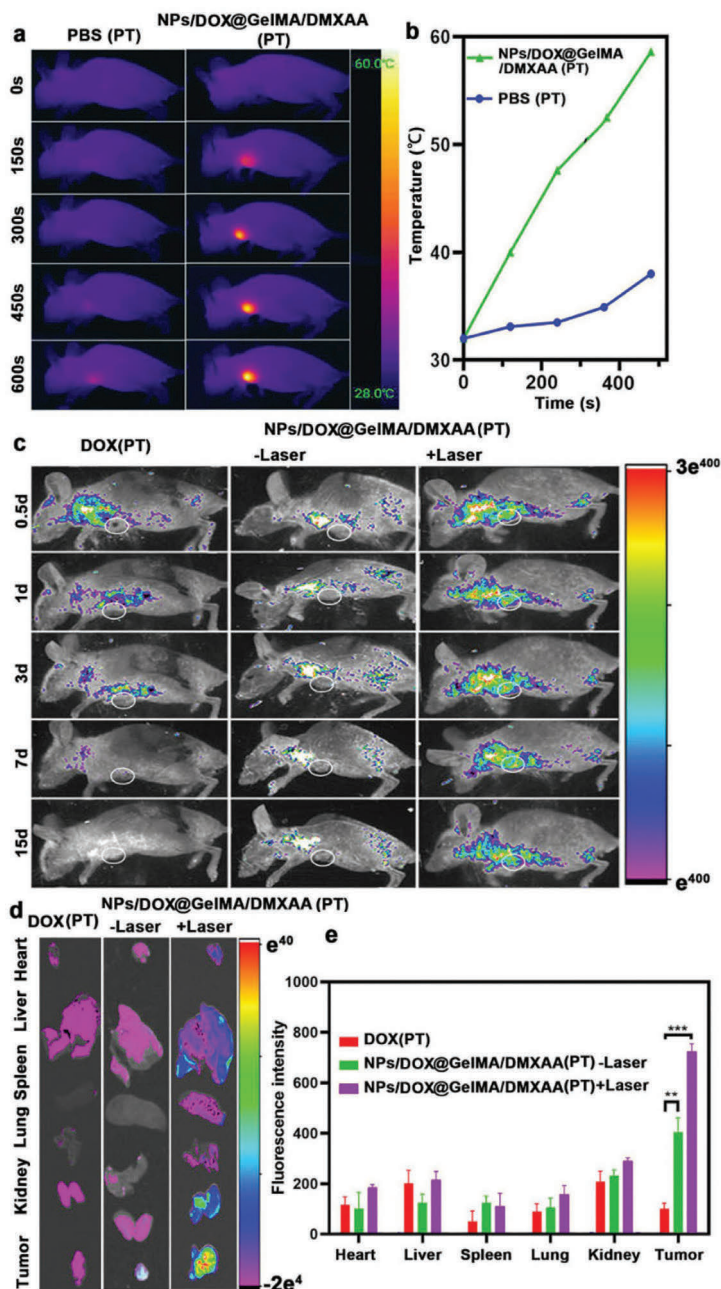


Figure 5. Thermal imaging photos of tumor bearing mice and the in vivo and in vitro doxorubicin biodistribution. a) Infrared thermal images of the tumor bearing mice at each time point while the tumor was continually irradiated by the 980 nm laser (1 W cm^{-2}) for 10 min. b) Time–temperature curve of the tumors from the mice after peritumoral (PBS, NPs/DOX@GelMA/DMXAA microgel) injection. c,d) In vivo and in vitro NIRF imaging of DOX fluorescence. e) Fluorescence intensity of DOX within different organs ($n = 3$, $^*p < 0.05$ and $^{***}p < 0.001$).

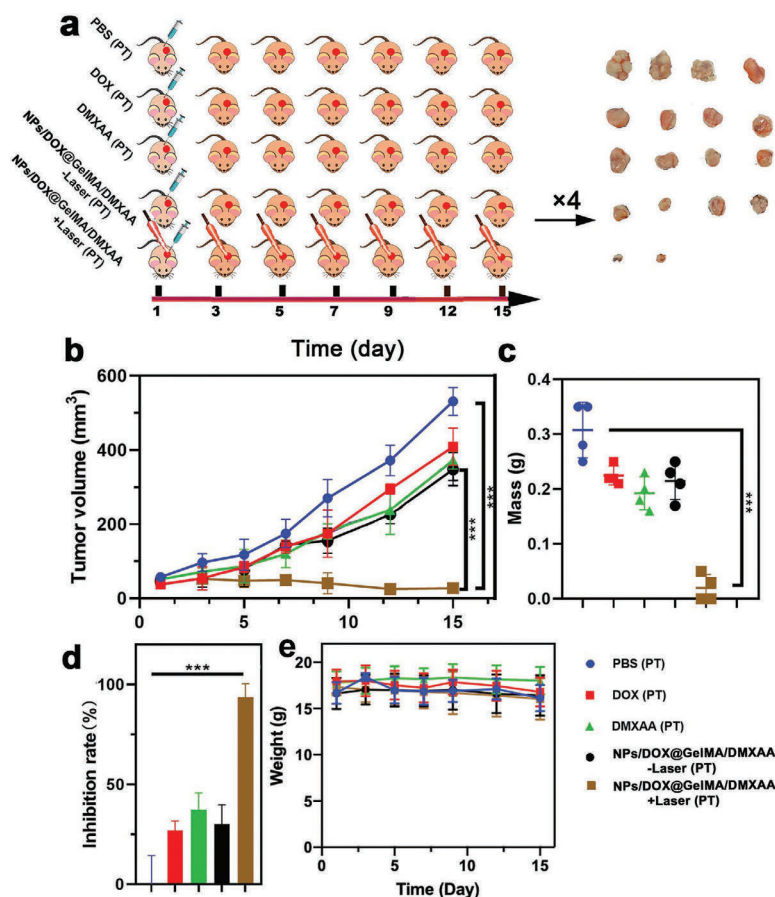


Figure 6. Treatments of tumors after peritumoral administration. a) Schematic diagram of the experimental design and the extracted tumor photos after the treatment. b) Tumor volume changes during the 15 days therapy. c) Mass of extracted tumors of different groups on 15th day. d) Tumor inhibition rates of different groups at 15th day. e) Body weight changes during 15 days therapy. ($n = 4$, ** $p < 0.01$ and *** $p < 0.001$).

2.6. In Vivo Tumor Inhibition Efficiency and Biosafety of Different Formulations

Encouraged by the gratifying tumor penetration ability of the nanocomposite microgel in vivo, we further verified the tumor inhibition capacity of different preparations, through seven groups of MNNG/HOS osteosarcoma xenograft tumor-bearing mice. For +Laser groups, the 980 nm laser (1 W cm^{-2}) was used for 10 min irradiation per time and carried out every three days. According to the extracted tumor photos and tumor growth curve, we found the NPs/DOX@GelMA/DMXAA +Laser (PT) group had the best therapeutic effect and the tumor volume gradually reduced until disappeared (Figure 6a,b; Figure S13a,b, Supporting Information). Meantime, the tumor weight results also showed that the microgel +Laser group had the lowest tumor weight (Figure 6c; Figure S13c, Supporting Information).

Moreover, the tumor inhibition rate (IR) was calculated by the following equation:

$$IR(\%) = (1 - T_{wt}/T_{wc}) \times 100 \quad (3)$$

where T_{wt} and T_{wc} are the mean tumor weight of treated and control groups, and the tumor suppression rate of the NPs/DOX@GelMA/DMXAA +Laser (PT) group was $94.5 \pm 5.5\%$ (Figure 6d). These results together implicated that the microgel system possessed strongest tumor growth inhibitory ability, which contributed by the long-term multi-round realization of precision chemo-antiangiogenesis-photothermal synergistic therapy and osteosarcoma cells enhanced uptake of ALN modified NPs/DOX.

Notably, compared with the pure drug and -Laser groups, DMXAA(PT) + NPs/DOX(IV) +Laser group also had a tumor

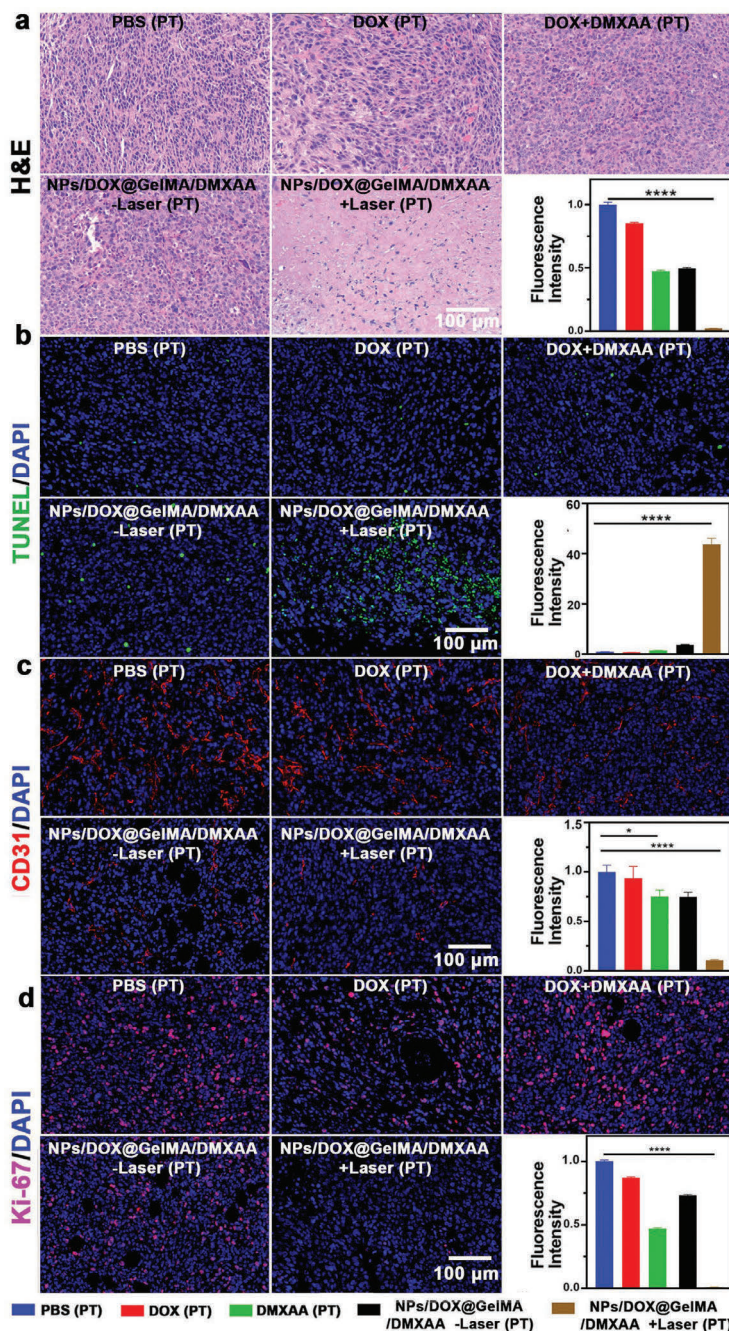


Figure 7. Histological analysis of tumors for different groups after peritumoral administration. a) H&E stained photos. b–d) DLSM imaging of TUNEL, Ki-67, CD31, and DAPI stained tumor sections (all bar equal to 100 μm, * $p < 0.05$, ** $p < 0.01$, *** $p < 0.001$, and **** $p < 0.0001$).

suppression effect, whereas the tumor volume still gradually increased. This was because that NPs/DOX through intravenous delivery had a better effect than the pure drug which is contributed by EPR effect and ALN receptor-mediated tumor cell enhanced uptake. However, when there was only single dose and only 20% of the normal dosage was used, the therapeutic effect was obviously not satisfactory and the tumor *IR* was only $58.5 \pm 7.3\%$ (Figure S13d, Supporting Information).

Moreover, the body weight and different organs (heart, liver, spleen, lung, and kidney) H&E staining picture of the mice were monitored for systemic safety evaluation. From the results, there was no significant difference between different groups about body weight (Figure 6e; Figure S13e, Supporting Information). Also for the H&E imaging, no obvious toxicity was found since the toxicity of high concentration was minimized (Figure S14, Supporting Information).

In order to further validate the tumor apoptosis and the inhibition degree of angiogenesis, the extracted tumor slices were further performed H&E, Ki-67, TUNEL, and CD31 staining for histological analysis. Very obvious nuclear shrinkage and cytosol degradation was found in the H&E stained tumor sections from NPs/DOX@GelMA/DMXAA +Laser group (Figure 7a). This result confirmed that this microgel system had the best tumor killing effect which can severely kill the tumor cells. Notably, several structure damages was also found in the H&E staining results from DMXAA(PT) + NPs/DOX(IV) +Laser group (Figure S15a, Supporting Information). This was because that the NPs/DOX can also kill the tumor cells after intravenous administration, since the NPs/DOX will accumulate in the tumor sites based on the EPR effect as well as possessing PTT and ALN receptor-mediated enhanced uptake at the same time. However, its drug delivery efficiency and retention ability were inferior to NPs/DOX-decorated microgel through peritumoral administration.

Furthermore, in the tumor slices from NPs/DOX@GelMA/DMXAA +Laser group, tremendous TUNEL signal and negligible Ki-67 signal was found, which means more apoptotic cells and less proliferating cells (Figure 7b,c). At the same time, DMXAA(PT) + NPs/DOX(IV) +Laser group also showed a certain degree of therapeutic effect compared with other groups, but its effectiveness was far less than that of NPs/DOX@GelMA/DMXAA +Laser group (Figure S15b,c, Supporting Information). Hence, the results of TUNEL signal and Ki-67 fluorescence were consistent with the results of H&E staining, which proved that the therapeutic effect of the microgel system was much better than that of the NPs group.

Later, CD31, as a typical vascular endothelial cell marker, was used to stain the tumor slices and assess the anti-angiogenesis degree.^[29] We can apparently see the CD31 red signal in the PBS (PT) and DOX (PT) group, which suggested strong tumor angiogenesis (Figure 7d). After DMXAA was peritumorally injected alone by a single dose, the expression of vascular marker CD31 in DMXAA (PT) group was reduced but not significant. However, for NPs/DOX@GelMA/DMXAA +Laser (PT) group, the blood vessels almost disappeared compared with the other groups, which was contributed to by the microgel based long-term multi-round drug release (Figure 7d; Figure S15d, Supporting Information). Therefore, this nanocomposite microgel system can not only achieve strong tumor suppression,

but also reduce blood vessel proliferation and prevent remote tumor metastasis.

3. Conclusion

In summary, with adjustable *in situ* retention and NIR-triggered receptor-mediated targeting ability, an ultra-efficient injectable nanocomposite microgel has been successfully prepared through a facile one-way microfluidic technology for repeated solid tumor chemo-photothermal therapy and angiogenesis inhibition. This novel dual-drug delivery system has demonstrated outstanding triple synergistic therapeutic effects in both *in vitro* and *in vivo* experiments. It is found that through a single administration, multiple rounds of light-controlled treatment can be achieved. Moreover, compared with intravenously administered nanosystems, this microgel can solve the shortcoming of insufficient targeting of NPs/DOX to solid tumors and significantly reduces the drug doses due to the PT regime and ALN mediated enhanced cell uptake. Furthermore, this microgel also possesses gratifying anti-capillary efficiency due to the long-term DMXAA vascular disturbing effect. In general, NPs/DOX@GelMA/DMXAA microgel is a promising drug delivery system for *in situ* administration for the treatment of solid tumors, which can allow a lower dosing regimen without losing the therapeutic effect and is thus promising for the treatment of solid tumors in the future.

4. Experimental Section

Seed@CTAB Preparation and Growth (AuNRs): Seed@CTAB was conducted according to a published protocol.^[30] Seed@CTAB was synthesized in a 30 °C water bath. First, 30 μ L of 50 mM HAuCl₄ solution was added to 5 mL of 0.1 M CTAB solution. After the solution was fully stirred for 5 min, 300 μ L of 10 mM NaBH₄ solution was injected. After that, another solution for NPs/DOX growth was prepared. First, 190 μ L HCl 1 M and 100 μ L HAuCl₄ 50 mM solution were added to 10 mL of 0.1 M CTAB. Adjust the pH to 1.5 by HCl. Then 120 μ L of AgNO₃ containing 10 mM and 100 μ L of ascorbic acid solution (100 mM) were added to the above solution. Finally, 24 μ L of the previously prepared Seeds@CTAB was added to the growth solution, stirred well and let stand at 30 °C for 2 h.

SiO₂ Coating (AuNR@SiO₂): Mesoporous silica coating on AuNRs was carried out according to a published protocol.^[37] The AuNRs prepared above were centrifuged at 15 000 g for 25 min, washed 3 times with Milli-Q water, and finally diluted to 20 mL with water. Then 200 μ L of 0.1 M NaOH solution was added under stirring. Subsequently, every 30 min, 60 μ L of 20% TEOS methanol solution was added to the above solution for a total of 3 times. Finally, the reaction continued for 3 days at room temperature. Later, -NH₂ modification (AuNR@SiO₂-NH₂) and -COOH modification (AuNR@SiO₂-COOH) were carried out according to the published protocol^[9,21] and described in the Supporting Information.

DOX Loading and ALN Surface Modification (DOX@AuNR@SiO₂-ALN): 10 mg of DOX and AuNR@SiO₂ nanoparticles which contained 10 mg of AuNRs were blended within 10 mL Milli-Q water, and stirred vigorously on a magnetic stirrer. After 24 h of drug loading, the NPs/DOX were centrifuged at 10 000 g and washed with ethanol three times. Then, the drug loaded DOX@AuNR@SiO₂-COOH NPs were put into 10 mL Milli-Q water, 0.1 mg NHS and 0.1 mg EDC were added together into the solution and stirred 1 h for carboxyl group activation. Subsequently, 10 mg of ALN was added and reacted with NPs/DOX for another 24 h at room temperature. Finally, NPs/DOX were centrifuged

at 10 000 g and washed with Milli-Q water for three times. The DOX LC and loading efficiency (LE) were calculated according to the following Equations (4) and (5):

$$LC(\%) = \frac{\text{entrapped drug}}{\text{weight of nanoparticles}} \times 100\% \quad (4)$$

$$LE\% = \frac{\text{total input of drug} - \text{amount of drug in the supernatant}}{\text{total input of drug}} \quad (5)$$

Measurement of Photothermal Performance: For measuring the photothermal conversion ability of the DOX@AuNR@SiO₂-ALN nanoparticles, three experiments were conducted. First, 1 mL aqueous dispersion of NPs/DOX with different concentrations (0, 0.25, 5, and 1 mg mL⁻¹) were introduced in a quartz cuvette and irradiated with an 980 nm NIR laser at a power density of 1 W cm⁻² for 300 s, and the thermal imaging pictures were simultaneously recorded by thermal imaging cameras. Second, 1 mL aqueous dispersion of NPs/DOX with same concentrations (1 mg mL⁻¹) were prepared in a quartz cuvette and irradiated at different power density (0.5, 1, and 1.5 W cm⁻²) for 300 s, respectively. Third, a heating-cooling cycles experiments was determined by using 1 mg mL⁻¹ NPs/DOX solutions and continually irradiated with a 1 W cm⁻² 980 nm NIR laser to the plateau temperature. Then it was cooled down naturally to the room temperature. A thermocouple probe with an accuracy of 0.1 °C was inserted into the upper mentioned DOX@AuNR@SiO₂-ALN aqueous solution. The temperature was recorded every 30 s by a digital thermometer.

NIR Triggered Pulsated Drug Release Experiment: The drug release experiment was divided into two groups, one was the laser group and the other was the without laser group. The release experiment of the two groups was all carried out in 1 mL PBS solution in a shaker at 37 °C, and all contained DOX@AuNR@SiO₂-ALN NPs/DOX which equally containing 0.5 mg AuNRs. For the laser group, the nanoparticles were irradiated with 1 W cm⁻² laser for 5 min at 2, 4, and 5 h. At each time point for both groups, solutions were centrifuged and the 0.9 mL of supernatant was taken out for drug concentration testing, then 0.9 fresh PBS also added back and dispersed well before putting back to the shaker.

GelMA Preparation: 20 g^[38] of gelatin was weighed and dispersed into 200 mL PBS (0.01 M). Then the procedure was carried within a water bath to make the temperature of gelatin reach 60 °C and stirred until dissolution was clear. Later, a syringe was used to draw 16 mL of MA and slowly added MA to the gelatin by using a micro syringe pump at a speed of 0.25 mL min⁻¹. After adding MA for 2 h, 200 mL PBS was then added to stop the reaction. After the reaction was terminated for 15 min, GelMA was put into a dialysis bag (MWCO 3500), dialyzed overnight at 38 °C, then centrifuged at 10 000 g for 15 min at 37 °C to remove insolubles, the supernatant was taken and dialysis was continued for 2–3 days. The GelMA was finally dispensed into multiple plates, and placed them in a minus 80 refrigerator for storage before lyophilized.

Microgel Preparation (NPs/DOX@GelMA/DMXAA): First^[39,40] 150 mg of lyophilized GelMA and 15 mg of photocrosslinker were dissolved into 3 mL of 0.1 M PBS. Then 1 mL of the above solution was taken and 9 mg DMXAA was added and ultrasonic at 60 °C for 30 min until it dispersed evenly. Then 10 mg NPs/DOX were added and dispersed again, finally the aqueous phase was prepared. Later the oil phase was also prepared by adding 5% Span 80 to the mineral oil. The aqueous phase and oil phase were co-flowed in a microfluidic droplet chips which was purchased from MesoBioSystem Company (Wuhan, China). Different flow rate of different liquids was controlled by a pump (PHD 2000, Harvard Apparatus, USA). A UV lamp was fixed on the droplets collection bottle, and the GelMA droplets will be crosslinked under the UV irradiation. Then the microgels were collected by centrifuged at 300 g and washed three times with 75% ethanol. The size of the obtained microgels was measured under NIH ImageJ software based on the pictures taken by the microscope.

NIR Triggered Accelerated Drug Release Experiment: NPs/DOX@GelMA/DMXAA^[41] microgel which equally containing 1 mg AuNRs was added to 1 mL Milli-Q water. Every three days, the solution was centrifuged and the supernatant was taken out to measure the drug concentrations of DOX and DMXAA, and the cumulative release of these two drugs were calculated separately. During the time, on the 6th and 12th day, 980 nm laser with 1 W cm⁻² was used to irradiate the microgel for 10 min.

In Vitro: Human osteosarcoma (MNNG/HOS) cells and HUVEC cells were provided by Department of Central Laboratory, The Second Hospital of Jiaxing (China). MNNG/HOS cells were grown in DMEM medium containing 10% FBS, 1% penicillin, and streptomycin. HUVEC cells were grown in 1640 medium containing 10% FBS, 1% penicillin, and streptomycin. The detailed steps of cell experiments including Cytotoxicity, CLSM Imaging, Calcein/PI Cell Viability/Cytotoxicity Assay, Annexin V-FITC cell apoptosis detection, and Tube formation experiments are described in the Supporting Information.

In Vivo: All experiments including animal operations were approved by the Animal Research Committee of Ruijin Hospital, Shanghai Jiao Tong University School of Medicine, China. The MNNG/HOS cells were cultured in large quantities around 40 bottles in the cell culture bottle (1 × 10⁷ cells per bottle). After the cells were grown sufficiently, each bottle of cells (1 × 10⁷ cells) was diluted with 100 µL cell medium and injected into the subcutaneous of axilla of BALB/c-nu nude mice. All nude mice were 6-week-old female mice. After weighing, the mice were evenly divided into seven groups according their weight for the tumor suppression test. The tumor volume was observed and recorded every day. The administration method for later treatment was divided into PT and tail vein injection (IV). When the tumor volume reached about 80 mm³, mice were divided into 7 groups including PBS (PT), DOX (PT), DMXAA (PT), DMXAA (PT) +NPs/DOX (IV) –Laser, DMXAA (PT) +NPs/DOX (IV) +Laser, NPs/DOX/DOX@GelMA/DMXAA (PT) –Laser, and NPs/DOX/DOX@GelMA/DMXAA (PT) +Laser group, and each group contained four mice. The in vivo experiments including In Vivo IR Thermo-imaging, In Vivo Fluorescence Imaging, In Vivo Anticancer Efficacy, H&E staining, and TUNEL, Ki-67, CD31 staining for tumor slices. The details for each experiment are explained in the Supporting Information.

Supporting Information

Supporting Information is available from the Wiley Online Library or from the author.

Acknowledgements

J.Y., Y.W., and M.R. contributed equally to this work. This work was supported by grants from the National Nature Science Foundation of China (81871472, 81772393), Beijing Municipal Natural Science Foundation (7192214), Special Project of Integrated Traditional Chinese and Western Medicine in General Hospitals of Shanghai (ZHYX-ZXYJHZX-201901), Academy of Finland (309374 and 328933), and Sigrid Jusélius Foundation.

Conflict of Interest

The authors declare no conflict of interest.

Data Availability Statement

Research data are not shared.

Keywords

modulatable biodegradability, nanocomposite microgel, osteosarcoma targeting, triple-synergetic therapy, ultra-low dosage

Received: January 25, 2021

Revised: May 16, 2021

Published online: June 25, 2021

- [1] A. I. Minchinton, I. F. Tannock, *Nat. Rev. Cancer* **2006**, *6*, 583.
- [2] H. Zhang, Y. Zhu, L. Qu, H. Wu, H. Kong, Z. Yang, D. Chen, E. Makila, J. Salonen, H. A. Santos, M. Hai, D. A. Weitz, *Nano Lett.* **2018**, *18*, 1448.
- [3] F. Zhang, A. Correia, E. Makila, W. Li, J. Salonen, J. J. Hirvonen, H. Zhang, H. A. Santos, *ACS Appl. Mater. Interfaces* **2017**, *9*, 10034.
- [4] H. Zhang, D. Liu, M. A. Shahbazi, E. Makila, B. Herranz-Blanco, J. Salonen, J. Hirvonen, H. A. Santos, *Adv. Mater.* **2014**, *26*, 4497.
- [5] S. Qi, P. Zhang, M. Ma, M. Yao, J. Wu, E. Makila, J. Salonen, H. Ruskoaho, Y. Xu, H. A. Santos, H. Zhang, *Small* **2019**, *15*, 1804332.
- [6] T. Yong, X. Zhang, N. Bie, H. Zhang, X. Zhang, F. Li, A. Hakeem, J. Hu, L. Gan, H. A. Santos, X. Yang, *Nat. Commun.* **2019**, *10*, 3838.
- [7] G. Ni, G. Yang, Y. He, X. Li, T. Du, L. Xu, S. Zhou, *Chem. Eng. J.* **2020**, *379*, 122317.
- [8] X. Zhou, X. He, K. Shi, L. Yuan, Y. Yang, Q. Liu, Y. Ming, C. Yi, Z. Qian, *Adv. Sci.* **2020**, *7*, 2001442.
- [9] J. Yan, C. Liu, Q. Wu, J. Zhou, X. Xu, L. Zhang, D. Wang, F. Yang, H. Zhang, *Anal. Chem.* **2020**, *92*, 11453.
- [10] H. Zhang, W. Cui, X. Qu, H. Wu, L. Qu, X. Zhang, E. Makila, J. Salonen, Y. Zhu, Z. Yang, D. Chen, H. A. Santos, M. Hai, D. A. Weitz, *Proc. Natl. Acad. Sci. USA* **2019**, *116*, 7744.
- [11] Y. Liang, Y. Wang, L. Wang, Z. Liang, D. Li, X. Xu, Y. Chen, X. Yang, H. Zhang, H. Niu, *Bioact. Mater.* **2021**, *6*, 433.
- [12] B. Liu, J. Sun, J. Zhu, B. Li, C. Ma, X. Gu, K. Liu, H. Zhang, F. Wang, J. Su, Y. Yang, *Adv. Mater.* **2020**, *32*, 2004460.
- [13] Z. Meng, Y. Chao, X. Zhou, C. Liang, J. Liu, R. Zhang, L. Cheng, K. Yang, W. Pan, M. Zhu, Z. Liu, *ACS Nano* **2018**, *12*, 9412.
- [14] R. A. Sheth, R. Murthy, D. S. Hong, S. Patel, M. J. Overman, A. Diab, P. Hwu, A. Tam, *JAMA Network Open* **2020**, *3*, e207911.
- [15] L. Zhang, H. Su, J. Cai, D. Cheng, Y. Ma, J. Zhang, C. Zhou, S. Liu, H. Shi, Y. Zhang, C. Zhang, *ACS Nano* **2016**, *10*, 10404.
- [16] D. Guo, Y. Huang, X. Jin, C. Zhang, X. Zhu, *Biomaterials* **2021**, *266*, 120400.
- [17] S. Geng, H. Zhao, G. Zhan, Y. Zhao, X. Yang, *ACS Appl. Mater. Interfaces* **2020**, *12*, 7995.
- [18] D. Bartczak, O. L. Muskens, S. Nitti, T. M. Millar, A. G. Kanaras, *Biomater. Sci.* **2015**, *3*, 733.
- [19] H. Song, T. Guo, Z. Zhao, Y. Wei, H. Luo, W. Weng, R. Zhang, M. Zhong, C. Chen, J. Su, W. Shen, *Biomaterials* **2018**, *178*, 23.
- [20] S. H. Chen, T. I. Liu, C. L. Chuang, H. H. Chen, W. H. Chiang, H. C. Chiu, *J. Mater. Chem. B* **2020**, *8*, 3789.
- [21] H. Ren, S. Chen, Y. Jin, C. Zhang, X. Yang, K. Ge, X. J. Liang, Z. Li, J. Zhang, *J. Mater. Chem. B* **2017**, *5*, 1585.
- [22] J. Yang, Y. Zhu, F. Wang, L. Deng, X. Xu, W. Cui, *Chem. Eng. J.* **2020**, *400*, 126004.
- [23] R. Cheng, L. Liu, Y. Xiang, Y. Lu, L. Deng, H. Zhang, H. A. Santos, W. Cui, *Biomaterials* **2020**, *232*, 119706.
- [24] H. Wang, A. J. Najibi, M. C. Sobral, B. R. Seo, J. Y. Lee, D. Wu, A. W. Li, C. S. Verbeke, D. J. Mooney, *Nat. Commun.* **2020**, *11*, 5696.
- [25] F. Gao, Z. Xu, Q. Liang, H. Li, L. Peng, M. Wu, X. Zhao, X. Cui, C. Ruan, W. Liu, *Adv. Sci.* **2019**, *6*, 1900867.
- [26] W. Tang, Y. Yu, J. Wang, H. Liu, H. Pan, G. Wang, C. Liu, *Biomaterials* **2020**, *232*, 119645.
- [27] J. Lee, V. Manoharan, L. Cheung, S. Lee, B. H. Cha, P. Newman, R. Farzad, S. Mehrotra, K. Zhang, F. Khan, M. Ghaderi, Y. D. Lin, S. Aftab, P. Mostafalu, M. Miscuglio, J. Li, B. B. Mandal, M. A. Hussain, K. T. Wan, X. S. Tang, A. Khademhosseini, S. R. Shin, *ACS Nano* **2019**, *13*, 12525.
- [28] W. Wu, Y. Dai, H. Liu, R. Cheng, Q. Ni, T. Ye, W. Cui, *Drug Delivery* **2018**, *25*, 1642.
- [29] D.-W. Z. Sheng Hong, C. Zhang, Q.-X. Huang, S.-X. Cheng, X.-Z. Zhang, *Sci. Adv.* **2020**, *6*, eabb0020.
- [30] L. Scarabelli, A. Sanchez-Iglesias, J. Perez-Juste, L. M. Liz-Marzan, *J. Phys. Chem. Lett.* **2015**, *6*, 4270.
- [31] J. Hu, H. Luo, Q. Qu, X. Liao, C. Huang, J. Z. Y. Bao, G. Chen, B. Li, W. Cui, *ACS Appl. Mater. Interfaces* **2020**, *12*, 42511.
- [32] X. Sun, Q. Lang, H. Zhang, L. Cheng, Y. Zhang, G. Pan, X. Zhao, H. Yang, Y. Zhang, H. A. Santos, W. Cui, *Adv. Funct. Mater.* **2017**, *27*, 1604617.
- [33] X. Zhao, S. Liu, L. Yildirim, H. Zhao, R. Ding, H. Wang, W. Cui, D. Weitz, *Adv. Funct. Mater.* **2016**, *26*, 2809.
- [34] L. Tamayo, D. Acuna, A. L. Riveros, M. J. Kogan, M. I. Azocar, M. Paez, M. Leal, M. Urzua, E. Cerda, *ACS Appl. Mater. Interfaces* **2018**, *10*, 13361.
- [35] G. Carpentier, S. Berndt, S. Ferratge, W. Rasband, M. Cuendet, G. Uzan, P. Albanese, *Sci. Rep.* **2020**, *10*, 11568.
- [36] J. He, C. Li, L. Ding, Y. Huang, X. Yin, J. Zhang, J. Zhang, C. Yao, M. Liang, R. P. Pirraco, J. Chen, Q. Lu, R. Baldrige, Y. Zhang, M. Wu, R. L. Reis, Y. Wang, *Adv. Mater.* **2019**, *31*, 1902409.
- [37] I. G. N. Matsuura, *Nano Lett.* **2007**, *8*, 369.
- [38] L. Shao, Q. Gao, H. Zhao, C. Xie, J. Fu, Z. Liu, M. Xiang, Y. He, *Small* **2018**, *14*, 1802187.
- [39] J. Bian, F. Cai, H. Chen, Z. Tang, K. Xi, J. Tang, L. Wu, Y. Xu, L. Deng, Y. Gu, W. Cui, L. Chen, *Nano Letters* **2021**, *21*, 2690.
- [40] J. Yan, X. Xu, J. Zhou, C. Liu, L. Zhang, D. Wang, F. Yang, H. Zhang, *ACS Appl. Bio Mater.* **2020**, *3*, 1216.
- [41] H. Luo, L. Kong, F. Zhang, C. Huang, J. Chen, H. Zhang, H. Yu, S. Zheng, H. Xu, Y. Zhang, L. Deng, G. Chen, H. A. Santos, W. Cui, *Adv. Funct. Mater.* **2021**, 2101262, <https://doi.org/10.1002/adfm.202101262>.

Self-assembly of DNA nanogels with endogenous microRNA toehold self-regulating switches for targeted gene regulation therapy

Jiaqi Yan, Haixia Zou, Wenhui Zhou, Xiaowan Yuan, Zhijun Li, Xiaodong Ma, Chang Liu, Yonghui Wang, Jessica M. Rosenholm, Wenguo Cui, Xiangmeng Qu* and Hongbo Zhang*. *Biomaterials Science*. **2022**, 10, 4119–4125. (DOI: 10.1039/d2bm00640e)



Cite this: *Biomater. Sci.*, 2022, **10**, 4119

Received 25th April 2022,
Accepted 18th June 2022

DOI: 10.1039/d2bm00640e

rsc.li/biomaterials-science

Self-assembly of DNA nanogels with endogenous microRNA toehold self-regulating switches for targeted gene regulation therapy†

Jiaqi Yan,^{†a,b,c} Haixia Zou,^{†a} Wenhui Zhou,^{†c} Xiaowan Yuan,^a Zhijun Li,^a Xiaodong Ma,^c Chang Liu,^c Yonghui Wang,^c Jessica M. Rosenholm,^{id c} Wenguo Cui,^{id b} Xiangmeng Qu^{id *a} and Hongbo Zhang^{id *b,c}

Herein, a smart nanohydrogel with endogenous microRNA-21 toehold is developed to encapsulate gemcitabine-loaded mesoporous silica nanoparticles for targeted pancreatic cancer therapy. This toehold mediated strand displacement method can simultaneously achieve specific drug release and miRNA-21 silencing, resulting in the up-regulation of the expression of tumor suppressor genes PTEN and PDCD4.

Abnormal expression of intracellular genes is the critical cause of tumor heterogeneity, which brings significant challenges to tumor treatment.¹ Gene regulation therapy is a promising and essential means of treating genetic or other gene disorder-related diseases. Recent studies exhibit that gene expression can be modulated by many oligonucleotide-based gene regulation tools, including anti-sense oligonucleotides,² or microRNA.³ Specifically, in recent gene therapy tools, supplementing endogenous down-regulated genes and silencing highly expressed pathogenic genes have become the most popular strategy.^{4–6} However, the development of reasonable design projects and efficient delivery vectors remain the key technical obstacles in target regulation therapy.^{7,8}

DNA hydrogels are biocompatible, and possess molecular recognition capabilities and nanoscale structure controllability,^{9–12} which show great potential for target regulation therapy. Further, they are colloiddally stable, enable rapid stimuli response, and can passively target the tumors relying on the enhanced permeability and retention effect in tumors.^{13–15} A

microRNA (miRNA) is an endogenous non-coding small RNA with a length of about 22 nucleotides.^{3,16} It has been found that the expression of multiple miRNAs is related to the development and differentiation of cancer cells.^{17–20} The construction of many miRNA-based antisense nucleic acid delivery systems is widely studied to achieve gene silencing effects.²¹ However, in this way, the ability of nucleic acid sequences as vector construction materials is wasted. Therefore, the preparation of miRNA responsive DNA nanohydrogels is a very promising design approach for the targeted regulation therapy of cancer.²² However, DNA exhibits a strong electronegativity, and it is challenging for DNA to be endocytosed by cancer cells.^{23,24} In addition, the DNA hydrogel bears low hydrophobic drug loading capacity,^{25–27} which greatly restricts its synergistic application with first-line anticancer drugs.^{28,29}

In this work, we developed a smart nanohydrogel system with effective drug delivery and endogenous microRNA toehold self-regulating switches for on-site targeted regulation therapy in cancer (Fig. 1). The system consists of a protective DNA nanohydrogel-shell (Fig. 1A) with miRNA recognizing ability (Fig. 1B), and a hydrophobic drug reservoir mesoporous silica nanoparticle (MSN),^{30,31} illustrated in Fig. 1C. By combining MSN and DNA nanohydrogel, a new core-shell structure MSN@DNA will perfectly inherit the advantages of the two materials. The porous structure of MSN can achieve a high hydrophobic drug loading rate, and the DNA nanohydrogel can be used as a gate of the pores of MSN for miRNA responsive decomposition by targeted microRNA toehold self-regulating switches, thereby controlling the release of drugs and in the meantime silencing the targeted gene. In this work, miRNA-21 as a model endogenous target molecule is selected as a pancreatic cancer precise target and chemo/gene combination therapy. Our smart nanohydrogel-based system as a universal platform has great potential to be used for combination therapy of various diseases.

Two acrydite-modified DNA sequences (strand A and strand B) were grafted onto linear polyacrylic acid (PAA) through free radical reactions to form the hydrogel liquid

^aKey Laboratory of Sensing Technology and Biomedical Instruments of Guangdong Province, School of Biomedical Engineering, Sun Yat-Sen University, 66 Gongchang Road, Shenzhen 518107, China. E-mail: quxm5@mail.sysu.cn

^bDepartment of Radiology, Shanghai Institute of Traumatology and Orthopaedics, Ruijin Hospital, Shanghai Jiao Tong University, 149 Chongqingnan Road, Shanghai, 200020, PR China. E-mail: hongbo.zhang@abo.fi

^cPharmaceutical Sciences Laboratory and Turku Bioscience Center, Åbo Akademi University, FI-20520 Turku, Finland

† Electronic supplementary information (ESI) available. See DOI: <https://doi.org/10.1039/d2bm00640e>

‡ Equal concentration.

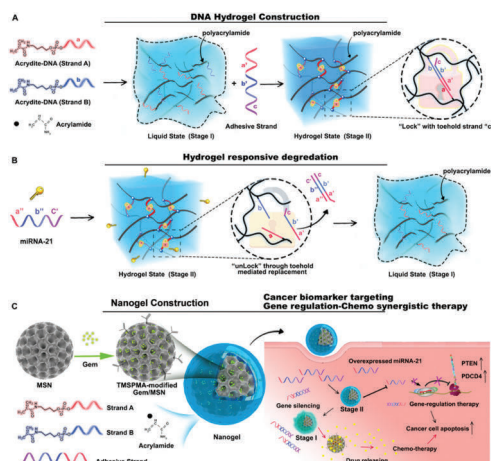


Fig. 1 (A) Construction and (B) degradation mechanisms of the designed DNA hydrogel. (C) The combination with MSN for targeted gene regulation therapy.

precursor (stage I), as depicted in Fig. 1A. Then the added adhesive strand linked strands A and B together to promote the formation of hydrogel (stage II). The interior of the hydrogel consisted of a lock structure with toehold strand "c". When miRNA-21 was used as the key to replace the adhesive strand through toehold-mediated strand displacement, the lock was opened, and the hydrogel returned to the liquid state (Fig. 1B).

Subsequently, gemcitabine (Gem) was loaded into the MSN, and the abovementioned DNA-grafted linear hybrid polymer was anchored to the 3-(trimethoxysilyl)propyl methacrylate (TMSPPMA) modified MSN surface based on the free radical reaction mechanism. Then, the miRNA-21 entirely complementary antisense strand anti-miR-21, which partially complements strand A and strand B was added as a "glue" for PAA crosslinking to develop the final nanogel (Gem@MSN@DNA), as shown in Fig. 1C. Anti-miR-21, which served as the adhesive strand, constructed the hydrogel shell in our multifunctional nanosystem. In turn, they were protected by the hydrogel from degradation by the enzyme during blood circulation. Cationic polymer PAA also promoted the endocytosis ability of negatively charged DNA strands. After encountering oncogenic gene miR-21, the DNA adhesive strands inside the nanohydrogel layer were competitively paired by miRNA-21 through the toehold mediated DNA strand displacement mechanism^{32,33} and specific cancer cell targeting drug release and microRNA-21 regulation therapy were achieved.

When designing the DNA hydrogel layer, the loading content of the miRNA-21 antisense strands is critical for the efficacy of cancer treatment. For pancreatic cancer cell lines, it has been reported that a single concentration (100 nmol L^{-1}) of miRNA-21 antisense oligonucleotides can achieve an obvious gene silencing effect for *in vitro* cytotoxicity study.^{34,35}

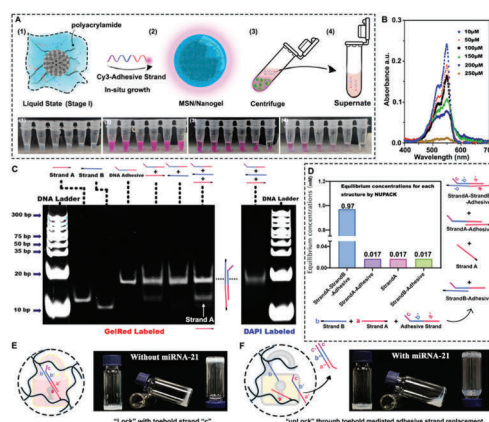


Fig. 2 Characterization of nanoparticles. (A) Prescription screening of the adhesion strand content. (B) Ultraviolet absorbance of Cy3 modified adhesion strand in the supernatant. (C) The cross-linking process of each chain was verified by the polyacrylamide gel experiment. (D) The cross-linking process of each chain was verified by the NUPACK web application. (E) Macroscopic photos for DNA hydrogels without the miRNA-21 strand. (F) Macroscopic photos for DNA hydrogels with the miRNA-21 strand.

Based on this dosage, 6 tubes that contained the same amount ($200 \mu\text{g}$) of MSN NPs (Fig. 2A1) were first prepared and numbered from one to six. Different concentrations of strand A and strand B grafted PAA (with concentrations of $10 \mu\text{M}$, $50 \mu\text{M}$, $100 \mu\text{M}$, $150 \mu\text{M}$, $200 \mu\text{M}$, and $250 \mu\text{M}$ for each type of strand) were compared. The same Cy3 modified adhesive strand concentration is added to each tube (the final volume and concentration were $50 \mu\text{L}$ and $200 \mu\text{M}$, as shown in Fig. 2A2). After 15 min of incubation at 60°C , all tubes were centrifuged (Fig. 2A3) and the supernatant was collected into new tubes (Fig. 2A4) for UV-vis absorption detection (Fig. 2B). We found that the Cy3 modified adhesive strand is effectively encapsulated into the DNA nanohydrogel and centrifuged to the bottom of the tube together with MSN NPs. These results indicated that the adhesive strand, as a functional building block for the designed miRNA-21 sensitive hydrogel, can successfully mediate the crosslinking of PAA on the surface of MSN. In the meantime, by increasing the content of A and B strands, $200 \mu\text{M}$ of adhesion strand has fully assembled inside the hydrogel, verified by the supernatant photos and UV absorbance results. The centrifuged NPs were repeatedly washed and diluted into 1 mL . The final concentration of miRNA-21 antisense strand is $10 \mu\text{M}$, which is a hundred times higher than the effective concentration mentioned before, therefore facilitating further investigation with a broad concentration range.

Strand A and strand B are partially complementary to the two ends of the adhesive strand and are riveted on the PAA linear polymer (Table S1†). Therefore, the adhesive strand will adhere to the A/B strand and promote the crosslinking of the polymer. We confirmed this anticipation through a polyacryl-

amide gel experiment. As shown in Fig. 2C, a strong band is observed at around 20 bp when strand A or strand B are added together with the adhesive strand and labelled with GelRed, accompanied by the disappearance of the band of the A/B strand. This phenomenon demonstrated the successful combination between each strand. However, the newly formed double-strand band seems to overlap with the previous adhesive strand, resulting in unobvious results. Since we cannot compare the moving speed of the single-strand and hybrid double-strand inside the polyacrylamide gel, another dye DAPI was chosen to verify the synthesis of new double-strands because DAPI can only bind to A-T base-pair regions compared to GelRed. As shown in Fig. 2C, after three single strands were added together, there was indeed only one new band formed by using DAPI as the labelling dye.

Due to the coincidence of the positions of the newly generated bands and the excess bands after the reaction of the three strands (strand A, B and adhesive strand), we used the NUPACK web application³⁶ to specifically analyze the possible reactions, as elucidated in Fig. 2D. We found that when each strand with 1 mM was added together, in addition to the 0.94 mM product, there was 0.017 mM strand A remaining, which explains that the band at around 14 bp was strand A (Fig. 2C). Meanwhile, 0.017 mM strand A-adhesive strand and 0.017 mM strand B-adhesive strand were also generated (Fig. 2D), where the two strands share the same location as the band of the final product (Fig. 2C).

Then, to verify the “unlock” system of our designed hydrogel through the toehold mediated strand replacement mechanism, we first prepared bulk hydrogels to facilitate observation of their macroscopic changes (Fig. 2E and F). We can clearly see that the DNA hydrogel changed (Fig. 2E) to a transparent milky white liquid (Fig. 2F). This result proved that miRNA-21 could competitively bind to the adhesive chains inside the hydrogel, leading to the disintegration of the hydrogel.

Subsequently, DLS data and TEM results are explored to confirm the successful combination between the DNA hydrogel and pure MSN NPs, and the miRNA-21 sensitivity of the hydrogel shell. We found that when the MSN surface was modified with the DNA nanogel, its particle size increased from 120 nm to about 150 nm, which was reflected in Fig. 3A. Moreover, the particle size of Gem@MSN@DNA NPs did not change after one week of storage in PBS buffer (Fig. S1†). However, when incubated with 5 nM miRNA-21 for 4 h, its particle size returned to 120 nm, which indicates that the nanogel shell has an excellent miRNA-21 responsive degradation capability. Meanwhile, from the zeta potential results, we can see that the TMSPMA modified MSN (Gem@MSN@DNA + miR-21 group) is negatively charged at around -33 mV. After being covered with DNA hydrogel, the zeta potential of the final NPs becomes neutral (Fig. 3B), which can promote the phagocytosis ability of negatively charged NPs by cancer cells.³⁷ Also, the formation of a DNA hydrogel layer is confirmed by TEM (Fig. 3C). We can clearly see a hydrogel layer grown on the surface of MSN NPs. More importantly, after incubation with 5 nM miRNA-21 for 4 hours, the polymer layer

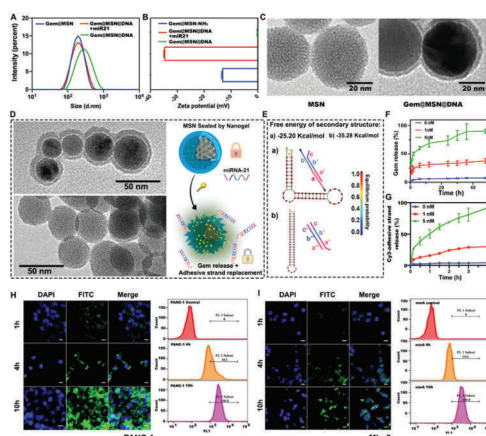


Fig. 3 Characterization and intracellular delivery of different nano-formulations. (A) Changes in the particle size of nanoparticles under dynamic light scattering (DLS). (B) Changes in the zeta potential of nanoparticles under DLS. (C) TEM results of different NPs before and after DNA hydrogel coating. (D) The TEM spectrum for DNA-hydrogel degradation and explanation of the therapeutic agent release mechanism. (E) Free energy of secondary structure of different DNA structures. (F) miRNA-21 mediated Gem drug release profile. (G) Cy3-labeled anti-miRNA21 strand release profile. (H) Confocal microscopy pictures of NPs in PANC-1 cells at different time periods and flow cytometry results of co-incubation of NPs and PANC-1 cells at different time periods. (I) Confocal microscopy pictures of NPs in Min6 cells at different time periods and flow cytometry results of co-incubation of NPs and Min6 cells at different time periods. Scale bar equal to 20 μ m.

on MSN surface disappeared (Fig. 3D), indicating the successful construction of a miRNA-responsive gating switch.

The Gem-loaded MSN NPs were protected by the “gate material” DNA nanogel, to prevent premature drug release before accumulating into the tumor tissue (Fig. 3D). The release profiles of Gem and the Cy3-labeled adhesive strand from DNA hydrogel-covered MSN were tested. Toehold mediated strand displacement between miRNA-21 and the adhesive strand is elucidated in Fig. 3E. When strands A and B were combined with the adhesive strand, their free energy of the secondary structure, calculated using NUPACK software, was $-25.20 \text{ kcal mol}^{-1}$, which was higher than the combination between miRNA-21 and adhesive strand ($-35.28 \text{ kcal mol}^{-1}$), as shown in Fig. 3E. These simulated results proved that the NPs could realize the responsive disintegration of miRNA-21. Furthermore, along with the degradation of NPs, miRNA-21 will also be consumed and silenced by adhesion strands (antisense sequences), realizing gene/chemo combination therapy.

Upon loading Gem into MSN, a drug loading degree of 22.95% is reached; that is 1 mg MSN can hold about 300 μ g of Gem (Table S2†). Subsequently, the miRNA-21 responsive release experiment was performed, and 0 nM, 1 nM and 5 nM were selected based on the previous study.^{38,39} The Gem inside NPs exhibited an accelerated release profile when the concen-

tration of miRNA-21 in the release environment increased. We found that within 40 hours, with a 5 nM concentration of miRNA-21 present in the release medium, the release content of Gem could reach more than 80%, but in the presence of less than 1 nM miRNA-21, only 30% of Gem was released within the same time frame. Negligible drug release was observed when there was no miRNA-21 in the release media, which demonstrated the NPs' excellent miRNA-21 recognition ability in controlling the drug release (Fig. 3F). Notably, the results of the release of Cy3-labeled adhesive strand were consistent with the gemcitabine release profile, which showed a miRNA-21 responsive release ability (Fig. 3G). However, Cy3 was released more rapidly and at a higher rate, and Cy3-anti-miRNA-21 was released more than 95% at 4 h with 5 nM miRNA-21, since the outermost nanogel shell can be easily degraded when encountering the miRNA-21.

Next, the endocytosis of NPs in pancreatic cancer cell PANC-1 and pancreatic islet B epithelial cell Min6 are studied. PANC-1 has a high expression of miRNA-21, and it has also been reported that after Gem administration, the miRNA-21 was greatly up-regulated, which could significantly reduce the efficacy of chemotherapy.⁴⁰ Compared with PANC-1 cells, the Min6 cells had a very low miRNA-21 expression,⁴¹ as shown in Fig. S2,† so it is selected as a negative control to evaluate the NPs' selectivity towards miRNA-21. We first loaded the FITC fluorescent dye inside NPs for tracking the endocytosis of NPs by different cells through confocal microscopy and flow cytometry experiments (Fig. 3H and I).

For the PANC-1 cell line, the results showed that with the extension of the incubation time, the amount of NP uptake by cells gradually increased. Within 10 hours, 100% of the cells had taken up NPs, which indicated that the NPs could be effectively endocytosed. Interestingly, due to high miRNA-21 content in PANC-1 cells, we have observed that the FITC dye inside the NPs was more likely to diffuse throughout the cells, which indirectly indicated that the DNA hydrogel shell was disintegrated and facilitated the FITC release. In the meantime, Min6 cells also displayed efficient endocytosis ability of NPs, 100% of the cells had taken up within 10 h. This may be because we did not modify the cell-targeting ligands on the surface of NPs, different cells possessed relatively the same endocytosis effect on NPs. However, the FITC inside the nanoparticles did not seem to diffuse after 16 h, but rather accumulated at a certain location in the cytoplasm. This phenomenon reflected that with less miRNA-21 content, it was difficult for FITC to diffuse through the intact DNA-hydrogel layer. Furthermore, since healthy tissue around the tumor can also internalize the nanosystem, therefore, within a certain period, the miRNA hydrogel layer would monitor the miRNA-21 content of healthy cells, and treat them in a timely manner when their miRNA-21 content showed abnormal change.

The fluorescence *in situ* hybridization (FISH) method was subsequently utilized to study the silencing effect of miRNA-21 in PANC-1 cells. The FITC green, fluorescent probe was used to observe the content of miRNA-21. We found that the cytoplasm of PANC-1 cells exhibited bright green fluorescence without

the addition of NPs, indicating the presence of a large number of proliferation miRNA-21 genes (Fig. 4A). Upon the addition of NPs, the content of miRNA-21 was significantly inhibited (Fig. 4B), especially when the concentration of NPs exceeded $0.2 \mu\text{g mL}^{-1}$ (adhesive strand concentration equal to 10 nM). In addition, when the concentration of NPs reached more than $2 \mu\text{g mL}^{-1}$, the cells gradually entered the apoptotic stage, and the red arrow indicates the occurrence of nuclear fragmentation (Fig. 4A). The permeability of the nucleus was also found to increase and green fluorescence was observed inside the nucleus, since during the process of cell apoptosis, the nuclear membrane permeability will be increased.^{42,43} These results fully proved the miRNA-21 recognition ability of the DNA hydrogel layer of the NPs and the silencing function of the miRNA-21 antisense building block inside the hydrogel.

To further explore the cytotoxicity of Gem-loaded and DNA hydrogel-wrapped Gem@MSN@DNA NPs, different drugs and NP groups were studied with the PANC-1 cells and Min-6 cells, as shown in Fig. 4C and Fig. S3.† For PANC-1 cells, pure Gem showed no obvious difference when Gem concentration exceeded $0.2 \mu\text{M}$ (calculated based on the loading degree). After Gem was loaded into MSN, the efficacy of Gem increased but still changed modestly when the MSN concentration was higher than $0.2 \mu\text{g mL}^{-1}$. On the other hand, MSN@DNA showed an excellent therapeutic effect, especially when the MSN concentration exceeded $2 \mu\text{g mL}^{-1}$ (miRNA-21 antisense strand equal to 100 nM). Finally, the Gem@MSN@DNA group showed a powerful cancer cell suppressing effect. The Gem@MSN@DNA group killed more than 50% of the cells only at the MSN concentration of $0.2 \mu\text{g mL}^{-1}$ (Gem and miRNA-21 antisense DNA concentration equal to $0.2 \mu\text{M}$ and

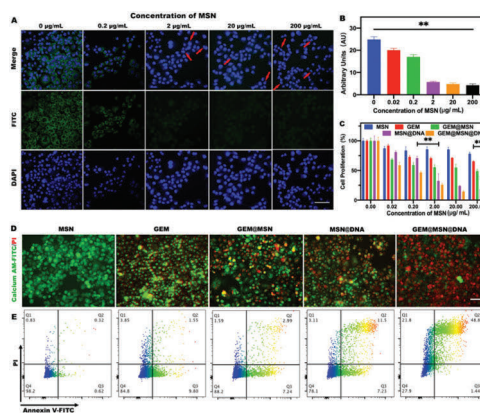


Fig. 4 miRNA-21 silencing effect and cytotoxicity. (A) Silencing effect of miRNA-21 in PANC-1 cells. (B) Fluorescence quantification of miRNA-21 in PANC-1 cells. (C) Toxicity evaluation of drugs and DNA hydrogel-based NPs for PANC-1 cells. (D) Live/dead cell imaging for PANC-1 cells with different therapeutic groups. (E) Cell apoptosis results from each treatment group. For each group, the scale bar is equal to $100 \mu\text{m}$.

10 nM) and killed more than 80% of the cells at the highest concentration (Gem and miRNA-21 antisense DNA concentration equal to 200 μM and 10 mM). These results confirmed that the nanosystem could achieve excellent synergistic effects for both chemo and gene therapy. Then, for Min6 cells, the Gem@MSN group showed serious toxicity when the MSN concentration becomes 2 $\mu\text{g mL}^{-1}$ (Gem concentration equal to 2 μM). However, when the hydrogel is wrapped on the surface of the nanoparticle, we can see that the Gem@MSN@DNA group possessed significantly higher safety than the pure Gem and Gem@MSN groups. These results indicated that the DNA hydrogel-encapsulated nanoformulations are highly selective for miRNA-21. Only under a high concentration of miRNA-21 can the NPs release gemcitabine and miRNA-21 antisense sequence together.

We then conducted the live/dead cell assay for the PANC-1 cell line with different groups, while green represented live cells and red represented apoptotic cells (Fig. 4D). The results exhibited that the GEM/MSN/DNA group possessed enhanced cytotoxicity, due to the synergistic effect of chemotherapy and gene therapy. At the same time, the experimental results of apoptosis (Fig. 4E) were consistent with those of the cytotoxicity assay, and over 70% of the cells in the Gem@MSN@DNA group went into the late apoptotic stage after 24 h of treatment. Gemcitabine can stimulate cells to further produce excessive miRNA-21,⁴⁰ which is one of the reasons for chemo-resistance. Therefore, the nano-system we designed has great synergistic therapeutic significance.

Later, the intracellular disintegration process of the hydrogel layer is verified through confocal microscopy. DAPI is used to mark the AT base pairs of the double-stranded building block inside the NPs (Fig. 5A). Through this method, the unwinding process of double-stranded DNA from the hydrogel shell of NPs can be observed. Because DAPI is toxic to cells, we only observed the fluorescence changes in the cytoplasm and nucleus within 8 h. After DAPI-labelled NPs are internalized into PANC-1 cells, DAPI will be released due to the unwinding between the adhesive strand, strand A and strand B. The released DAPI will increase the fluorescence in the nucleus, as elucidated in Fig. 5A. We confirmed this phenomenon in PANC-1 cells, as shown in Fig. 5B. Software Image J was used to quantify the fluorescence image (Fig. 5Ba), and the nucleus and cytoplasm were manually distinguished (Fig. 5Bb), and fluorescence intensity analysis was performed separately (Fig. 5Bc and d). Mean fluorescence intensity of PANC-1 cell nucleus showed that the DAPI blue fluorescence in the nucleus gradually increased during incubation within 6 h (Fig. 5C). Furthermore, the blue fluorescence in the cytoplasm gradually decreased (Fig. 5D), indicating that DAPI is released due to the degradation of the hydrogel shell from NPs and entered the nucleus. However, this phenomenon was not observed in Min6 cells (Fig. S4A–C†), indicating that the Gem@MSN@DNA nano-platform had great miRNA-21 targeting specificity.

The silencing of miRNA-21 can cause changes in the expression of various genes in pancreatic cancer cells (Fig. 5E). It is reported that miR-21 targets and inhibits PDCD4 and

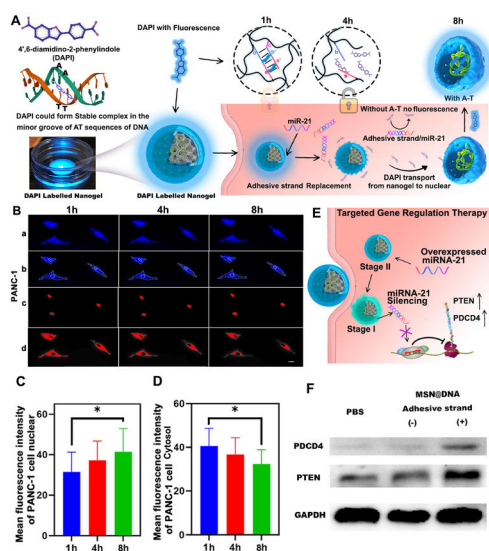


Fig. 5 Observation of the changes of NPs in cells and the silencing effect of miRNA-21. (A) Schematic illustration of the unwinding process of double-stranded DNA from the hydrogel shell of NPs inside cells. (B) Observation of DAPI-labeled NPs inside cells under a fluorescence microscope. The scale bar is 20 μm . (C and D) Quantitative analysis of intracellular DAPI fluorescence intensity using software Image J. (E) Explanation of target gene regulation therapy. (F) The effect of miRNA-21 silencing on the expression of PTEN and PDCD4 protein.

PTEN tumor suppressor genes.^{34,35} By inhibiting miRNA-21, we discovered that the tumor suppressor genes PTEN and PDCD4 in the PANC-1 cells significantly increased through western blot assay (Fig. 5F). It is worth mentioning that in the process of constructing a DNA hydrogel, we introduced strand A and strand B, and these two strands have the same sequence of partial miRNA-21. Hence, they may have the same function as miRNA-21. Therefore, MSN@DNA NPs with or without adhesive strands were prepared in comparative experiments, to ensure that strand A and strand B will not have the same function as miRNA-21 to cause cell proliferation (Fig. 5F). Of note, strands A and B can also be anchored to the surface groups of NPs without the adhesion strand by the aforementioned free radical reaction. The results found that the MSN@DNA (without the adhesive strand) group is the same as the PBS group and had no effect on PDCD4 and PTEN expression. However, for the adhesive strand group, PTEN and PDCD4 are significantly up-regulated, demonstrating the successful inhibition of the miRNA-21 gene (Fig. S5†).

Conclusions

In conclusion, a simple yet multifunctional targeting strategy is successfully developed by encapsulating the Gem-loaded

MSN with an miRNA-21 responsive DNA hydrogel through a simple *in situ* growth technology for pancreatic cancer-targeted chemo/gene synergistic treatment. The antisense strand of miRNA-21 is used as a recognition building block to participate in the cross-linking of DNA hydrogels. The targeting strategy applied by the Gem@MSN@DNA nanosystem is completely different from the receptor-mediated and normal tumor microenvironment-mediated targeting strategies (such as pH or redox). Its targeting is based on the unique oncogene gene of pancreatic cancer cells, and thus will not be heavily interfered with by protein adsorption during blood circulation. Only after the nanocarrier encounters miRNA-21, which is highly expressed by the pancreatic cancer cells, can the hydrogel layer achieve responsive disintegration through the toehold mediated strand displacement mechanism. Subsequently, with the degradation of the DNA protective layer, the Gem inside MSN is gradually released, which greatly enhanced the bio-availability of Gem. Moreover, the degradation of the DNA hydrogel resulted in a significant consumption and silencing of miRNA-21, leading to an enhancement of the expression of tumor suppressor genes PTEN and PDCD4, which promoted cell apoptosis and realized gene/chemotherapy synergistic therapy. Finally, it is theoretically possible to synthesize DNA hydrogel structures responsive to any miRNA by designing different DNA sequences. Thereby different miRNA targeted therapeutic systems can be designed.

Author contributions

Jiaqi Yan, Haixia Zou and Wenhui Zhou conceived the study. Xiangmeng Qu and Hongbo Zhang supervised the project. Wenguo Cui designed the experiments. Jiaqi Yan, Xiaodong Ma, Chang Liu, and Yonghui Wang performed the experiments. Xiaowan Yuan and Zhijun Li, analyzed the experimental results. Jiaqi Yan wrote the manuscript. Jessica M. Rosenholm edited the manuscript.

Conflicts of interest

The authors declare no competing financial interest.

Acknowledgements

This work was funded by National Natural Science Foundation of China (81871472 and 21705048), the Natural Science Foundation of Guangdong Province (2021A1515012333), Research Fellow (Grant No. 328933), the Solution for Health Profile (336355), and the InFLAMES Flagship (337531) grants from the Academy of Finland, and the Finland China Food and Health International Pilot Project funded by the Finnish Ministry of Education and Culture. The Key Laboratory of Sensing Technology and Biomedical Instruments of Guangdong Province (2020B1212060077). Ruijin Hospital Guangci Introducing Talent Project. Electron microscopy

samples were processed and analyzed in the Electron Microscopy Laboratory, University of Turku; confocal/flow cytometry were performed at the Cell Imaging Core, Turku Bioscience Centre. Biocenter Finland is acknowledged for providing support and infrastructure.

References

- 1 J. Li, C. Zheng, S. Cansiz, C. Wu, J. Xu, C. Cui, Y. Liu, W. Hou, Y. Wang, L. Zhang, I. t. Teng, H.-H. Yang and W. Tan, *J. Am. Chem. Soc.*, 2015, **137**, 1412–1415.
- 2 H. Qiao, L. Zhang, D. Fang, Z. Zhu, W. He, L. Hu, L. Di, Z. Guo and X. Wang, *Chem. Sci.*, 2021, **12**, 4547–4556.
- 3 L. Wu, W. Zhou, L. Lin, A. Chen, J. Feng, X. Qu, H. Zhang and J. Yue, *Bioact. Mater.*, 2021, **7**, 292–323.
- 4 S. Banerjee, H. Cui, N. Xie, Z. Tan, S. Yang, M. Icyuz, V. J. Thannickal, E. Abraham and G. Liu, *J. Biol. Chem.*, 2013, **288**, 35428–35436.
- 5 V. Baumann and J. Winkler, *Future Med. Chem.*, 2014, **6**, 1967–1984.
- 6 C. F. Bennett, A. R. Krainer and D. W. Cleveland, *Annu. Rev. Neurosci.*, 2019, **42**, 385–406.
- 7 J. Shen, L. Zhang, J. Yuan, Y. Zhu, H. Cheng, Y. Zeng, J. Wang, X. You, C. Yang, X. Qu and H. Chen, *Anal. Chem.*, 2021, **93**, 15033–15041.
- 8 Y. Zhang, J. Tu, D. Wang, H. Zhu, S. K. Maity, X. Qu, B. Bogaert, H. Pei and H. Zhang, *Adv. Mater.*, 2018, **30**, e1703658.
- 9 Y. S. Zhang and A. Khademhosseini, *Science*, 2017, **356**(6337), eaaf3627.
- 10 R. Zhong, Q. Tang, S. Wang, H. Zhang, F. Zhang, M. Xiao, T. Man, X. Qu, L. Li, W. Zhang and H. Pei, *Adv. Mater.*, 2018, **30**, e1706887.
- 11 N. Li, X. Y. Wang, M. H. Xiang, J. W. Liu, R. Q. Yu and J. H. Jiang, *Anal. Chem.*, 2019, **91**, 2610–2614.
- 12 Z. Li, L. Jiang, Y. Jiang, X. Yuan, M. Aizitaili, J. Yue and X. Qu, *Adv. Intell. Syst.*, 2020, **2**, 2000086.
- 13 T. Yata, Y. Takahashi, M. Tan, H. Nakatsuji, S. Ohtsuki, T. Murakami, H. Imahori, Y. Umeki, T. Shiomi, Y. Takakura and M. Nishikawa, *Biomaterials*, 2017, **146**, 136–145.
- 14 J. Song, K. Im, S. Hwang, J. Hur, J. Nam, G. O. Ahn, S. Hwang, S. Kim and N. Park, *Nanoscale*, 2015, **7**, 9433–9437.
- 15 J. Zhao, P. Zhang, Z. He, Q. H. Min, E. S. Abdel-Halim and J. J. Zhu, *Chem. Commun.*, 2016, **52**, 5722–5725.
- 16 S. Griffiths-Jones, R. J. Grocock, S. van Dongen, A. Bateman and A. J. Enright, *Nucleic Acids Res.*, 2006, **34**, D140–D144.
- 17 Y. H. Feng and C. J. Tsao, *Biomed. Rep.*, 2016, **5**, 395–402.
- 18 F. Sicard, M. Gayral, H. Lulka, L. Buscail and P. Cordelier, *Mol. Ther.*, 2013, **21**, 986–994.
- 19 S. R. Pfeffer, C. H. Yang and L. M. Pfeffer, *Drug Dev. Res.*, 2015, **76**, 270–277.
- 20 M. Aizitaili, Y. Jiang, L. Jiang, X. Yuan, K. Jin, H. Chen, L. Zhang and X. Qu, *Nano Lett.*, 2021, **21**, 2141–2148.

- 21 L. Chen, G. Li, X. Wang, J. Li and Y. Zhang, *ACS Nano*, 2021, **15**, 11929–11939.
- 22 Y. Chen, X. Gong, Y. Gao, Y. Shang, J. Shang, S. Yu, R. Li, S. He, X. Liu and F. Wang, *Chem. Sci.*, 2021, **12**, 15710–15718.
- 23 T. Kim, K. Nam, Y. M. Kim, K. Yang and Y. H. Roh, *ACS Nano*, 2021, **15**, 1942–1951.
- 24 S. Dobres, G. Mula, J. Sauer and D. Zhu, *Eng. Regen.*, 2022, **3**, 13–23.
- 25 J. Gaćanin, C. V. Synatschke and T. Weil, *Adv. Funct. Mater.*, 2020, **30**, 1906253.
- 26 S. Liu, W. Su, Y. Li, L. Zhang and X. Ding, *Biosens. Bioelectron.*, 2018, **103**, 1–5.
- 27 K. Shi, B. Dou, C. Yang, Y. Chai, R. Yuan and Y. Xiang, *Anal. Chem.*, 2015, **87**, 8578–8583.
- 28 G. Brachi, F. Bussolino, G. Ciardelli and C. Mattu, *Front. Bioeng. Biotechnol.*, 2019, **7**, 307.
- 29 X. Fu, X. Zhang, D. Huang, L. Mao, Y. Qiu and Y. Zhao, *Chem. Eng. J.*, 2022, **431**, 133362.
- 30 C. Chen, W. Yao, W. Sun, T. Guo, H. Lv, X. Wang, H. Ying, Y. Wang and P. Wang, *Int. J. Biol. Macromol.*, 2019, **122**, 1090–1099.
- 31 Z. Lu, J. Wang, L. Qu, G. Kan, T. Zhang, J. Shen, Y. Li, J. Yang, Y. Niu, Z. Xiao, Y. Li and X. Zhang, *Bioact. Mater.*, 2020, **5**, 1127–1137.
- 32 Q. Hu, H. Li, L. Wang, H. Gu and C. Fan, *Chem. Rev.*, 2019, **119**, 6459–6506.
- 33 S. Jiang, Z. Ge, S. Mou, H. Yan and C. Fan, *Chem*, 2021, **7**, 1156–1179.
- 34 T. A. Mace, A. L. Collins, S. E. Wojcik, C. M. Croce, G. B. Lesinski and M. Bloomston, *J. Surg. Res.*, 2013, **184**, 855–860.
- 35 Y. Li, Y. Chen, J. Li, Z. Zhang, C. Huang, G. Lian, K. Yang, S. Chen, Y. Lin, L. Wang, K. Huang and L. Zeng, *Cancer Sci.*, 2017, **108**, 1493–1503.
- 36 B. R. Wolfe, N. J. Porubsky, J. N. Zadeh, R. M. Dirks and N. A. Pierce, *J. Am. Chem. Soc.*, 2017, **139**, 3134–3144.
- 37 J. Yan, X. Xu, J. Zhou, C. Liu, L. Zhang, D. Wang, F. Yang and H. Zhang, *ACS Appl. Bio Mater.*, 2020, **3**, 1216–1225.
- 38 W. Mao, C. Hu, H. Zheng, J. Xie, X. Shi, Y. Du and F. Wang, *Mol. Ther.–Nucleic Acids*, 2020, **22**, 27–37.
- 39 J. Liu, W. Liu, K. Zhang, J. Shi and Z. Zhang, *Adv. Healthcare Mater.*, 2020, **9**, e1901316.
- 40 E. Giovannetti, N. Funel, G. J. Peters, M. Del Chiaro, L. A. Erozeñci, E. Vasil, L. G. Leon, L. E. Pollina, A. Groen, A. Falcone, R. Danesi, D. Campani, H. M. Verheul and U. Boggi, *Cancer Res.*, 2010, **70**, 4528–4538.
- 41 S. R. Filios and A. Shalev, *Diabetes*, 2015, **64**, 3631–3644.
- 42 C. Strasser, P. Grote, K. Schauble, M. Ganz and E. Ferrando-May, *Nucleus*, 2012, **3**, 540–551.
- 43 L. Lindenboim, H. Zohar, H. J. Worman and R. Stein, *Cell Death Discovery*, 2020, **6**, 29.

An Autocatalytic Deoxyribozyme Based Nanomachine for Orthotopic Pancreatic Tumor Targeted and Multilevel Synergistic Photothermal Therapy

Jiaqi Yan, Xiaodong Ma, Danna Liang, Dongdong Zheng, Meixin Ran, Shichong Zhou, Weijian Sun*, Xian Shen*, Hongbo Zhang*. *Nature Communications*. **2023**, 14, 6905. (<https://doi.org/10.1038/s41467-023-42740-2>)



An autocatalytic multicomponent DNzyme nanomachine for tumor-specific photothermal therapy sensitization in pancreatic cancer

Received: 25 May 2023

Accepted: 20 October 2023

Published online: 30 October 2023



Jiaqi Yan^{1,2,3,4,7}, Xiaodong Ma^{3,4,7}, Danna Liang^{5,7}, Meixin Ran^{1,2,3,4,7}, Dongdong Zheng⁶, Xiaodong Chen^{1,2}, Shichong Zhou⁶, Weijian Sun⁵✉, Xian Shen^{1,2}✉ & Hongbo Zhang^{1,2,3,4}✉

Multicomponent deoxyribozymes (MNAzymes) have great potential in gene therapy, but their ability to recognize disease tissue and further achieve synergistic gene regulation has rarely been studied. Herein, Arginylglycylaspartic acid (RGD)-modified Distearyl acylphosphatidyl ethanolamine (DSPE)-polyethylene glycol (PEG) (DSPE-PEG-RGD) micelle is prepared with a DSPE hydrophobic core to load the photothermal therapy (PTT) dye IR780 and the calcium efflux pump inhibitor curcumin. Then, the MNAzyme is distributed into the hydrophilic PEG layer and sealed with calcium phosphate through biomineralization. Moreover, RGD is attached to the outer tail of PEG for tumor targeting. The constructed nanomachine can release MNAzyme and the cofactor Ca^{2+} under acidic conditions and self-assemble into an active mode to cleave heat shock protein (HSP) mRNA by consuming the oncogene miRNA-21. Silencing miRNA-21 enhances the expression of the tumor suppressor gene PTEN, leading to PTT sensitization. Meanwhile, curcumin maintains high intracellular Ca^{2+} to further suppress HSP-chaperone ATP by disrupting mitochondrial Ca^{2+} homeostasis. Therefore, pancreatic cancer is triple-sensitized to IR780-mediated PTT. The in vitro and in vivo results show that the MNAzyme-based nanomachine can strongly regulate HSP and PTEN expression and lead to significant pancreatic tumor inhibition under laser irradiation.

Mild photothermal therapy can avoid inflammation and tumor metastasis caused by excessive hyperthermia during cancer therapy¹. However, the curative effect of mild PTT is dramatically compromised by heat shock proteins (HSPs), which are produced by the cellular thermal defense mechanism^{2,3}. The combination of HSP small molecule inhibitors and photothermal agents has been considered an effective PTT strategy^{4,5}. Nevertheless, small molecule inhibitors normally suffer from obvious hysteric effects, since they can only inhibit already generated HSPs, rather than prevent the production of HSPs

before treatment⁶. Furthermore, small molecule inhibitors will inevitably inhibit HSPs in peritumoral tissues; therefore, unavoidable thermal diffusion during PTT will intensify the side effects of tumor treatment⁷. More importantly, targeting not only HSPs but also PTT-associated targets such as ATP^{8,9} and miRNA-21¹⁰ could also lead to a synergistic effect. Therefore, achieving multilevel PTT sensitization in specific cancer cells is of great significance.

Oligonucleotide therapeutic agents can regulate target genes intracellularly by means of supplementing downregulated genes¹¹ or

A full list of affiliations appears at the end of the paper. ✉ e-mail: fame198288@126.com; shenxian@wmu.edu.cn; hongbo.zhang@abo.fi

by sterically blocking or cleaving overexpressed genes¹² and possess irreplaceable advantages compared with traditional drugs¹³. A deoxyribozyme (DNAzyme) is a single-stranded DNA-based oligonucleotide therapeutic agent¹⁴ that contains a catalytic core flanked by two substrate arms that can be endowed with immense biocatalytic functions by employing various metal cofactors^{15,16}. Leveraging excellent programmability and intrinsic biocompatibility, DNAzymes can be constructed as specific-mRNA hydrolysis machines with multiple turnover rates¹⁷. Thus far, they have been utilized in many advanced applications, including disease biomarker detection¹⁸, intelligent release system construction^{19,20}, specific mRNA applications²¹, or even double-stranded DNA regulation with higher efficiency than the CRISPR-Cas9 system²². However, although researchers can accurately design DNAzymes with target gene-silencing functions, the “off-target” effects are still serious since the DNAzymes cannot regulate target genes in specific tissues²³. For example, under photothermal therapy (PTT), it is very difficult to use DNAzymes to silence HSP70 mRNA only in pancreatic tumor sites while retaining HSP70 function in paracancerous tissues, therefore distinguishing the two sites with different photothermal responsive sensitivities.

Multicomponent deoxyribozymes (MNAzymes) are further engineered inventions from the two most widely used DNAzymes (17E and 10-23)²⁴, which contain two partzyme strands created by splitting the DNAzyme at the catalytic core (Fig. 1a, b)²⁵. Each partzyme comprises half of each substrate's binding arm, target binding arm, and catalytic core²⁶. This engineered segmentation process endows MNAzymes with the ability to recognize cancer biomarkers^{27,28}. Although the category of target biomarker sequence (miRNA-155²⁷, miRNA-21²⁸, miRNA-10b²⁹, antibiotic resistance genes³⁰, SARS-CoV-2 virus sequence³¹, etc.) has been broadly explored for more than 10 years of MNAzyme development, the MNAzyme substrate strand has been mainly a stereotype for fluorescence/quencher-based signal detection (Fig. 1c) rather than biomarker-responsive target gene silencing (common stereotype sequences of

the cleavage site for 17E-based MNAzyme: 3'-TrArGG-5'^{24,25,27,28,32} and 10-23-based MNAzyme: 3'-CrUrGC-5'^{25,29,33}). Encouragingly, a recent study has demonstrated the potential of using miRNA for the self-assembly of MNAzymes to achieve tumor-targeted delivery³⁴. However, the investigation into the silencing of miRNA to further enhance the therapeutic effect has been neglected. The lack of such research represents a significant gap in the current understanding of this MNAzyme therapeutic concept, which therefore warrants further exploration in future studies.

Therefore, designing an MNAzyme system for mild PTT that considers the targeting effect of the cancer biomarker miRNA-21 and further regulates both miRNA-21³⁵ and HSP70 mRNA (substrate sequence) could effectively overcome the off-target problem and achieve a significant synergistic PTT effect. Silencing miRNA-21 can upregulate PTEN expression, which in turn sensitizes the tumor to PTT¹⁰, while inhibiting HSP70 can directly reduce the tumor's heat resistance. Notably, hybridization between miRNA and the partzyme target binding arm will silence the miRNA via a steric blocking function rather than RNase H-dependent degradation process^{36,37}. This silencing mechanism ensures the stable structure of partzyme/miRNA and guarantees the multiple-turnover substrate cleavage activity of MNAzyme.

Meanwhile, poor oligonucleotide delivery efficiency and low content of metal cofactors in tumor microenvironments also challenge the activity of MNAzyme in vivo for cancer therapy³⁸. As a result of the rapid and thriving development of nanomedicine, metal ion cofactors can be utilized for nanocarrier construction, with excellent particle encapsulation efficiency achieved through electrostatic interactions between the DNA phosphate backbone and mineral cofactors^{39,40}. In our case, to further enhance PTT sensitization, Ca²⁺ was chosen as a cofactor to activate the MNAzyme system. Calcium ions can also mediate mitochondrial calcium dysregulation, which disrupts the mitochondrial structure and results in the inhibition of the HSP-chaperone molecule ATP⁴¹.

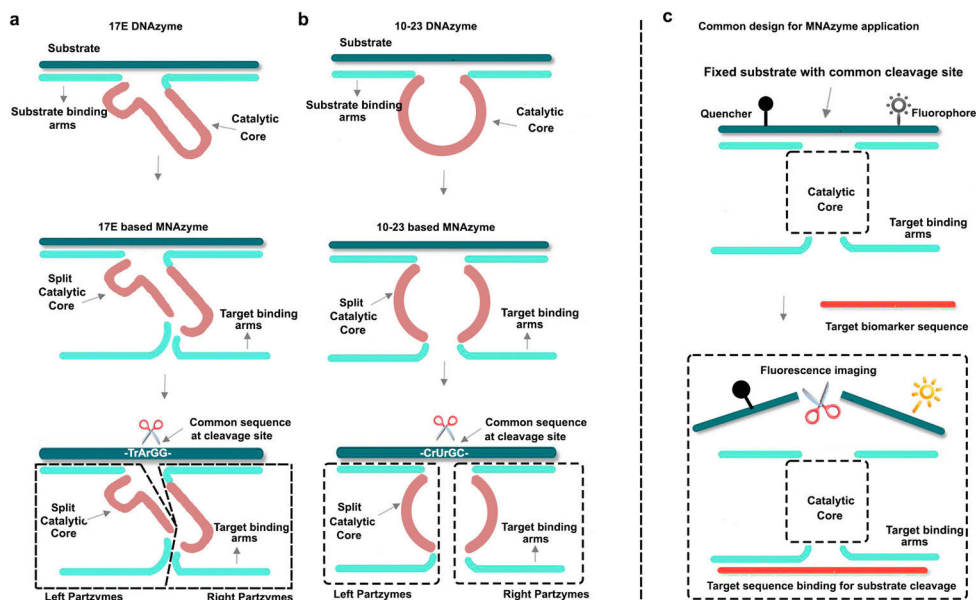


Fig. 1 | Structures of MNAzymes. a 17E-based MNAzyme. **b** 10-23-based MNAzyme. **c** Common design for MNAzyme-based applications.

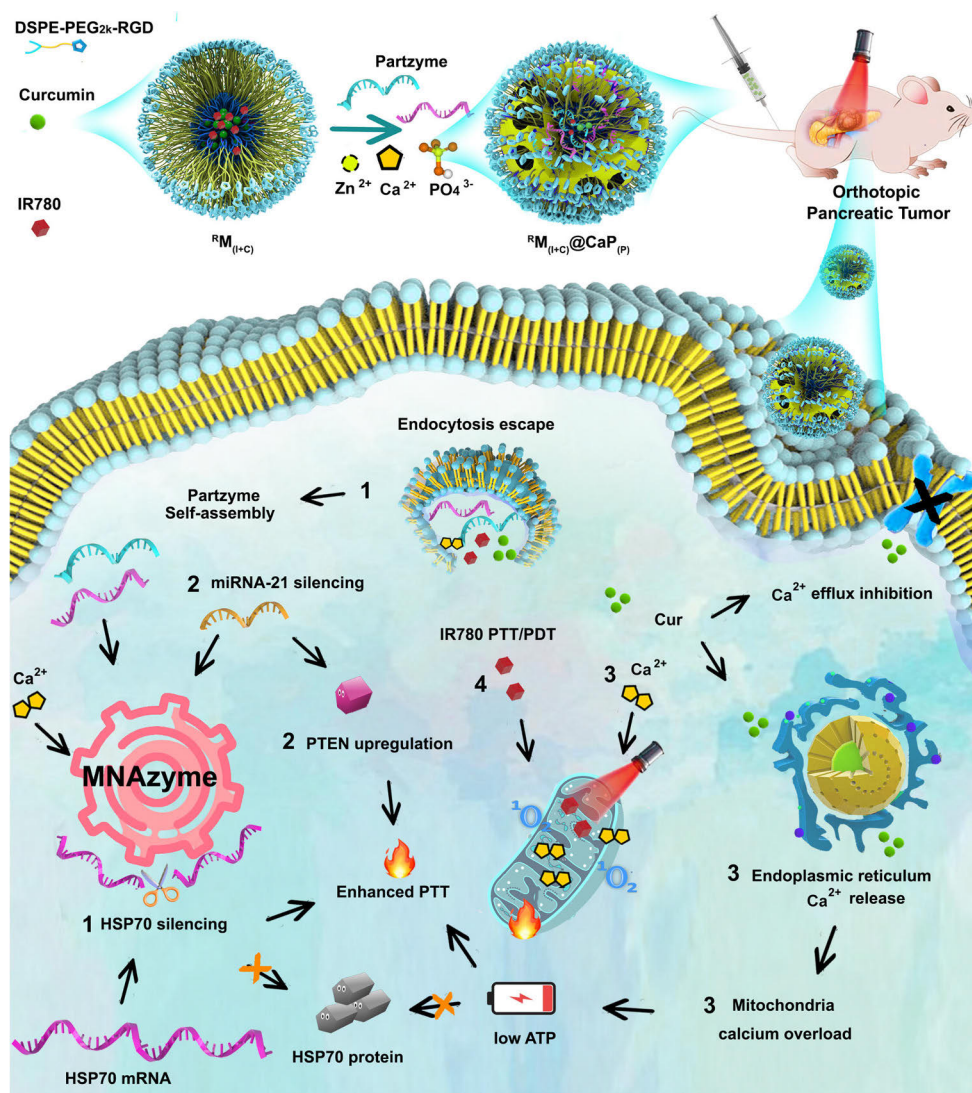


Fig. 2 | Illustration of four-step reactions after nanosystem fabrication and delivery. (1): The MNazyme will self-assemble on-site by consuming miRNA-21 and Ca²⁺ ions and silencing HSP70 mRNA before photothermal therapy (PTT) treatment. (2) Silencing miR-21 causes Phosphatase and TENSin homolog deleted on chromosome 10 (PTEN) upregulation for PTT sensitization. (3) Ca²⁺ will be

absorbed by mitochondria, and curcumin will promote the further release of Ca²⁺ from the ER and inhibit the Ca²⁺ efflux pump. Mitochondrial calcification can reduce HSP-chaperones adenosine triphosphate (ATP) production. (4): IR780 will target mitochondria to achieve precise mild PTT treatment and produce ROS-mediated photodynamic therapy.

In this work, we construct a miR-21-targeted MNazyme-powered HSP70 mRNA cleavage machinery to restrain HSP70 production before PTT treatment. We fabricate a DSPE-PEG_{2k} micelles modified with the tumor-targeting peptide RGD for the co-loading of the mitochondrion-targeted PTT dye IR780 and the Ca²⁺ efflux pump inhibition agent curcumin (abbreviated as $^R M_{(H+C)}$). The MNazyme is mineralized on the PEG layer of the micelle system using calcium

phosphate to form the final nanodevice, $^R M_{(H+C)}@CaP_{(P)}$ (Fig. 2). After cell internalization, CaP produce tremendous Ca²⁺ for lysosomal escape. As a result, some enzymes consume miRNA-21 and self-assemble into Ca²⁺-assisted MNazyme-powered HSP70 mRNA silencing machines in tumor tissues while retaining the HSP70 protection effect in healthy tissues. The silencing of miRNA-21 causes PTEN expression to be upregulated, which also sensitizes the tumor tissues to

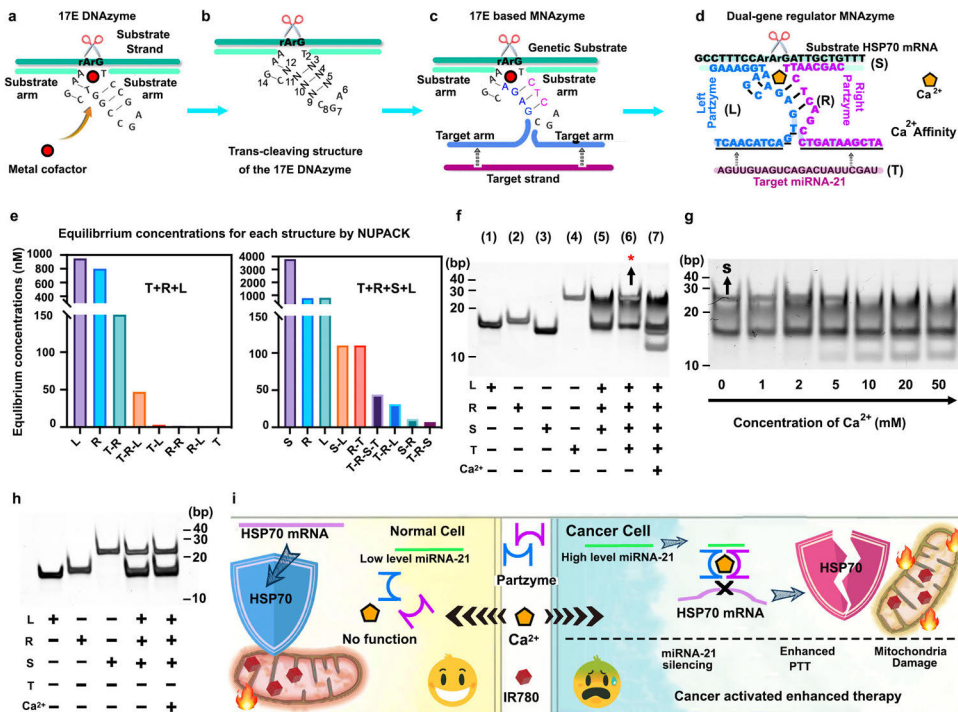


Fig. 3 | Architecture of the Ca²⁺-responsive MNazyme system for dual-gene adjustment. **a** Secondary structure of the traditional 17E DNAzyme. **b** Variant structures of the 17E DNAzyme. N represents the alternative site and can be an A, T, G, or C deoxynucleotide. **c** Structure of the Ca²⁺-responsive 17E-based MNazyme system. **d** The final MNazyme system with high Ca²⁺ affinity for miRNA-21 triggered HSP70 mRNA cleavage. **e** The NUPACK web application simulated the equilibrium concentration of each binding chance. **f** Twenty percent polyacrylamide gel

electrophoresis experiments for different formulations. **g** Verification of the Ca²⁺ concentration-dependent MNazyme system. **h** Cancer biomarker response test. **i** Construction logic of the cancer biomarker-responsive MNazyme system. The experiments in (f–h) were repeated three times independently with similar results. PTT photothermal therapy, T target strand, R right partzyme, L left partzyme, S substrate mRNA.

increase PTT efficiency. Further sensitization to IR780-mediated PTT is accomplished through Ca²⁺-induced multichannel mitochondria disruption due to curcumin-mediated calcium efflux pump inhibition and Ca²⁺ release from the endoplasmic reticulum (ER) in cancer cells. The addition of zinc prevents the phase transformation of amorphous CaP to hydroxyapatite, enhancing the stability of the nanoformulations during storage. Finally, we demonstrated the ability of the MNazyme system to selectively regulate tumor tissue and adjacent tissue in an orthotopic pancreatic cancer model.

Results

To build a miR-21 responsive DNAzyme system for HSP70 mRNA depletion, two common DNAzyme models (17E and 10-23) were chosen. These two DNAzymes are substrate-universal and can be tailored to recognize specific mRNAs by designing the substrate arm sequence⁴². Interestingly, the 17E DNAzyme was recently found to be more active than the 10-23 DNAzyme when the same metal cofactor at the same concentration was implemented⁴³. The catalytic ring structure of the 17E DNAzyme has also been fundamentally studied (Fig. 3a, b), and the substitution of different sequence fragments in the catalytic ring can affect the catalytic activity and responsiveness of the DNAzyme to different metal ions. For instance, 3-base-pair replacements at the stem position (N³-N⁵, N⁹-N¹¹), as well

as replacement of thymine (T) at the N¹² position adenine (A), can significantly enhance the Ca²⁺ affinity of the 17E DNAzyme (Fig. 3c)^{32,44}. Therefore, in this study, 17E DNAzyme was applied to design an efficient Ca²⁺-responsive MNazyme dual-gene regulation machine.

We first designed the Ca²⁺-specific MNazyme system by setting the target sequence as one complementary to miRNA-21 (abbreviated as T), while the substrate arm was engineered to match HSP70 mRNA (abbreviated as S). The MNazyme was split from the catalytic core and divided into the right partzyme (abbreviated as R) and left partzyme (abbreviated as L) (Fig. 3d). The NUPACK web application⁴⁵ was utilized to understand the possible reaction scenarios (Fig. 3e). From the final equilibrium system of the T + R + L system (each strand concentration was set as T = 0.2 μM, R = 1 μM and L = 1 μM), T (miRNA-21) showed a strong affinity with R (right partzyme), which formed a 150 nM complex; T and L (left partzyme) showed less combination efficiency (only 3 nM). Surprisingly, T, R and L formed a 47 nM MNazyme system (T-R-L). These simulation results unexpectedly indicated that the self-building of MNazyme consists of two processes: T and R achieve the first conjugation, and then L combines with the T-R complex to realize the second step of MNazyme construction. This step-by-step assembly can theoretically enhance the utilization efficiency of miRNA-21 for multiple-turnover cleavage of HSP70 mRNA in the case of low

partzyme content (Supplementary Fig. 1). Similarly, the T + R + S + L reaction simulation results (L = 1 μ M, R = 1 μ M, T = 0.2 μ M and S = 4 μ M) showed that the T-R-L system bound to the substrate S sequence and formed a 44 nM (T-R-S-L) complex. Of note, the T-R-S-L complex exhibited a lower free energy of secondary structure (−38.96 kcal/mol) compared with that of the T-R-L system (−27.84 kcal/mol), which revealed that the T-R-S-L structure was more stable (Supplementary Fig. 1).

Then, the feasibility of MNAzyme-based dual-gene modulation was evaluated in reality by 20% polyacrylamide gel electrophoresis (PAGE) tests (Fig. 3f). The individual L, R, S and T strands all showed clear bands (Lanes 1, 2, 3 and 4), while an obvious new band appeared upon incubation of L, R and T for 30 min at 37°C (L = 1 μ M; R = 1 μ M; T = 0.2 μ M, Lane 5). These results indicated that partzymes possessed strong binding affinity with miRNA-21, which facilitated efficient MNAzyme construction. For a deeper understanding of the multiple turnover catalytic cleavage effect of the MNAzyme system on the HSP70 substrate strand (S), we incubated excess S chain (4 μ M) with the abovementioned system, as revealed in Lane 6. A large amount of unreacted S strand appeared at the top of the band (marked with a red asterisk in Fig. 3f, Lane 6). Importantly, the S strand was not cleaved due to the lack of catalysis by the metal ions in Lane 6. Subsequently, when 10 mM Ca^{2+} was added to the system in Lane 7, the substrate chain S was cleaved and disappeared, and a new band was formed from the PAGE test result, as shown in Fig. 3f, Lane 7. These results demonstrated that our designed partzymes could utilize 0.2 μ M miRNA to achieve Ca^{2+} -mediated 4 μ M HSP70 multiple-turnover cleavage and consume all miRNA-21 to achieve dual gene regulation.

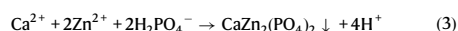
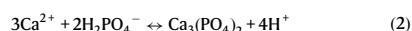
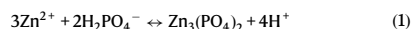
To further verify the metal ion dependence of the partzyme system, a substrate catalytic hydrolysis test was performed under different Ca^{2+} concentrations for 4 h (Fig. 3g). L (1 μ M) and R (1 μ M) strands together with 0.2 μ M T strand were applied. We found that as the Ca^{2+} concentration increased from 0 to 50 mM, the content of substrate S (4 μ M) gradually decreased, and the product amount consistently increased. Furthermore, the hydrolysis rate of substrate strand HSP70 mRNA reached saturation at ~20 mM Ca^{2+} . These results reflected that a high catalyst rate of the MNAzyme system could be guaranteed when sufficient calcium ions were present in the mRNA regulation system.

Ultimately, to demonstrate the cancer responsiveness of the designed partzymes, i.e., their safety in healthy tissues, we carried out another PAGE assessment to investigate the hydrolysis performance of the MNAzyme system for HSP70 mRNA in the absence of miRNA-21 (with 50 mM Ca^{2+}) (Fig. 3h). We observed that although in the presence of sufficient Ca^{2+} , partzymes could not self-assemble into MNAzymes to mediate the catalytic hydrolysis of HSP70 mRNA. Therefore, hypothetically, when partzymes, Ca^{2+} and a photothermal therapeutic agent (IR780) are simultaneously delivered to the tumor microenvironment (TME), the partzymes can distinctively self-assemble into an MNAzyme-driven HSP70 mRNA-regulating machine in specific miRNA-21-overexpressing pancreatic cancer cells. These processes avoid hysteresis effects by preventing the generation of heat shock proteins at the mRNA level before photothermal treatment. Moreover, during the assembly process of MNAzymes, most of the miRNA-21 within the TME will be consumed, thus realizing dual-gene regulation for both the pathogenic gene miRNA-21 and the therapeutic stimulated gene HSP70 (Fig. 3i).

The miRNA-21-dependent self-construction process of MNAzyme and the specific gene cleaving function under Ca^{2+} triggering have been verified, yet the intracellular activation of the MNAzyme system suffers from poor cellular internalization and low cytoplasmic Ca^{2+} content (~0.1 μ M)⁴⁶. Therefore, a smart and robust partzyme delivery strategy using Ca^{2+} as the multicargo carrier component to achieve target site Ca^{2+} enhancement has been explored. Nanostructured amorphous calcium phosphate (CaP) has been broadly investigated as an excellent nuclear acid delivery system owing to its high affinity for

the gene phosphate backbone (Fig. 4a)⁴⁷, pH-responsive degradability and sustained release performance⁴⁸. However, amorphous calcium phosphate (ACP) composed of Posner's clusters ($\text{Ca}_9(\text{PO}_4)_6$) is an unstable precursor that can dissolve and renucleate as hydroxyapatite (HA) within a few minutes in aqueous solution^{49,50}, causing inefficient cargo delivery. To verify this phenomenon, transmission electron microscopy (TEM) was utilized to systematically observe the crystal transformation of ACP, as shown in Fig. 4b. We found that the ACP was a complete and smooth sphere with irregular channels on its surface within 10 min of preparation. However, the storage of APC in Milli-Q water resulted in the dissolution of ACP (>1 h), nucleation (>3 h) and full crystallization to HA after 48 h. Moreover, we also found that this crystal transformation process could take place in the cell culture medium after 24 h of incubation and that the large size and irregular needle-like shape structure made it difficult to deliver nucleotide drugs and even calcium ions into cells (Fig. 4c).

The zinc additive was found to stabilize the ACP phase for more than 20 days when the Zn/Ca ratio was 10%⁵¹. In the reaction system in which Zn^{2+} and Ca^{2+} existed simultaneously, the chemical reactions followed the equations below⁵²:



In this way, highly stable ACP NPs were fabricated, as depicted in Fig. 4d, which contributed to the mechanism by which smaller zinc ions can easily replace Ca^{2+} in ACP and inhibit crystallization by distorting atomic order and reducing ACP solubility⁵¹. To assess the content of Ca^{2+} and DNAs, we used two different assay kits to measure the concentrations of Ca^{2+} and Zn^{2+} ions within the nanosystem, and we found the concentration of zinc ions to be 196 μ g and the concentration of calcium ions to be 1280 μ g within 3.5 mg Zn-doped CaP NPs.

Nevertheless, Zn^{2+} -substituted APC NPs did not possess cancer cell-enhanced endocytosis, and surface pores were reduced by the tight cooperation between zinc and phosphate ions, resulting in the inability to load multiple therapeutics. To resolve the abovementioned difficulties, RGD-modified DSPE-PEG amphiphilic micelles (⁶M) were used as the synthesis template of Zn^{2+} -doped CaP since the negatively charged oxygen atom of the $\text{CH}_2\text{-O-CH}_2$ group in PEG can attract Ca^{2+} or Zn^{2+} through electrostatic attraction (Fig. 4e)⁵³. Meanwhile, the micelles can be loaded with multiple hydrophobic drugs, and RGD can realize cancer cell targeting⁵⁴.

We first synthesized IR780/Cur-loaded micelles, and a spherical structure of ~50 nm could be seen under TEM (Fig. 4f, ⁸M_(1+1C)). During preparation, we found that 50 mg of DSPE-PEG-RGD could carry up to 7.98 mg of IR780 and 2.06 mg of Cur. (Tables S1 and S2). To achieve the optimal synergistic treatment ratio of both drugs after being loaded by the nanosystem, the loading weight ratio of IR780:Cur (mg) was adjusted to 0:2, 0.5:2, 1:2, 2:2, 4:2, and 8:2 to calculate the coefficient of drug interaction (CDI)^{55,56}. The calculation was based on the WST-1 absorbance results, which compared the viability of cells after treatment with different drug ratios of nanoparticles. The equation is as follows:

$$\text{CDI} = \text{AB}/(\text{A} \times \text{B}) \quad (4)$$

where AB is the absorbance of the combination groups to the control group, while A or B is the absorbance of the single-agent group to the control group (CDI > 1, =1, <1 indicates antagonism, additivity and synergism). In accordance with the WST-1 results, a 4:2 ratio (4 mg

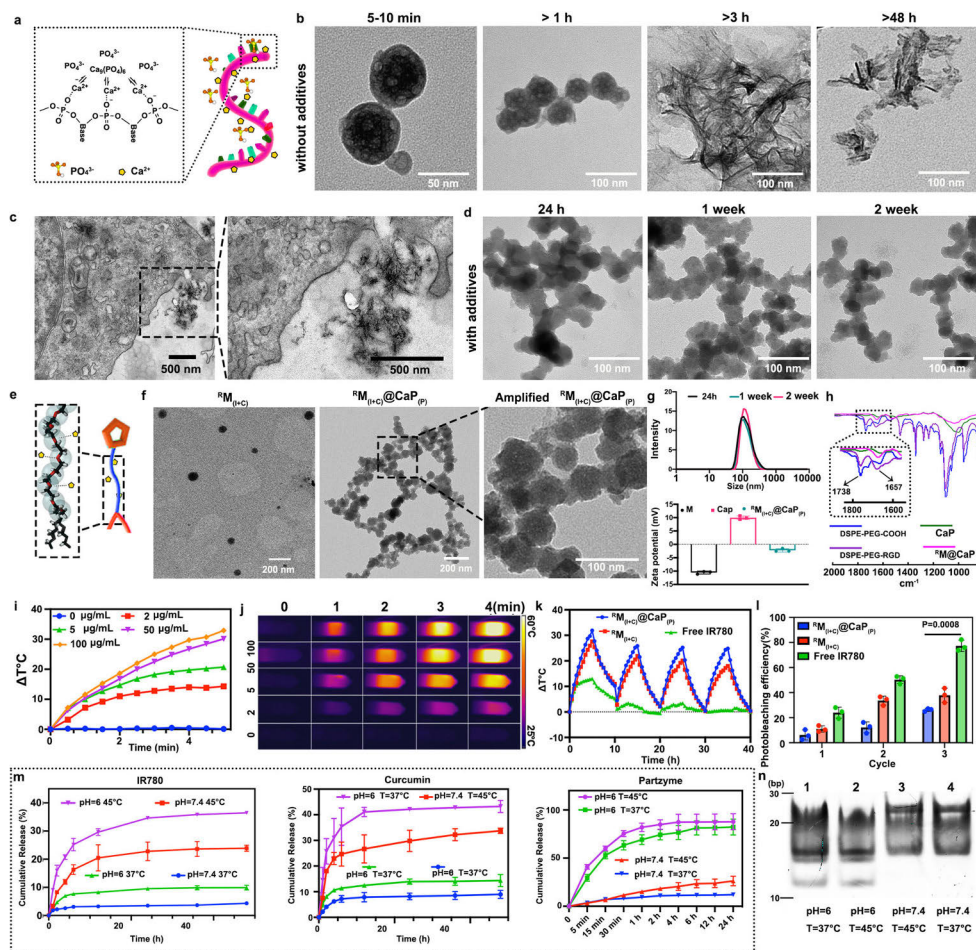


Fig. 4 | Construction, drug loading and photothermal characterization of the designed nanosystem. **a** Schematic illustration of the DNA and CaP biomimetic mineralization process. **b** Degradation process of CaP in Milli-Q aqueous solution. **c** PANC-1 cells were incubated with APC nanoparticles for 24 h. **d** Stability for Zn-substituted CaP in Milli-Q aqueous solution. **e** Interaction between PEG and Ca^{2+} and Zn^{2+} . Carbon, oxygen, and hydrogen atoms are labeled with black, red, and white, respectively. **f** TEM images of $^6\text{M}_{(\text{I-C})}$ and $^6\text{M}_{(\text{I-C})}@\text{CaP}_{(\text{p})}$. **g** Size distribution of $^6\text{M}_{(\text{I-C})}@\text{CaP}_{(\text{p})}$ NPs within 2 weeks and zeta potential results for $^6\text{M}_{(\text{I-C})}$, Zn-doped CaP and $^6\text{M}_{(\text{I-C})}@\text{CaP}_{(\text{p})}$ ($n = 3$ independent experiments, and the data are presented as the mean values \pm SDs). **h** FTIR results for Zn-substituted CaP and $^6\text{M}@\text{CaP}$. **i** Photothermal heating curves of $^6\text{M}_{(\text{I-C})}@\text{CaP}_{(\text{p})}$ NPs with different

concentrations of IR780. **j** The infrared thermal images correspond with photothermal heating curves. **k** Temperature elevation of $^6\text{M}_{(\text{I-C})}@\text{CaP}_{(\text{p})}$ NPs over four rounds of NIR on-off irradiation cycles. **l** Photobleaching effects of pure drug and nanoparticles after three rounds of laser irradiation ($n = 3$ independent experiments, and the data are presented as the mean values \pm SDs). **m** Drug-releasing capacity of $^6\text{M}_{(\text{I-C})}@\text{CaP}_{(\text{p})}$ under different situations ($n = 3$ independent experiments and the data are presented as the mean values \pm SDs). **n** Cleavage capacity of HSP70 mRNA after partzyme release from different environments. All statistics were calculated using two-tailed paired t tests, and the experiments in (b–d, f, n) were repeated three times independently with similar results. The source data from (g, h, i, k, l, m) are provided as a Source Data file.

IR780 and 2 mg Cur within 50 mg DSPE-PEG-RGD) exhibited the best CDI = 0.52 (Tables S3 and S4).

After attaining the proper drug loading, we further determined the optimum dose of partzyme, and PO_4^{3-} , Zn^{2+} and Ca^{2+} were utilized to mineralize partzyme (P), as shown in Fig. 4f, $^6\text{M}_{(\text{I-C})}@\text{CaP}_{(\text{p})}$. For silencing miRNA-21 in pancreatic cancer cell lines, it has been reported that the concentration of miRNA-21 antisense oligonucleotides needs to reach 100 nM to achieve a significant gene-silencing effect^{57,58}.

Hence, the therapeutic concentration of partzyme, which also serves as a miRNA silencing agent, should also reach 100 nM. To confirm the efficient partzyme loading content of our designed nanosystem, we carried out a gradient partzyme loading test (Supplementary Fig. 2). Left and right partzymes were labeled with Cy3 and mixed with 1 ml $^6\text{M}_{(\text{I-C})}$ solution (one/tenth upper-mentioned micelle volume, which contained 0.4 mg IR780 and 0.2 mg Cur) to yield different concentrations of each partzyme (1, 10, 50, 100, and 200 μM). After

calcium phosphate mineralization, we found that all partzymes were centrifuged to the bottom of the tube (even when the content was as high as 200 μM), and there was no leakage of partzyme after several washes with Milli-Q water. Therefore, the system had excellent partzyme encapsulation efficiency and eliminated the burst release phenomenon of oligonucleotides through a rational biomineralization process to easily achieve a 100 nM therapeutic concentration.

To further demonstrate the successful synthesis of $^{\text{M}}_{\text{(I+C)}}$, $\text{CaP}_{\text{(p)}}$ and $^{\text{M}}_{\text{(I+C)@CaP}_{\text{(p)}}$, dynamic light scattering (DLS) and Fourier transform infrared spectroscopy (FTIR) were used to characterize the particle size, zeta potential and characteristic chemical bond of the nanocarrier. The particle size analysis revealed that $^{\text{M}}_{\text{(I+C)}}$ possessed a similar average diameter as $^{\text{M}}_{\text{(I+C)@CaP}_{\text{(p)}}$, at -100 ± 15 nm (Supplementary Fig. 3), which was larger than the TEM results (~ 50 nm) due to the aqueous layer out of the DLS specimen³⁹. Notably, $^{\text{M}}_{\text{(I+C)@CaP}_{\text{(p)}}$ was found to be very stable (with the same size) in aqueous solution for more than 2 weeks (Fig. 4g), suggesting that this nanosystem possessed excellent stability, which may have occurred through a combination of zinc-additive and steric repulsion forces between the PEG chains. Additionally, in PBS buffer at pH = 7.4 (Fig. 4g), $^{\text{M}}_{\text{(I+C)}}$ was observed to have a zeta potential of -10.21 mV, which may have been attributable to the carboxyl groups on RGD. Furthermore, the Zn^{2+} -substituted $\text{CaP}_{\text{(p)}}$ showed a strong positive charge (10.01 mV). Through the elemental mapping experiment, we found that the Zn ions and calcium ions were distributed throughout the NPs; hence, the positive charge may have been due to the uncoordinated calcium and zinc ions on its surface (Supplementary Fig. 4). Finally, we found that the final formulation $^{\text{M}}_{\text{(I+C)@CaP}_{\text{(p)}}$ exhibited -2.53 mV, which might have been caused by the outermost exposed RGD that renders the formulation slightly electronegative. Based on the aforementioned results, we conducted stability assessments on the final formulation of our nanomaterial in accordance with the guidelines provided by the International Council for Harmonisation of Technical Requirements for Pharmaceuticals for Human Use (ICH) Supplementary Table S5. We investigated the stability of the formulation at refrigerator temperature ($4-8^{\circ}\text{C}$) and under accelerated conditions at 40°C , by following with the ICH guidelines, specifically ICH Q1A(R2) for long-term stability testing. The results of these stability studies indicated that there was no significant increase ($p > 0.05$) in particle size or polydispersity index (PDI) throughout the 3-month experimental period.

The FT-IR spectrum of DSPE-PEG-COOH reflected an absorbance band at 1738 cm^{-1} , corresponding to the $-\text{COOH}$ groups⁶⁰. After RGD modification, there was a newly formed band at 1657 cm^{-1} belonging to the $\text{O}=\text{C}-\text{N}-\text{H}$ group between PEG and RGD connections within micelles⁶⁰. Subsequently, the micelles were coated by CaP, and the band at 1657 cm^{-1} was also found in the $^{\text{M}}_{\text{(I+C)@CaP}}$ group compared with the pure CaP group. These results together demonstrated the successful incorporation of CaP nanoparticles with the DSPE-PEG-RGD micelles (Fig. 4h).

IR780, as a PTT and PDT agent, suffers from poor aqueous solubility and high photobleaching properties and was protected inside micelles in this study for higher drug loading content and enhanced therapeutic effects. To examine the photothermal conversion properties of the final formulation, $^{\text{M}}_{\text{(I+C)@CaP}_{\text{(p)}}$, which contains different concentrations of IR780 (0, 2, 5, 50, 100 $\mu\text{g}/\text{ml}$), was irradiated with an 808 nm laser (1 W cm^{-2}) for 300 s (Fig. 4i). The corresponding infrared photos are shown in Fig. 4j. The results showed that the photothermal conversion properties of $^{\text{M}}_{\text{(I+C)@CaP}_{\text{(p)}}$ displayed a positive correlation with the NP concentration. The solution temperature increased by up to 20°C when only $5\text{ }\mu\text{g}/\text{ml}$ IR780 NPs were irradiated for 5 min (Fig. 4i, j), while pure water did not increase the temperature.

Furthermore, the photothermal conversion efficiency (η) of pure IR780, $^{\text{M}}_{\text{(I+C)}}$ and $^{\text{M}}_{\text{(I+C)@CaP}_{\text{(p)}}$ NPs was also studied through NIR heating-cooling cycles (1.0 W cm^{-2} , 808 nm) with $50\text{ }\mu\text{g}/\text{ml}$ IR780

(Fig. 4k). (η) was calculated by following Eqs. (5) and (6)⁵⁹:

$$\eta = \frac{hs\Delta T_{\text{max}} - Q}{I(1 - 10^{-A_{808}})} \quad (5)$$

Here, ΔT_{max} is the maximum temperature change value, while Q is the solvent increased heat, I is the power of the laser, A_{808} is the absorbance of the NPs at a wavelength of 808 nm, and hs is defined by another formula:

$$hs = \frac{mc}{\tau} \quad (6)$$

in which m and c are the specific heat capacity and mass of the solution, respectively, while τ is the slope of the fitted line of time to $-\ln \frac{\Delta T}{\Delta T_{\text{max}}}$.

The photothermal conversion efficiency of the pure drug was only 23.70% (Supplementary Fig. 5) due to the poor stability of IR780 in aqueous solution. In contrast, the η of $^{\text{M}}_{\text{(I+C)}}$ was converted up to 29.25% (Supplementary Fig. 6), which demonstrated that the micelle could prevent IR780 degradation. Surprisingly, the Zn^{2+} -containing dense CaP mineralization layer further improved the η of IR780 (33.70%, Supplementary Fig. 7), indicating that the final formulation significantly improved the photothermal stability of IR780. Furthermore, the photobleaching efficiency was additionally evaluated for the abovementioned IR780, $^{\text{M}}_{\text{(I+C)}}$ and $^{\text{M}}_{\text{(I+C)@CaP}_{\text{(p)}}$ groups (Fig. 4l). After three cycles of irradiation (1 W cm^{-2} , 5 min, 808 nm), free IR780 showed an $\sim 80\%$ decrease in absorbance at 780 nm, illustrating that free IR780 was rapidly degraded. Conversely, $^{\text{M}}_{\text{(I+C)}}$ reflected a 41% decrease in absorbance, and $^{\text{M}}_{\text{(I+C)@CaP}_{\text{(p)}}$ showed only a 23% decrease after 3 cycles of irradiation. Hence, compared with $^{\text{M}}_{\text{(I+C)}}$, $^{\text{M}}_{\text{(I+C)@CaP}_{\text{(p)}}$ realized an effective photothermal conversion ability of IR780.

To further estimate the pH-responsive drug release capacity, $^{\text{M}}_{\text{(I+C)@CaP}_{\text{(p)}}$ NPs (containing 0.4 mg of IR780, 0.2 mg of Cur and 200 μM partzyme) were subjected to release tests by dialysis membranes. Since IR780 generates heat under laser irradiation, it will promote the diffusion of drug molecules from the material, so different drug release environments with pH and temperature were designed (pH = 7, 37°C ; pH = 7, 45°C ; pH = 6, 37°C ; pH = 6, 45°C). Therapeutic agents were observed through UV-visible spectroscopy at 780, 425 and 560 nm (Supplementary Fig. 8). We observed that at 45°C , there was an increased release of the drug. Approximately 35% IR780 and 43% Cur were released at pH = 6 and 45°C , whereas only 9% IR780 and 14% Cur were released at pH = 6 and 37°C . A similar phenomenon was also found in the pH = 7 group. More than 20% IR780 and 30% curcumin were released at pH = 7 and 45°C . However, less than 5% of IR780 and 10% of curcumin were released at pH = 7 at 37°C .

Furthermore, we observed a pronounced pH-responsive release profile for partzymes since CaP possessed excellent pH-sensitive degradation performance, and more than 90% of the partzyme was released from the system after 4 h incubation at pH = 6 (Fig. 4m, partzyme). However, the degradation of CaP did not mediate significant release of Cur and IR780 at pH 6 compared to partzymes loaded in the CaP shell, reflecting that IR780 and Cur were loaded mainly inside the micelles. Subsequently, $1\text{ }\mu\text{l}$ of released medium from each group was further incubated with $1\text{ }\mu\text{l}$ of miRNA-21 (10 μM) and $2\text{ }\mu\text{l}$ of HSP70 mRNA (10 μM). We found that the released media in the pH = 6 groups efficiently cleaved HSP70 (Fig. 4n). Rapid release of partzymes ensured silencing of HSP70 before PTT treatment and prevented the previously mentioned hysteric effect.

Given the successful design and construction of the dual-gene regulation MNAzyme system and the productive fabrication of the $^{\text{M}}_{\text{(I+C)@CaP}_{\text{(p)}}$ nanovector with high partzyme loading and excellent aqueous stability, we next closely investigated the biocompatibility of

the carrier system by testing the toxicity of the pure nanocarrier and laser to the normal human dermal fibroblast NFDH cell line (Supplementary Fig. 9). We found that pure nanovehicle $^{\text{M}}\text{M}_{(\text{I+C})}\text{@CaP}_{(\text{p})}$ at a maximum concentration of 40.5 $\mu\text{g}/\text{ml}$ (which could carry 6 $\mu\text{g}/\text{ml}$ IR780 and 3 $\mu\text{g}/\text{ml}$ curcumin) was not toxic to healthy cells. Hence, based on the results in Supplementary Table S3, at effective therapeutic concentrations for PANC-1 cells (IR780: 4 $\mu\text{g}/\text{ml}$, Cur: 2 $\mu\text{g}/\text{ml}$), pure carriers should have negligible side effects. In addition, NFDH cells were irradiated with an 808 nm laser at different laser intensities (0, 0.5, 1, 1.5 and 2 W cm^{-2}), and it was found that a pure laser did not inhibit the growth of healthy cells (Supplementary Fig. 9). These results suggest that the $^{\text{M}}\text{M}_{(\text{I+C})}\text{@CaP}_{(\text{p})}$ system holds good biocompatibility and that the laser power we selected is safe for healthy cells.

Next, the cellular uptake of the pure drug, $\text{M}_{(\text{I+C})}\text{@CaP}_{(\text{p})}$ and $^{\text{M}}\text{M}_{(\text{I+C})}\text{@CaP}_{(\text{p})}$ groups by PANC-1 cells and the healthy control cell line NHDF (after 1 h and 8 h incubation) was observed by tracking the fluorescence of IR780 (red), Cy3-modified partzymes (green) and Cur (light blue) via confocal laser scanning microscopy (CLSM) and flow cytometry (Fig. 5a and Supplementary Figs. 10–12). The therapeutic concentrations were as follows: IR780: 4 $\mu\text{g}/\text{ml}$, Cur: 2 $\mu\text{g}/\text{ml}$ and partzyme: 2 μM . In the case of PANC-1 cells, the results revealed that the uptake content of each therapeutic agent gradually increased with the extension of the incubation time (Supplementary Figs. 10 and 5a). After 8 h of incubation with the pure drug group, IR780 and Cur were pronounced diffused into PANC-1 cells, while Cy3-labeled partzyme exhibited no internalization. However, for the $\text{M}_{(\text{I+C})}\text{@CaP}_{(\text{p})}$ group, IR780, Cur and Cy3-labeled partzyme were all endocytosed, which proved that the nanocarrier could ensure the internalization of partzyme. Meanwhile, after the decoration of RGD on top of the nanosystem, the $^{\text{M}}\text{M}_{(\text{I+C})}\text{@CaP}_{(\text{p})}$ group exhibited 2.2 times higher uptake efficiency than the $\text{M}_{(\text{I+C})}\text{@CaP}_{(\text{p})}$ group, which reflected that RGD, as a tumor-targeting tripeptide, could promote the endocytosis of NPs by pancreatic cancer PANC-1 cells. Inductively coupled plasma–optical emission spectrometry (ICP–OES) results indicated that the calcium ion concentration in the cancer cells was ~240 parts per million (ppm), which was sufficient to activate MNazymes (Supplementary Fig. 10).

In contrast, for NHDF cells, the pure drug, $\text{M}_{(\text{I+C})}\text{@CaP}_{(\text{p})}$ and $^{\text{M}}\text{M}_{(\text{I+C})}\text{@CaP}_{(\text{p})}$ groups all showed negligible uptake after 1 h of treatment (Supplementary Fig. 11). Meanwhile, only sporadic drug fluorescence signals were exhibited for the $\text{M}_{(\text{I+C})}\text{@CaP}_{(\text{p})}$ and $^{\text{M}}\text{M}_{(\text{I+C})}\text{@CaP}_{(\text{p})}$ groups after 8 h of incubation (Supplementary Fig. 12). These phenomena may be attributable to the weaker uptake capacities of normal cells⁴¹. The surface modification of RGD did not promote the ingestion of NPs by healthy NHDFs.

Having determined that the $^{\text{M}}\text{M}_{(\text{I+C})}\text{@CaP}_{(\text{p})}$ group could effectively deliver multiple cargoes into PANC-1 cells, we explored the intracellular endosomal escape. For both groups, after NPs and cells were cultured together for 2 h and 24 h, the cell media were replaced, and a 1 W laser was applied for 5 min. Here, IR780 is presented in red, and the lysosome is labeled in green. Pearson correlation coefficients (PCCs) were utilized to determine whether the two colors colocalized (>0.5 indicates moderate correlation; <0.5 indicates low correlation)^{61,62}. After 2 h of treatment with $^{\text{M}}\text{M}_{(\text{I+C})}\text{@CaP}_{(\text{p})}$ NPs without laser irradiation, we found that the red fluorescence (IR780) overlapped well with the green fluorescence of lysosomes (Fig. 5b). In addition, the PCC was calculated as 0.673 (higher than 0.5), demonstrating the colocalization of IR780 and lysosomes. After 1 W cm^{-2} 808 nm laser irradiation for 5 min, the PCC number dropped to 0.582 but still showed a colocalized effect. For the $^{\text{M}}\text{M}_{(\text{I+C})}\text{@CaP}_{(\text{p})}$ NPs after 24 h of treatment, lower overlap between IR780 and lysosomes was observed, and the PCC value was 0.454. Notably, there was almost no overlap between red and green fluorescence after laser irradiation (PCC = 0.413), confirming that the therapeutic agents could efficiently escape from the lysosome.

After validating that the therapeutics could be efficiently delivered to the cytoplasm, we further studied the functional performance of each nanosystem component (MNazyme, IR780, Cur and Ca^{2+}) in PANC-1 cells. For the MNazyme system, self-assembly into MNazyme should be achieved by the released partzymes and endogenously overexpressed miRNA-21, which then autocatalytically trigger its substrate (HSP70 mRNA) cleavage function with the assistance of Ca^{2+} (Fig. 5c). Subsequently, the silencing of miRNA-21 can mediate the increased expression of the tumor suppressor protein PTEN, while the HSP70 protein should be downregulated after HSP70 mRNA cleavage.

Based on the above assumptions, to verify that the partzymes could bind to intracellular miRNA-21, the fluorescence in situ hybridization (FISH) method was used to observe intracellular free miRNA-21 (Fig. 5d). Four groups, including the PBS, IR780+Cur, $^{\text{M}}\text{M}_{(\text{I+C})}\text{@CaP}_{(\text{p})}$ (without partzymes) and $^{\text{M}}\text{M}_{(\text{I+C})}\text{@CaP}_{(\text{p})}$ (with partzymes) groups, were used, and endogenous miRNA-21 was labeled red. From the results, we observed that the PBS groups exhibited tremendous Cy5.5 fluorescence (miRNA), while when IR780 and curcumin were added, the fluorescence intensity of miRNA decreased by nearly 32%. It has been reported that curcumin can regulate a variety of miRNAs (including miRNA-21) in other cancer cell lines⁶³. Hence, curcumin could also inhibit endogenous miRNA-21 in the PANC-1 cell line. Of note, during the experiments, all the therapeutics containing cell culture medium were replaced at the 6 h timepoint, which resulted in a shorter intracellular retention time for the pure drug, while the nanosystem promoted the retention time and therapeutic efficiency of Cur. As a result, the red fluorescence intensity in the $^{\text{M}}\text{M}_{(\text{I+C})}\text{@CaP}_{(\text{p})}$ group was decreased by ~76%. More interestingly, from the results of the $^{\text{M}}\text{M}_{(\text{I+C})}\text{@CaP}_{(\text{p})}$ group, the red fluorescence intensity was reduced almost to zero, indicating that the partzyme system could efficiently utilize miRNA-21 and ensure MNazyme formation.

Subsequently, to explore whether MNazyme can effectively downregulate the expression of HSP70 protein and mediate the increase in the expression of PTEN protein in PANC-1 cells, western blot experiments were performed, and the relative HSP70/GAPDH and PTEN/GAPDH ratios were calculated with ImageJ, as shown in Fig. 5e. For the HSP70 protein, compared with | PBS (1 and 2), we found that IR780+Cur with laser treatment (4) significantly upregulated HSP70 expression (1.8 times), which indicates that PTT can activate HSP70 to protect cells from thermal stress⁴⁴. Surprisingly, for the $^{\text{M}}\text{M}_{(\text{I+C})}\text{@CaP}_{(\text{p})}$ groups (5 and 6), the expression of HSP70 was downregulated by nearly 40% (-laser) and 20% (+laser). It has been reported that the generation of HSPs highly depends on ATP production^{8,9}. Since our nanosystem will trigger multichannel Ca^{2+} ions inside cells to cause mitochondrial calcium overload (Figs. 6 and 7), ATP production by damaged mitochondria should decline and lead to a decrease in HSP70 content. Ultimately, from the results of the $^{\text{M}}\text{M}_{(\text{I+C})}\text{@CaP}_{(\text{p})}$ groups with partzymes 7 and 8, the HSP70 gene was fully eliminated for both the \pm laser groups, suggesting the effective HSP70 mRNA cleavage function of the MNazyme system.

PTEN protein expression should be upregulated owing to the silencing of miRNA-21. From the results, compared with the PBS groups (1 and 2), the pure drug groups (3 and 4) showed slight upregulation of PTEN expression due to the inhibitory effect of curcumin. Meanwhile, the relative ratio of PTEN/GAPDH for the $^{\text{M}}\text{M}_{(\text{I+C})}\text{@CaP}_{(\text{p})}$ groups (5 and 6) was ~2 times higher than that of the PBS groups, which might have been caused by the long-term Cur-mediated decrease in miRNA-21. Furthermore, for the $^{\text{M}}\text{M}_{(\text{I+C})}\text{@CaP}_{(\text{p})}$ groups (7 and 8), a significant increase in the PTEN/GAPDH relative ratio (3 times higher than that of the PBS groups) was observed, demonstrating the miRNA-21 silencing effect of the MNazyme system.

Considering that the MNazyme system has a targeted therapeutic effect on cancer cells, we further investigated MNazyme function in healthy NFDH cells in eight groups. The FISH method was first utilized to compare the miRNA-21 content between NFDH cells and PANC-1

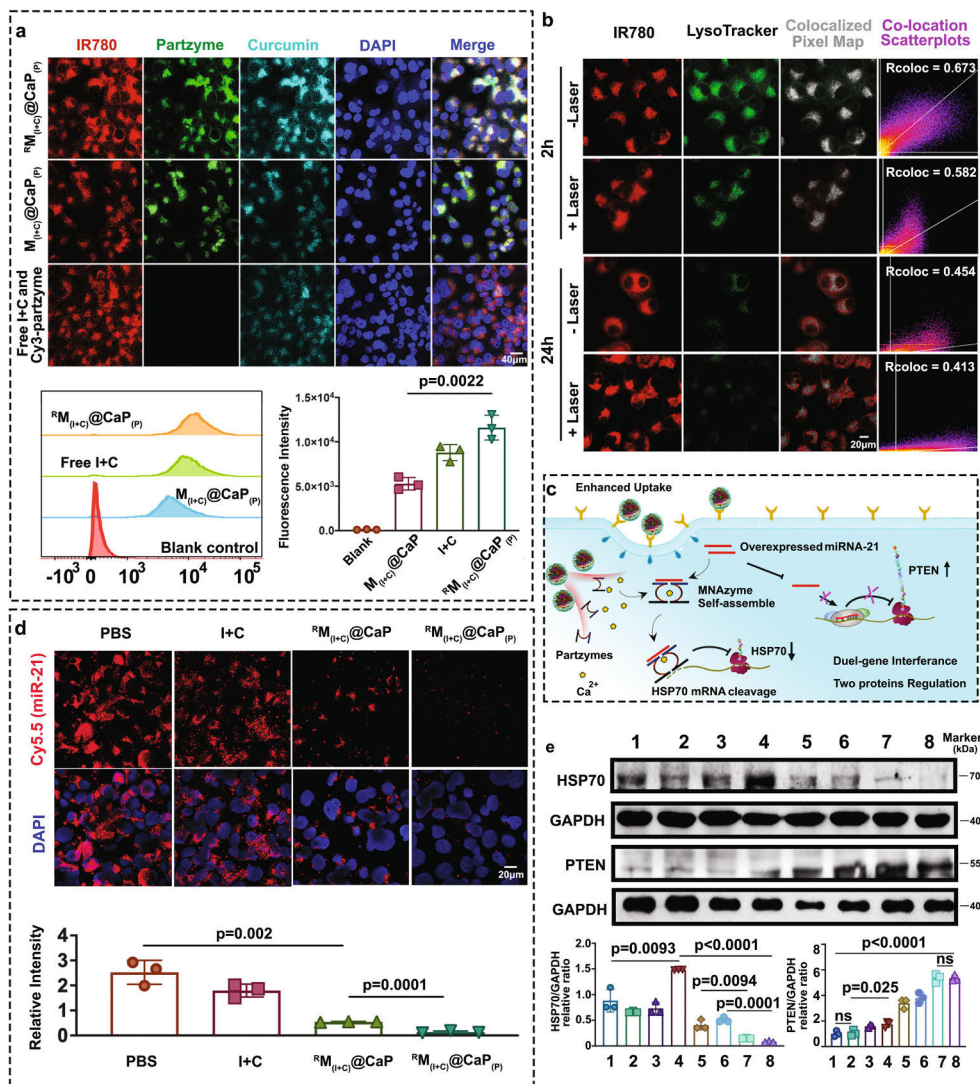


Fig. 5 | Therapeutic delivery by nanosystems and the intracellular function of the MNAzyme. **a** Uptake of pure drug, $M_{(I+C)}@CaP_{(p)}$ and $^6M_{(I+C)}@CaP_{(p)}$ groups by PANC-1 cells ($n = 3$ independent experiments, and the data are presented as the mean values \pm SDs). **b** Lysosomal escape profiles of $^6M_{(I+C)}@CaP_{(p)}$ groups (\pm Laser) by PANC-1 cells at 2 h and 24 h. The Pearson value Rcoloc was calculated by using ImageJ with the Coloc 2 plugin. **c** The schematic diagram depicts the intracellular self-assembly of the MNAzyme system for regulating the protein expression of PTEN and HSP70. **d** Intracellular miRNA-21 content was determined by the fluorescence in situ hybridization (FISH) method ($n = 3$ independent experiments and

the data are presented as the mean values \pm SDs). **e** The expression of HSP70 and PTEN protein was evaluated by western blotting. The final concentrations of the components in the different groups were as follows: IR780: 4 μ g/ml, Cur: 2 μ g/ml, each partzyme: 2 μ M ($n = 3$ independent experiments, and the data are presented as the mean values \pm SDs). Groups 1–8 represent the following: 1: PBS, 2: PBS + Laser, 3: 1 + C, 4: 1 + C + Laser, 5: $^6M_{(I+C)}@CaP$, 6: $^6M_{(I+C)}@CaP$ + Laser, 7: $^6M_{(I+C)}@CaP_{(p)}$, and 8: $^6M_{(I+C)}@CaP_{(p)}$ + Laser. All statistics were calculated using two-tailed paired t tests, and the experiments in (a, b, d, e) were repeated three times independently with similar results. The source data from (a, d, e) are provided as a Source Data file.

cells (Supplementary Fig. 13). The green fluorescence in NFDH cells was clearly ~ 7 times weaker than that in PANC-1 cells, indicating that partzymes might not effectively use miRNA-21 to construct the MNAzyme system. Moreover, due to the absence of RGD receptors on the

surfaces of healthy cells, the construction of the MNAzyme system was hampered by both poor partzyme delivery efficiency and the absence of miRNA-21, which could not further regulate the expression of HSP70 proteins. (Supplementary Fig. 14). Western blotting was then applied

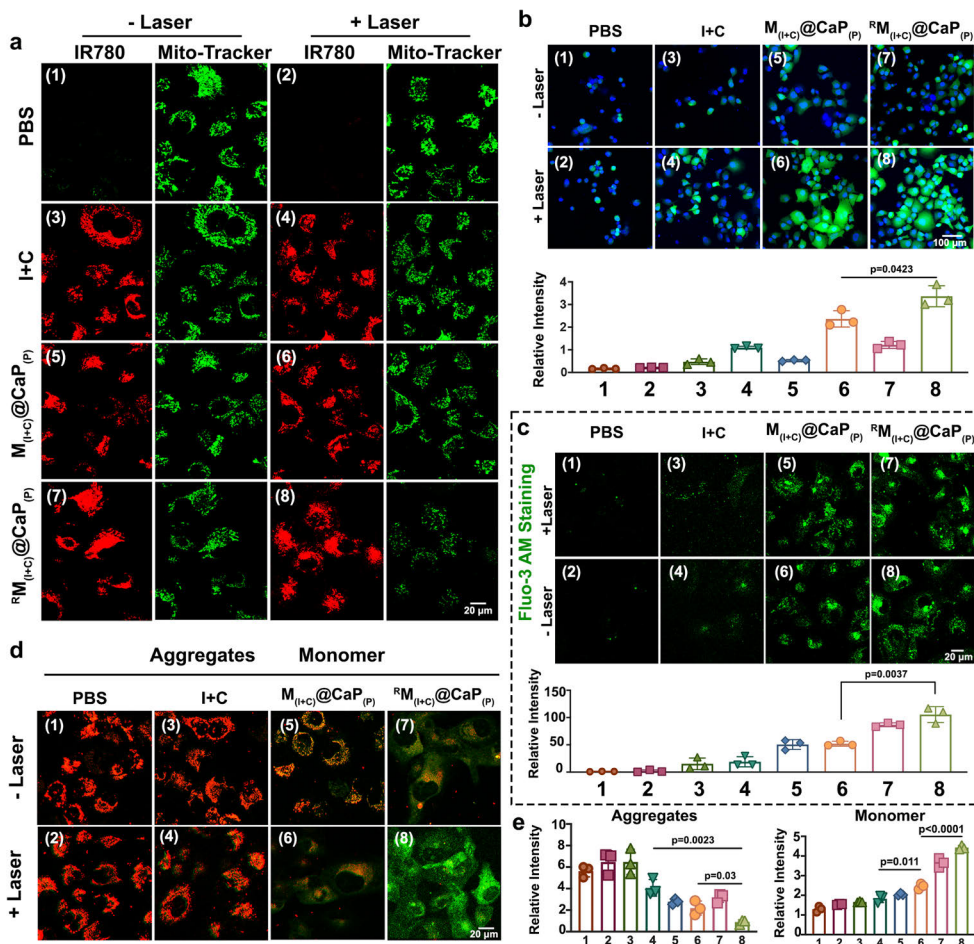


Fig. 6 | Multidimensional mitochondrial therapeutics mediated by IR780, Cur and Ca^{2+} . **a** Colocalization between IR780 and mitochondria. **b** 1O_2 generation capability of each treatment group ($n=3$ independent experiments, and the data are presented as the mean values \pm SDs). **c** Ca^{2+} concentration level visualization by using Fluo-3 AM as a labeling dye ($n=3$ independent experiments and the data are presented as the mean values \pm SDs). **d** $\Delta\Psi_m$ detection by tracking of the JC-1 monomer and aggregates through CLSM. **e** Relative fluorescence intensity of JC-1 signals for each group as calculated by ImageJ. The eight groups are labeled from 1

to 8, including PBS (1), PBS +Laser (2), IR780+Cur (3), IR780+Cur +Laser (4), $M_{(I+C)}@CaP_{(p)}$ (5), $M_{(I+C)}@CaP_{(p)}$ +Laser (6), $RM_{(I+C)}@CaP_{(p)}$ (7) and $RM_{(I+C)}@CaP_{(p)}$ +Laser (8). The final concentrations of the components in the different groups were as follows: IR780: 4 μ g/ml, Cur: 2 μ g/ml, and each partzyme: 2 μ M ($n=3$ independent experiments, and the data are presented as the mean values \pm SDs). All statistics were calculated using two-tailed paired t tests, and the experiments in (a–d) were repeated three times independently with similar results. The source data from (b, c, e) are provided as a Source Data file.

to test the generation of HSP70 in NFDH cells. The results showed that IR780 + Cur + laser (4) increased HSP70 expression by 2 times compared with that in the PBS group, while $RM_{(I+C)}@CaP_{(p)}$ + laser (6) and $RM_{(I+C)}@CaP_{(p)}$ + laser (8) increased the HSP70/GAPDH relative ratio by 3.4 times (Supplementary Fig. 14), demonstrating that the nanosystem did not affect the thermal protection mechanism of healthy cells.

After confirming the cancer-specific dual-gene regulatory capability of the MNazyme system, we further studied subcellular-based ion therapy with our nanoplateform in PANC-1 cells. Multidimensional mitochondrial therapeutics was realized through the following synergistic mechanisms: (1) IR780 targeted mitochondria to generate PTT

and PDT therapy; (2) CaP-composed nanocarriers released tremendous amounts of Ca^{2+} , mediating intramitochondrial Ca^{2+} overload; and (3) Cur further promoted the release of Ca^{2+} from the ER and inhibited Ca^{2+} efflux pumps in cancer cells.

We first verified the mitochondria-targeted therapy with IR780 through CLSM, as shown in Fig. 6a. Eight groups, including PBS \pm Laser, I+C \pm Laser, $M_{(I+C)}@CaP_{(p)}$ (without RGD) \pm Laser and $RM_{(I+C)}@CaP_{(p)}$ (with RGD) \pm Laser, were established and marked as 1 to 8. The laser groups were under $1W\text{ cm}^{-2}$ 808 nm irradiation for 5 min. IR780 exhibited red fluorescence, and mitochondria were marked in green. As expected, IR780 colocalized with mitochondria in each treatment

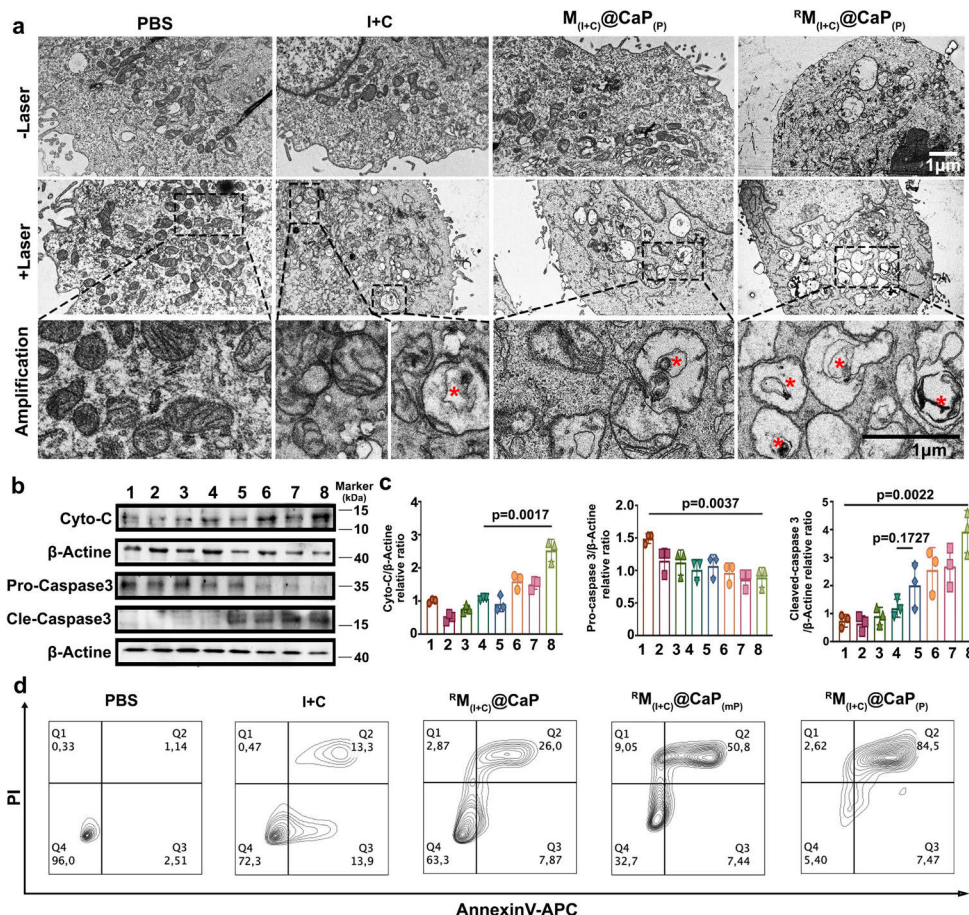


Fig. 7 | Mitochondrial morphology changes and the apoptosis mechanism.

a Bio-TEM image for mitochondrial morphology observation. **b** Western blot experiments for apoptosis-related protein detection. Eight groups (1–8) were tested, including the PBS, PBS + Laser, I + C, I + C + Laser, $M_{(I+C)}@CaP$, $M_{(I+C)}@CaP$ + Laser, $RM_{(I+C)}@CaP$ and $RM_{(I+C)}@CaP$ + Laser groups. ($n = 3$ independent experiments). **c** The relative ratio of each protein was calculated with ImageJ ($n = 3$ independent experiments, and the data are presented as the mean values \pm SDs).

d Apoptosis analysis of PANC-1 cells under Annexin V-APC/PI staining. (mP means mutated partzyme, which can only target miRNA but cannot achieve HSP70 silence; all groups were under laser irradiation). All statistics were calculated using two-tailed paired t tests, and all experiments (**a**, **d**) were repeated three times independently with similar results. The source data from (**b**, **c**) are provided as a Source Data file.

group. Compared with those of the PBS and pure drug groups (groups 1–4), the green fluorescence signals of the $M_{(I+C)}@CaP$ group without laser (5) were decreased, which might have been caused by Ca^{2+} -mediated mitochondria disruption. $M_{(I+C)}@CaP$ + Laser (6) showed less green signal than (5) due to the synergistic effect of IR780 and calcium overload. In contrast, after modification with RGD, the $RM_{(I+C)}@CaP$ \pm Laser group (7 and 8) exhibited the least green fluorescence, indicating the most severe mitochondrial damage caused by RGD-mediated enhanced endocytosis of the nanosystem by cancer cells.

In addition, the intracellular 1O_2 generation capability was also monitored to investigate the PDT effect of IR780. The same groups mentioned above were implemented, and the ROS were tracked with 2',7'-dichlorofluorescein diacetate (which emits a green signal after

oxidation by 1O_2), as depicted in Fig. 6b. All +Laser treatment groups produced observable 1O_2 upon laser irradiation for 5 min (808 nm 1.0 W cm^{-2}). We found that the pure drug I + C + Laser group (4) showed less relative fluorescence intensity, which was due to poor drug stabilization and solubility in the cell culture medium. The $RM_{(I+C)}@CaP$ + Laser group (8) produced the strongest green signal; comparatively, only 75% of the relative fluorescence intensity in the $M_{(I+C)}@CaP$ + Laser group (6) was found, which was calculated by ImageJ, reflecting the enhanced therapeutic effect mediated by RGD decoration.

Later, Ca^{2+} -based ion therapy was further studied by using Fluo-3 AM (green fluorescence) to visualize intracellular Ca^{2+} via CLSM, and the relative intensity of Ca^{2+} was calculated with ImageJ (Fig. 6c). The same groups were selected, and an 808 nm 1 W cm^{-2} laser was chosen for 5 min. As expected, a noticeable increase in Ca^{2+} concentration was

found in the ${}^{\text{R}}\text{M}_{(\text{I+C})}@\text{CaP}_{(\text{p})}$ \pm Laser groups (7 and 8), indicating the high efficiency of our designed nanoplatfor for inducing mitochondrial Ca^{2+} overload. Meanwhile, compared with $\text{M}_{(\text{I+C})}@\text{CaP}_{(\text{p})}$ \pm Laser (5 and 6), Groups 7 and 8 showed 2 times higher Ca^{2+} relative intensity levels, and the increases were attributable to the RGD-mediated enhancement of the endocytosis effect. In addition, with the assistance of curcumin, the ${}^{\text{R}}\text{M}_{(\text{I+C})}@\text{CaP}_{(\text{p})}$ group showed an excellent plasma membrane calcium pump (PMCA ATPase) silencing effect and achieved higher Ca^{2+} levels than the group without Cur (Supplementary Fig. 15), indicating the synergistic function of curcumin and Ca^{2+} -containing nanocarriers.

Mitochondrial transmembrane potential ($\Delta\Psi\text{m}$) represents the hyperpolarization/depolarization of mitochondria. To ascertain that the mitochondria experienced a disruption effect from our designed nanosystem, JC-1 dye was further employed as a sensor (JC-1 aggregates exhibit a red signal for healthy cells with high $\Delta\Psi\text{m}$, and the JC-1 monomer exhibits a green signal for damaged cells with low $\Delta\Psi\text{m}$). The same groups were used as elucidated in Fig. 6d, and the relative signal intensities of aggregates and monomers were calculated by ImageJ (Fig. 6e). After laser irradiation for 5 min ($808\text{ nm } 1.0\text{ W cm}^{-2}$), compared with the PBS group (1 and 2), the I + C + Laser group (4) showed 1.5 times higher green fluorescence, suggesting a decrease in $\Delta\Psi\text{m}$. In contrast, the 2-fold higher monomer content in the $\text{M}_{(\text{I+C})}@\text{CaP}_{(\text{p})}$ + Laser group (6) suggested synergistic mitochondrial damage by IR780 and Ca^{2+} overload. Surprisingly, with RGD decoration, the ${}^{\text{R}}\text{M}_{(\text{I+C})}@\text{CaP}_{(\text{p})}$ \pm Laser group (7 and 8) showed 3.16 and 3.6 times higher monomer signals, respectively, indicating that RGD modification significantly enhanced the therapeutic efficiency of the pure drug and efficiently mitigated mitochondrial dysfunction by inducing the synergistic effect of PDT/PTT and Ca^{2+} overload.

Later, to directly observe the mitochondrial morphology changes, bio-TEM was used to analyze each aforesaid group, and the inclusions inside mitochondria were marked with a red star (Fig. 7a). In general, a higher energy requirement for cancer cells results in more mitochondria with abundant cristae. As expected, we found tremendous amounts of mitochondria with dense cristae in PANC-1 cells in the PBS \pm Laser groups. In addition, mild mitochondrial destruction (slight swelling) was observed in the I + C + Laser groups, while the therapeutic effect was not prominent. Of note, noticeable mitochondrial swelling and cavitation effects were detected in the $\text{M}_{(\text{I+C})}@\text{CaP}_{(\text{p})}$ + Laser groups, which proved that the nanosystem could significantly enhance mitochondrial dysfunction through IR780 and superabundant calcium. It is worth mentioning that with RGD modification, negligible cristae were found in the ${}^{\text{R}}\text{M}_{(\text{I+C})}@\text{CaP}_{(\text{p})}$ group, suggesting that RGD mediated enhanced curative efficiency.

MNAzyme-mediated enhanced photothermal therapy and Ca^{2+} overload treatment increased mitochondrial permeability, resulting in the release of Cyto-C and finally activating Caspase-3 to mediate apoptosis. The apoptosis mechanism was investigated through western blot experiments (Fig. 7b), and the relative ratio of each protein was calculated by ImageJ (Fig. 7c). From the results, compared with the PBS group (1 and 2), the I + C + Laser group (4) showed a slight increase in Cyto-C, which reflected inefficient damage to mitochondria. In contrast, the ${}^{\text{R}}\text{M}_{(\text{I+C})}@\text{CaP}_{(\text{p})}$ + Laser group (6) showed ~ 1.5 times higher Cyto-C release than the I + C + Laser group (4), which was related to enhanced mitochondrial calcium overload. Importantly, due to the MNAzyme-mediated PTT-enhancing effect, the ${}^{\text{R}}\text{M}_{(\text{I+C})}@\text{CaP}_{(\text{p})}$ + Laser treatment (8) greatly led to the release of Cyto-C from mitochondria into the cytoplasm (2.5 times higher than that in the PBS group), which mediated pro-caspase cleavage, and cleaved caspase-3 was found at up to 3 times higher levels than that in the PBS group, as shown in Fig. 7c. Therefore, the ${}^{\text{R}}\text{M}_{(\text{I+C})}@\text{CaP}_{(\text{p})}$ nanosystem efficiently upregulated apoptosis-related proteins, resulting in significant apoptosis.

Based on the aforementioned experiments, we successfully validated the upregulation effect of the nanosystem on PTEN, the

silencing effect on HSP70, and the calcification effect on mitochondria. Given ample evidence that these rationally designed nanoformulations can achieve excellent cancer therapy, we further investigated their multiple synergistic effects through WST-1 and flow cytometry for both the NHDF and PANC-1 cell lines (Supplementary Figs. 16–17 and 7d). Different groups, including PBS, I + C, ${}^{\text{R}}\text{M}_{(\text{I+C})}@\text{CaP}$ (without partzymes), ${}^{\text{R}}\text{M}_{(\text{I+C})}@\text{CaP}$ (with mutated partzymes) and ${}^{\text{R}}\text{M}_{(\text{I+C})}@\text{CaP}_{(\text{p})}$ (with partzymes), were implemented under laser irradiation at 808 nm and 1 W cm^{-2} for 5 min. The mutated partzyme can only bind with miRNA-21 but cannot recognize HSP70. The final concentrations in the different groups were IR780: $4\text{ }\mu\text{g/ml}$, Cur: $2\text{ }\mu\text{g/ml}$, and partzyme: $2\text{ }\mu\text{M}$. After 24 h of treatment, compared with the PBS group, the pure drug I + C group showed $\sim 20\%$ inhibition of healthy NHDFs. However, the ${}^{\text{R}}\text{M}_{(\text{I+C})}@\text{CaP}$, ${}^{\text{R}}\text{M}_{(\text{I+C})}@\text{CaP}_{(\text{mp})}$ and ${}^{\text{R}}\text{M}_{(\text{I+C})}@\text{CaP}_{(\text{p})}$ groups exhibited almost no killing effect on healthy NHDFs due to less NP endocytosis and the miRNA-21 targeting effect of the MNAzyme system (Supplementary Fig. 16). For PANC-1 cancer cells, compared with the PBS group, the pure drug I + C group exhibited an $\sim 48\%$ inhibitory effect. However, 63% of the cancer cells were inhibited in the ${}^{\text{R}}\text{M}_{(\text{I+C})}@\text{CaP}$ group, which suggested that Ca^{2+} enhanced the mitochondrial dysfunction effect. Approximately 75% of cells were inhibited in the ${}^{\text{R}}\text{M}_{(\text{I+C})}@\text{CaP}_{(\text{mp})}$ group (Supplementary Fig. 17), indicating that the MNAzyme system boosted cancer therapy through miRNA-21 silencing. Of note, almost 90% of the cancer cells were inhibited in the ${}^{\text{R}}\text{M}_{(\text{I+C})}@\text{CaP}_{(\text{p})}$ group, which revealed that the partzyme could achieve both miRNA and HSP70 regulation and realize an excellent synergistic effect.

From the apoptosis assay results, within 8 h of treatment (IR780: $2\text{ }\mu\text{g/ml}$, Cur: $1\text{ }\mu\text{g/ml}$, partzyme: $1\text{ }\mu\text{M}$), $\sim 13.3\%$ of the cells in the pure drug I + C group had entered the late apoptotic phase, while the percentage was 26.0% for the ${}^{\text{R}}\text{M}_{(\text{I+C})}@\text{CaP}$ group, reflecting Ca^{2+} -mediated synergistic ion therapy. Moreover, 50.8% of the cells in the ${}^{\text{R}}\text{M}_{(\text{I+C})}@\text{CaP}_{(\text{mp})}$ group were shown to enter the late apoptotic state (Fig. 7d), which indicates the existence of a synergistic effect through mutated partzyme-based miRNA regulation. Finally, for the final formulation, 84.5% of the cells entered the late apoptotic phase, which was attributed to the MNAzyme-enhanced PTT, PTEN regulation, PDT and Ca^{2+} overload. The gating/sorting strategies are shown in Supplementary Fig. 18.

Encouraged by the selective suppressing ability and excellent biocompatibility in vitro, we further explored the performance of each nanosystem in vivo, which was approved by the Institutional Animal Care and Use Committee, Zhejiang Center of Laboratory Animals (Approval No. ZJCLA-IACUC-20020090). A pancreatic orthotopic tumor model was constructed by injecting 10^7 PANC-1-luc cells into the pancreatic site. The blood circulation and the blood half-life of the nanomachine were investigated first to determine its pharmacokinetics and potential efficacy in vivo (Supplementary Fig. 19). Three groups, including the pure drug (IR780 + curcumin + partzymes), $\text{M}_{(\text{I+C})}@\text{CaP}_{(\text{p})}$ and ${}^{\text{R}}\text{M}_{(\text{I+C})}@\text{CaP}_{(\text{p})}$ groups, were compared. From the results, we found that the $\text{M}_{(\text{I+C})}@\text{CaP}_{(\text{p})}$ and ${}^{\text{R}}\text{M}_{(\text{I+C})}@\text{CaP}_{(\text{p})}$ groups had longer circulation times, with elimination half-lives ($t_{1/2\beta}$) of 26.69 h and 25.53 h, respectively, compared to the free drug, which had a $t_{1/2\beta}$ of 5.34 h. The prolonged circulation time of NPs is thought to be due to the PEG shell, which shields the nanoparticle from being recognized and cleared by the immune system.

Live animal imaging was then performed to demonstrate the biodistribution of NPs after intravenous administration (Fig. 8a). Three groups, including the pure drug (IR780 + curcumin + partzymes), $\text{M}_{(\text{I+C})}@\text{CaP}_{(\text{p})}$ and ${}^{\text{R}}\text{M}_{(\text{I+C})}@\text{CaP}_{(\text{p})}$ groups, were tracked at 1, 8, 24 and 48 h timepoints (IR780: 1 mg/kg). For the pure drug I + C + P group, the majority of the signal was found throughout the mouse body at the 1 h timepoint, while a negligible signal was observed after 8 h due to the rapid metabolism of IR780. In contrast, $\text{M}_{(\text{I+C})}@\text{CaP}_{(\text{p})}$ NPs gradually released the drug, which reached its maximum concentration at the

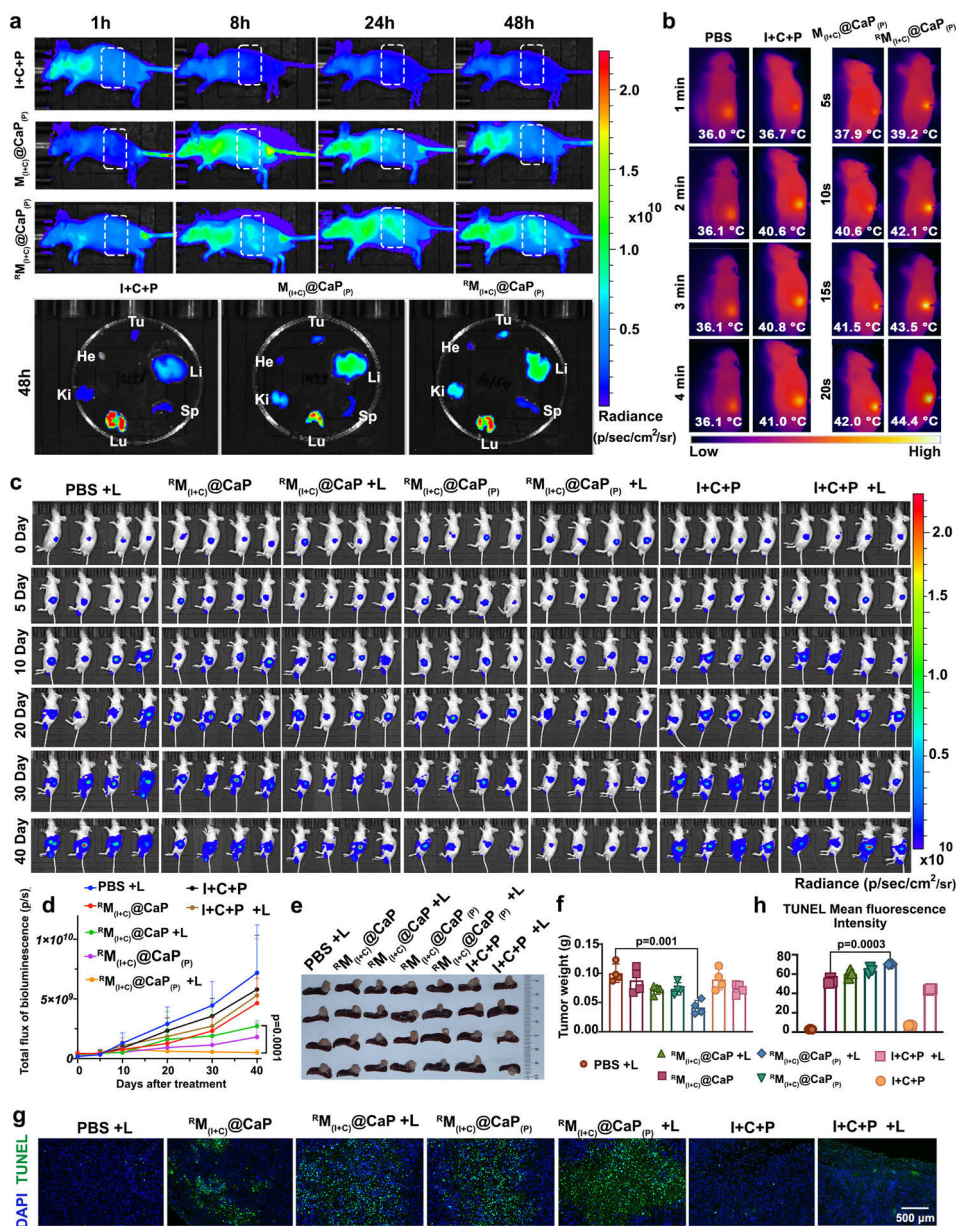


Fig. 8 | Distributions and curative effects of different preparations in vivo. **a** In vivo biodistribution of nanomaterial. Tu Tumor, Li Liver, Sp Spleen, Lu Lung, Ki Kidney, He Heart. **b** Tumor temperature elevation pictures. **c** Bioluminescence at different timepoints. **d** Quantitative analysis of total flux signal intensity (photons/sec) over time ($n = 4$ independent experiments, and the data are presented as the mean values \pm SDs). **e** Isolated tumor photos. **f** Tumor weight ($n = 4$ independent

experiments, and the data are presented as the mean values \pm SDs). **g** TUNEL labeling of each tumor slice. **h** TUNEL fluorescence quantitated by ImageJ ($n = 3$ independent experiments, and the data are presented as the mean values \pm SDs). All statistics were calculated using two-tailed paired t tests, and all experiments were repeated three times independently with similar results. The source data from (**d**, **f**, **h**) are provided as a Source Data file.

tumor site after 8 h of intravenous administration. Moreover, due to RGD modification, the $^8\text{M}_{(\text{I+C})}@\text{CaP}_{(\text{p})}$ group showed better tumor accumulation, achieving the highest fluorescence signal among the groups. Subsequently, the main organs were further harvested and imaged to evaluate the drug biodistribution. Compared with the free drug and $\text{M}_{(\text{I+C})}@\text{CaP}_{(\text{p})}$ NPs, $^8\text{M}_{(\text{I+C})}@\text{CaP}_{(\text{p})}$ NPs resulted in pronounced fluorescence in the tumor tissue, proving that RGD can facilitate tumor targeting.

Later, to assess mild PTT efficiency, a tumor temperature elevation experiment was performed. Four groups (PBS, I + C + P, $\text{M}_{(\text{I+C})}@\text{CaP}_{(\text{p})}$, and $^8\text{M}_{(\text{I+C})}@\text{CaP}_{(\text{p})}$) were treated with a 1 W cm⁻² 808 nm laser at 24 h after drug administration (IR780: 1 mg/kg), and the results are elucidated in Fig. 8b. From the results, the PBS group elicited the least change in temperature even after 4 min of irradiation. The pure drug I + C + P group showed an ineffective treatment temperature after 4 min of irradiation (below 43 °C) due to the poor solubility and unstable property of IR780. The $\text{M}_{(\text{I+C})}@\text{CaP}_{(\text{p})}$ NP group exhibited an enhanced photothermal conversion effect, and the tumor temperature increased to 42 °C with only 20 s of irradiation. Surprisingly, owing to the RGD-mediated enhanced tumor cell uptake, the $^8\text{M}_{(\text{I+C})}@\text{CaP}_{(\text{p})}$ group showed a dramatic temperature increase to 44.4 °C after 20 s of laser irradiation, exhibiting favorable mild photothermal activity.

Subsequently, the luciferase activity of PANC-1-luc cells within in situ carcinoma xenografts was measured to test the therapeutic efficiency of the pure drug and $^8\text{M}_{(\text{I+C})}@\text{CaP}$ nanosystems with/without partzymes in vivo (Fig. 8c). The quantitative analysis of luciferase intensity is shown in Fig. 8d. First, the results showed that the pure drug with laser group (I + C + P + Laser) could not effectively inhibit tumor growth, which might have been due to the easy degradation of the pure drug in vivo. In contrast, the $^8\text{M}_{(\text{I+C})}@\text{CaP}$ + Laser group effectively inhibited tumor growth for the first 10 days during the treatment period due to its excellent photothermal therapeutic effect and tumor targeting. However, the tumor showed a second round of growth after the 20th day, and the total flux changed from 5.09×10^8 p/s to -2.72×10^8 p/s, which might be attributable to acquired drug and heat resistance. Surprisingly, when partzyme was encapsulated into the nanosystems, the therapeutic efficacy of the $^8\text{M}_{(\text{I+C})}@\text{CaP}_{(\text{p})}$ + Laser group increased significantly and continued until Day 40, and the total flux equaled 5.04×10^8 p/s. It is possible that after the HSP70 gene was silenced by the MNAzyme, the tumor was unable to produce heat resistance, and the silencing of miRNA-21 also promoted the expression of the tumor suppressor gene PTEN protein and accelerated the apoptosis of the tumor. Furthermore, the photographs of tumors in situ (Fig. 8e) and tumor weight (Fig. 8f) indicated that the $^8\text{M}_{(\text{I+C})}@\text{CaP}_{(\text{p})}$ + Laser group had the best therapeutic effect, and its tumor weight was 0.049 g, which was ~50% of that of the PBS group. The TUNEL assay also demonstrated the therapeutic efficiency of partzyme (Fig. 8g), and the $^8\text{M}_{(\text{I+C})}@\text{CaP}_{(\text{p})}$ + Laser group revealed an 18% greater TUNEL signal than the $^8\text{M}_{(\text{I+C})}@\text{CaP}$ without partzymes + Laser group (Fig. 8h).

As mentioned previously, HSP70 can protect healthy cells from high temperature, but it is also the resistance mechanism for cancer cells against photothermal therapy (Fig. 9a). Therefore, smart nanomachines that can process biological signal input (miRNA-21) will significantly increase the selectivity and efficiency of PTT (Fig. 9b). To further verify the tumor-targeted silencing function of our nanodevices, the gene and protein expression levels of HSP70 were evaluated in both tumor and paracancerous tissues. Pure drug and $^8\text{M}_{(\text{I+C})}@\text{CaP}$ nanosystem with/without partzymes groups were used.

For tumor tissue, the HSP70 protein expression level in the pure drug group increased by ~66% under laser irradiation (Fig. 9c, d) compared with that in the PBS + Laser group. Moreover, the $^8\text{M}_{(\text{I+C})}@\text{CaP}$ (without partzymes) + Laser group also showed ~34% HSP70 upregulation. Previous in vitro experiments showed that

$^8\text{M}_{(\text{I+C})}@\text{CaP}$ could downregulate HSP70 by regulating mitochondrial function (Fig. 9e). However, these in vivo experiments suggested that the nanomachine could mediate more efficient photothermal conversion efficiency than the pure drug, which exacerbated the production of HSP70 (Fig. 9c, d). Hence, the enhancement of HSP70 expression could explain how the PTT resistance caused a second round of tumor growth (Fig. 9d). Importantly, the nanocarrier loaded with partzymes ($^8\text{M}_{(\text{I+C})}@\text{CaP}_{(\text{p})}$) could achieve effective downregulation of HSP70 even under laser irradiation (Fig. 9c, d), which proved the successful MNAzyme assembly. The results of the western blot experiment also provided ample evidence of the silencing effect of MNAzymes on HSP70 (Supplementary Fig. 20).

Nevertheless, in healthy pancreatic tissue, the HSP70 levels at the outer edge of healthy tissue were elevated in the pure drug and $^8\text{M}_{(\text{I+C})}@\text{CaP}$ groups as well as in the $^8\text{M}_{(\text{I+C})}@\text{CaP}_{(\text{p})}$ + Laser group. Hence, as we expected, NPs and drugs inevitably penetrated healthy paracancerous tissues, but our intelligent nanomachine was able to distinguish cancer cells from healthy cells by virtue of its tumor signal recognition function. Later, the qPCR results correlated with the above phenomenon. Compared with those in the $^8\text{M}_{(\text{I+C})}@\text{CaP}$ group, the HSP70 mRNA levels within the $^8\text{M}_{(\text{I+C})}@\text{CaP}_{(\text{p})}$ group were reduced by nearly 90% (Fig. 9e) in tumor tissue. However, for healthy tissues around tumors, our intelligent nanosystem did not affect HSP70-based self-protection, thereby remarkably improving the targeting of the treatment.

Subsequently, the MNAzyme system-mediated miR-21 silencing effect was further studied. The miR-21 content was measured through fluorescence in situ hybridization (FISH) (Fig. 9f), and the downstream protein PTEN was characterized through IHC (Fig. 9g). First, the results clearly showed that the content of miR-21 had no relationship with laser irradiation and that the control group contained the highest amount of miR-21. The content of miR-21 decreased in both the pure drug and $^8\text{M}_{(\text{I+C})}@\text{CaP}$ groups since Cur can reduce the level of miR-21. However, we found that miR-21 was almost completely silenced within the partzyme-containing $^8\text{M}_{(\text{I+C})}@\text{CaP}_{(\text{p})}$ group. These results indicated that partzymes can utilize and consume miRNA at tumor sites, which can further achieve miR-21 silencing-based gene therapy (Fig. 9g).

PTEN has been found to be a tumor suppressor with growth and survival regulatory functions, and silencing of miR-21 can mediate PTEN upregulation, which in turn inhibits tumor growth⁶⁵. The results in Fig. 9g revealed that, for the $^8\text{M}_{(\text{I+C})}@\text{CaP}$ and I + C + P groups, the PTEN levels were all increased, which was ascribed to Cur. The $^8\text{M}_{(\text{I+C})}@\text{CaP}_{(\text{p})}$ group exhibited the highest PTEN level due to the excellent miR-21 silencing effects of both Cur and the MNAzyme system. These results reflect the cleverness of our designed MNAzyme. It can not only recognize miR-21 and use it as the building block for MNAzyme self-assembly but also silence miR-21 to achieve gene therapy.

Discussion

For pancreatic cancer treatment, in addition to the regulation of relevant oncogenes, regulation of the immune response is also a crucial aspect that cannot be overlooked⁶⁶. Furthermore, the high degree of fibrosis is another reason for the lack of effective drug interventions in clinical cancer treatment⁶⁷. Therefore, in future experiments, utilizing immunocompetent animal models and observing whether our designed MNAzyme system can activate the immune response, attenuate fibrosis in pancreatic cancer, and consequently enhance the accessibility of tumor cells to nanoparticle drugs will be highly meaningful.

In this work, we successfully constructed an intelligent nanomachine for multimodule synergistic photothermal therapy with the ability to distinguish between tumor and paracancerous tissues. In vivo experiments confirmed that the nanomachine, upon processing biological signals (miRNA-21), was activated and specifically modulated HSP70 mRNA only in tumor cells while maintaining the HSP protective

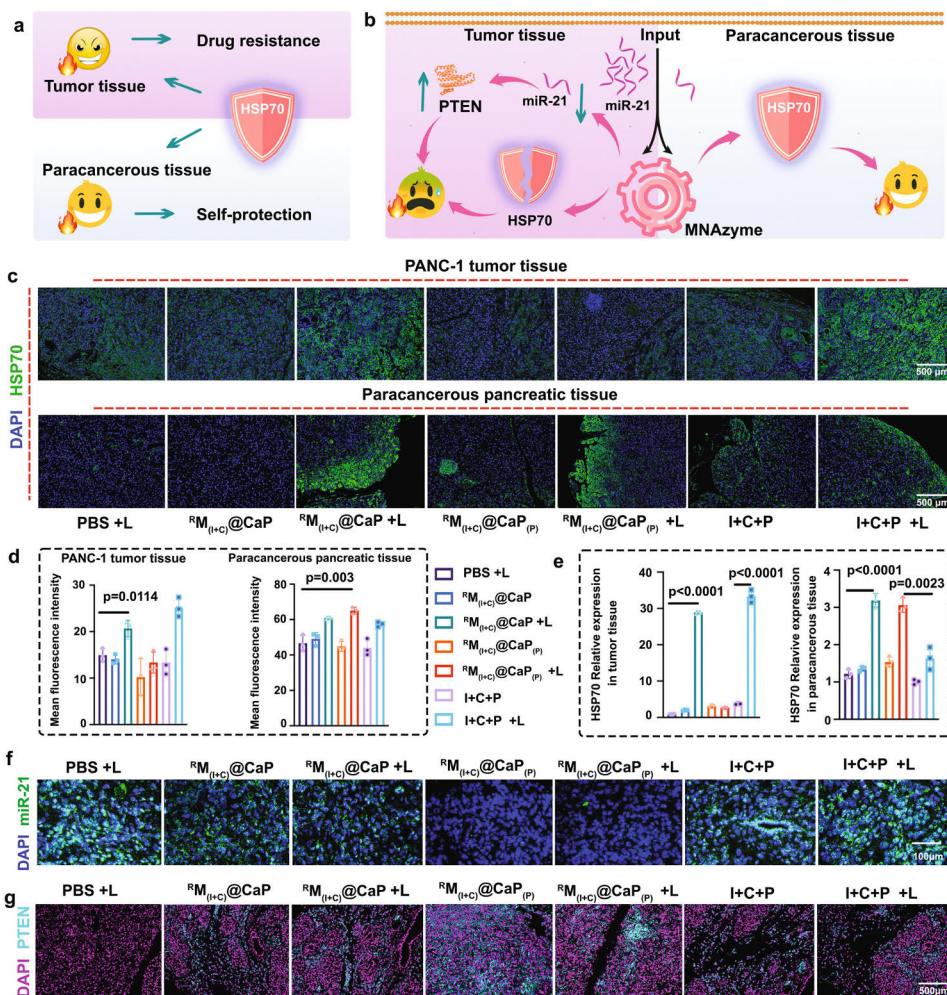


Fig. 9 | Tumor-targeting function of the MNAzyme. **a** Roles of HSPs in different cells. **b** Tumor-targeting mechanism for our intelligent nanodevice. **c** Immunohistochemical characterization of HSP70 in tumor tissues and healthy tissues. **d** HSP70 quantitated by ImageJ in tumor tissue and paracancerous tissue ($n = 3$ independent experiments, and the data are presented as the mean values \pm SDs). **e** qPCR results for HSP70 mRNA levels ($n = 3$ independent experiments, and

the data are presented as the mean values \pm SDs). **f, g** miR-21 content and PTEN protein expression levels ($n = 3$ independent experiments). All statistics were calculated using two-tailed paired t tests, and all experiments (**c, f, g**) were repeated three times independently with similar results. The source data from (**d, e**) are provided as a Source Data file.

function in healthy cells. Furthermore, the system broke through the stereotype of MNAzyme design and simultaneously utilized the steric blocking mechanism of the miRNA/partzyme complex^{36,37} as well as multiturnover catalytic rates to achieve up to 90% target gene silencing. Meanwhile, the nanocarrier was constructed with Ca^{2+} , which solved the problem of insufficient endogenous metal cofactors. It was also found that Ca^{2+} and Cur could mediate calcium overload, mediating mitochondrial fragmentation and Cyto-C release as well as apoptosis promotion. In addition, the addition of zinc ions prevented the disadvantage of easy phase transition of calcium phosphate during storage in water and improved the stability of the formulation.

Therefore, this multisynergistic nanomachine is expected to promote the application of MNAzymes in the clinical treatment of cancer.

Methods

Ethical statement

Our research complied with all relevant ethical regulations. All animal protocols were performed in line with the Guidelines for the Care and Use of Laboratory Animals and approved by the Institutional Animal Care and Use Committee (IACUC) of Zhejiang Center of Laboratory Animals (ZJCLA) (Approval No. ZJCLA-IACUC-20020090). The animal experiments also follow the PREPARE Guidelines Checklist⁶⁸.

Materials

All oligonucleotides were synthesized and HPLC-purified by Sangon Biotechnology Co., Ltd. (Shanghai, China) and are listed in Table S6. Ammonium persulfate (APS), N,N,N',N'-tetramethylethylenediamine (TEMED), zinc nitrate, calcium chloride, and sodium dihydrogen phosphate were all purchased from Sigma (Finland). Tris-HCl buffer solution (pH 8.8 and 6.8), 30% acrylamide/bis, and TBS/Gly/SDS buffer were purchased from Bio-Rad Laboratories, Inc. (Finland). Solutions involved in microRNA-related experiments were prepared with DEPC-treated water (RNase-free) (Sigma, Switzerland). A BCA kit, RIPA, Tris-Triton, protease inhibitor, EDTA, and GelRed were purchased from Thermo Fisher, Finland. DSPE-PEG_{2K}-RGD, DSPE-PEG-COOH, and RGD were acquired from Xi'an Ruixi Biological Technology Co. Ltd. IR780 and curcumin were purchased from Macklin Inc. (China). Anti-mouse PTEN antibody, (Catalog no. ab267787), Anti-Rabbit GAPDH, (Catalog no. ab210113), Anti-mouse Anti-Cytochrome C, (Catalog no. ab13575), Anti-mouse Anti-beta Actin antibody [mAbcam 8226], Anti-rabbit Anti-pro Caspase-3, (Catalog no. ab32150), Anti-rabbit Anti-Cleaved Caspase-3 (Catalog no. ab32042) were provided from Abcam. Anti-mouse HSP70 Antibody, (Catalog no. #4872) is purchased from Cell Signaling Technology. PMCA ATPase Monoclonal Antibody (Catalog # MA3-914) was provided from ThermoFisher.

Twenty percent polyacrylamide gel electrophoresis (PAGE) tests

Twenty percent gel solution was transferred into a plate with a shim, and the comb was inserted immediately to ensure that there were no air bubbles in the gel. The gel was allowed to set at room temperature for ~30–60 min. After coagulation, the samples were loaded into a vertical electrophoresis tank, and a prerun of ~10 min was first performed at a voltage of 5 V. Oligonucleotide samples were prepared by mixing 2 μ l of sample with 8 μ l of water and 2 μ l of loading buffer. At least 10 μ g of oligonucleotide sample was needed for loading. The sample was carefully loaded into the well without introducing any air bubbles. The gels were run at 90 V for ~2 h until the dye front was near the bottom of the gel. The glass plates were opened with a spatula to separate the upper glass plate. GelRed was diluted to 1:10,000, and the gel was stained for 5–10 min. The gel was then immersed in distilled water for 10 min to remove excess stain and reduce background staining.

Fabrication of CaP nanoparticles

Pure CaP NPs were synthesized through a simple one-step method at room temperature by combining two solutions for 5 min. Solution A was composed of 0.42 ml of CaCl₂ (2.0 M) and 0.84 ml of Tris buffer (pH = 10, 10 mM) in 2 ml of Milli-Q H₂O. Solution B contained 0.43 ml HEPES buffer (280 mM NaCl, 15 mM Na₂HPO₄ and 50 mM HEPES) and 0.3 ml of Milli-Q H₂O. Solution B was added dropwise into solution A with stirring for 5 min at room temperature. Then, the NPs were washed with pure ethanol 3 times to remove water molecules. The nanoparticle stock solution was kept in ethanol.

Observation of cell morphology with unstable CaP

PANC-1 cells were seeded in 6-well plates at a density of 1×10^6 cells in one well and cultured for 12 h. Then, the medium was replaced with 2 ml of DMEM containing Pure CaP NPs at a concentration of 50 μ g ml⁻¹ for 12 h. After washing with PBS twice, the cells were treated with trypsin and then centrifuged at $150 \times g$ to collect the precipitate. The obtained precipitate was fixed, dehydrated, embedded, sliced, and measured by transmission electron microscopy.

Fabrication of Zn-substituted CaP nanoparticles

Zn-stabilized CaP NPs were synthesized based on the abovementioned simple method at room temperature by combining two solutions for 30 min. The Zn/Ca molecular ratio was 1:20. Solution A was composed of 0.42 ml of CaCl₂ (2.0 M), 0.021 ml ZnCl₂ (2.0 M) and 0.84 ml of Tris

buffer (pH = 7, 10 mM) in 2 ml of Milli-Q H₂O. Solution B contained 0.43 ml HEPES buffer (280 mM NaCl, 15 mM Na₂HPO₄ and 50 mM HEPES) and 0.3 ml of Milli-Q H₂O. Solution B was added dropwise into solution A with stirring for 30 min at room temperature.

Fabrication of ⁶⁴M_(1+Cl) and ⁶⁴M_(1+Cl)@CaP_(p)

For both drug loadings, 50 mg of DSPE-PEG-RGD polymers were dissolved in 5 ml of organic solvent composed of 70% ethanol and 30% chloroform. Different concentrations of drugs with different IR780/Cur ratios (0:2; 0.5:2; 1:2; 2:2; 4:2; 8:2 mg) were also dissolved in the abovementioned organic solvent. The solution was then placed into a rotary evaporator for film formation. Subsequently, 10 ml of water was added for hydration for 24 h and centrifuged for 5 min at 1400 g to remove the unencapsulated drugs⁶⁹ since both drugs possessed very low water dissolving ability. Then, 10 ml ⁶⁴M_(1+Cl) micelles were prepared. To study the drug-loading capacity of IR780 and Cur separately, we explored the loading amount of 50 mg DSPE-PEG polymer with gradient drug concentrations. The specific method was the same as above, with concentration ranges of 2 to 10 mg for IR780 and 0.5 to 3 mg for Cur. Drug-loading capacity = (weight of drug input minus the undissolved drug/weight of nanoparticles) \times 100%, drug loading efficiency = (weight of drug in nanoparticles/weight of drug used for nanoparticle preparation) \times 100%. For ⁶⁴M_(1+Cl)@CaP_(p) NPs, a 1 ml micelle solution with 1 ml of Milli-Q H₂O was used to replace the 2 ml of Milli-Q H₂O in the abovementioned solution A when preparing the CaP NPs. Before CaP mineralization, partzymes at different concentrations (1, 10, 50, 100, and 200 μ M) were precultured with solution A. The M_(1+Cl) and M_(1+Cl)@CaP_(p) NPs were fabricated through the same procedure, and DSPE-PEG-RGD was replaced by DSPE-PEG. The partzymes were modified with Cy3, enabling the measurement of non-encapsulated DNAzymes in the supernatant after centrifugation using UV spectrophotometry. The drug loading for IR780, Cur and DNAzymes was carried out through UV-Visible spectroscopy at 780, 425 and 560 nm, respectively. For CaP-containing NPs, we used centrifugation to isolate the NPs from the reaction mixture and subsequently washed the NP solution multiple times with a suitable solvent to remove any impurities.

Characterization of the nanoparticles

The particle sizes of CaP, ⁶⁴M_(1+Cl), and ⁶⁴M_(1+Cl)@CaP_(p) NPs were determined using dynamic light scattering with a Zetasizer Nano ZS. For each measurement, the sample (1.0 ml) was placed in a disposable polystyrene cuvette. The nanocarrier surface ζ -potential was measured with a Zetasizer Nano ZS by using disposable cells. Both the size and ζ -potential were recorded as the average of three measurements. The TEM samples were prepared by dropping the particle solution on top of carbon-coated copper grids and then drying it in air prior to imaging. Fourier transform infrared spectroscopy (FTIR) was performed in the 4000–1000 cm⁻¹ range with a resolution of 4 cm⁻¹ at room temperature by using a Thermo Nicolet IS10 spectrometer.

Photothermal properties of ⁶⁴M_(1+Cl)@CaP_(p) NPs

⁶⁴M_(1+Cl)@CaP_(p) NPs were diluted with PBS (concentration of IR780 was from 0 to 100 μ g/ml), and 1 ml of sample was added to a cuvette and irradiated with an 808 nm NIR laser source at 1.0 W/cm² for 5 min. The temperature changes of the samples were recorded by the infrared imaging device at intervals of 30 s. Temperature elevations of free IR780 (dissolved in PBS), ⁶⁴M_(1+Cl) and ⁶⁴M_(1+Cl)@CaP_(p) NPs over four NIR on-off irradiation cycles were conducted through a 1.0 W cm⁻² 808 nm laser with 50 μ g/ml IR780. The photobleaching properties of free IR780, ⁶⁴M_(1+Cl) and ⁶⁴M_(1+Cl)@CaP_(p) NPs were investigated by diluting the IR780 content in each group to 50 μ g/ml, and laser irradiation (808 nm, 1.0 W/cm²) was continued for 5 min. Then, the UV absorbance of each group was monitored. The irradiation process was conducted 3 times.

Drug release experiment

One milliliter of $^{64}\text{M}_{(\text{I+C})}@\text{CaP}_{(\text{p})}$ NPs (containing 0.4 mg IR780, 0.2 mg Cur and 200 μM partzymes) was tied into a dialysis bag and released under 20 ml sink conditions. The release medium contained 2% Tween-80. There were four drug release conditions: pH = 7, 37 °C; pH = 7, 45 °C; pH = 6, 37 °C and pH = 6, 45 °C. At each time point, 1 ml of release medium was extracted for drug concentration measurement and then added back to the system. The absorbance characteristic peak wavelengths of IR780, Cur and partzymes were observed using a NanoDrop™ 2000 spectrophotometer. For MNAzyme, 1 μl of released medium was mixed with 1 μl of miRNA-21 (10 μM). Then, 2 μl of 10 μM HSP70 mRNA was added to the reaction, resulting in a 4 μl volume, with a maximum of 2.5 μM MNAzyme to mediate 5 μM HSP70 mRNA cleavage.

Cell culture and maintenance

The pancreatic cancer cell line PANC-1 and normal human dermal fibroblast NHDFs were grown in DMEM with 10% FBS at 37 °C. Cells were passaged 2–3 times a week once they reached 90–100% confluency. The human pancreatic cancer cell line PANC-1 was purchased from ATCC® (CRL-1469™), and normal human dermal fibroblast (NHDF) cells were purchased from PromoCell®. The cell lines were directly purchased without further authentication, and the cell line were tested negative for mycoplasma contamination.

Cellular uptake study

Cells were incubated in 6-well plates (1×10^5 cells per well) overnight. When the cells were attached, solutions of free IR780 + Cur + partzyme, $\text{M}_{(\text{I+C})}@\text{CaP}_{(\text{p})}$, and $^{64}\text{M}_{(\text{I+C})}@\text{CaP}_{(\text{p})}$ were utilized to replace the cell growth media. All the groups were kept at a concentration of 4 $\mu\text{g}/\text{ml}$ for IR780, 2 $\mu\text{g}/\text{ml}$ for Cur and 2 μM for partzymes at 37 °C. After incubation for 1 h and 8 h, the cells were observed under CLSM. Additionally, the cells were collected with trypsin and washed with PBS. Cellular uptake was determined with a BD LSRFortessa flow cytometer (BD Biosciences), and the results were analyzed with FlowJo V10. The gate was defined for live cells only; 10,000 cells were recorded per sample. The concentrations of Ca^{2+} in PANC-1 cells were measured using inductively coupled plasma–optical emission spectrometry (ICP-OES). The same experimental groups were treated with final concentrations of IR780 at 4 $\mu\text{g}/\text{ml}$, Cur at 2 $\mu\text{g}/\text{ml}$, and partzyme at 2 μM . After washing the cells with PBS twice, the cells were treated with trypsin and collected through centrifugation. Finally, 1.0 ml of concentrated nitric acid was added, and the samples were measured by using ICP-OES to determine the Ca^{2+} concentration.

Fluorescence in situ hybridization (FISH) detection

A fluorescence in situ hybridization (FISH) kit was purchased from Guangzhou Exons Biological Technology Co., Ltd. The probe was diluted with hybridization buffer and denatured at 85 °C for 2 min. Then, the probe was used for hybridization with 4% paraformaldehyde-fixed cells for 72 h. The cells were labeled with DAPI (Amax = 358, Emax = 461). The fluorescence of the probe was Cy5.5 (Amax = 683, Emax = 703). The relative intensity of each group was calculated with ImageJ.

Lysosome escape

IR780 and LysoTracker Green were used as the probe of the drug and lysosome, respectively. PANC-1 cells were seeded on confocal dishes overnight. Then, the lysosomal escape profile of the $^{64}\text{M}_{(\text{I+C})}@\text{CaP}_{(\text{p})}$ groups ($\pm\text{Laser}$) by PANC-1 cells at 2 h and 24 h was determined. For both groups, after NPs and cells were cultured together for 2 h and 24 h, the cell media were replaced, and a 1 W laser was applied for 5 min. After laser irradiation, the cells were incubated with LysoTracker Green for another 2 h, after which a 5 min incubation was performed

with 4% paraformaldehyde. Then, the cells were observed under a fluorescence confocal microscope. The colocalization scatterplots of each group were calculated by ImageJ.

Western blot analysis

After the cells were incubated with different groups of nanomaterials for 48 h, the cells were lysed with RIPA and Tris-HCl lysis buffer. RIPA was used for whole-cell lysis and is suitable for destroying mitochondria. For 2 ml of RIPA buffer, 20 μl of 1% protease inhibitor and 20 μl of 1% 0.5 M EDTA were added. Tris-HCl was used for cytoplasmic cleavage. The final concentration of Tris was 20 mM. Twenty microliters of 1% protease inhibitor and 20 μl of 1% 0.5 M EDTA were added to 2 ml of Tris-HCl. After 1 h of lysis, the medium buffer was centrifuged at $16,000 \times g$ for 10 min, and the supernatant was taken for quantification. Cell proteins were separated by SDS-PAGE gradient gel and transferred to PVDF membranes. After adding protein loading buffer, the samples were mixed well and fully denatured at 98 °C for 10 min. The membranes were incubated with primary antibodies against PTEN, HSP70, Cyto-C, β -Actine, Pro-Caspase 3, cleaved-caspase 3 and GAPDH (Abcam, Cambridge, UK) (1:1000) at 4 °C overnight. Then, the membranes were incubated with the secondary antibody at 37 °C for 1 h. A GelDoc Go Gel Imaging System (Bio-Rad) was used to evaluate protein bands. ImageJ software was used for fluorescence quantitative analysis.

Colocalization between IR780 and mitochondria

Eight groups, including the PBS $\pm\text{Laser}$, I + C $\pm\text{Laser}$, $\text{M}_{(\text{I+C})}@\text{CaP}_{(\text{p})}$ (without RGD) $\pm\text{Laser}$ and $^{64}\text{M}_{(\text{I+C})}@\text{CaP}_{(\text{p})}$ (with RGD) $\pm\text{Laser}$ groups, were established and marked from 1 to 8. The laser groups were under 1 W cm^{-2} 808 nm irradiation for 5 min. IR780 exhibited red fluorescence, and mitochondria were labeled with MitoTracker Green. The mitochondrial tracker was purchased from Beyotime Biotechnology Co., Ltd. After nanosystems with a concentration of IR780: 4 $\mu\text{g}/\text{ml}$, Cur: 2 $\mu\text{g}/\text{ml}$, and each partzyme: 2 μM were cultured with PANC-1 cells for 6 h, the medium was replaced, and a laser was applied for 5 min. The cells were then cultured with the mitochondrial tracker for another 2 h. Then, the samples were observed under fluorescence confocal microscopy. ImageJ software was used for fluorescence quantitative analysis.

ROS detection

PANC-1 cells were cultured in confocal dishes at 1×10^5 cells per well. When the PANC-1 cells reached 70–80% confluency, they were treated under different conditions, including incubation with PBS $\pm\text{Laser}$, I + C $\pm\text{Laser}$, $\text{M}_{(\text{I+C})}@\text{CaP}_{(\text{p})}$ (without RGD) $\pm\text{Laser}$ and $^{64}\text{M}_{(\text{I+C})}@\text{CaP}_{(\text{p})}$ (with RGD) $\pm\text{Laser}$ for 6 h at 37 °C. After 6 h of incubation, dichlorodihydrofluorescein diacetate (DCFH-DA) solution was added to the cell medium⁷⁰. The ROS signals were quantitatively analyzed with ImageJ software, which indicated the intracellular IO_2 levels generated under different experimental conditions.

Ca^{2+} concentration visualization

PANC-1 cells were cultured in confocal dishes at 1×10^5 cells per well. When PANC-1 cells reached 70–80% confluency, they were treated under different conditions, including incubation with PBS $\pm\text{Laser}$, I + C $\pm\text{Laser}$, $\text{M}_{(\text{I+C})}@\text{CaP}_{(\text{p})}$ (without RGD) $\pm\text{Laser}$ and $^{64}\text{M}_{(\text{I+C})}@\text{CaP}_{(\text{p})}$ (with RGD) $\pm\text{Laser}$ for 6 h at 37 °C. After 6 h of incubation, the Fluo-3 AM solution was subsequently added to the cell medium. The concentration of the Fluo-3 AM probe in all samples was 1.0 μM . ImageJ software was used for fluorescence quantitative analysis.

$\Delta\Psi\text{m}$ detection by tracking of JC-1 monomers and aggregates

To measure the changes in mitochondrial membrane potential, PANC-1 cells were seeded in a 6-well plate at a density of 2×10^5 cells per well in 2.0 ml of FPS-DMEM and cultured for 24 h. The medium was then

replaced with 1.0 ml of PBS \pm Laser, I + C \pm Laser, $M_{(I+C)}@CaP_{(p)}$ (without RGD) \pm Laser and $^8M_{(I+C)}@CaP_{(p)}$ (with RGD) \pm Laser at the same concentrations, IR780: 4 μ g/ml, Cur: 2 μ g/ml, each partzyme: 2 μ M, and cultured for 12 h. After washing with PBS twice, the cells were stained with JC-1 and measured by CLSM. In this detection, 1.0 ml of JC-1 working solution was added to cells containing 1.0 ml of DMEM.

Observation of mitochondrial morphology

To measure mitochondrial morphology, PANC-1 cells were seeded in a 100 mm \times 20 mm dish at a density of 3.0×10^6 cells per dish and cultured for 24 h. The medium was then replaced with 5.0 ml of PBS \pm Laser, I + C \pm Laser, $M_{(I+C)}@CaP_{(p)}$ (without RGD) \pm Laser and $^8M_{(I+C)}@CaP_{(p)}$ (with RGD) \pm Laser at the same concentrations, IR780: 4 μ g/ml, Cur: 2 μ g/ml, each partzyme: 2 μ M, and cultured for 12 h. After being washed with PBS twice, the cells were treated with trypsin and then centrifuged at $150 \times g$ to collect the precipitate. The cells were then fixed for 1 day at room temperature. After fixation, the cells were washed in the same buffer and postfixed in 1% osmium tetroxide in 0.1 M sodium cacodylate buffer (pH 7.4) for 1 h at room temperature. The cells were then washed again with the same buffer and dehydrated in a graded series of ethanol solutions. The obtained cells were then embedded in epoxy resin (Epon 812) and polymerized for 48 h at 60 °C. The polymerized blocks were then sectioned into ultrathin sections using a Leica EM UC7 ultramicrotome. The sections were collected on copper grids and stained with uranyl acetate and lead citrate before being examined under a JEM-1400 Plus transmission electron microscope (TEM). During TEM imaging, at least 3 random images were taken at a magnification of 5000–10,000 \times to observe the mitochondrial ultrastructure. The mitochondrial morphology was analyzed based on the presence or absence of cristae, the shape of the mitochondrial membrane, and the size of the mitochondria. The sample preparation was carried out in the Laboratory of Electron Microscopy, Medisina C, 2nd floor, University of Turku. A JEM-1400 Plus transmission electron microscope was used to monitor mitochondrial morphology.

Annexin V-APC/PI apoptosis detection

Cells were digested with trypsin solution and aspirated until the adherent cells could be blown down by gentle pipetting. Then, the cells were transferred into a centrifuge tube and centrifuged at $1000 \times g$ for 5 min, and the supernatant was discarded. Subsequently, the cells were gently resuspended in PBS and counted. A total of 50,000–100,000 resuspended cells were collected and centrifuged at $1000 \times g$ for 5 min. Then, 195 μ l of Annexin V-APC binding solution was added to gently resuspend the cells. Then, 10 μ l of propidium iodide staining solution containing Annexin V-APC was added and mixed gently. After incubation for 10–20 min at room temperature (20–25 °C) in the dark, the cells were placed in an ice bath. Apoptosis was determined with a BD LSRFortessa flow cytometer (BD Biosciences), and the results were analyzed with FlowJo V10; 10000 cells were recorded per sample.

Cytotoxicity assay

The concentrations of the therapeutics were as follows: IR780: 4 μ g/ml, Cur: 2 μ g/ml and partzymes: 2 μ M. The stock solution of $^8M_{(I+C)}@CaP_{(p)}$ NPs (containing 0.4 mg IR780, 0.2 mg Cur and 200 μ M partzyme per ml) was diluted 100-fold to obtain 4 μ g/ml IR780 and 2 μ g/ml Cur, and there was 2 μ M partzyme. After 24 h of incubation, the cells were subjected to standard WST-1 experiments. All dilutions for the cell viability assay were prepared in cell growth medium. After incubation with free drug or nanoparticles, 10 μ l of WST-1 reagent was added to each well, and the cells were incubated for 2 h at 37 °C with 5% CO₂. After incubation, the absorbance was measured with a Varioskan Flash Multimode Reader (Thermo Scientific Inc., Waltham, MA, USA) at 440 nm.

Detection of IR780 by HPLC

The detection wavelength of IR780 was 700 nm with a Waters 2695 Alliance HPLC. The mobile phase flow rate was set at 1.0 ml/min. The chromatographic column used was an Eclipse plus C18 column. Mobile phase A contained methanol and 0.2% FA, and mobile phase B contained water and 0.2% FA. The ratio was 4:1 (A:B, v/v).

Orthotopic model construction procedure

The experimental procedure was based on previously reported methods⁷¹ with certain improvements. BALB-cu (6–8 weeks old) nude mice were anesthetized and positioned in a left lateral recumbent position. Following routine skin disinfection, a 1 cm oblique incision was made just below the right costal margin, allowing access to the abdominal cavity. Afterward, the abdominal cavity was opened, revealing the spleen and pancreas. A prepared cell suspension was then precisely injected into the pancreas, with attention to minimizing tissue damage. Hemostasis was performed if necessary, and the incision was sutured to close the abdominal cavity. Finally, the surgical site was disinfected once more, and the mouse was placed in a warm incubator or recovery area for postoperative care, all while adhering to ethical and animal care guidelines. The mice feeding conditions of mice are: 12/12 day and night alternating, humidity at 50–60%, temperature at 22–26 °C.

In vivo biodistribution

The I + C + P, $M_{(I+C)}@CaP_{(p)}$ and $^8M_{(I+C)}@CaP_{(p)}$ groups were used to observe the biodistribution of nanodevices after intravenous administration. The concentrations of the therapeutics were as follows: IR780: 2 mg/kg, Cur: 1 mg/kg and partzymes: 1 μ mol/kg. In vivo imaging was performed at 1, 8, 24 and 48 h timepoints. On the 48th day, the mice from each group were sacrificed, and the tumor, heart, liver, spleen, lungs and kidneys were collected for in vitro fluorescence detection.

In vivo IR thermography

Four groups, including the PBS, I + C + P, $M_{(I+C)}@CaP_{(p)}$ and $^8M_{(I+C)}@CaP_{(p)}$ groups, were established. First, the nude mice were anesthetized, and the tumor site was observed and marked with an in vivo imaging system. Then, the mice were fixed, and at 12 h after administration, the tumor site was irradiated with an 808 nm laser.

In vivo anticancer efficacy analysis

PANC-1 cells containing luciferase were injected into the pancreases of BALB/c-nu (6–8 weeks old) female mice. The mice were divided into seven groups: the PBS + Laser, $^8M_{(I+C)}@CaP_{(p)}$, $^8M_{(I+C)}@CaP_{(p)}$ + Laser, $^8M_{(I+C)}@CaP_{(p)}$, $^8M_{(I+C)}@CaP_{(p)}$ + Laser, I + C + P, and I + C + P + Laser groups. The concentrations of the therapeutics were as follows: IR780: 2 mg/kg, Cur: 1 mg/kg and partzymes: 1 μ mol/kg. For the laser treatment groups, the temperature of the tumor site was monitored in real time by the in vivo imaging system. Radiation was stopped when the temperature reached -45 °C and continued when the temperature dropped. The total treatment time was 5 min. The tumor volumes were calculated using the in vivo imaging system software by monitoring the total flux of bioluminescence. After 40 days of treatment, the tumors connected to the spleen were taken for comparison. For orthotopic tumor models, the maximum tumor diameter allowed was 1.5 cm. Humane endpoints encompass tumor burden exceeding 10% of normal body weight, animal weight loss surpassing 20% of the normal animal weight, and persistent self-harm by the animal. Humane endpoints involve euthanasia through cervical dislocation under deep anesthesia. All animal procedures adhere to the guidelines approved by the Institutional Animal Care and Use Committee (IACUC) of Zhejiang Center of Laboratory Animals (ZJCLA). Pre-experimentation ensures that orthotopic tumor weights align with established

standards during the treatment period. Also, the ex vivo photographs in this experiment confirmed that none of the tumors exceeded this limit.

TUNEL, HSP70, and PTEN staining

After the slices were dried slightly, a circle around the tissue was drawn with a histochemical pen (to prevent liquid from flowing away), proteinase K was added to the circle to cover the tissue, and the tissue was incubated in a 37 °C incubator for 25 min. The slides were placed in PBS (pH 7.4) on a decolorizing shaker and washed 3 times with 5 min shaking each time. After the slices were slightly dried, working rupture solution was added to the circle to cover the tissue, and the slides were incubated at room temperature for 20 min. The slides were placed in PBS (pH 7.4) and washed 3 times on a decolorizing shaker. Subsequently, for TUNEL staining, appropriate amounts of reagent 1 (TdT) and reagent 2 (dUTP) were taken from the TUNEL kit, mixed 1:9 and added to the circle to cover the tissue. Then, the slides were flattened in a wet box and incubated for 2 h at a constant temperature of 37 °C. A small amount of water was added to the humid box to maintain humidity. For HSP70 staining, HSP70 antibody was added to the sample after dilution at 1:100–1:500. After washing with PBS three times, the secondary antibody, Cy3-conjugated goat anti-rabbit IgG, was added, and the slides were incubated for 60 min. For PTEN staining, the tumor sections were stained with anti-PTEN antibody. Later, the sections were all washed with PBS (pH = 7.4) 3 times for 5 min each. After removing the PBS, the secondary antibody, Cy3-conjugated goat anti-rabbit IgG, was added, and the sections were incubated for 60 min. DAPI staining solution was also added to the circle, and the sections were incubated for 10 min at room temperature in the dark. Then, the slides were placed in PBS (pH 7.4) and washed 3 times. Finally, the slices were observed under a fluorescence microscope. The positivity rate of the experiment was calculated with ImageJ.

Analysis of HSP70 levels by qPCR

The intratumoral and paracancerous tissue HSP70 mRNA levels were assessed with qPCR. The forward primer and reverse primer for HSP70 were 5'-ACCAAGCAGACGCAGATCTTC-3' and 5'-CGCCCTCGTACACCTGGAT-3', respectively. The forward primer and reverse primer for GAPDH were 5'-GGCATGGACTGTGGTCATGA-3' and 5'-GGCATGGACTGTGGTCATGA-3', respectively.

Statistics and reproducibility

All results are expressed as the mean value \pm standard deviation. Student's unpaired *t* test (two-tailed) was employed for comparisons between different groups. All statistical analyses were performed using GraphPad Prism 9.0. and $p < 0.05$ was considered to indicate statistical significance. The measurements were taken from distinct samples. No statistical method was used to predetermine the sample size. No data were excluded from the analyses. Data collection and analysis were not performed blind to the conditions of the experiments. All results may be duplicated from the available source data files.

Reporting summary

Further information on research design is available in the Nature Portfolio Reporting Summary linked to this article.

Data availability

The authors declare that all the data supporting the findings of this study are available within the Article, Supplementary Information or Source Data file. The source data generated in this study have been deposited in the Figshare database at: https://figshare.com/articles/dataset/Source_Data_xlsx/24271477. Source data are provided with this paper.

References

- Ding, F. et al. Polydopamine-coated nucleic acid nanogel for siRNA-mediated low-temperature photothermal therapy. *Biomaterials* **245**, 119976 (2020).
- Wang, B. K. et al. Gold-nanorods-siRNA nanoplex for improved photothermal therapy by gene silencing. *Biomaterials* **78**, 27–39 (2016).
- Li, G. C., Li, L., Liu, R. Y., Rehman, M. & Lee, W. M. Heat shock protein hsp70 protects cells from thermal stress even after deletion of its ATP-binding domain. *Proc. Natl Acad. Sci. USA* **89**, 2036–2040 (1992).
- Luo, H. et al. Mutually synergistic nanoparticles for effective thermo-molecularly targeted therapy. *Adv. Funct. Mater.* **27**, 1702834 (2017).
- Tian, H. et al. Low side-effect and heat-shock protein-inhibited chemo-phototherapy nanoplatfrom via co-assembling strategy of biotin-tailored IR780 and quercetin. *Chem. Eng. J.* **382**, 123043 (2020).
- Wang, Y. et al. Engineering electronic band structure of binary thermoelectric nanocatalysts for augmented pyrolytic tumor nanotherapy. *Adv. Mater.* **34**, 2106773 (2022).
- Chang, M. et al. Single-atom Pd nanozyme for ferroptosis-boosted mild-temperature photothermal therapy. *Angew. Chem. Int. Ed.* **60**, 12971–12979 (2021).
- Chen, W.-H. et al. Overcoming the heat endurance of tumor cells by interfering with the anaerobic glycolysis metabolism for improved photothermal therapy. *ACS Nano* **11**, 1419–1431 (2017).
- Chen, Q.-W. et al. Self-mineralized photothermal bacteria hybridizing with mitochondria-targeted metal-organic frameworks for augmenting photothermal tumor therapy. *Adv. Funct. Mater.* **30**, 1909806 (2020).
- Wu, C. et al. Acid-triggered charge-convertible graphene-based all-in-one nanocomplex for enhanced genetic phototherapy of triple-negative breast cancer. *Adv. Healthc. Mater.* **9**, e1901187 (2020).
- Xin, X. et al. Redox-responsive nanoplatfrom for codelivery of miR-519c and gemcitabine for pancreatic cancer therapy. *Sci. Adv.* **6**, eabd6764 (2020).
- Gong, X. et al. A smart theranostic nanocapsule for spatiotemporally programmable drug delivery and efficient gene silencing. *Angew. Chem. Int. Ed. Engl.* **59**, 21648–21655 (2020).
- Ämmälä, C. et al. Targeted delivery of antisense oligonucleotides to pancreatic β -cells. *Sci. Adv.* **4**, eaat3386 (2018).
- Borggräfe, J. et al. Time-resolved structural analysis of an RNA-cleaving DNA catalyst. *Nature* **601**, 144–149 (2022).
- Yi, D., Zhao, J. & Li, L. An enzyme-activatable engineered DNzyme sensor for cell-selective imaging of metal ions. *Angew. Chem. Int. Ed. Engl.* **60**, 6300–6304 (2021).
- Ma, L. & Liu, J. Catalytic nucleic acids: biochemistry, chemical biology, biosensors, and nanotechnology. *iScience* **23**, 100815 (2020).
- Wang, J. et al. A self-catabolic multifunctional DNzyme nanosponge for programmable drug delivery and efficient gene silencing. *Angew. Chem. Int. Ed.* **60**, 10766–10774 (2021).
- Yin, Y. et al. DNzyme-powered three-dimensional DNA walker nanoprobe for detection amyloid beta-peptide oligomer in living cells and in vivo. *Anal. Chem.* **92**, 9247–9256 (2020).
- Li, F. et al. A proton-activatable DNA-based nanosystem enables co-delivery of CRISPR/Cas9 and DNzyme for combined gene therapy. *Angew. Chem. Int. Ed. Engl.* **61**, e202116569 (2022).
- Peng, H., Li, X.-F., Zhang, H. & Le, X. C. A microRNA-initiated DNzyme motor operating in living cells. *Nat. Commun.* **8**, 14378 (2017).
- Wang, Y., Nguyen, K., Spitale, R. C. & Chaput, J. C. A biologically stable DNzyme that efficiently silences gene expression in cells. *Nat. Chem.* **13**, 319–326 (2021).

22. Lyu, M. et al. PNA-assisted DNazymes to cleave double-stranded DNA for genetic engineering with high sequence fidelity. *J. Am. Chem. Soc.* **143**, 9724–9728 (2021).
23. Liu, S.-Y. et al. Ultrathin 2D copper(I) 1,2,4-triazolate coordination polymer nanosheets for efficient and selective gene silencing and photodynamic therapy. *Adv. Mater.* **33**, 2100849 (2021).
24. Zhou, W., Chen, Q., Huang, P.-J. J., Ding, J. & Liu, J. DNzyme hybridization, cleavage, degradation, and sensing in undiluted human blood serum. *Anal. Chem.* **87**, 4001–4007 (2015).
25. Mokany, E., Bone, S. M., Young, P. E., Doan, T. B. & Todd, A. V. MNazymes, a versatile new class of nucleic acid enzymes that can function as biosensors and molecular switches. *J. Am. Chem. Soc.* **132**, 1051–1059 (2010).
26. Safdar, S., Lammertyn, J. & Spasic, D. RNA-cleaving NAzymes: the next big thing in biosensing? *Trends Biotechnol.* **38**, 1343–1359 (2020).
27. Zhu, D. et al. Encoding DNA frameworks for amplified multiplexed imaging of intracellular microRNAs. *Anal. Chem.* **93**, 2226–2234 (2021).
28. Wang, N., Song, L., Qiu, Y., Xing, H. & Li, J. Hybridization-activated spherical DNzyme for cascading two-photon fluorescence emission: applied for intracellular miRNA measurement by two-photon microscopy. *Sens. Actuators B Chem.* **286**, 250–257 (2019).
29. Yin, X., Chen, B., He, M. & Hu, B. A homogeneous multicomponent nucleic acid enzyme assay for universal nucleic acid detection by single-particle inductively coupled plasma mass spectrometry. *Anal. Chem.* **93**, 4952–4959 (2021).
30. Abdou Mohamed, M. A. et al. Diagnosing antibiotic resistance using nucleic acid enzymes and gold nanoparticles. *ACS Nano* **15**, 9379–9390 (2021).
31. Kozłowski, H. N. et al. A colorimetric test to differentiate patients infected with influenza from COVID-19. *Small Struct.* **2**, 2100034 (2021).
32. Zhou, W., Zhang, Y., Ding, J. & Liu, J. In vitro selection in serum: RNA-cleaving DNazymes for measuring Ca²⁺ and Mg²⁺. *ACS Sensors* **1**, 600–606 (2016).
33. Safdar, S. et al. DNA-only, microwell-based bioassay for multiplex nucleic acid detection with single base-pair resolution using MNazymes. *Biosens. Bioelectron.* **152**, 112017 (2020).
34. Wang, Z. et al. An intelligent nanomachine guided by DNzyme logic system for precise chemodynamic therapy. *Angew. Chem. Int. Ed.* **61**, e202204291 (2022).
35. Giovannetti, E. et al. MicroRNA-21 in pancreatic cancer: correlation with clinical outcome and pharmacologic aspects underlying its role in the modulation of gemcitabine activity. *Cancer Res.* **70**, 4528–4538 (2010).
36. Davis, S., Lollo, B., Freier, S. & Esau, C. Improved targeting of miRNA with antisense oligonucleotides. *Nucleic Acids Res.* **34**, 2294–2304 (2006).
37. Lima, J. F., Cerqueira, L., Figueiredo, C., Oliveira, C. & Azevedo, N. F. Anti-miRNA oligonucleotides: a comprehensive guide for design. *RNA Biol.* **15**, 338–352 (2018).
38. Wang, Z. et al. A bimetallic metal–organic framework encapsulated with DNzyme for intracellular drug synthesis and self-sufficient gene therapy. *Angew. Chem. Int. Ed.* **60**, 12431–12437 (2021).
39. Liu, C. et al. Self-assembly of copper–DNzyme nanohybrids for dual-catalytic tumor therapy. *Angew. Chem. Int. Ed.* **60**, 14324–14328 (2021).
40. Fan, H. et al. A smart DNzyme–MnO₂ nanosystem for efficient gene silencing. *Angew. Chem. Int. Ed.* **54**, 4801–4805 (2015).
41. Zheng, P. et al. A multichannel Ca(2+) nanomodulator for multilevel mitochondrial destruction-mediated cancer therapy. *Adv. Mater.* **33**, e2007426 (2021).
42. Santoro, S. W. & Joyce, G. F. A general purpose RNA-cleaving DNA enzyme. *Proc. Natl Acad. Sci.* **94**, 4262–4266 (1997).
43. Moon, W. J., Yang, Y. & Liu, J. Zn²⁺-dependent DNazymes: from solution chemistry to analytical, materials and therapeutic applications. *ChemBioChem* **22**, 779–789 (2021).
44. Peracchi, A. Preferential activation of the 8–17 deoxyribozyme by Ca²⁺ ions: evidence for the identity of 8–17 with the catalytic domain of the Mg⁵⁺ deoxyribozyme*. *J. Biol. Chem.* **275**, 11693–11697 (2000).
45. Wolfe, B. R., Porubsky, N. J., Zadeh, J. N., Dirks, R. M. & Pierce, N. A. Constrained multistate sequence design for nucleic acid reaction pathway engineering. *J. Am. Chem. Soc.* **139**, 3134–3144 (2017).
46. Clapham, D. E. Calcium signaling. *Cell* **131**, 1047–1058 (2007).
47. Liu, X. et al. DNA framework-encoded mineralization of calcium phosphate. *Chem* **6**, 472–485 (2020).
48. Qi, C., Musetti, S., Fu, L. H., Zhu, Y. J. & Huang, L. Biomolecule-assisted green synthesis of nanostructured calcium phosphates and their biomedical applications. *Chem. Soc. Rev.* **48**, 2698–2737 (2019).
49. Roohani, I., Cheong, S. & Wang, A. How to build a bone?—Hydroxyapatite or Posner’s clusters as bone minerals. *Open Ceram.* **6**, 100092 (2021).
50. Lai, R.-H., Dong, P.-J., Wang, Y.-L. & Luo, J.-B. Redispersible and stable amorphous calcium phosphate nanoparticles functionalized by an organic bisphosphate. *Chin. Chem. Lett.* **25**, 295–298 (2014).
51. Schweikle, M. et al. Stabilisation of amorphous calcium phosphate in polyethylene glycol hydrogels. *Acta Biomater.* **90**, 132–145 (2019).
52. Olesen, P. T., Steenberg, T., Christensen, E. & Bjerrum, N. J. Electrolytic deposition of amorphous and crystalline zinc–calcium phosphates. *J. Mater. Sci.* **33**, 3059–3063 (1998).
53. Chen, F. et al. Europium-doped amorphous calcium phosphate porous nanospheres: preparation and application as luminescent drug carriers. *Nanoscale Res. Lett.* **6**, 67 (2011).
54. Wang, Q. et al. Multifunctional shell-core nanoparticles for treatment of multidrug resistance hepatocellular carcinoma. *Adv. Funct. Mater.* **28**, 1706124 (2018).
55. Chen, L. et al. Autophagy inhibition contributes to the synergistic interaction between EGCG and doxorubicin to kill the hepatoma Hep3B cells. *PLoS ONE* **9**, e85771 (2014).
56. Luchtel, R. A. et al. High-dose ascorbic acid synergizes with anti-PD1 in a lymphoma mouse model. *Proc. Natl Acad. Sci.* **117**, 1666–1677 (2020).
57. Li, Y. et al. Co-delivery of microRNA-21 antisense oligonucleotides and gemcitabine using nanomedicine for pancreatic cancer therapy. *Cancer Sci.* **108**, 1493–1503 (2017).
58. Patutina, O. A. et al. Methyl phosphoramidate backbone modified antisense oligonucleotides targeting miR-21 with enhanced in vivo therapeutic potency. *Proc. Natl Acad. Sci. USA* **117**, 32370–32379 (2020).
59. Yan, J. et al. Peritumoral microgel reservoir for long-term light-controlled triple-synergistic treatment of osteosarcoma with single ultra-low dose. *Small* **17**, 2100479 (2021).
60. Kebebe, D. et al. Dimeric α (RGD) peptide conjugated nanostructured lipid carriers for efficient delivery of Gambogic acid to breast cancer. *Int. J. Nanomed.* **14**, 6179–6195 (2019).
61. Calkins, K. G. *Measuring Correlation* (Andrews University, 2005).
62. Zhang, L. et al. Mitochondria-targeted artificial “Nano-RBCs” for amplified synergistic cancer phototherapy by a single NIR irradiation. *Adv. Sci.* **5**, 1800049 (2018).
63. Liu, Y. et al. The targeting of non-coding RNAs by curcumin: facts and hopes for cancer therapy (Review). *Oncol. Rep.* **42**, 20–34 (2019).
64. Hu, Y. et al. Preparation of photothermal responsive and ROS generative gold nanocages for cancer therapy. *Chem. Eng. J.* **421**, 129744 (2021).

65. Yan, J. et al. Self-assembly of DNA nanogels with endogenous microRNA toehold self-regulating switches for targeted gene regulation therapy. *Biomater. Sci.* **10**, 4119–4125 (2022).
66. Cappellesso, F. et al. Targeting the bicarbonate transporter SLC4A4 overcomes immunosuppression and immunotherapy resistance in pancreatic cancer. *Nat. Cancer* **3**, 1464–1483 (2022).
67. Zheng, D. et al. Biomimetic nanoparticles drive the mechanism understanding of shear-wave elasticity stiffness in triple negative breast cancers to predict clinical treatment. *Bioact. Mater.* **22**, 567–587 (2023).
68. Smith, A. J., Clutton, R. E., Lilley, E., Hansen, K. E. A. & Brattelid, T. PREPARE: guidelines for planning animal research and testing. *Lab. Anim.* **52**, 135–141 (2017).
69. Yan, J. et al. Lymphatic clearance is the main drainage route of lamotrigine-loaded micelles following delivery to the brain. *J. Pharm. Pharmacol.* **71**, 1488–1496 (2019).
70. Wang, K. et al. Gas therapy potentiates aggregation-induced emission luminogen-based photoimmunotherapy of poorly immunogenic tumors through cGAS-STING pathway activation. *Nat. Commun.* **14**, 2950 (2023).
71. Wang, J. et al. Orthotopic and heterotopic murine models of pancreatic cancer exhibit different immunological microenvironments and different responses to immunotherapy. *Front. Immunol.* **13**, 863346 (2022).

Acknowledgements

This work was supported by the National Science Foundation (Grant No. 82372145 (H.Z.)). It was also supported by the Research Fellow (Grant No. 353146 (H.Z.)), Project (Grant No. 347897 (H.Z.)), Solution for Health Profile (Grant No. 336355 (H.Z.)), and InFLAMES Flagship (Grant No. 337531 (H.Z.)) grants from the Academy of Finland, Finland, The China Food and Health International Pilot Project (H.Z.) funded by the Finnish Ministry of Education and Culture, The Leading Talents in Scientific and Technological Innovation from Zhejiang Provincial Ten Thousand Talents Plan (Grant No. 2019R52021 (X.S.)), The Key Research and Development Program of Zhejiang Province (Grant No. 2021C03120 (X.S.)), The Key Research and Development Program of Wenzhou (Grant No. ZY2021003 (X.S.)), the National Natural Science Foundation (Grant Nos. 82272172 (W.S.), 81972261 (W.S.)), the Medical Health Science and Technology key Project of Zhejiang Provincial and Ministry Health Commission (Grant No. WKJ-ZJ-2322 (W.S.)), the National Natural Science Foundation of China (Grant No. 82071945 (S.Z.)), Shanghai Committee of Science and Technology, China (Grant No. 21S31905400 (S.Z.)), and the Shanghai Anticancer Association EYAS PROJECT (Grant No. SACA-CY22C07 (D.Z.)). M.R. (CSC202207960005) and J.Y. (CSC202107960001) were sponsored by the China Scholarship Council. We are grateful to Qian Zhou, Ph.D., from the Fudan University Shanghai Cancer Center. We are grateful to Gösta Branders research fund, Åbo

Akademi Research Foundation (Gösta Branders forskningsfond, Stiftelsen för Åbo Akademi).

Author contributions

J.Y. and H.Z. conceived the idea and wrote the manuscript. J.Y., X.M., D.L., and M.R. were responsible for carried out the experiments, material synthesis and animal experiments. D.Z. and S.Z. assisted in manuscript revision related to pancreatic cancer. X.C. helped to conduct parts of the characterization. W.S., X.S., and H.Z. supervised the project and helped with language editing. All authors discussed the results and have given approval to the final version of the paper.

Competing interests

The authors declare no competing interests.

Additional information

Supplementary information The online version contains supplementary material available at <https://doi.org/10.1038/s41467-023-42740-2>.

Correspondence and requests for materials should be addressed to Weijian Sun, Xian Shen or Hongbo Zhang.

Peer review information *Nature Communications* thanks Wing Hin Lee, and the other, anonymous, reviewer(s) for their contribution to the peer review of this work. A peer review file is available.

Reprints and permissions information is available at <http://www.nature.com/reprints>

Publisher's note Springer Nature remains neutral with regard to jurisdictional claims in published maps and institutional affiliations.

Open Access This article is licensed under a Creative Commons Attribution 4.0 International License, which permits use, sharing, adaptation, distribution and reproduction in any medium or format, as long as you give appropriate credit to the original author(s) and the source, provide a link to the Creative Commons license, and indicate if changes were made. The images or other third party material in this article are included in the article's Creative Commons license, unless indicated otherwise in a credit line to the material. If material is not included in the article's Creative Commons license and your intended use is not permitted by statutory regulation or exceeds the permitted use, you will need to obtain permission directly from the copyright holder. To view a copy of this license, visit <http://creativecommons.org/licenses/by/4.0/>.

© The Author(s) 2023

¹Joint Centre of Translational Medicine, Wenzhou Key Laboratory of Interdiscipline and Translational Medicine, The First Affiliated Hospital of Wenzhou Medical University, Wenzhou, China. ²Department of General Surgery, The First Affiliated Hospital of Wenzhou Medical University, Wenzhou, Zhejiang, China. ³Pharmaceutical Sciences Laboratory, Faculty of Science and Engineering, Åbo Akademi University, Turku, Finland. ⁴Turku Bioscience Centre, University of Turku and Åbo Akademi University, Turku, Finland. ⁵Department of Gastrointestinal Surgery, The Second Affiliated Hospital and Yuying Children's Hospital of Wenzhou Medical University, Wenzhou 325027 Zhejiang, China. ⁶Department of Ultrasound, Fudan University Shanghai Cancer Center, Shanghai 200032, P.R. China. ⁷These authors contributed equally: Jiaqi Yan, Xiaodong Ma, Danna Liang, Meixin Ran.
✉ e-mail: fame198288@126.com; shenxian@wmu.edu.cn; hongbo.zhang@abo.fi

